

# **Investigation of Contact Mechanics and Friction of Rubber Compounds by Experimental Techniques and Numerical Simulations**

Von der Fakultät für Maschinenbau  
der Gottfried Wilhelm Leibniz Universität Hannover zur Erlangung des Grades  
Doktor-Ingenieur

Dr.-Ing.

genehmigte Dissertation von

**M.Sc. Jacopo Cugliari**

**2021**

**Vorsitzender: Prof. Dr.-Ing S. Kabelac, IFT**

**1. Referent: Prof. Dr.-Ing. G. Poll, IMKT**

**2. Referent: Prof. Dr.-Ing. J. Wallaschek, IDS**

**3. Referent: Prof. Dr. habil. M. Klüppel, DIK**

**Tag der Promotion: 27.04.2021**

# Acknowledgement

My thesis could not be possible without the help of many people and institutions.

Firstly, I would like to express my sincere gratitude to my advisor Prof. Dr.-Ing. G. Poll for the opportunity to attend my Ph.D.

I am also deeply thankful to my supervisor Prof. Manfred Klüppel who pushed me to do creative research and for being available for illuminating theoretical and experimental explanations. I would also like to thank Dr. Jens Meier who always had an open ear for easy questions and more advanced problems, at every time willing to interrupt his own work for the sake of this research project. Their experience and guidance contributed a large part to this work.

The Bridgestone Corporation is acknowledged for financial support during these three years of my work at DIK. About this, I would like to thank the project partners P. Straffi and P. Agoretti for their insightful comments, support and motivation who have had a huge impact on my professional and communication skills.

Additionally, I would like to thank all the current and former members of my departments “Elastomer Physics” and “Material Concept and Modeling” especially Dr. Andrej Lang, who was a wonderfully helpful colleague not only for technical aspects. Part of my results is due to his ingenious spirit.

Of course, all members of DIK contributed to this thesis by always supporting me to work with a sense of energy and teaching me the German language and the instructions for laboratory and research facilities.

A special thanks also go to A. Sarmukaddam and the other colleagues from EDV-Labor for their helpful introduction into the Finite Element world.

A special thank you I would give to my girlfriend Christine who supported and encouraged me especially before the dissertation.

Last but not least, I would like to thank my parents and my brother Manuel for supporting me spiritually and always being by my side throughout the most challenging moments of my life.

# Abstract

## **Title: Investigation of Contact Mechanics and Friction of Rubber Compounds by Experimental Techniques and Numerical Simulations**

The contact of car tires with road tracks is a research field of high practical importance since grip properties during tire-road interaction have a direct impact on safety issues. To improve the tire properties it is necessary a deep understanding of the tire-road contact mechanics, as well as the underlying rubber friction physics. Despite this topic is widely investigated, there are no complete predictive models capable to describe the friction interaction for practical applications, for this reason, it still means a big challenge for the scientific community. Therefore, the main objective of the present research is to predict the performances of different rubber materials on dry and wet rough road tracks.

The effect of many intrinsic and extrinsic factors such as substrate roughness, rubber-surface affinity, temperature, load, sliding speed, lubrication, geometrical parameters and viscoelastic material properties on contact properties and the resulting friction behavior is investigated. Hence, the complex friction process is split into different subtopics, which are analyzed and modeled. From one perspective, the contact mechanics through a 2D FEM tool is investigated on different substrates to determine the main friction contribution called hysteresis. This contribution is based on the energy losses in a broad frequency scale due to cyclic deformations of the rubber by asperities. An accompanying experimental tool based on the measurement of rubber indentation into substrate asperities is designed to provide a physical understanding of static and dynamic contact problems and to validate the FEM model. The tools developed also provide access to unavailable data, such as local pressures, dissipated energies, contact area and rubber indentation. It was also figured out the effect of rubber geometry on dynamic contact mechanics through experimental and 3D FEM simulations. On the other side, the adhesion is studied as the second main friction contribution, defined as a result of the peeling effects governed by viscoelastic crack opening mechanisms between rubber and substrate on dry and wet surfaces, by considering the physical-chemical nature of the contact. It is found that the hysteresis response is enhanced with the so-called dry patches effect in the water condition. Consequently, a partial adhesion occurs where the water is wiped away due to the dewetting phenomena.

Furthermore, the thermal effect (heat build-up) which occurs during sliding friction on dry and wet rough surfaces is investigated with a thermographic camera. Dry friction heating arises differently between short/wide and long/narrow rubber blocks. By considering wet conditions, the presence of lubricant with high thermal diffusivity cools down the system generating less heat build-up in comparison to a dry surface. An analytical solution of lubricated heat build-up generated in the rubber during sliding due to the viscoelastic losses, is provided and shows qualitatively good agreement with the experiment.

By recombining the modeled subtopics of the split friction process it was built-in a hybrid model composed of a FEM tool and an analytical adhesion model which shows a good prediction of dry/water grip at low macroscopic speeds where mainly adhesion and hysteresis occur. Finally, a continuous dry friction master curve is constructed by the combination of measured friction branches for different temperatures over a wide range of sliding speeds, even close to ABS range.



Keywords: *rubber friction, contact mechanics, finite element analysis*

## **Kurzzusammenfassung**

### **Titel: Untersuchung der Reibkontaktmechanik von Gummimischungen durch Experimentelle Techniken und Numerische Simulationen**

Der Kontakt von Autoreifen mit der Fahrbahn ist ein Forschungsfeld von hoher praktischer Bedeutung, da die Hafteigenschaften bei der Reifen/Fahrbahn-Wechselwirkung einen direkten Einfluss auf Sicherheitsaspekte haben. Um die Reifeneigenschaften zu verbessern, ist ein tieferes Verständnis des Kontaktmechanismus zwischen Reifen und Fahrbahn sowie der zugrunde liegenden Physik der Gummireibung unerlässlich. Ein vollständiges Modell, mit dem die Reibung für praktische Anwendungen beschrieben werden kann, ist nach wie vor eine große Herausforderung für die Wissenschaft. Das Hauptziel dieser Arbeit ist es, die Reibung verschiedener Gummimaterialien auf trockener und nasser Fahrbahn vorherzusagen.

Einflüsse innerer und äußerer Faktoren, wie Rauheit, Affinität zur Gummioberfläche, Temperatur, Belastung, Gleitgeschwindigkeit, Schmierung, geometrische Parameter und viskoelastische Materialeigenschaften auf die Kontakteigenschaften und das resultierende Reibungsverhalten wurden untersucht. Daher wurde der komplexe Reibungsprozess in verschiedene Bereiche unterteilt, in denen jeder Beitrag separat analysiert und modelliert wurde. Es wurde die Kontaktmechanik mit einem 2D-FEM-Werkzeug auf verschiedenen Substraten untersucht, um den Haupttreibungsbeitrag, der als Hysterese bezeichnet wird, zu bestimmen. Sie wird durch Energieverluste, die auf einer breiten Frequenzskala angesiedelt sind, wegen zyklischer Verformungen des Gummis durch Unebenheiten verursacht. Hierzu wurde ein geeigneter experimenteller Aufbau zur Messung der Gummieindrückung (der Unebenheiten des Substrats) in Form eines Reibschlittens entwickelt, um ein physikalisches Verständnis der statischen und dynamischen Kontaktprobleme zu ermöglichen und das FEM-Modell zu validieren. Außerdem wurden Softwaretools entwickelt, die eine Quantifizierung relevanter lokaler Größen ermöglichen, wie lokale Drücke, Energieverlust, wahre Kontaktfläche oder Gummieindrückung. Weiterhin wurde auch die Auswirkung der Gummigeometrie auf die dynamische Kontaktmechanik durch experimentelle und 3D-FEM-Simulationen ermittelt.

Es wurde der als Adhäsion bezeichnete weitere Haupttreibungsbeitrag analysiert. Dieser ergibt sich aus dem Peeling-Effekt, welcher auf viskoelastischen Rissöffnungsmechanismen zwischen Gummi und Substrat auf trockener und nasser Oberfläche, unter Berücksichtigung der physikalisch-chemischen Natur des Kontakts, beruht. Es wurde festgestellt, dass die Hystereseantwort durch den sogenannten Trockenfleckeffekt unter Wasserbedingungen verstärkt wird, was bedeutet, dass eine teilweise Adhäsion auftritt, wenn das Wasser aufgrund von Entnetzungsphänomenen abgewischt wird. Außerdem wurde der thermische Effekt (HBU), der bei Gleitreibung auf trockenen und nassen rauen Oberflächen auftritt, mit einer Infrarotkamera untersucht. Die Ergebnisse der Trockenreibungserwärmung sind für kurze / breite und lange / schmale Gummiblöcke unterschiedlich. Im nassen Zustand kühlt das Vorhandensein eines Schmiermittels mit hoher

thermischer Diffusionsfähigkeit das System ab und erzeugt im Vergleich zu einer trockenen Oberfläche weniger HBU. Eine analytische Lösung für HBU unter geschmierten Bedingungen, die aufgrund viskoelastischer Verluste im Reifen während des Gleitens erzeugt wird, wurde bereitgestellt, und es wurde eine qualitativ gute Übereinstimmung mit dem Experiment festgestellt.

Durch die Rekombination der modellierten Einzeleffekte des Spaltreibungsprozesses wurde ein Hybridmodell erzeugt, das aus dem FEM-Tool und dem analytischen Adhäsionsmodell besteht, erzeugt und eine gute Vorhersage des Trocken-Wasserhaftungsverhaltens bei niedrigen makroskopischen Geschwindigkeiten zeigt, bei denen hauptsächlich Adhäsion und Hysterese auftreten.

Schließlich wurde durch die Kombination einzelner Reibmessungen für verschiedene Temperaturen und Gleitgeschwindigkeiten, inklusive des ABS-Bereiches, eine kontinuierliche Reibmasterkurve erstellt, welche für weitergehende praxisrelevante Materialbewertungen herangezogen werden kann.

Schlagworte: *Elastomerreibung, Kontaktmechanik, Finite Elemente Analyse*

# Contents

<b>ACKNOWLEDGEMENT</b> .....	<b>I</b>
<b>ABSTRACT</b> .....	<b>II</b>
<b>KURZZUSAMMENFASSUNG</b> .....	<b>III</b>
<b>CONTENTS</b> .....	<b>V</b>
<b>1. INTRODUCTION</b> .....	<b>1</b>
1.1 MOTIVATION .....	1
1.2 STRUCTURE OF THE THESIS .....	3
<b>2. ELASTOMERS AND GENERAL PROPERTIES</b> .....	<b>4</b>
2.1 NATURAL RUBBER (NR) .....	5
2.2 STYRENE-BUTADIENE RUBBER (SBR) .....	6
2.3 VULCANIZATION PROCESS .....	8
2.4 FILLED RUBBER REINFORCEMENT .....	10
2.4.1 Carbon black .....	13
2.4.2 Silica .....	17
2.4.3 Silica versus Carbon black as reinforcing fillers .....	20
2.4.4 Filler-polymer interactions .....	20
2.4.5 Mullins effect .....	21
2.5 DYNAMIC - MECHANICAL PROPERTIES OF ELASTOMERS .....	23
2.5.1 Linear viscoelasticity .....	23
2.5.2 Time-temperature superposition principle .....	29
2.6 ELASTOMER FRICTION PHYSICS .....	35
2.6.1 Numerical models .....	41
2.6.2 Hysteresis and adhesion friction .....	42
2.7 MODELLING RUBBER FRICTION .....	48
2.7.1 Surface roughness description .....	48
2.7.2 Modeling in contact mechanics .....	51
2.7.3 Analytical friction model .....	53
2.8 CONTINUUM MECHANICS FOR FINITE ELEMENT ANALYSIS .....	60
2.8.1 Kinematics .....	60
2.8.2 Basic balance equations .....	62
2.9 CONSTITUTIVE EQUATIONS FOR FILLED RUBBER .....	64
2.9.1 Hyperelasticity: Invariant-based continuum mechanics treatments .....	65
2.9.2 Derivation of finite linear viscoelasticity for numerical approach .....	66
2.9.3 Overview of the main rubber material models and its parameters identification .....	69
2.9.4 Finite Element Analysis: fundamental concepts of contact mechanics .....	77
<b>3. EXPERIMENTAL METHODS AND MATERIALS</b> .....	<b>81</b>
3.1 RUBBER MATERIALS SELECTION .....	81
3.2 MIXING AND VULCANIZATION .....	83
3.3 QUASI-STATIC STRESS-STRAIN MEASUREMENT .....	85
3.4 DYNAMIC MECHANICAL ANALYSIS .....	87

3.5	FRICION MEASUREMENTS .....	89
3.5.1	Substrates .....	91
3.5.2	Measurement of the roughness .....	92
3.6	INDENTATION MEASUREMENT BY LASER DISPLACEMENT SENSOR .....	94
3.7	THERMOGRAPHIC MEASUREMENT .....	95
3.8	CONTACT ANGLE MEASUREMENT .....	97
<b>4.</b>	<b>RESULTS AND DISCUSSION .....</b>	<b>102</b>
4.1	FRICION MEASUREMENT ON ROUGH SUBSTRATE .....	102
4.2	MECHANICAL BEHAVIOUR .....	107
4.2.1	Quasi static analysis .....	107
4.2.2	Dynamic mechanical analysis .....	109
4.3	FINITE ELEMENT ANALYSIS FOR THE HYSTERESIS FRICTION .....	116
4.3.1	Material modelling .....	116
4.3.2	Simulation results for model surfaces .....	127
4.3.3	Simulation results for real rough surfaces .....	132
4.3.4	Dependence of the friction on rubber geometry .....	134
4.4	INVESTIGATION OF RUBBER INDENTATION AND RELAXATION ON DRY SUBSTRATE.....	144
4.4.1	Static indentation.....	146
4.4.2	Dynamic indentation .....	152
4.4.3	Validation of the FEM model through indentation experiments .....	155
4.4.4	Indentation master curve .....	157
4.5	NUMERICAL SIMULATION OF ADHESION FRICTION .....	161
4.5.1	Dry friction.....	162
4.5.2	Water friction .....	164
4.6	THERMAL EFFECT INVESTIGATION .....	171
4.6.1	Estimation of heat build-up on dry rough substrate .....	171
4.6.2	Estimation of heat build-up on wet rough substrate .....	178
4.7	FRICION PREDICTION ON DRY/WET ROUGH SURFACES .....	180
4.8	DRY FRICTION MASTER CURVES .....	185
<b>5.</b>	<b>SUMMARY AND CONCLUSIONS .....</b>	<b>188</b>
	<b>APPENDIX .....</b>	<b>192</b>
	<b>REFERENCES.....</b>	<b>203</b>
	<b>CURRICULUM VITAE.....</b>	<b>214</b>



## List of symbols and abbreviations

$\gamma$	Shear deformation
$\varepsilon$	Strain
$\zeta$	Entropy
$\eta$	Viscosity
$\Theta$	Absolute temperature
$\kappa$	Thermal diffusivity
$\lambda$	Wavelength of sinusoidal substrate
$\lambda_1, \lambda_2, \lambda_3$	Principal extension ratio
$C_{10}, C_{20}, C_{30}$	Parameter of hyperelastic model
$\mu_{adh}$	Adhesion friction coefficient
$\mu_{hys}$	Hysteresis friction coefficient
$\alpha$	Dry patches (level of adhesion in water condition)
$S$	Spreading coefficient
$\gamma_{ij}$	Interfacial surface free energy between the bodies i and j
$\rho$	Density
$A_c$	Real contact area
$z_p$	Rubber indentation
$\sigma$	Engineering stress
$\tau$	Relaxation time
$\tau_s$	Interfacial shear strength
$\omega$	Angular frequency
$\psi$	Helmholtz energy

$I_1, I_2, I_3$	First, second, third invariant of the stretch tensor
$K$	Thermal conductivity
$\mathbf{L}$	Linear momentum
$m$	Mass
$M$	Torque
$\mathbf{q}$	Heat flux vector
$\dot{Q}$	Heat rate production per unit time and volume
$R$	Asperity radius
$t$	Time
$T$	Temperature
$\tan \delta$	Loss factor
$G'$	Storage modulus (shear mode)
$G''$	Loss modulus (shear mode)
$G^*$	Complex modulus (shear mode)
$u$	Internal energy
$v$	Velocity
$V$	Volume
$v_c$	Critical velocity (adhesion friction)
$W_F$	Friction work

---

SBR	Styrene Butadiene rubber
FEA	Finite Element Analysis
FEM	Finite Element Method
CENER	Energy per volume dissipated due to viscoelasticity
HDC	Height difference correlation
HBU	Heat build-up
NR	Natural rubber
phr	Parts per hundred rubber
DMTA	Dynamic Thermal Mechanical Analysis
WLF	Williams Landel and Ferry
C1,C2	WLF parameters
$a_T$	Horizontal shift factor
$b_T$	Vertical shift factor
$E_a$	Activation energy
R	Gas constant
CB	Carbon black
Si	Silica





# 1.Introduction

## 1.1 Motivation

The friction behaviour of elastomers plays a central role in the functionality of smart rubber materials as well as for energy efficiency and environmental protection. The friction behaviour of rubber products such as seals, conveyor belts, dampers and tires require a deep understanding. Especially, the continuous improvement of high-performance tires remains a challenging task for tire manufacturers.

Tire manufacturers face several challenging tasks in the development process of new tires. The superior aim is to optimize characteristics like rolling resistance, handling, noise, wear or braking performance among others. These aims partly contradict themselves leading to complex relationships and target conflicts during the development process. In order to face the challenges in the tire industry (Figure 1 top), experimental tests in laboratory and simulation techniques are widely used. More sophisticated and improved simulation tools are essential in combination with new experimental approaches for further improvement of the complex grip behaviour of tires, containing multiple physical phenomena (see Figure 1 bottom).

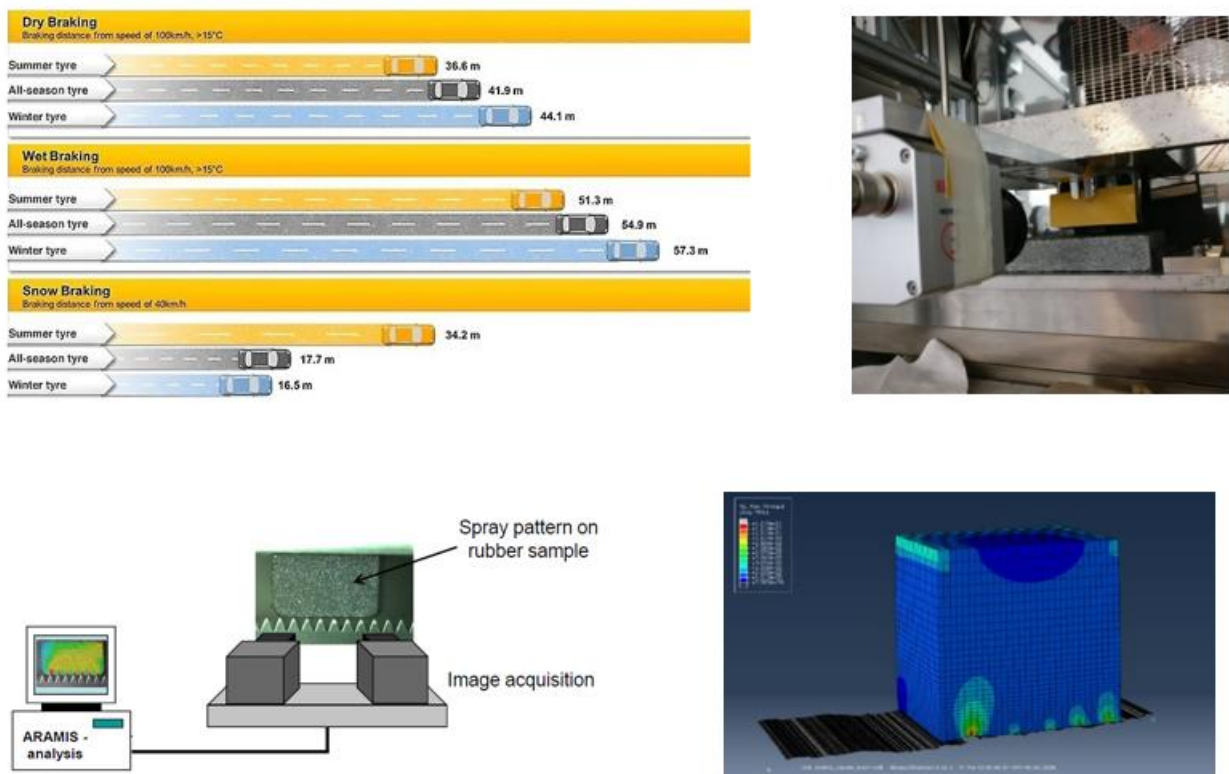


Figure 1. Exemplary braking distance of different summer, winter and all-season tyres in dry, wet and snow conditions (top left). Fundamental studies: friction experiments measuring the temperature build up with an infrared-camera (top right), strain level with ARAMIS equipment (bottom left) and FEM of a sliding rubber blocks (bottom right).

This work concentrates on the improvement of modeling the safety-relevant aspect of grip performance on wet and dry surfaces. A massive improvement of the car braking performance was achieved over the last decades by introducing for example anti-lock braking systems (ABS) or compounds with an improved grip level. Reduced braking distances based on tire optimized performances will help to reduce the number of traffic fatalities in the future, contributing to the desired goal of zero fatalities and accidents, called vision zero.

One of the main goals of this work is to improve the understanding of the physical processes of rubber friction, which take place on a large band of length scales. To achieve this goal, the work concentrates on the effects of a macroscopic rubber block with the size of a few centimeters down to the smallest relevant length scales of some micrometers excluding the analysis of tire mechanics. The method is validated with experimental results for a deeper understanding of the process. This provides useful information, which is currently inaccessible in experimental studies. Therefore, the tire engineers can further improve the grip performance of the new innovative tires.

The work investigate the frictional behavior of a rubber block (e.g. the tread profile of a tire) on a rough surface like road track. The roughness of the surface has an essential influence on the frictional resistance. Because of its relative softness, the rubber undergoes large deformations and is therefore able to adapt to the asperities of the track. The degree of flexibility of the material depends on multiple factors. Due to the viscoelastic behavior of the rubber, its reaction is much stiffer in the case of large sliding velocities than for small speeds. The actual temperature of the material plays an important role and changes mechanical properties. Hence, the temperature will be influenced by the amount of heat, which is generated due to friction. The possible influence of rainwater and lubrication films between road and rubber increases the complexity of the problem.

Adhesion effects may have great relevance, wear and abrasion of the rubber change its profile and during extreme brake applications, even the track profile may be battered. Practical experiments are often limited in their results. Experimental rigs have mostly crucial restrictions concerning the applicable sliding velocity or the normal pressure. Exact temperature measurements in the contact zone are always difficult or sometimes even impossible, the penetration depth and true contact area can only be estimated and the repetition of measurements will often take place under different environmental conditions. During the performance of measurements, it is in most cases impossible to separate the various effects, which influence the frictional behavior.

Local heating can not be excluded, the rubber may suffer from microcracks or the surface characteristics change because of dust or lubrication. Practically none of these influences can be switched off or separated in real-life experiments. The interpretation of experiments suffers from the complexity and inseparability of the multiple conditions related to material and environment. Hence, it is necessary to understand the fundamental mechanisms of rubber friction by dividing the topic into different subareas to seal off the single effects.

A numerical simulation using the Finite Element Method seems to be ideally suited to understand the basic principles of rubber friction. Numerical tests are repeatable under different conditions, whereas the user can select the interesting effects. However, computational methods represent only virtual reality and the results depend on the model definitions. The purpose of this work is to find proper models and formulations to simulate the most important effects of rubber friction and figure out the

connections between them. Besides the derivation of a friction law using numerical calculations, the relation between the different friction contributions as well as their relevance should become clearer. The surface of a road track has a fractal character, it is rough over many decades in length scales and each of them contributes to rubber friction. A reasonable finite element analysis of models, which includes three to four different length scales, is prohibitively expensive despite the rapidly growing of computational power. A multiscale method is required to determine the effects from micro-roughness of single asperities to macro-roughness of the track. Since the length scales range occur from some micrometers to a few millimeters, several intermediate steps are necessary instead of a singular scale transition. A defined frequency of the rubber is excited based on the roughness scale. Hence, different roughness yield a widespread loading frequency range, which is important due to the damping characteristics of the elastomer.

## 1.2 Structure of the thesis

First, a general knowledge about polymer structure and filler reinforcement is provided in chapter 2. Furthermore, the dynamic mechanical properties of elastomers are described, especially the viscoelastic properties and an overview of rubber friction physics including experimental studies, the contributing effects and modelling approaches in chapters 2.5 and 2.6. Afterwards, the continuum mechanical fundamentals and basic equations for the solution of contact problems are presented, including rough surfaces and viscoelastic rubber materials in a geometrically nonlinear setting, in chapter 2.8 as a prerequisite to understand friction mechanisms. The governing equations are solved with the finite element method, therefore the background of finite elements for solid mechanics and contact problems is explained in chapter 0. In chapter 3, the material and methodology to solve the friction topic is provided. The results of the research work are illustrated in chapter 4 where the rubber friction topic is divided into different physical effects, these are one at a time modelled and explained. First, the mechanical characterization under static and dynamic condition is presented in chapter 4.2. An experimental friction campaign on dry/wet rough substrate is reported in chapter 4.1 to define the friction dependence on viscoelastic properties of the material and to validate the friction prediction.

In chapter 4.3, the FEM simulation on the model and randomly rough substrates are shown to predict hysteresis friction contribution. The validation of the FEM as well as a physical understanding of contact mechanism rubber/rough track is described (chapter 4.4) through a new experimental method based on indentation measurements. Chapter 4.5 shows the prediction of adhesion contribution determined through an analytical model, followed by a deep insight study of water grip through a physical-chemical investigation of nature as well as the so-called dry patches effect. Thermal effect (Heat Build-up HBU) on friction by depending on rubber geometry and lubricant are studied in chapter 4.6. In chapter 4.7, the global response of the friction model composed by adhesion and hysteresis contributions is validated with experimental results to prove the prediction quality of the method used. The results are summarized in chapter 5 where conclusions and outlook are given.

## 2. Elastomers and general properties

The history of elastomers in the form of natural rubber can be traced back to many centuries before Christ. Nevertheless, it was not until Charles Goodyear discovered the possibility of chemically crosslinking rubber in 1839 by adding sulphur to dry it, that rubber could be used economically and in many components.

Looking at the properties of an uncrosslinked rubber, it can be seen that the elastomer melt is very soft and sticky, especially at high temperatures, and quickly loses its dimensional stability under load. The polymer matrix, which is present in the form of billets, is stabilized by chemical crosslinking, e.g. by linking the polymer chains with sulfur bridges so the flow of the material only takes place at considerably higher temperatures. This leads to an increase in the temperature window in which an elastomer material can be technically used.

In addition to the natural rubber obtained from the sap of the rubber tree "hevea brasiliensis", various synthetically produced rubbers are also used, extending greatly the functional spectrum of the elastomers. As a result, many material properties, whether hardness or tensile strength or chemical compatibility or resistance, can be adapted to the application. Further development is by no means complete. With the introduction of blend technology, in which a blend between several polymer types or even thermoplastics is produced, and the currently innovative silica-silane technology, the property profile of rubber materials is controlled even more specifically and optimized for the intended application. The use of novel carbon-based fillers such as carbon nanotubes (CNTs), graphenes and magneto-sensitive particles also opens up many possibilities for adapting the rubber material to future requirements. Today, rubber is one of the most important raw materials, not only in the automotive industry, and has become indispensable for many applications. The special properties of rubber make it a very valuable material in the manufacture of many products such as rubber clothing, rubber soles and tyres, gaskets, conveyor belts and other technical articles. In addition, many conventional materials are being replaced by elastomeric materials.

In general, it can attribute the following properties to a rubber material:

- Rubbers are polymers consisting mostly of long carbon chains with and without subgroups, which can be of different lengths and branched.
- In the case of rubbers, a distinction is made between natural and synthetic rubbers, which are divided into further groups according to their chemical structure [1].
- Elastomers have high ductility and elasticity as well as low modulus of elasticity compared to metals, ceramics and other materials. The residual deformation remains at a low level. The rubber material shows viscoelastic behaviour.
- The glass transition temperature at which the elastomer suddenly shows a change e.g. in the mechanical modulus, the specific heat or the refractive index and behaves like a glassy, frozen solid during cooling is below the usual service temperature or 0°C [2].
- In the presence of reinforcing fillers (see chapter 2.4) or other additives, the property profile of rubber materials can be significantly improved or controlled.

The variety of rubber grades, reinforcing fillers and other additives available on the market today implies that friction properties can also be adapted to the corresponding application. Different elastomers behave very differently. The origin the friction behavior is the viscoelastic properties, which are caused by the molecular structure of the polymers and influenced to the greatest extent. But also the reinforcing fillers can strongly influence the friction process. In this work a typical elastomer for tyre application namely S-SBR and different fillers (carbon black and silica) were therefore considered, these will be briefly presented and explained in the following. In addition, the interactions between the polymer and filler are discussed.

Nowadays there are several types of elastomer available, each of them showing different features. The type of polymer with the longest history of use is polyisoprene, the constituent of natural rubber (NR), which is the concentrated and purified form of latex extracted from a tree, most usually the *Hevea Brasiliensis*, cultivated in tropical regions, mostly South East Asia. In the 1940s several synthetic rubbers were developed to provide an alternative to natural rubber. The most used are styrene-butadiene rubber (SBR) and polybutadiene rubber (BR), which derived from the synthesis of petroleum and natural gas products. The process of synthesis often consists in a free radical emulsion polymerization, whereby a vinyl monomer is polymerized by itself or combined with another monomer to create a high molecular weight polymer. In recent years, the anionic polymerization in solution with use of alky lithium catalysts has become very important to manufacture SBR, in this case known as S-SBR, it is widely used in the tire industry.

Although historically natural latex has always enjoyed a cost benefit advantage over synthetic versions, the great advantage of synthetic rubbers is the possibility to obtain products with specifically tailored properties. Hence, a clear comprehension of rubber molecular structure is essential for an understanding of its physical properties.

The chemical structure and physicochemical properties of each polymer will be briefly explained.

## 2.1 Natural rubber (NR)

The rubber hydrocarbon component of NR consists of over 99.99% of linear cis-1.4 polyisoprene (Figure 2) and its average molecular weight ranges from 200,000 to 400,000 with a relatively broad molecular weight distribution [3]. As a result NR has a peculiar processing behavior.

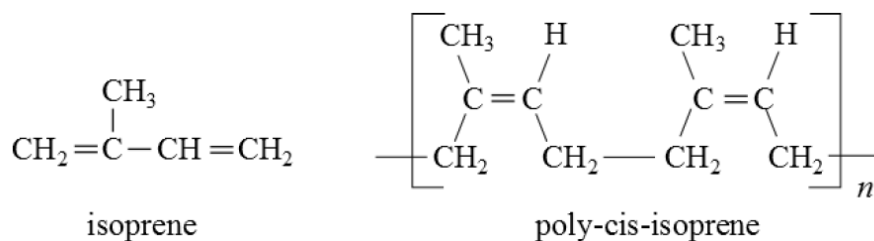


Figure 2. Chemical structure of isoprene and poly-cis-isoprene, which is the main constituent of natural rubber.

The double bonds present in the isoprene unit are a reactive group for the vulcanization reactions with sulphur, but double bonds can also react readily with oxidizing agents, like oxygen and ozone, thus making NR very sensitive to oxidations processes which can significantly degrade its properties (aging). In order to obtain a good aging resistance it is necessary to use protective agents in the compound, and use thiazol accelerators in short cure cycles with not too high temperatures. Nevertheless, even under optimum conditions, the aging and heat resistance of NR vulcanizates does not reach that of most SBR and BR vulcanizates.

Concerning its compounding, NR is too hard to be directly processed therefore it has to be masticated first. The mastication process consists of high shear mixing under the influence of small amounts of oxygen. In this way a scission of polymer chains takes place and the molecular weight is broken down to facilitate the processing of the material [4]. NR vulcanizates show very interesting mechanical properties [5]. In particular, when NR is stretched more than 80 % of its original length, crystallization occurs due to the orientation of the polymer chains (strain crystallization). As a consequence a high tensile strength is observed along the axis of deformation, about 20 MPa or more, contrary to most types of synthetic rubbers [6] [7]. The ultimate elongation is generally about 500 to 1000 %.

Natural rubber (NR) is a renewable resource that is used for several applications in which tires take up a large portion of NR consumption. NR is used in many parts of the tires, especially for truck tire tread compounds as it provides low heat build-up and excellent mechanical properties derived from its ability to form crystals upon being stretched, i.e. strain-induced crystallization.

## 2.2 Styrene-Butadiene rubber (SBR)

SBR is a general purpose synthetic rubber, produced from the copolymerization of styrene and butadiene, as illustrated in Figure 3. The styrene content ranges usually from about 20 to 40%.

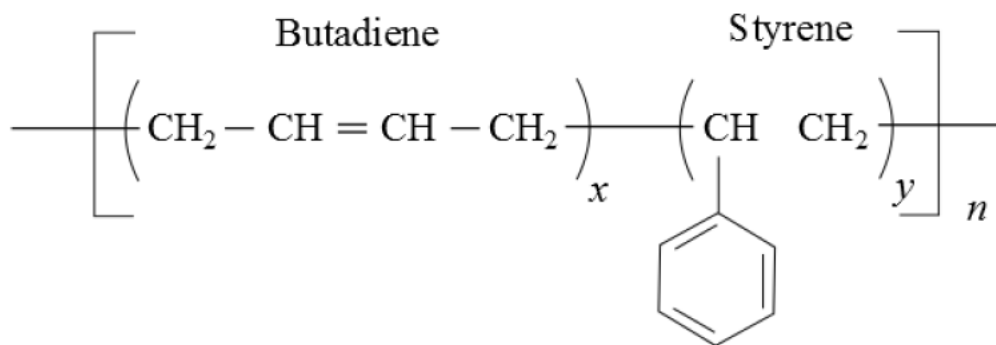


Figure 3. Chemical structure of SBR comprising of styrene and butadiene monomers.

SBR was the first successful commercial grade of synthetic rubber, which was then named as Buna S in the 1930s in Germany [8]. Today, SBR ranks first in world annual production of all the synthetic rubbers, which finds extensive applications in manufacturing tire treads, accounting for over 65% of the synthetic rubbers used in tire industry [9]. SBR can be polymerized either from emulsion or

solution, with the products named as ESBR (Emulsion SBR) and SSBR (Solution SBR) respectively. Emulsion polymerization of SBR follows the mechanism of free radical polymerization, leading to a copolymer with a broad MWD (molecular weight distribution), random copolymer composition, and long chain branching.

The microstructure is generally not controllable, because the temperature of the polymerization affects the ratio of trans to cis formation. Solution SBR is synthesized in a living anionic polymerization reaction usually initiated by alkyl lithium compounds. This kind of polymerization gives products with narrower MWD and lower  $T_g$  than corresponding emulsion polymerized polymers. ESBRs show superior performance in wet traction, while a SSBR with the same styrene content gives lower rolling resistance and better tread wear. The living feature of the solution polymerizations brings a wide degree of freedom to design a polymer microstructure, polymer modification, composition and molecular weight distribution [10].

As the styrene content in the SBR increases, the glass transition temperature becomes higher, while abrasion resistance and resilience become smaller (see Figure 4). A similar effect is induced by varying the amount of vinyl groups. Good dynamic properties, aging and heat resistance as well as abrasion resistance make SBR a product of high versatility for many technological applications.

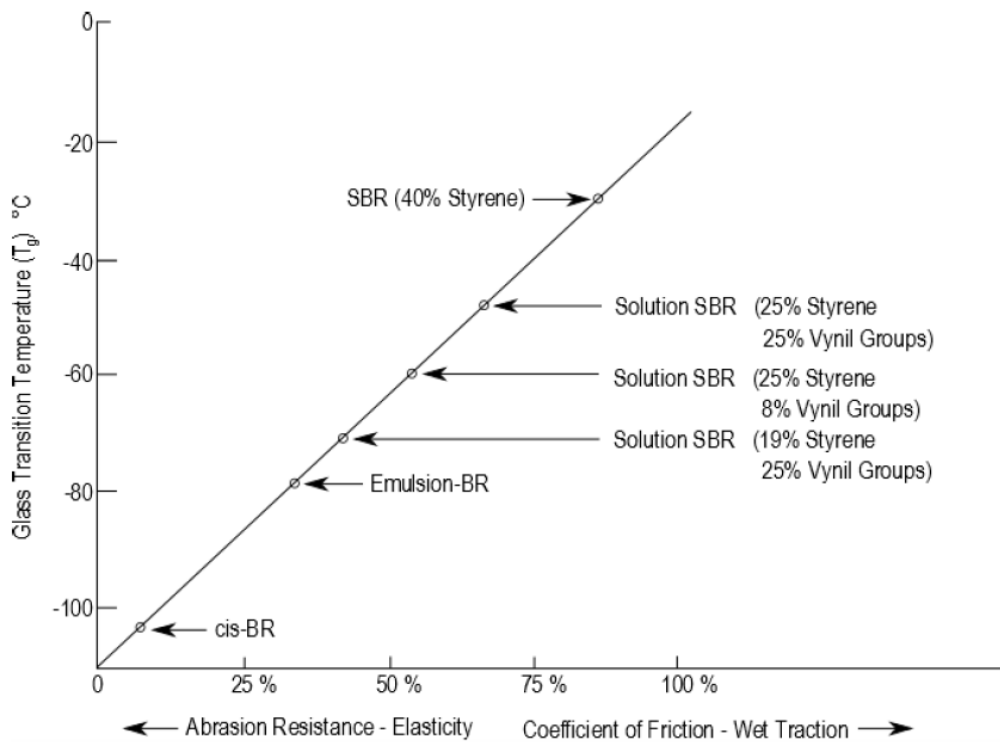


Figure 4. Dependence of the glass transition temperature on the styrene and the 1,2-component of BR. Several cases of synthetic rubbers are reported as example (from [11]).

Compared with E-SBR, S-SBR has the advantage to be produced in stereospecific combinations thanks to catalysts based on organo-metallic compounds. This means that it is possible to obtain a custom-made SBR with a wide range of specific properties by choosing appropriate polymerization systems and conditions. Thus for high performance products S-SBR is usually preferred to E-SBR [12].

## 2.3 Vulcanization process

Raw elastomers consist of long polymer chains, which can flow under the applied strain. In order to make elastomers mechanically more useful, a process named vulcanization/curing is usually carried out. Figure 5 shows the polymer structure before and after the vulcanization process. This process involves the conversion of a raw rubber into a network due to the formation of crosslinks, chemical bonds or bridges by using curing systems like sulfur based and/ or peroxide based systems. During the process, a viscous entanglement of long chain molecules are converted into a three dimensional elastic network by insertion of crosslinks.

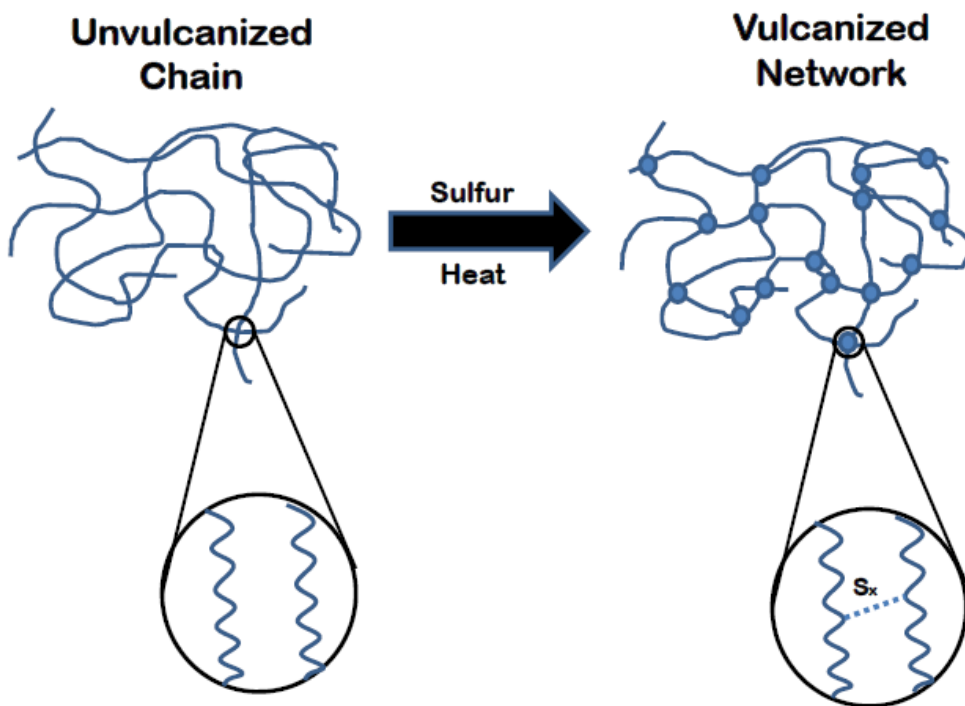


Figure 5. Vulcanization process works by forming cross-links between sections of polymer chain which results in increased rigidity and durability, as well as other changes in the mechanical and electrical properties of the material.

When the rubber melts, it can be seen that the polymer chains form into a clew by maximizing entropy [13] [14]. The chains are statistically distributed in all directions and are physically interlocked. If a force is exerted on the melt, the individual polymer chains can slide against each other - the highly viscous liquid deforms permanently. In order to prevent this viscous flow and thus guarantee a dimensional stability of the material, firm links must be inserted between the individual polymer chains. In general, this is achieved by chemical cross-linking with the aid of sulphur. Another possibility is cross-linking with peroxides.

By introducing the crosslinking points, the elastomer network is stabilized, but still contains free chain ends, chain loops or interlocks. The cross-linking leads to the fact that the slippage of the chains is strongly limited to completely prevented. The slippage manifests itself in the slight formation of hysteresis in cyclic stress-strain or pressure/compression measurements and leads to energy losses in the form of heat due to internal friction between the chains. In addition to sulfur, accelerators or activators - usually zinc oxide and stearic acid - are also used to completely change the reaction



processes. This means that it is only possible to characterise technically relevant compounds to a limited extent more precisely in regard to their vulcanisation reactions without making systematic changes to the vulcanisation system. The carbon-carbon double bonds in the polymer chains are required for sulfur crosslinking. These double bonds react with the sulfur and can thus form a sulfur bridge between the chains. Usually elemental sulphur in the form of S<sub>8</sub> rings is used for sulphur vulcanisation. In the course of the vulcanization process, longer bridges are first built into the network, which are then split by thermal excitation and thus shorten as they react with further double bonds. The length of the sulphur bridges also influences the mobility of the elastomer network. The more short bridges (mo-no-, disulfidic) exist in the network, the stiffer the reaction of the cross-linked polymer to a force. This is referred to as "efficiently crosslinked". The vulcanization process can be characterized, for example, by recording a "vulcameter curve", in which the shear modulus is recorded continuously and time-resolved during crosslinking. An example is shown in Figure 6. The module increases as the degree of crosslinking increases until the maximum is reached and continuous vulcanization can lead to three different curves [15]. In the first case (Figure 6 solid line), a wide plateau is formed, which then changes into a slight reversion. Here the vulcanization is completed and a dynamic equilibrium between building and decomposition of the polymer network can be found. The situation is different in the case of two (Figure 6 dashed line), in which a reversion occurs, i.e. the polymer network is degraded by thermal excitation of the molecular chains and bridges. Thermal aging begins. In the case of three (Figure 6 dotted line) a slightly increasing vulcanization characteristic is observed, which indicates that a secondary cross-linking is present, which continues with a slower speed.

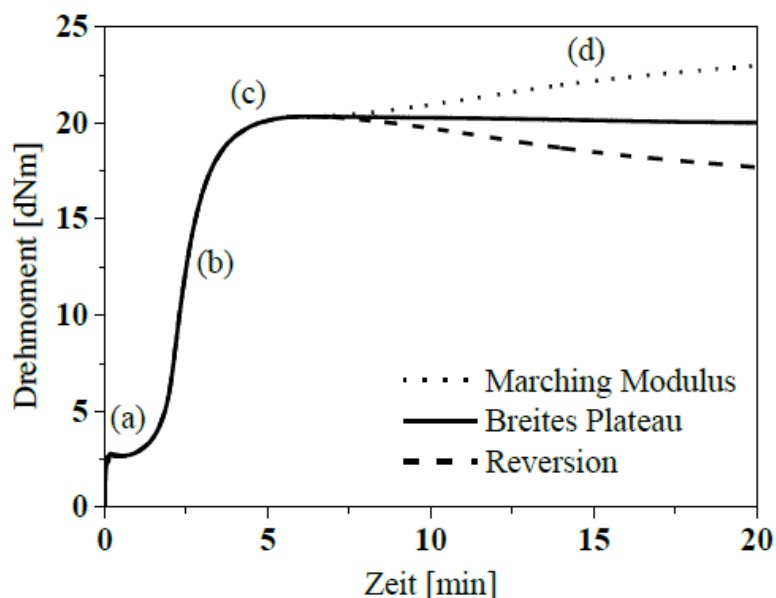


Figure 6. Schematic representation of the vulcanisation process with sulphur for different cases. Area (a) shows the initial viscosity and the duration until the start of vulcanization (incubation time). Area (b) describes the crosslinking reaction and its speed (the steeper the increase, the faster the reaction). Area (c) indicates the position of the optimum degree of crosslinking. Area (d) shows the possible progressions (marching modulus, wide plateau and Reversion) after overcure.

Crosslinking with peroxides is preferably used for rubbers, which have no double bonds in the polymer chain. These include e.g. silicone, EPDM, urethane or the HNBR rubbers. In addition, peroxides are also used for special purposes, e.g. for thermo-oxidative stability of the vulcanizates compared to sulfur crosslinking.

Figure 7 presents the effects of vulcanization on the final rubber properties. As it can be observed, the static modulus increases at higher rate than dynamic modulus during vulcanization. Static modulus refers to the elastic component of the rheological behavior, while dynamic component refers to the viscoelastic behavior. Additionally, it can be noticed that the hysteresis ratio is reduced during vulcanization and properties like tear strength, fatigue life and toughness increase to an optimum value and subsequently decrease as well as the strength properties [16].

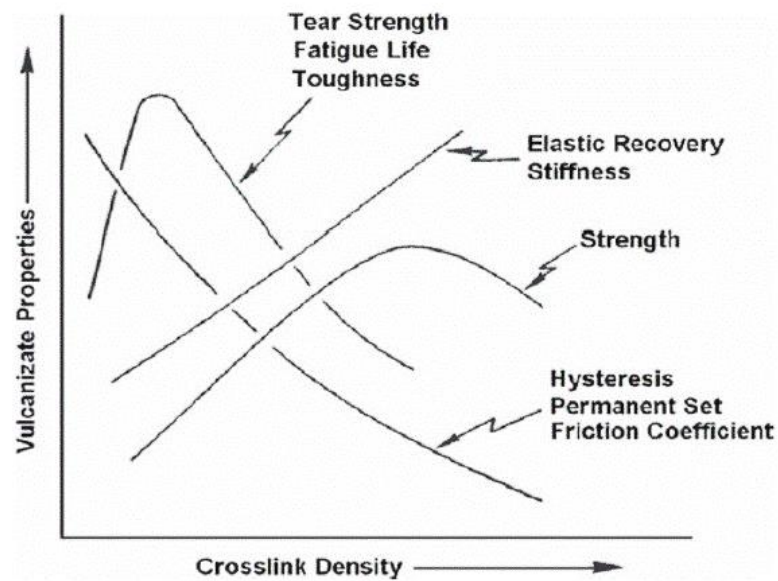


Figure 7. Effect of the vulcanization process on final rubber properties [16].

## 2.4 Filled rubber reinforcement

Gum or unfilled rubbers are seldomly used due to their low performance, i.e. lack of hardness, strength properties and abrasion resistance, to fulfill practical requirements for many applications especially for tires. In order to enhance the properties, several types of fillers are utilized in the rubber compounds. The classification of fillers employed in rubber formulations is shown in Figure 8.

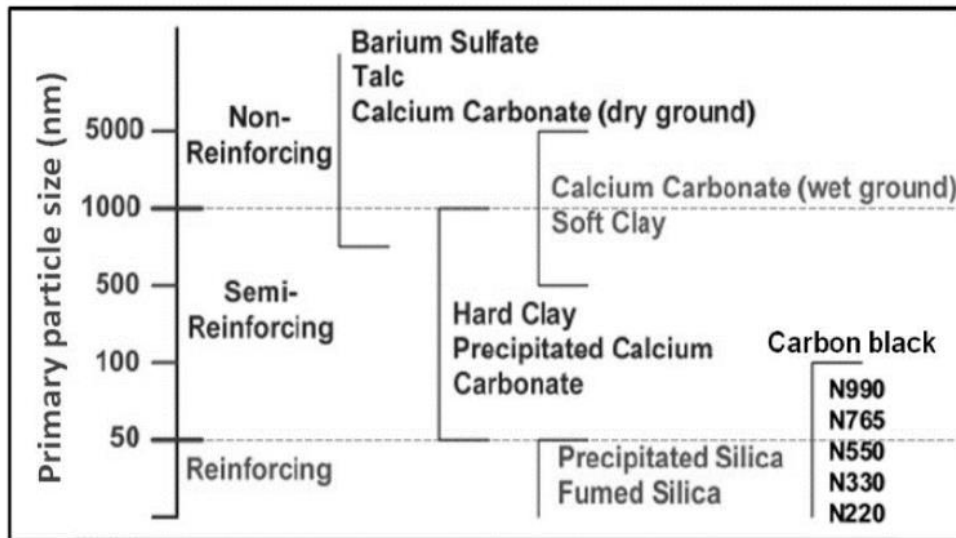


Figure 8. Classification of the fillers based on the size of the primary filler particles [17].

The reinforcement efficiency by incorporating the filler particles into the rubber compounds is dependent on many factors, such as particle surface activity, particle size, specific surface area, and filler structure [18] [19].

*Particle surface activity:* The surface nature of the fillers used in the rubber compounds is either active or inactive type. The silica surface consists of highly polar silanol groups that are active to react with other functional groups and can form strong hydrogen bonding between silica particles themselves. The silanol groups on the silica surface enable the reaction with a silane coupling agent to enhance filler-rubber interaction and to finally chemically bond to rubber molecules *via* silane bridges. In the case of carbon black, the surface consists of only a very small amount of polar functional groups such as carboxyl, quinone, lactone, phenol and hydroxyl groups where these functional groups have almost a negligible effect on the reinforcement efficiency. The reinforcement of rubber compounds by carbon black is derived from the much weaker interactions between the carbon black surface and rubber molecules *via* physical adsorption and mechanical interlocking.

*Particle size and specific surface area:* The most important parameter for the reinforcement efficiency is the primary particle size of the filler materials. According to Figure 8, there are three groups of fillers: non-reinforcing, semi-reinforcing and reinforcing fillers. The smaller particle sizes give higher reinforcement efficiency. The fillers with particle size over 1000 nm are classified as non-reinforcing fillers, while a filler size in the range of 50-1000 nm is categorized as semi-reinforcing. Silica and carbon black have very small primary particle size, i.e. lower than 50 nm, therefore are classified as a reinforcing filler. The specific surface area of fillers relates to the particle size, which is a reduction in particle size increases the specific surface area. The specific surface area of fillers is generally determined by using the Brunauer-Emmett-Teller (BET) adsorption method. The BET method based on nitrogen adsorption provides the outer geometrical surface and inner surface, which is the surface within the porous structure. In addition to the BET, the Cetyl-Trimethyl-Ammonium Bromide (CTAB) method is applied to evaluate the surface area especially for silica while the size of a CTAB molecule is similar to a silane coupling agent. The CTAB method is useful to characterize the outer surface of silica due to the bulky nature of the molecule of CTAB [4].

*Filler structure:* Even though silica and carbon black have a very small particle size, they occur mainly in agglomerate and aggregate forms due to interaction between adjacent particles. The aggregate and agglomerate forms are described as “structure”. The higher structure gives more potential to promote filler-rubber interaction and therefore reinforcement.

The reinforcing fillers for tire rubber compounds are carbon black and silica. Carbon black has been conventionally used as reinforcing filler for more than a century. Later, the innovation of the “Green Tire” by Michelin led to a new facet of tire technology [20]. Silica-reinforced tire tread compounds show lower rolling resistance and better wet traction while maintaining the abrasion resistance when compared to carbon black-filled tire compounds, as shown in Figure 9 [21]. A reduction of rolling resistance of about 20% of a silica-filled tire tread rubber compared to one with carbon black can save 3-6% of fuel [22] [23].

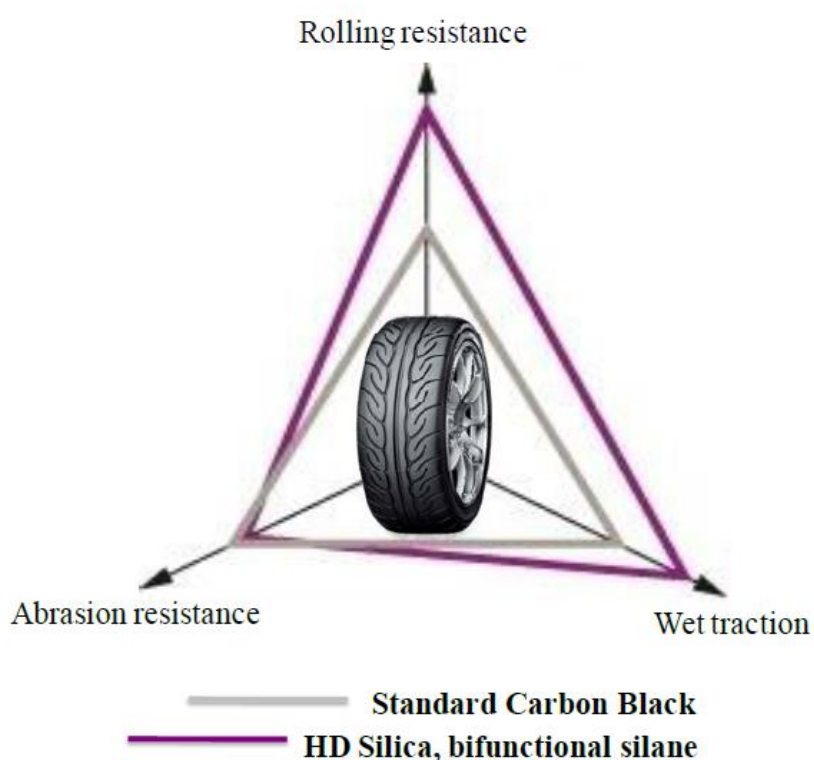


Figure 9. Magic triangle of the tread tire performances with carbon black and silica.

The stiffness  $G'$  is mildly affected by the addition of fillers at low temperatures in the glassy region. However, at high temperature in the plateau range the  $G'$  becomes systematically dependent on the filler loadings. This particular feature shows the filler-induced reinforcement in the soft elastomer matrix. The degree of reinforcement is mainly governed by two effects: (i) the formation of a physically bonded flexible filler network and (ii) strong polymer-filler couplings. Both of these effects originate from the specific surface nature of the filler particles [24] [25].

The basic equation used to describe the surface energy of fillers is:

$$\gamma_s = \gamma_s^d + \gamma_s^{sp} \tag{1}$$

where  $\gamma_s$  is the surface energy (also called surface tension),  $\gamma_s^d$  is the dispersive component of the surface energy and based on dispersive (Van der Waals) forces among the fillers, and  $\gamma_s^{sp}$  is the specific component of the surface energy and it is the sum of polar or hydrogen bond interactions between the fillers. Hence, the single most important parameter to enhance reinforcement is the average particle size. Particles having size larger than 1  $\mu\text{m}$  do not have reinforcing capacity due to less interactive surface and they only increase the reinforcement by the simple hydrodynamic effect. Reinforcement can be realized with a filler size smaller than 100 nm [35]. Figure 10 highlights the typical dimensions considered for both silica and carbon black fillers.

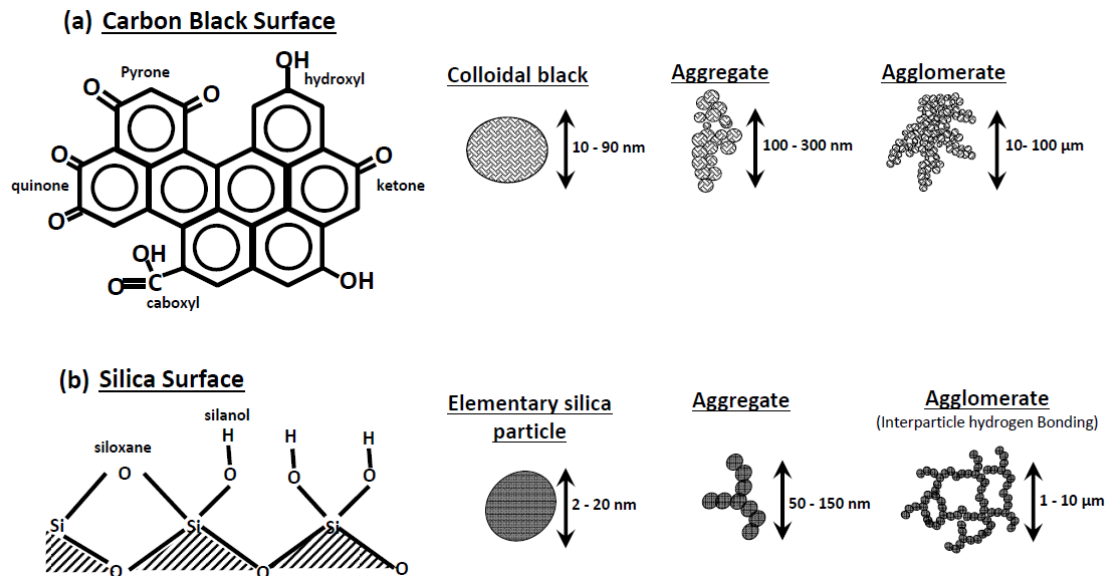


Figure 10. Filler morphology and the relevant dimensions of carbon black (a) and silica (b) filler [26].

## 2.4.1 Carbon black

Carbon black is the most used reinforcing filler for polymers, particularly in the rubber industry for tyre applications. Basically, carbon black consists of extremely fine amorphous particles of elemental carbon owing its reinforcing potential to its surface properties and its colloidal morphology.

There are two basic methods to produce carbon black, incomplete combustion of hydrocarbons and thermal cracking. Based on their production process, carbon blacks can be classified as furnace blacks, channel blacks, thermal blacks and lamp black, accounting for over 95 % carbon black produced by furnace process [27].

A schematic of the furnace production process is reproduced from Klüppel [27] and given in Figure 11. The hydrocarbon mixture is injected and vaporised, mixed with air, combusted and then quenched by water. Early in the combustion process spherical primary particles of CB are formed and increase in size due to surface deposition of carbon - indicated as surface growth (SG) in the diagram. Primary particles rapidly coalesce to form small aggregates which continue to undergo surface growth. Aggregate growth (AG) occurs when two or more of these aggregates come into contact forming

larger aggregates. During this process the surface growth mechanism continues to solidify the particles and increase their size and mass. Eventually the process is quenched and particles are recovered from the reactor. Varying factors such as the quench time, furnace temperature and feedstock injection rate alter the physicochemical properties of the recovered CBs [28] [29].

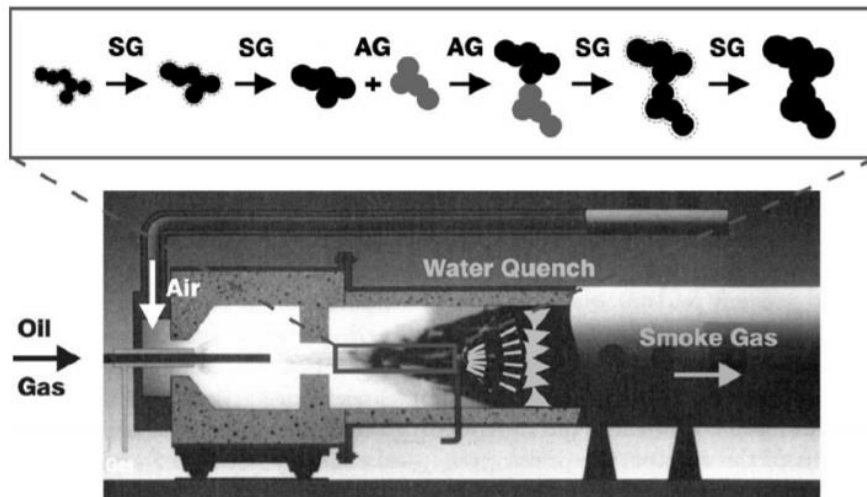


Figure 11. Schematic of a carbon black production furnace with a schematic of the aggregate growth mechanism. SG refers to the surface growth mechanism and AG refers to the aggregate growth mechanism (from Klüppel [29]).

It is common to differentiate between primary and secondary structures of carbon black [28]. Figure 12 presents an illustration of these two possible structures. Primary structures consist of primary particles that fuse together to form three dimensional aggregates. High structure carbon blacks present strong aggregation containing a high number of primary particles per aggregate, while low structure carbon blacks present weak aggregation. Primary structures require great amount of energy to undergo breakdown during mixing and dispersion [30] [8]. Secondary structures make reference to the agglomeration of a number of these aggregates by Van der Waals attractive forces and/or polymer bridges. During mixing and dispersion these secondary structures are easily and irreversibly disrupted. It is possible that the disrupted agglomerates reversibly fuse together again and this is reflect the so-called phenomenon flocculation [31].

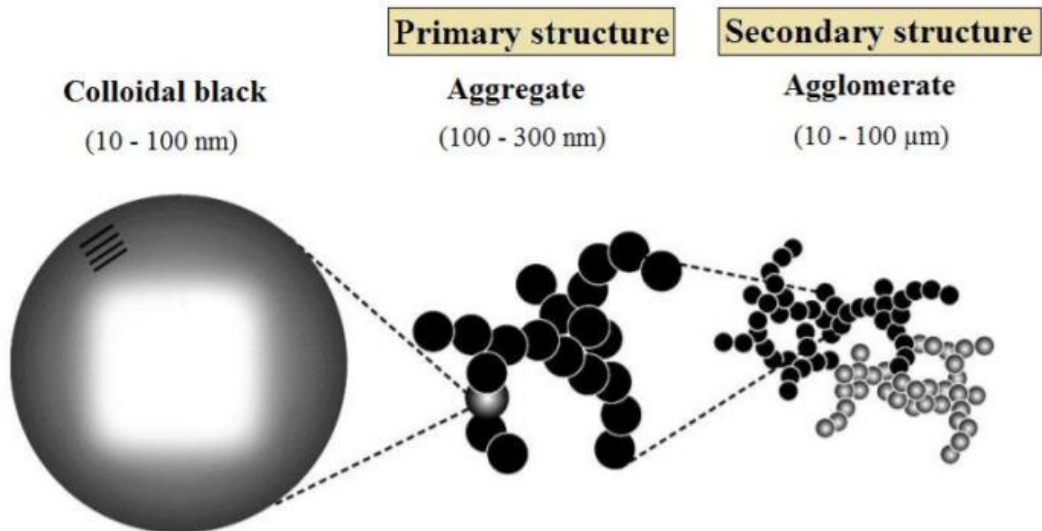


Figure 12. Basic forms of carbon black [32].

The resulting structures are generally aciniform in morphology (resembling a bunch of grapes) made up of many primary particles fused together. Figure 13 describes the transmission electron microscopy (TEM) images of carbon black aggregates of various grades. The typically branched morphology can be clearly distinguished. Higher structures generally refer to more branched, anisotropic morphologies [33].

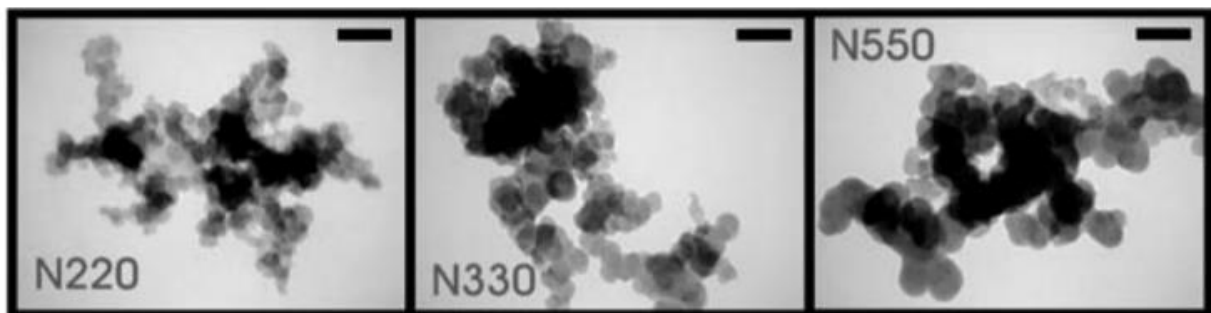


Figure 13. TEM images of carbon black aggregates of varying particle size and morphology [29].

CBs are ASTM graded [34] according to both their primary particle size and aggregate structure. A typical ASTM CB grading is assigned as follows:

- The first letter of the grade corresponds to the degree to which the CB interacts with the sulphur cure system. For rubber applications the letter N designates 'non-interacting, or normal curing' and the letter S indicates 'slow curing'.
- The first number relates to the average primary particle size (1-7 = 10 - 700 nm diameter).
- The final two numbers refer to CB structure. Generally, a higher number indicates a higher level of structure. For example, N110 is a non-interacting carbon black with an average primary particle diameter of 10 nm and a relatively low structure. The slight exception to this trend is the case of N990

grade CB. N990 exhibits no aggregate structuring, instead it consists of isolated spherical particles with a diameter of around 250 nm. N990 is one of the largest particle size CBs with the lowest surface area and is the least reinforcing grade. Reported values for surface areas of CBs are usually determined specific to the surface absorption of a probe gas or liquid. Inert gases such as argon and nitrogen are routinely used to determine the surface area via the Brunauer-Emmett-Teller (BET) isotherm method. Larger probe liquids such as iodine or cetyltrimethylammonium bromide (CTAB) are often used to provide surface areas which may better correspond with the surface area of filler accessible to the rubber polymer. Typical BET and CTAB surface areas for a range of CB grades are given in Table 1.

Table 1. Primary particle diameters (note that this is not the total aggregate size) and specific surface areas of various CB grades. BET SSA refers to nitrogen specific surface area and CTAB refers to cetyltrimethylammonium bromide specific surface area (Reproduced from [28]).

<b>ASTM Grade</b>	<b>Mean particle diameter / nm</b>	<b>BET SSA - <math>m^2/g</math></b>
N110	18	138
N220	21	116
N330	30	83
N550	56	41
N660	67	36
N762	107	26
N990	285	9

An industry standard measure of carbon black structure is given by the dibutyl phthalate (DBP) absorption capacity of the carbon black in units of ml DBP per 100 g of carbon black. A plot of the DBP capacity of a range of carbon blacks versus their nitrogen surface area is given in Figure 14.



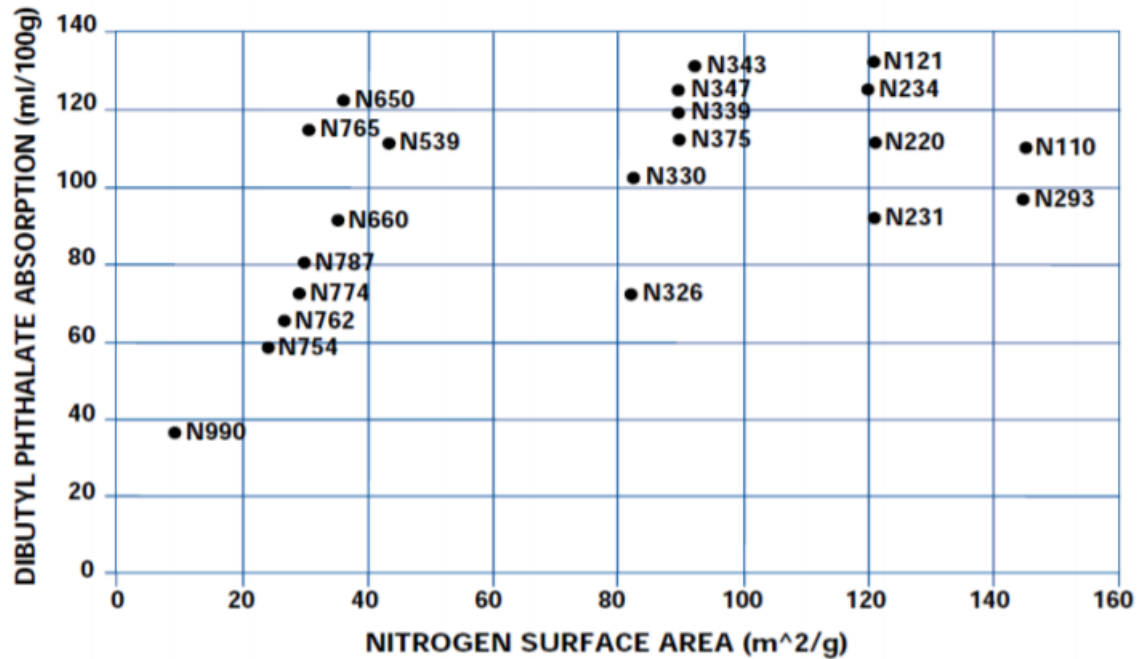


Figure 14. DBP absorption levels (structure) versus nitrogen BET surface area for a range of carbon black grades (From Cancarb N990 technical data sheet [35]).

## 2.4.2 Silica

Nowadays, several forms of silica (SiO<sub>2</sub>) are commercially available for different industrial applications, including natural and synthetic varieties. Two types of synthetic silica based on their manufacturing methods are currently used in elastomer technology. These are precipitated silica and fumed silica. Precipitated silicas (PSi) are the second most used type of filler particle after carbon black. PSis are an amorphous form of silica produced via acidification of sodium silicate under controlled conditions [18]. Figure 15 illustrates this process. Sodium silicate and sulphuric acid are first mixed and continually agitated. Initially primary particles with diameters of a few 10s of nanometres are formed and tend to cluster together to create chemically bonded aggregate structures similar in geometry to those of carbon black. Subsequent filtering, drying and milling stages also influence the structure of the precipitated silica [36].

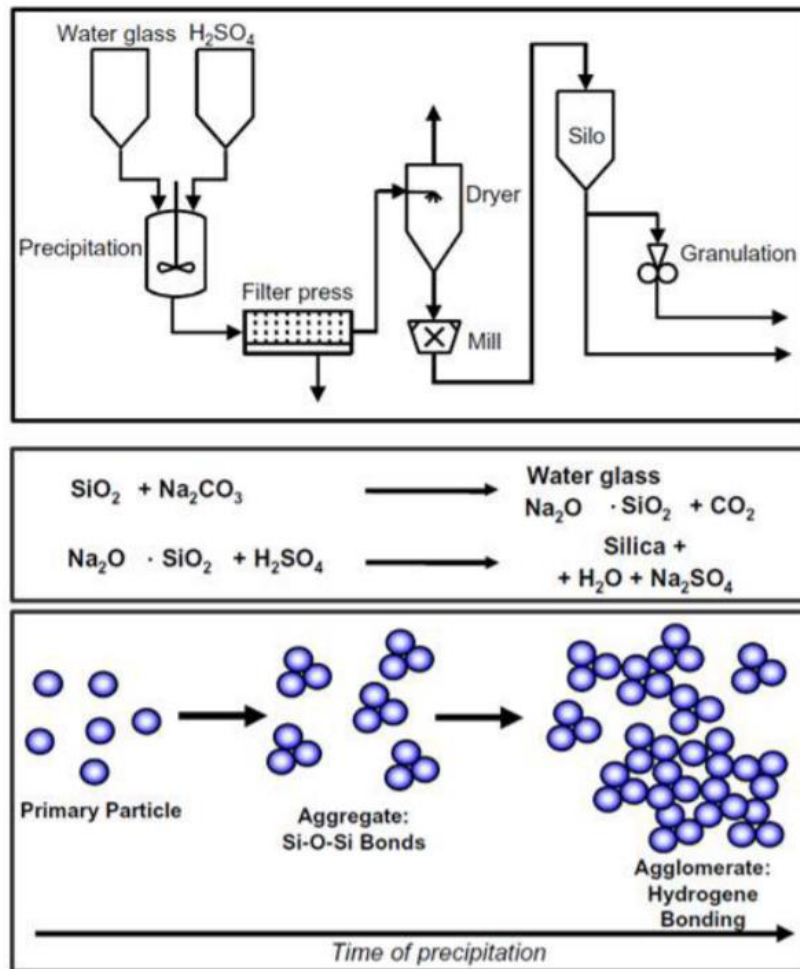


Figure 15. Schematic of the process for synthesis of precipitated silica (top). Chemistry of the synthesis process (middle). Schematic of the aggregate growth mechanism (bottom) [18].

Silica is characterized according to its particle size, distribution, structure and surface chemistry.

*Surface area:* Primary particles of precipitated silica normally range from 10 to 100 nm and its specific surface area is usually determined by two different techniques: BET and CTAB methods [37] [38]. BET method provides measurements of the total surface area of the particles including pores, thus, magnifying the accessible surface area. Normal BET values range from 50 to 350 m<sup>2</sup> /g [35]. CTAB is the most common method used to determine the surface area of silica particles since CTAB molecules are not able to penetrate the pores due to their larger size, therefore providing more accurate values of the external surface area of the particles. Typical values of CTAB methods range from 100 – 200 m<sup>2</sup> /g [37] [39]. High surface area of silica leads to better filler dispersion in the rubber matrix, however, it affects negatively its processing behavior since it causes an increment in the compound viscosity [40].

*Structure:* The structure of silica is a very important parameter that highly influences the reinforcement mechanism. Precipitated silica is amorphous, consisting of very small particles that fuse together forming larger structures called aggregates. Aggregates can contain several hundreds of primary particles and are assumed as the effective units reinforcing rubber compounds. Many

different particle arrangements can be reached with the formation of aggregates, strongly affecting the physical properties and performance of silica [9]. The structure of silica is normally measured by adsorption of dibutylphthalate, known as DBP method. This method provides values of 175g/ 100g for conventional silicas and 200 g/ 100 g for highly dispersible silicas [37].

To use the precipitated silica as an active filler in a polymer matrix, an additional step must be done. The polar surface of silica with its silanol groups couple the water with hydrogen bonds, which prevents the bonding to the non-polar rubber matrix. In order to make the surface hydrophobic and increase the interaction between filler and polymer, additional coupling additives such as silanes are used. The most frequently used silanes in the tire industry are the bifunctional bis-(triethoxysilylpropyl)-tetrasulphides (TESPT) and bis-(triethoxysilylpropyl)-disulphides.

A schematic illustration of the silica surface (a) with the enrichment in water (b) and the reaction mechanisms between the silica and a bifunctional silane (c) are shown in Figure 16. In addition, the sulfur group enables a direct covalent bond to the polymer matrix established during the vulcanization process, as shown in Figure 16d.

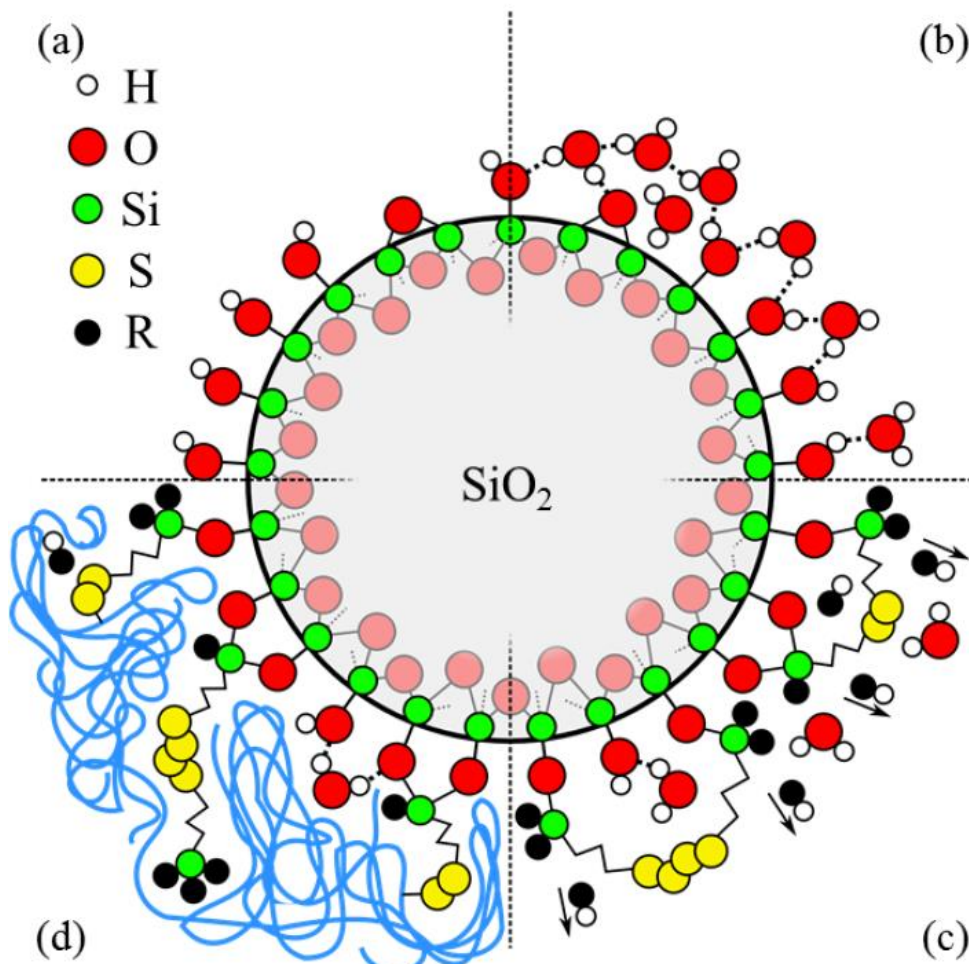


Figure 16. Schematic representation of a silica particle with the OH groups on the surface (a), which is strongly hydrophilic and binds water (H<sub>2</sub>O) to itself by hydrogen bridge bonds (b). The surface of the silica particles is functionalized by silanization with elimination of alcohol (e.g. ethanol at Si69) (c) and the silane produces a chemical bond to the polymer (blue) (d). The remainder R is an alkoxy group, e.g. ethoxy in the case of Si69 [41].

### 2.4.3 Silica versus Carbon black as reinforcing fillers

Carbon black and silica are the most used reinforcing fillers in the tyre industry. Properties of both fillers differ greatly from each other resulting on different reinforcing capabilities. When comparing silica and carbon black, the most perceptible difference is the weaker filler-polymer interactions of silica filler and the stronger tendency of filler particles to interact with each other. This characteristic of silica leads to poor filler dispersion resulting in an increased viscosity of the compound, lower modulus at high strain amplitudes, higher modulus at low strain amplitudes and low formation of bound rubber. Nevertheless, the use of coupling agents along with silica significantly enhances its reinforcing capability compared with carbon black affecting numerous mechanical properties including: resilience, heat build-up, tear resistance, abrasion resistance, heat resistance, tack, shore hardness, stiffness, modulus and flex stability [40] [42]. Due to the greater reinforcing capability of silica, it is possible to decrease the filler content during compounding without adverse effects on the final properties of the material. In addition, the increased ratio of the elastic component to damping filler of silica leads to a reduction of the tyre rolling resistance.

Silica-polymer networks present lower loss modulus ( $G''$ ) than carbon black-polymer networks due to lower breaking and reformation rates during deformation cycles. Storage modulus ( $G'$ ) of silica filled rubber is also enhanced resulting in a lower phase angle ( $\tan \delta = G''/G'$ ). The phase angle increases at higher deformations since both loss modulus and storage modulus are influenced by the deformation. Figure 17 presents the temperature dependence of  $\tan \delta$  as well as the strain-dependence of loss modulus (Payne effect).

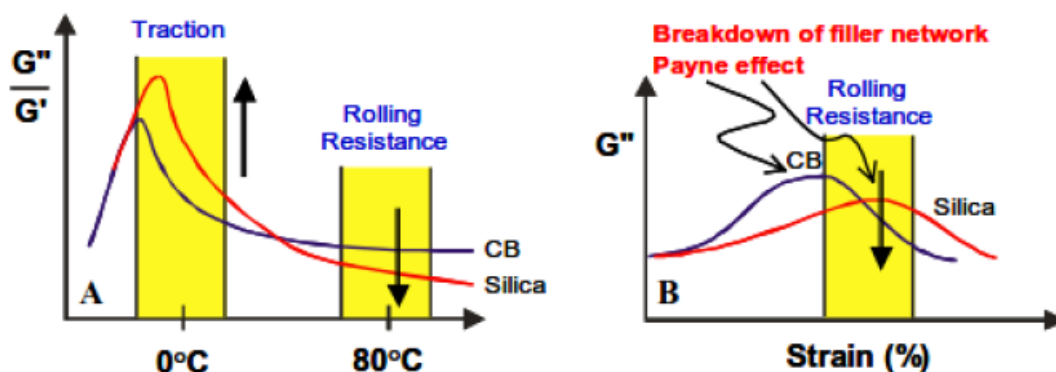


Figure 17. Comparison of silica and carbon black mechanical properties. (A:  $\tan \delta$  dependence of temperature, B: Payne effect) [40].

### 2.4.4 Filler-polymer interactions

By adding active fillers, many mechanical properties of rubbers can be controlled or improved [41]. The reinforcing effect depends on the filler content or filler volume fraction (volume fraction of the filler in relation to the volume fraction of the rubber) and the associated interaction mechanisms. Payne focused on understanding the relationship between the polymer matrix and filler by performing dynamic mechanical measurements on different elastomer materials [43] [44] [45] [46] [47] [48].

In addition to the polymer type, he also varied the filler content and the deformation amplitude. As a result, he was able to determine the material softening for filled systems with increasing deformation, being more pronounced for higher filling degrees. By determining the complex modulus of elasticity or shear modulus, he recognized at a very early stage that the elastomer reinforcement is generally composed of four contributions.

Figure 18 shows the individual contributions schematically. The first contribution is caused by the pure elastomer matrix and its elasticity. The filler particles contribute to the increase in the stiffness through three further interaction mechanisms. The first is hydrodynamic reinforcement, this describes the change in viscosity or stiffness solely due to the presence of foreign particles in the medium. If these filler particles have higher stiffness compared to the surrounding elastomer matrix, an external force only leads to a deformation of the elastomer phase and not of the particles. In addition, the filler content lowers the elastomer volume of a test specimen, so that the polymer matrix is stretched even stronger. This results in a lower expansion of the specimen at the same force or a higher force at the same strain. The other mechanisms underlying the effect of particulates on the deformation and flow of rubber are the occlusion of polymer chains within the void structure of the particles, enhancing their effective concentration and a filler network structure when the amount of particles exceeds their percolation threshold.

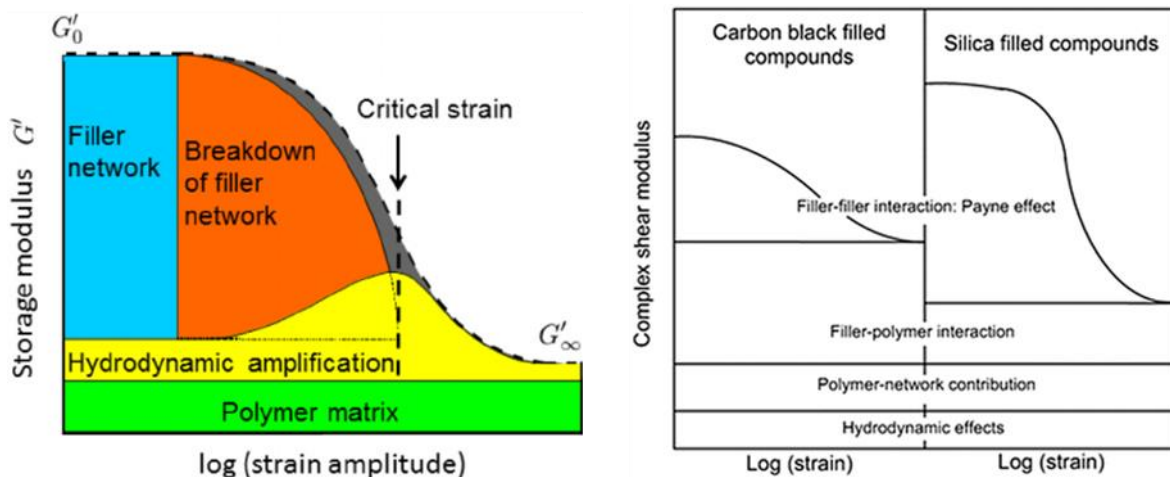


Figure 18. (a) Schematic representation of Payne effect resulting from different contribution. (b) Silica vs carbon black rubber system [49].

## 2.4.5 Mullins effect

A change in the mechanical behaviour occurs as a consequence of the deformation applied during the deformation of elastomeric products. This phenomenon was first observed in filled elastomers by Bouasse and Carrière in 1903 [50] and later investigated by Mullins and co-workers in the 1950s [51]. The phenomenon is generally referred to as the Mullins Effect, and is defined as a permanent or semipermanent change in the response of the material after it is subjected to deformation. This leads to a difference in the mechanical response if it is unloaded and reloaded. As a consequence, a smaller amount of energy is required to generate the same deformation in any of the following loadings compared to the first one. An idealized version of the Mullins effect in the stress-strain response is



presented in Figure 19. During the first loading of the virgin material, the response follows path A until reaching point a. If unloading begins immediately, the material follows a different path B, due to changes in the network structure during the deformation. During subsequent smaller or equal loadings the stress-strain relation follows path B back up to point a. The reloading path is similar, but not identical, to the first unloading one since the viscoelastic effects in rubber materials are generally small. An ideal Mullins behaviour follows the same path B when loading and unloading. However, a real rubber will show a difference in the loading-unloading path due to viscoelasticity. If the strain of a subsequent loading step exceeds point a, the material will deform along path A'. The path A-A' represents the behaviour of a non-deformed material loaded until the point b. After loading the material to the point b and releasing the stress, it unloads along a new path, C. Hence, the stress-strain response (path B or C) is dependent on the load history (path A or A') experienced by the material.

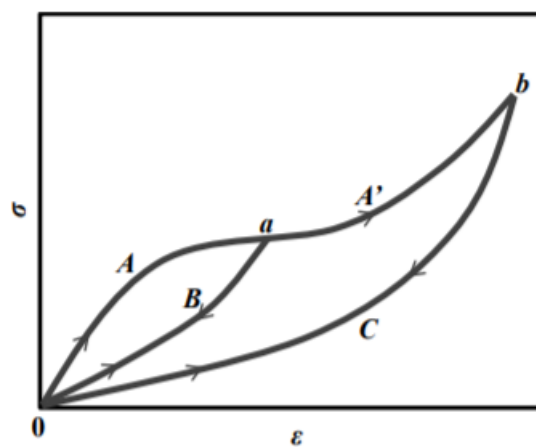


Figure 19. Stress,  $\sigma$ , response as function of strain,  $\epsilon$ , showing an idealized Mullins effect under uniaxial tension [52].

The stress-softening phenomenon occurs after the first loading cycle. It can be identified by observing the stress-strain relation as a modification of the unloading-reloading path after a loading path. The material responds in a similar way after the first cycle (when subsequent loads are applied) as long as the deformation does not exceed the maximum reached in the first cycle. Thus, the material exhibits a softening effect that grows progressively with the increasing of deformation [53].

Figure 19 shows an idealised response although there are other effects present in the material associated to the viscoelasticity behaviour of the material such as residual strain and hysteresis. Mullins et al. [50] [52] attributed this softening phenomenon to changes in two phases formed in the vulcanised chain network. They considered a filled elastomer as a two phase system, a soft region that allows deformation and a hard region that creates the resistance in the network. The soft region is formed mainly by the rubber matrix as the hard phase includes the filler together with rubber in direct contact with the filler. During deformation, the hard region can be broken down and incorporated into the soft region, reducing the resistance in the network. Therefore, as the fraction of the soft region increases, subsequent deformations up to the same value will require less stress. Pre-conditioning to a specific strain, called scragging, is usually applied in the industry, so the service conditions will not exceed this strain [54]. This pre-conditioning avoids any changes in the constitutive response due to softening. However, under an unexpected event during service (e.g. a higher strain than the scragging strain), the deformation history can change and consequently the

corresponding mechanical behaviour. A change in the mode of deformation applied could also lead to a modified response. If some of these events take place, the mechanical response will not be dictated by the scragging process any more. Other properties such as hysteresis, anisotropy and the time dependent response may also be affected by the deformation history. The consideration of these aspects during the design is crucial to ensure the proper performance of the final product. Nevertheless, the combination of all these influences complicates the analysis of the mechanical response of filled elastomers. Therefore, many of them are usually neglected during rubber investigations. A better understanding of these phenomena will allow a proper prediction how an elastomer will behave under different conditions.

## 2.5 Dynamic - mechanical properties of elastomers

The dynamic mechanical properties of filled rubber directly influence the final performance of a tyre. Thus, the understanding of the theory of viscoelasticity is extremely important in tyre industry in order to reach favourable final properties of the rubber compounds [40]. Rubber is a viscoelastic material, this means that when it is deformed, part of the energy is stored elastically and the rest is dissipated as heat into the material hysterically. This hysteric loss is not recoverable and contributes to the total drag force on a moving vehicle [40] [42].

### 2.5.1 Linear viscoelasticity

Apart from the nonlinear stress-strain relation, rubber-like materials are typically characterised by pronounced rate or frequency dependence. This behaviour is classified as viscoelasticity and occurs through hysteresis, stress relaxation, creep or damping effects. For an overview about the mathematical concepts of linear viscoelasticity, the reader is referred to the manuscripts of Lion [55] [56] or Jöhlitz [57]. In general, viscoelasticity can be described by a dependence of the stress response  $\sigma$  of the material on strain  $\varepsilon$  and strain rate  $\dot{\varepsilon}$ . Figure 20 illustrates the stress response of viscoelastic materials, which typically increases for larger rates of strain ( $\dot{\varepsilon}_1 > \dot{\varepsilon}_2$ ).

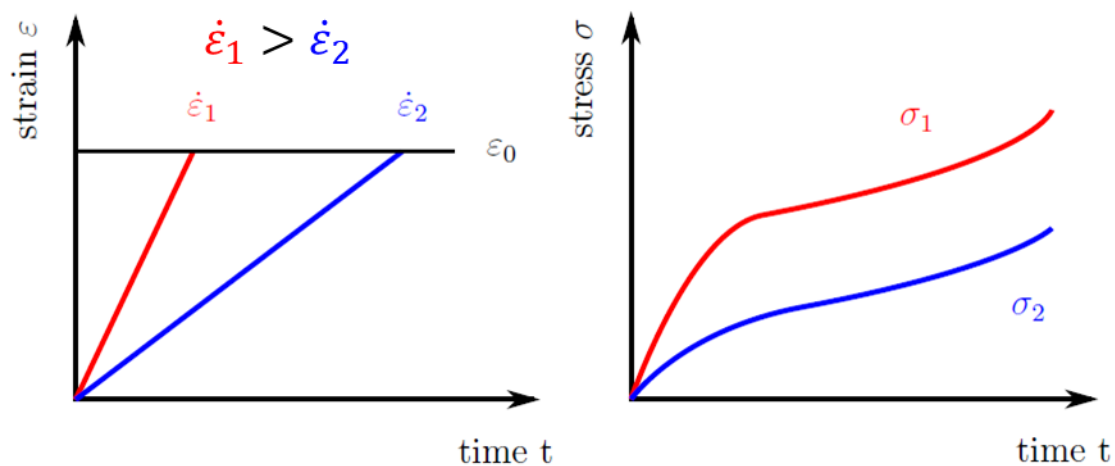


Figure 20. Viscoelastic material behaviour: dependence on the rate of strain.

Linear viscoelasticity can be applied to viscoelastic solids which exhibit time dependent mechanical properties but independent of the strain amplitude. To find out this behaviour, it may be considered the case of a body undergoing a dynamic oscillatory excitation, where the material is subjected to sinusoidal strain and its corresponding stress response is analyzed. The energy applied to a viscoelastic material can be modelled in case of a sinusoidal shear deformation  $\gamma(t)$  and an angular frequency  $\omega$ .

$$\gamma(t) = \gamma_0 \sin(\omega t) \quad (2)$$

The sinusoidal deformation with the amplitude  $\gamma_0$  and the excitation frequency  $\omega=2\pi f$  results in a linear response of the material by a shear stress  $\tau$  time dependent.

$$\tau(t) = \tau_0 \sin(\omega t + \delta) \quad (3)$$

with the amplitude  $\tau_0$  and a phase  $\delta$ . Figure 21 schematically illustrates the signal curves for stress and strain with the resulting phases  $\delta$  for elastic, viscous and viscoelastic materials.

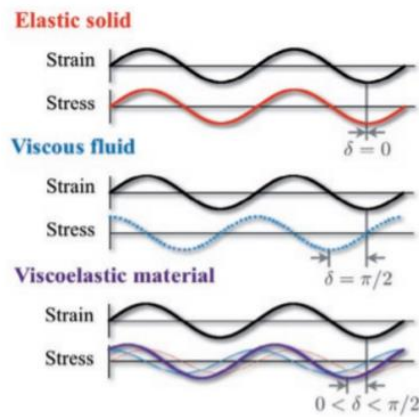


Figure 21. Time dependence of sinusoidal-shaped signals for shear stress  $\tau$  and shear deformation  $\gamma$  with phase  $\delta$  for ideally elastic (top), ideally viscous (middle) and viscoelastic materials (bottom).

The time delay in the form of the phase difference between deformation-stress signals can be between  $0^\circ$  and  $90^\circ$  and describes the redistribution of the applied energy. For an ideally elastic body, which reacts instantaneously,  $\delta=0^\circ$ , i.e. the entire energy is stored elastically in the body during loading, whereas this energy becomes completely free during complete unloading. With an ideal fluid, on the other hand,  $\delta=90^\circ$ ; as a result, the energy supplied is completely released in the form of heat due to the internal friction in the fluid. Thus, these cases represent borderline cases, which never occur under real conditions. All materials have elastic and dissipative viscous parts, whereby one of the two dominates strongly. It is the elastic part for solids and the viscous part for liquids. For viscoelastic materials, however, both components are equally represented, depending on the state of the material. Therefore, only a part of the energy is stored in the rubber materials, the rest is dissipated.

The shear stress signal  $\tau(t)$  can be divided into two different contributions: one in phase with the strain  $\tau_0 \cos \delta$  and the other  $90^\circ$  out of phase with the strain  $\tau_0 \sin \delta$ . Both components can be defined by two moduli as follows:



$$G' = \frac{\tau_0}{\gamma_0} \cos \delta \quad (4)$$

$$G'' = \frac{\tau_0}{\gamma_0} \sin \delta \quad (5)$$

$$G^* = G' + iG'' = \frac{\tau_0}{\gamma_0} \cos \delta + i \frac{\tau_0}{\gamma_0} \sin \delta \quad (6)$$

where  $G'$  is the storage or elastic modulus, which is the component in phase,  $G''$  is the loss or viscous modulus, which is the component out of phase with the oscillatory strain and  $G^*$  is the complex modulus. The ratio between the loss modulus and the storage modulus is called the loss tangent or loss factor and describes the ratio between dissipated and elastic energy.

$$\tan \delta = \frac{G''}{G'} \quad (7)$$

Both  $G'$  and  $G''$  have strong dependence on frequency and temperature. Figure 22 illustrates the frequency dependence of elastic and viscous modulus of a viscoelastic material.

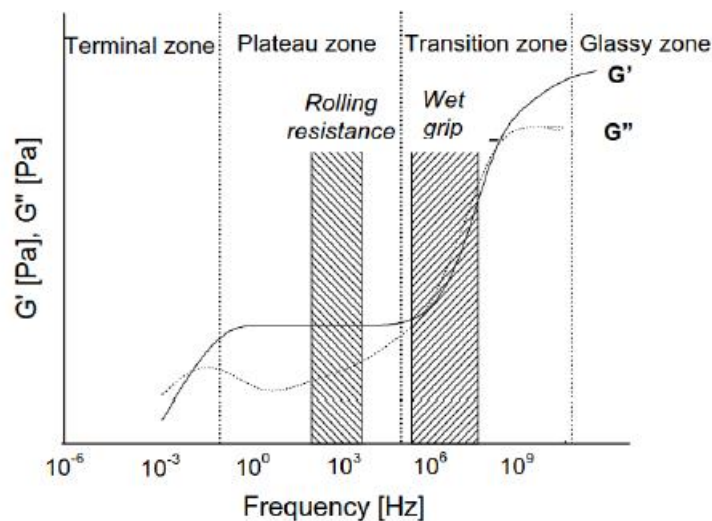


Figure 22. Frequency dependence of the elastic  $G'$  and viscous  $G''$  modulus of a viscoelastic material [58].

This frequency dependence can best be described by using phenomenological models constructed by a sequence of spring (Hooke element) and damper elements (Newton element).

### Maxwell model

The Maxwell model can be represented by a purely viscous damper and a purely elastic spring connected in series, as shown in Figure 23 [59]. When a load is applied, the stress is the same in both elements, while the overall deformation  $\gamma_T$  is equal to the sum of  $\gamma_D$  and  $\gamma_S$ , where the subscripts D and S stand for dashpot and spring respectively.

The model can be represented by the following equation:

$$\frac{d\gamma_T}{dt} = \frac{d\gamma_D}{dt} + \frac{d\gamma_S}{dt} = \frac{\sigma}{\eta} + \frac{1}{G} \frac{d\sigma}{dt} \quad (8)$$

The stress gradually relaxes with the following exponential law if the material is kept under constant strain [39]:

$$\sigma(t) = \gamma_T G e^{-\frac{t}{\tau}} \quad (9)$$

The time required to reach the stress relaxation of the element is then called relaxation time and is equal to  $\tau = \frac{\eta}{G}$ .

The Maxwell model predicts that the stress decays exponentially with time, which is accurate for most polymeric materials like rubber, but its limitation is that it does not predict creep accurately [60]. In fact, under constant stress, the strain has two components: an elastic component that occurs instantaneously, plus a viscous component that grows linearly with the time in which the stress is applied.

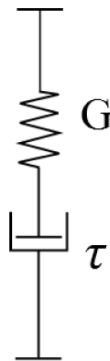


Figure 23. Schematic representation of the Maxwell element.

### **Kelvin Voigt element**

If the viscous damper and the elastic spring are arranged in parallel the so called Kelvin–Voigt model, (also known as the Voigt model) is obtained, as shown in Figure 24. In this case, when a load is applied, both elements experience the same deformation while the total stress is the sum of the stresses in each element [61].

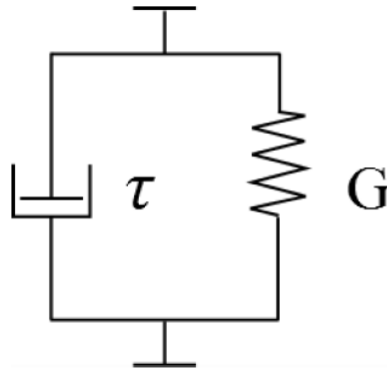


Figure 24. Schematic representation of the Kelvin Voigt element.

The constitutive relation is expressed as a linear first-order differential equation:

$$\sigma(t) = G\gamma(t) + \eta \frac{d\gamma}{dt} \quad (10)$$

This model represents a solid undergoing reversible and viscoelastic strain. Upon application of a constant stress, the material deforms at a decreasing rate, asymptotically approaching the steady-state strain equal to  $\sigma/G$  as time approaches infinity. When the stress is released, the material gradually relaxes to its undeformed state in agreement with the behavior typically shown by elastomers. Therefore, the model is extremely good to predict creep in materials, nevertheless contrary to the Maxwell model, the relaxation response is not well predicted.

However, the simple models mentioned above, featuring a single exponential response function, do not well approximate the behavior of real rubber materials. Specifically, a single exponential relaxation function undergoes most of its relaxation over about one decade in time scale, while real materials relax or creep over many decades. Hence, the representation of the behavior for most viscoelastic materials requires models with a large number of elements. Such models can be derived from the extension or generalization of the Maxwell and Voigt models. One of the most frequently used models in polymer physics is the generalized Maxwell model where a finite number of Maxwell elements are arranged in parallel with an elastic spring Figure 25 [62]. This group of elements represents a discrete spectrum of relaxation times, each time being associated with a spectral strength  $G_k$ . Since in a parallel arrangement, forces or equivalently stresses are additive, it is possible to obtain the overall stress response considering the sum of  $N$  Maxwell elements [63].

$$\sigma(t) = G_{\infty}\gamma_T + \sum_{k=1}^{k=N} G_k e^{-\frac{t}{\tau_k}} \quad (11)$$

Where  $G_\infty$  is the long-term modulus, obtained after a period of time long enough to reach all dashpots relaxation.

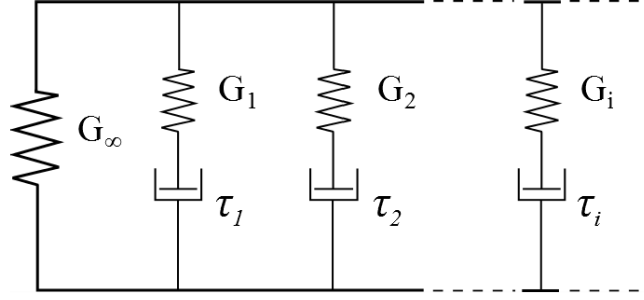


Figure 25. Schematic representation of the generalized Maxwell model.

The formulations valid for the time dependent behavior apply at the same manner for a dynamic oscillatory test. In fact, although sometimes a distinction is made between stress relaxation and dynamic tests, in reality, they both depend on the same viscoelastic principles. Therefore, the transition from one aspect to the other is every time possible using the Fourier transform and its inverse, respectively defined as:

$$\Gamma\{f(t)\} = \bar{f}(i\omega) = \int_0^{\infty} e^{-i\omega t} f(t) dt \quad (12)$$

$$\Gamma^{-1}\{\bar{f}(i\omega)\} = f(t) = \frac{1}{2\pi} \int_0^{\infty} e^{i\omega t} \bar{f}(i\omega) d\omega \quad (13)$$

Such Fourier transform pair, indeed, allows the conversion from time to frequency domain and vice versa. Therefore, applying Eq. (13) to Eq. (12) the analytical form of the complex modulus, as a function of the angular frequency, for a viscoelastic solid whose constitutive equation is based on the generalized Maxwell model can be obtained [64]

$$\begin{aligned} G^*(i\omega) &= i\omega \int_0^{\infty} \left[ G_\infty + \sum_{k=1}^N G_k e^{-\frac{t}{\tau_k}} \right] e^{-i\omega t} dt \\ &= i\omega \left[ G_\infty \int_0^{\infty} e^{-i\omega t} dt + \sum_{k=1}^N G_k \int_0^{\infty} e^{-\left(\frac{1+i\omega\tau_k}{\tau_k}\right)t} dt \right] \end{aligned} \quad (14)$$

Solving the integrals, the complex modulus becomes:

$$G^*(i\omega) = G_\infty + \sum_{k=1}^N G_k \frac{i\omega\tau_k}{1 + i\omega\tau_k} = G_\infty + \sum_{k=1}^N G_k \frac{\omega^2\tau_k^2}{1 + \omega^2\tau_k^2} + i \sum_{k=1}^N G_k \frac{\omega\tau_k}{1 + \omega^2\tau_k^2} \quad (15)$$

According to Eq. (6), the real and the imaginary part of Eq. (15) represent the expressions of the storage and loss modulus respectively, in dependence of the excitation frequency. This transformation will be useful for the derivation of material parameters necessary to perform finite element simulations.

Such model is valid only for linear viscoelastic materials, but storage and loss modulus are significantly varying with strain amplitude. Moreover, the time scales as well as the frequencies of excitation depend on the temperature at which the rubber body is working. Therefore, an insight into these aspects will be presented in the following sections.

### **2.5.2 Time-temperature superposition principle**

The dependence of the dynamic moduli on the frequency, or time, at which the strains are applied, results from the chain and the segment mobility in rubber compounds [63].

At low frequency, all rubber polymer chains are capable of following deformation without delay and the energy loss during one cycle of deformation is low [65]. As the frequencies of strain increase, the polymer entanglements are no longer able to follow the strain during one cycle of deformation. As a result, entanglements act as crosslink points, thus implying an increase in the elastic modulus [66].

Based on the excitation frequency, some defined zones or regions can be distinguished to describe the behaviour of the storage and loss modulus for a rubber compound, as shown in Figure 26 [67]. In the plateau region, a constant storage modulus and the minimum loss modulus can be seen since many movements are still possible on the micro scale and, therefore, an almost ideal elastic behavior is still taking place. By increasing the frequency, after the rubber plateau region, rubber compounds reach the transition state between the rubbery and the glassy regimes, corresponding to restricted polymer mobility in comparison with the low frequency state. Finally, rubber compounds reach the glassy state because the rubber behaves like a glassy material. In this region, polymer chains are unable to move flexibly enough to follow the applied strain rate, except for small local polymer chain motions, resulting in a very high plateau of the storage modulus and a very high energy dissipation.

On the contrary, by considering the temperature, the free volume in the polymer is so small at low temperatures that the movements of polymer segments and adjustments to their relative position can hardly take place within the time-scale involved in the dynamic experiment, resulting in low energy dissipation. Under this condition, the polymer is in a glassy state with a very high elastic modulus. Molecular motions of polymer chains are energetically promoted with increasing temperature. It follows a regime characterized by a decrease of the viscosity and high energy dissipation referred to molecular adjustments scaling with the dynamic excitation of the system. In this regime, the temperature associated with the maximum of the loss modulus  $G''$  is known as dynamic glass transition temperature.

Elastomers differ from polymers in which their glass transition temperature is located below room temperature. Above the glass transition, the molecular segment can rearrange so rapidly and the viscosity is so low that the solid polymer is able to follow the dynamic deformation. The material drops in the rubbery region characterised by a low elastic modulus and low energy dissipation.

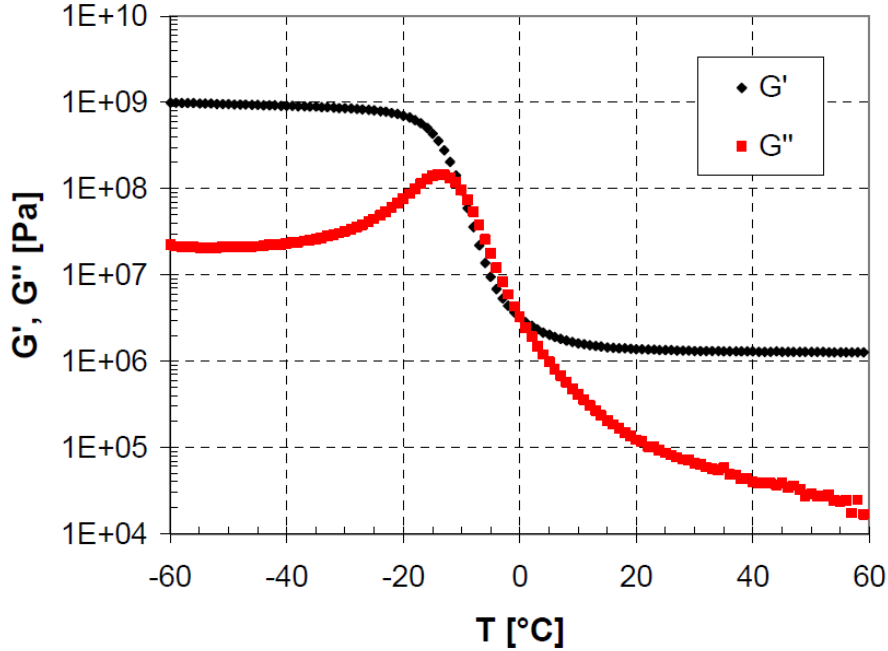


Figure 26. Temperature sweep for an unfilled S-SBR  $\varepsilon = 0.5\%$ ,  $f = 1$  Hz.

The viscoelastic processes are strongly dependent on temperature and a relation is noticeable between frequency and temperature in dynamic measurements.

While the measurement of dynamic modulus at a given frequency can be realised over a broad range of temperatures, the same mechanical characterisation carried out at a fixed temperature by varying the frequency can be applied only up to about 100 Hz. The estimation of high frequency moduli is however accessible via the time-temperature superposition principle proposed by Williams, Landel and Ferry in 1955 [68]. It states that the effect of changing the temperature is equivalent to the application of a multiplication factor  $a_T$  on the time scale. Reducing the relaxation data to the reference temperature  $T_{ref}$  leads to the following expression:

$$\log a_T = \frac{-C_1(T - T_{ref})}{C_2 + T - T_{ref}} \quad (16)$$

where  $C_1$  and  $C_2$  are numerical parameters depending on the reference temperature  $T_{ref}$ . They were first thought to be universal constants for all polymers where  $T_{ref}$  was set at  $T_g + 50^\circ\text{C}$ , with  $T_g$  the glass-transition temperature of polymer. However, later studies showed that the values vary from one polymer to another [63]. Also, the WLF equation is only valid within the range of temperatures  $[T_g \dots T_g + 100^\circ\text{C}]$ .

Thus, it is possible to extend the measuring range for isothermal processes by several decades and to combine the measured curves to a master curve. An example measurement converted into a master curve is shown in Figure 27.

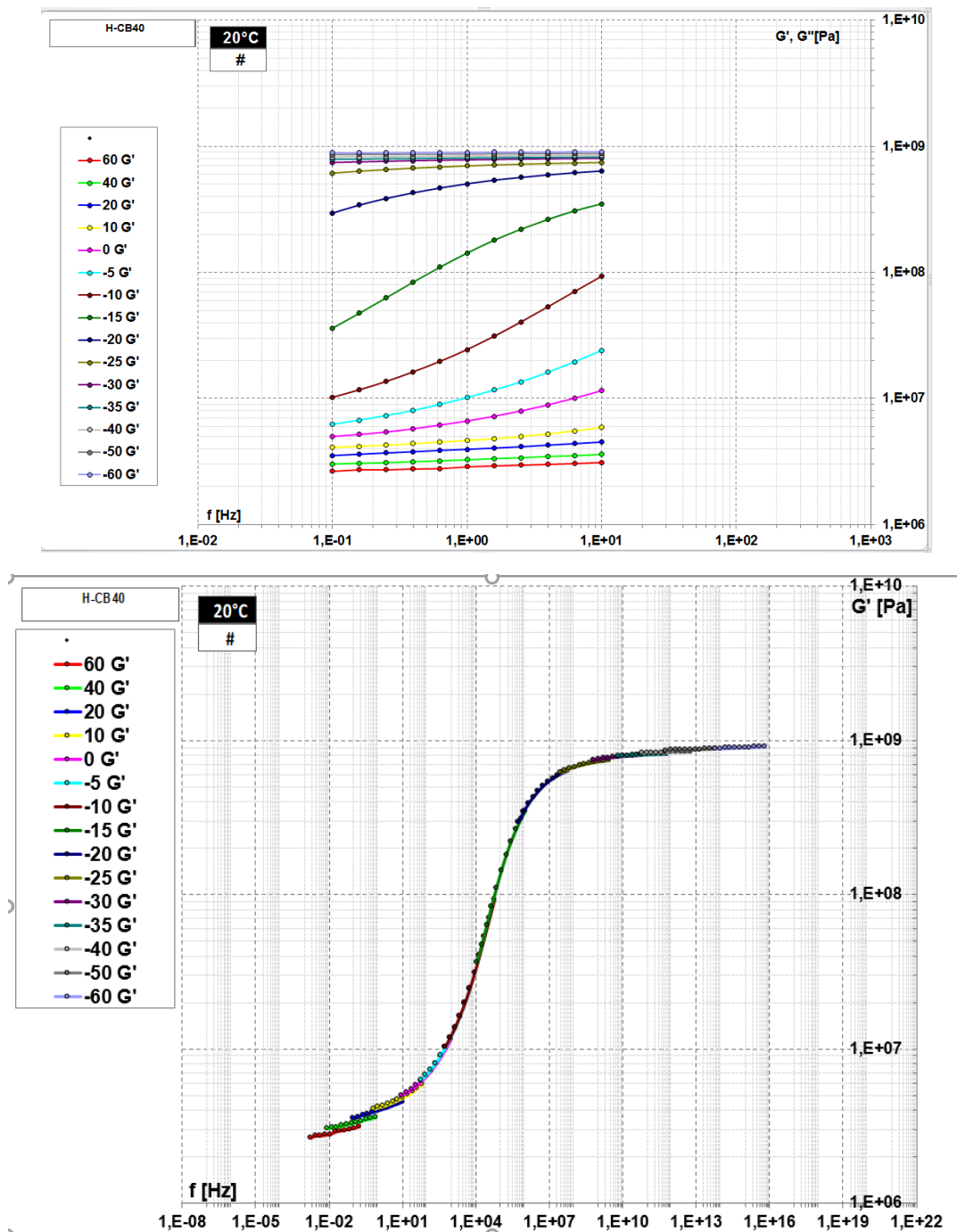


Figure 27. Application of the time-temperature superposition principle to the measured data (top) to filled SBR sample to create a master curve (bottom) for a reference temperature of 20 ° C at a deformation amplitude of  $\gamma=0.1\%$ .

This method is used to characterize the material behaviour for technical applications, especially with high-frequency excitations. A good agreement can be found with alternative measurement methods such as dielectric relaxation spectroscopy or ultrasonic analysis [69] [70].

Once the displacement factors for a fixed reference temperature  $T_{ref}$  have been determined, it is possible to calculate the corresponding master curve for a different service temperature  $T'$ . The associated parameters are converted as follows:

$$C_1' = \frac{C_1 C_2}{C_2 + T' - T_{ref}} \quad (17)$$

$$C_2' = C_2 + T' - T_{ref}$$

and inserted into Eq. (17):

$$\log a_{T'} = \frac{-C_1'(T_{ref} - T')}{C_2 + (T_{ref} - T')} \quad (18)$$

Accordingly, it is possible to determine the corresponding viscoelastic master curves for any service temperature within the validity range of the method (see Figure 28). It can be concluded that a temperature change is consequently equivalent to a change in frequency and a shifting of the viscoelastic behavior is produced along the frequency axis, whenever a temperature change occurs.

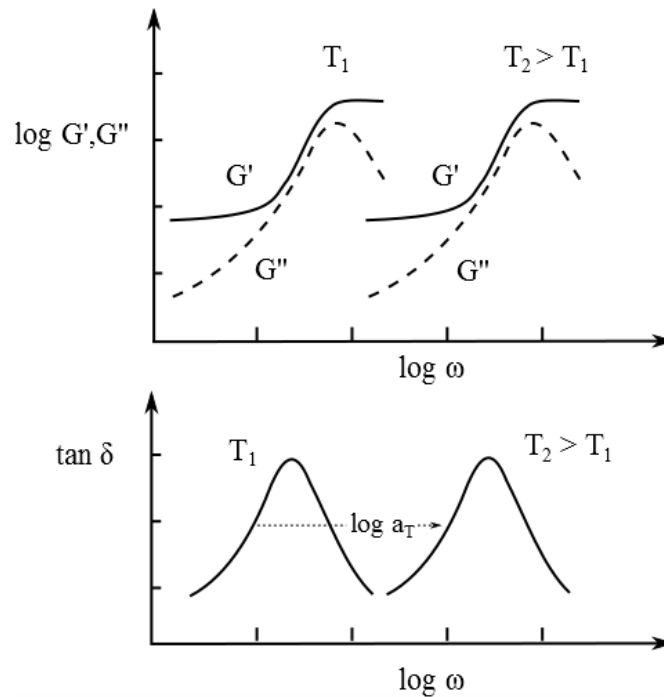


Figure 28. Dynamic properties of rubber as a function of frequency and temperature. The curves are displaced along the frequency axis by a distance  $\log a_T$  given by the WLF relation.

The glass transition and thus the loss maximum shift to higher frequencies in case of a higher reference temperature. This proves that the free volume for higher temperatures only decreases



significantly at higher frequencies and thus leads to internal friction with higher thermal losses. The storage and loss modulus increase strongly. Tire manufacturers design rubber products with the maximum of loss tangent at a typical service temperature of approximately 40-60°C in order to use the smallest amount of energy during rolling by internal losses, while during the braking process as much energy as possible should be dissipated. The nature of the asphalt surface also plays an important role in terms of the excitation frequency, for this reason some tyres perform better on a particular type of asphalt than on others.

### 2.5.2.1 Influence of the filler on the dynamics of elastomer materials

The time-temperature superposition principle according to Vogel et al. and Williams et al. can be very good for unfilled polymer systems with small deformation amplitudes. The situation is different for systems with reinforcing fillers since such vulcanizates show strong non-linearities at high loads. As discussed before (Section 2.4.4), Klüppel et al. [71] [72] shows that a smooth viscoelastic master curve ( $G^*(\omega)$ ) for the carbon black filled composites can be constructed by shifting the isothermal frequency curves horizontally on the frequency scale and after that vertically on the modulus scale. He assumed that the significant decrease of the storage modulus with increasing temperature is due to the loss of filler-filler bonds or glassy bridges. Hence, this model takes into account the changes in the structure of a filler network by vertically shifting the isotherms.

The same method can be applied on silica-filled SBR composites to verify the validity of this mastering procedure for both  $G'(\omega)$  and  $G''(\omega)$  by shifting the isotherms horizontally on  $\omega$ -scale and then vertically on  $G'(\omega)$  scale. Isothermal frequency sweeps of 80 phr ( $\Phi_{\text{silica}}=0.213$ ) silica-filled composite can be measured in the temperature range -35°C to 150°C with a strain amplitude of 0.2%.

Figure 29a shows the horizontally shifted isothermal frequency sweeps of silica-filled composite based on the shift factors determined for a pure SBR (see inset Figure 29a). The shift factors obtained for pure SBR can be fitted with the WLF function with  $T_{\text{ref}}=0^\circ\text{C}$ . In Figure 29a, high frequency isotherms ( $\omega_T > 1$  rad/s) properly overlap corresponding to a temperature range of 5°C to -35°C. The isotherms of  $G'(\omega)$  and  $G''(\omega)$  in the range of 5°C to 150°C do not overlap for the frequencies lower than 1 rad/s,. This result is a typical behaviour for filled elastomers and an additional vertical shifts  $b_T$  has to be applied to construct a smooth and continuous master curve. The result of this procedure is shown in Figure 29b. The non-overlapping  $G'$  isotherms can be shifted vertically on the modulus scale with a reference temperature of 5°C and the respective vertical shift factors were reported accordingly in the inset Figure 29b. A similar procedure can be applied for the  $G''$  isotherms using the vertical shifts previously obtained.

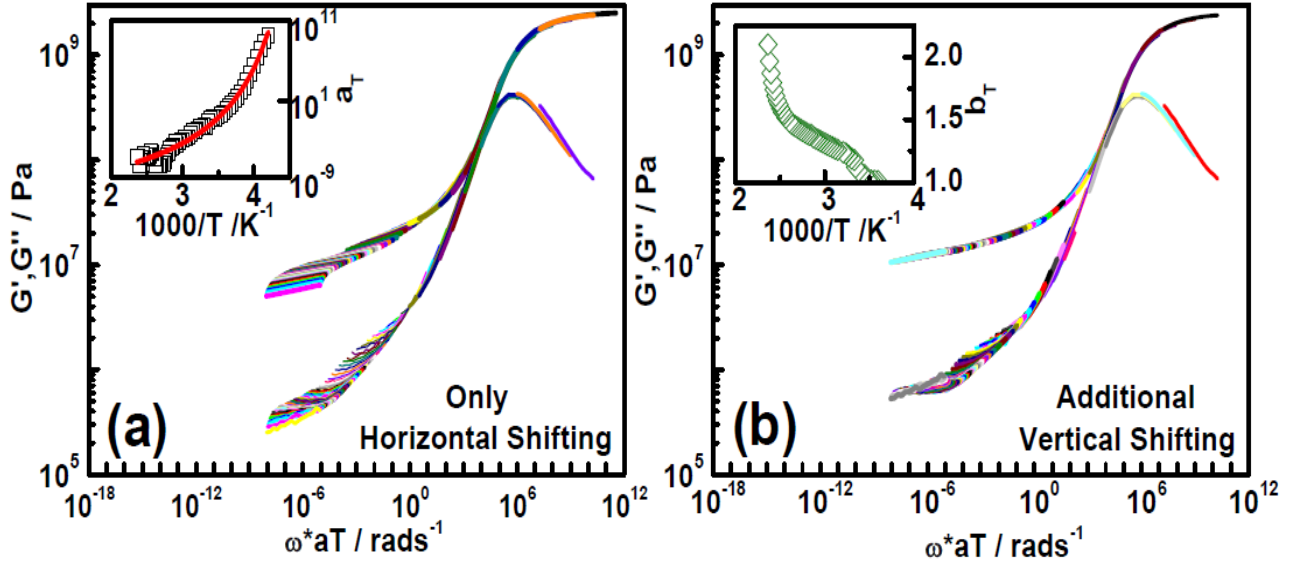


Figure 29. (a) Master curves constructed from the isothermal frequency sweeps of 80phr silica filled composite by using horizontal shift factors of pure SBR (inset as empty squares). (b) Master curves as in a) with additional vertical shifts. The vertical shift factors (empty diamonds) are shown in the inset.

The WLF description can not adequately map the thermal activation of the filler network according to Figure 29a, resulting from the immobilized polymer bridges between adjacent filler particles [71] [73]. However, to obtain a continuous curve, an additional vertical shift of the data must be performed.

For the modules follows:

$$G'(f, T) \rightarrow b_{T,G'} \cdot G'_T(a_T f) \quad (19)$$

$$G''(f, T) \rightarrow b_{T,G''} \cdot G''_T(a_T f) \quad (20)$$

The shift factors is related to the Arrhenius activation process. This results in the following dependency for the vertical shift factors with the gas constant R:

$$b_T \sim e^{-\frac{E_A}{R \cdot T}} \quad (21)$$

An example for silica and carbon black systems is shown in Figure 30. The apparent activation energy is identical for small amplitudes in the case of the storage modulus and loss modulus, as well as the vertical shift factors. This fulfils the Kramers-Kronig relationship for the complex modulus [74] [75]. On the other hand, the activation energies of the storage and loss modulus differ for higher deformation amplitudes, where they are higher in the case of  $G''$  in comparison with  $G'$ . This difference arises by increasing the filler content [73] [76]. An approximately constant value was found for temperatures below the glass transition temperature. Hence, the influence of the filler on the viscoelastic master curve is taken into account by introducing a temperature-dependent vertical shift

factor, which is interpreted physically as an apparent activation energy of the glassy polymer bridges in the nanoscopic interstices between adjacent filler particles.

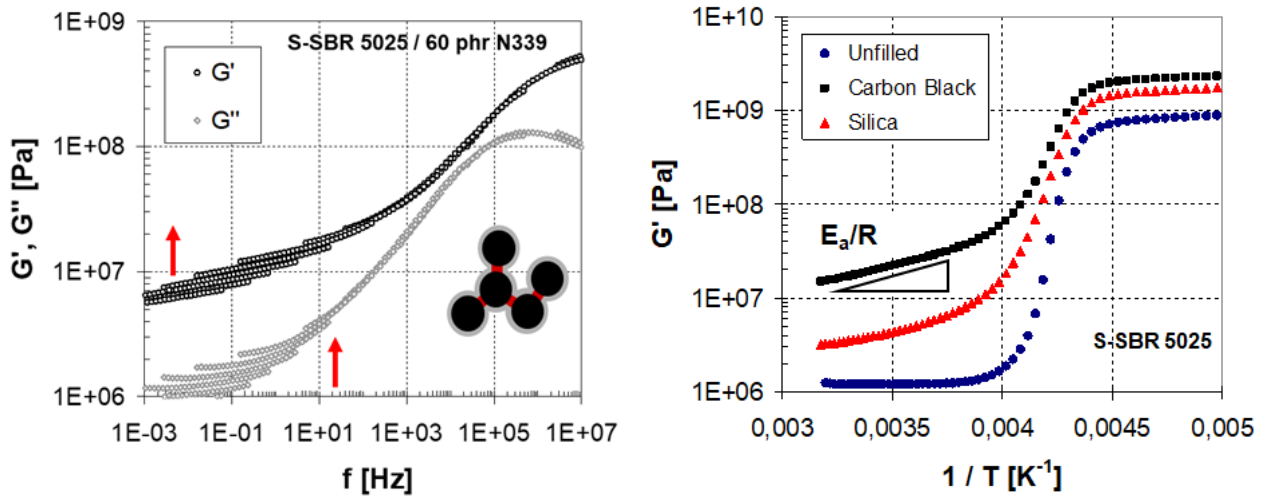


Figure 30. Introduction of the vertical shift factors for silica and carbon black filled rubber (left) and temperature dependent process related to the activation energy (right) [77].

Silica is dynamically softer than carbon black (e.g. better interlocking properties should result) and show a lower energy activation of filler-filler bonds above the glass transition temperature due to the temperature process.

Table 2. Energy activation of filler-filler bonds for S-SBR filled with silica and carbon black.

	Ea (kJ/mol)	
	Carbon black (80phr)	Silica (80phr)
G'	11.57	7.93

## 2.6 Elastomer friction physics

A deep understanding of the experimental observations and physical processes is essential for an appropriate modelling of rubber friction (see Figure 31). First, it is necessary to carry out laboratory tests in order to understand the complex contact mechanism tyre/rough road, which occurs from different length scales of roughness (macro, meso and micro).

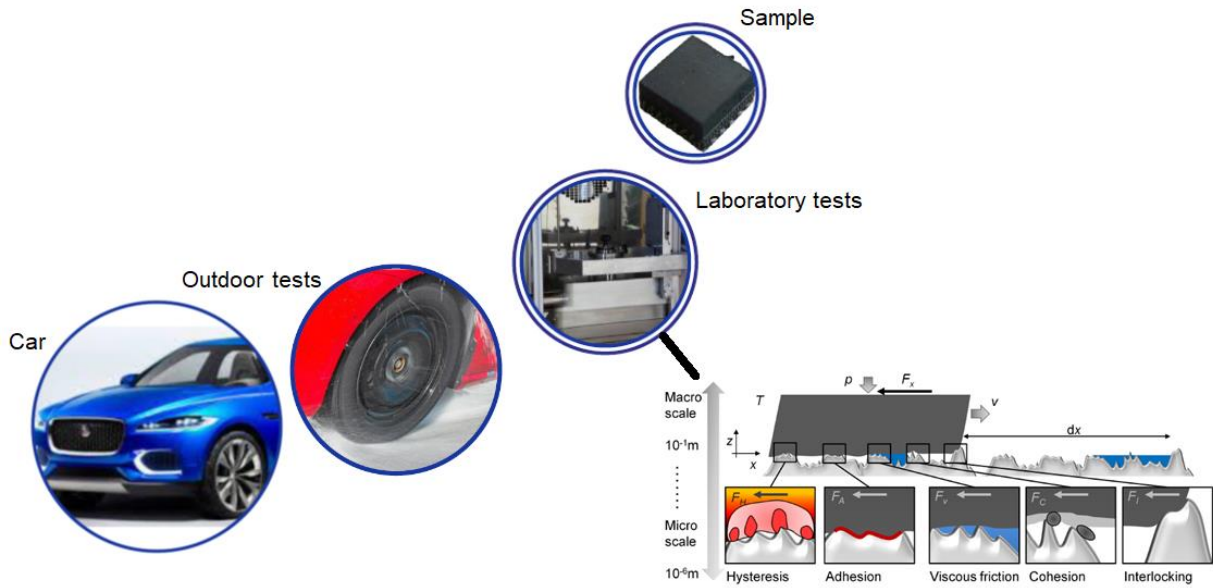


Figure 31. Approach used for the tyre traction prediction. The complex tyre road concept is investigated macroscopically and microscopically which shows the relevant physical effects for rubber friction [78].

In this paragraph is presented an illustration of the physical effects contributing to the frictional response of sliding rubber and a brief overview of the modelling approaches. Afterwards, the results of the most important fundamental experimental studies are summarized, followed by a short review of the current experimental techniques. Analytical approaches are summarized and compared with the proposed multiscale framework. Finally, the main aspects of rubber friction properties about grip performance of tyres are discussed.

Friction properties of elastomers have been extensively studied for decades [79] [77] [80] [81] [82]. Considering a rubber block sliding over a rigid substrate with a sliding velocity  $v$  (Figure 32) the friction coefficient  $\mu$  between the two solids is defined as:

$$\mu = \frac{F_R}{F_N} \quad (22)$$

where  $F_R$  denotes the friction force (tangential force) and  $F_N$  is the normal force (load). According to this definition, the friction coefficient is expected to be independent of the specimen size. This is based on the assumption that both forces increase at the same rate, e.g. the friction coefficient is independent of the load. Studies of friction between solid bodies started a few hundred years ago with the pioneering works of Da Vinci, Amontons and Coulomb using simple experimental setups.

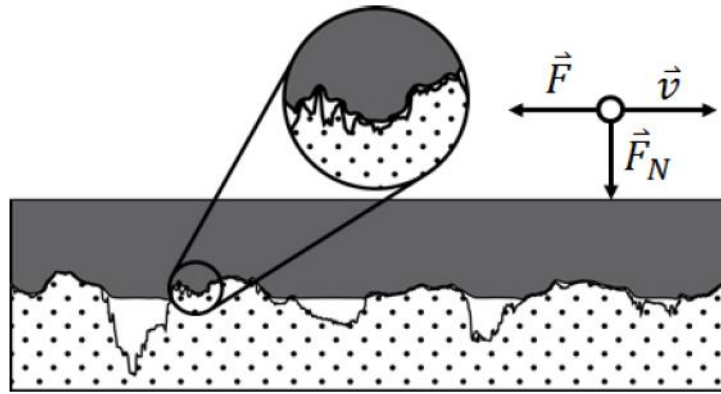


Figure 32. Representation of a frictional process between a rubber sample and rough granite with the direction of movement to the right and the opposite frictional force at a load [41].

Despite often  $\mu$  is expressed as a coefficient, in real application friction is a much more complex phenomena which can not be described by a linear relation. In the case one of the friction “body partners” is made of rubber, indeed, the friction coefficient is not a constant value but it depends rather on both external factors as seen in Figure 33.

Road	Contaminant (fluid)	Tyre
Macrotecture	Chemical structure	Tread pattern design
Microtecture	Viscosity	Rubber composition
Unevenness/Megatecture	Density	Inflation pressure
Chemistry of materials	Temperature	Rubber hardness
Temperature	Thermal conductivity	Load
Thermal conductivity	Specific heat	Sliding velocity
Specific heat	Film thickness	Temperature
		Thermal conductivity
		Specific heat

Figure 33. Factors influencing the road surface friction (reproduced from Kummer [83] and Sandberg [84]).

Considering a tyre submitted to a load  $F_N$  and a tangential force  $F_x$  in the sliding direction. During acceleration and braking phases, the velocity of the wheel differs from the vehicle speed and one can define a slip as following:

$$s_l = \frac{v_r - v_0}{v_0} \quad (23)$$

Where  $v_r$  is the rotational velocity of the wheel and  $v_0$  is the rotational velocity without braking or accelerating torque (vehicle). For instance, during braking,  $s_l = 1$  means that the vehicle wheels are completely blocked. From these considerations, the level of longitudinal performance characterised by the friction coefficient  $\mu(s_l) = F_x / F_N$  can be represented on a unique curve (Figure 34). The level and the position of the  $\mu(s_l)$  maximum depend on the type of rubber, road texture, and operating conditions (temperature, vehicle velocity). Under given conditions, the friction maximum  $\mu_{max}$

corresponds to the optimum that can be achieved during braking process. The following decrease at high slip rates displays the negative impact of the temperature on wet grip performance since this effect is amplified at higher starting vehicle velocity.

In a similar way, a side-force coefficient can be defined when the tyre makes an angle with the trajectory of the vehicle. A  $\mu$ -slip curve can be assessed for an estimation of the tyre performance during cornering.

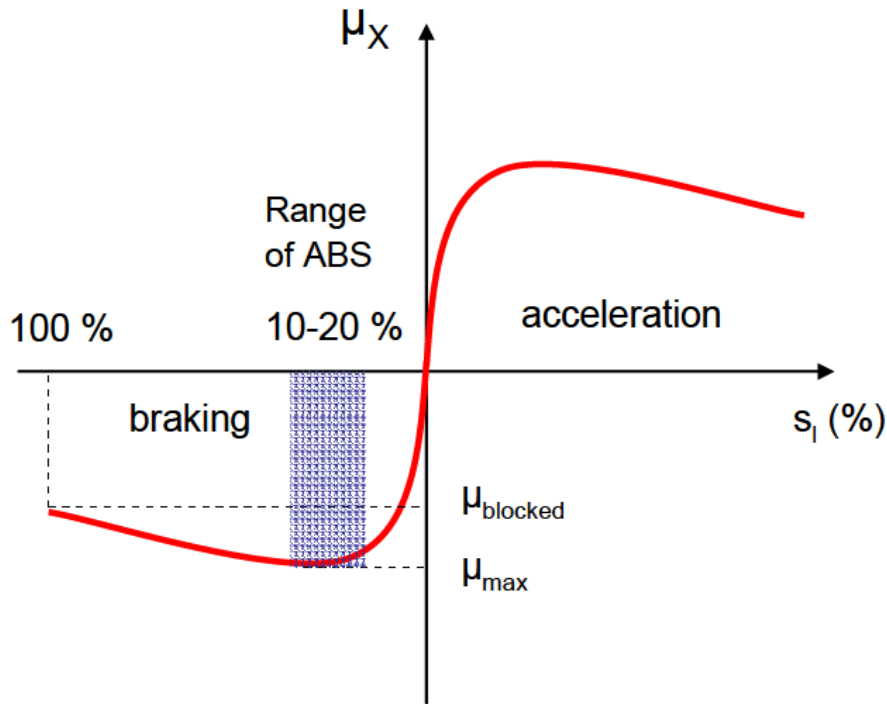


Figure 34. Typical  $\mu$ -slip curves for longitudinal accelerating and braking phases. The ABS range is indicated in the braking region [85].

Locked wheel becomes impossible with the introduction of ABS-Braking system. The braking torque is constantly adjusted in the range of slip associated with the maximal adherence ( $s_1 \sim 10\%$ ). The work of Roth gave some precisions on the mechanisms involved during ABS braking phases [86]: in the entrance zone of the contact, the rubber is first compressed and then brought into shear through the velocity of the vehicle (deformation regime). If the potential of adherence of the rubber is reached, the tread element starts to slide and friction takes place at the interface until the exit region (slip regime). The deformation regime is associated with sliding velocities around  $v \sim 1$  cm/s, which gradually increase in the slip regime up to  $v \sim 1-3$  m/s. The level of skid resistance is determined via the ability of the material to generate tangential stresses in the contact area.

The present work is focused on the understanding of the contact mechanics especially on the friction between rubber and rigid rough substrates. Generally, the following mechanisms are admitted for friction forces generated between rubber and a rigid surface:

- *Hysteresis*, friction caused by the energy loss occurring during the indentation of rough asperities. As rubber is viscoelastic, a part of the work done to deform it is not given back, resulting in a resistance to the movement;

- *Adhesion*, friction force generating on molecular length scale between the surfaces which come into a close contact;
- *Viscous*, friction force caused by the shearing of a viscous medium present in the contact zone.
- *Abrasion*, mechanical failure induced by high stresses generating in presence of sharp asperities. The energy required to cut out material generates a friction force;
- *Interlocking*, the rubber block hits with its edges asperities of the rough road surface causing a horizontal resistance force (especially expected at the leading edge of the rubber block and increases with the surface roughness).

The individual friction contributions can be considered separately and treated additively [87] [88]. Eq. shows the individual contributions:

$$\mu_{tot} = \mu_{Hys} + \mu_{adh} + \mu_{visc} + \mu_{coh} + \mu_{inter} \quad (24)$$

The dewetting phenomena occurring between the bodies in contact also plays a role. The lubricant between substrate and rubber may not remain in sealed off regions within the contact producing dry patches (more water is wiped away) or less dry patches and therefore changing the friction behaviour.

A closer look at the friction phenomena reveals that for many applications, especially for tire-road contacts, only the first two contributions (hysteresis and adhesion friction) dominate the entire friction process. The hysteresis contribution mainly plays a role on rough surfaces where the size of the asperities is sufficiently large to locally deform the rubber. On dry and smooth surfaces, the friction coefficient is mainly affected by the adhesion contribution. The latter three occur only in special cases and have only a small share in some cases. The proportion that contributes to abrasion is less than 1% of the total friction contribution as showed in the middle of the 20th century [89]. Therefore, only the hysteresis and adhesion friction are considered in more detail below.

The first systematic experimental investigation about rubber friction was carried out by Grosch [90]. He proved in his pioneering studies that the friction force has two main contributions as adhesion and hysteresis, respectively. He carried out friction measurements on both smooth wavy glass and silicon carbide abrasive paper. In order to get rid of adhesion interactions and to obtain a measure of hysteresis, he dusted the substrates with alumina powder as lubricant. A general trend of the overall friction coefficient as a function of the sliding velocity is shown in Figure 35. The friction curve shows two peaks, one at lower velocities coming from the adhesion component and the second one at higher velocities, due to the hysteresis component.

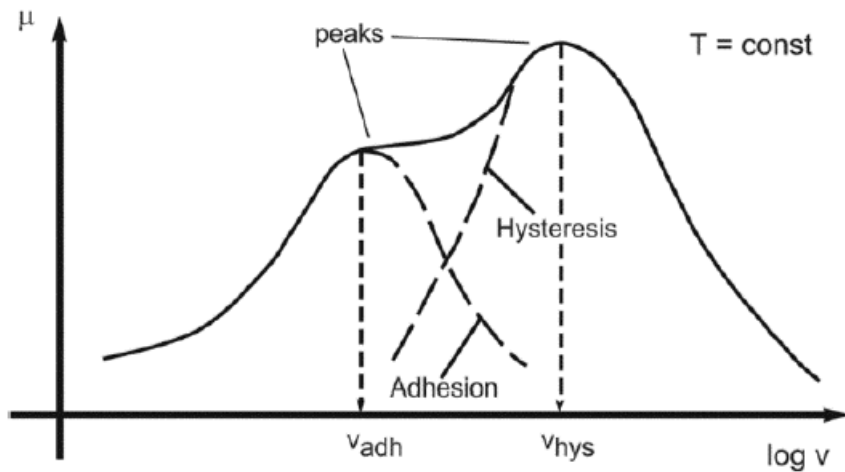


Figure 35. General trend of the friction coefficient between rubber and a rigid rough surface as a function of the sliding velocity, from [90]. The overall friction corresponds to the sum of hysteresis and adhesion.

Grosch also gave the first valuable results on the temperature and velocity dependence of rubber friction, which is related to the WLF theory. In fact, he proved that, similar to the viscoelastic moduli, friction can also be extrapolated beyond the measurement range using master curves based on the time-temperature superposition principle [90].

Comparing the results obtained in the case of lubricated rough surface with a dry and apparently smooth surface, he observed a shift of the friction curve to lower speeds, as schematically illustrated in Figure 36. Therefore, he concludes that the shift is induced by the different characteristic distance between the asperities, that are smaller in the case of a dry smooth surface in comparison to macroscopic rough surfaces.

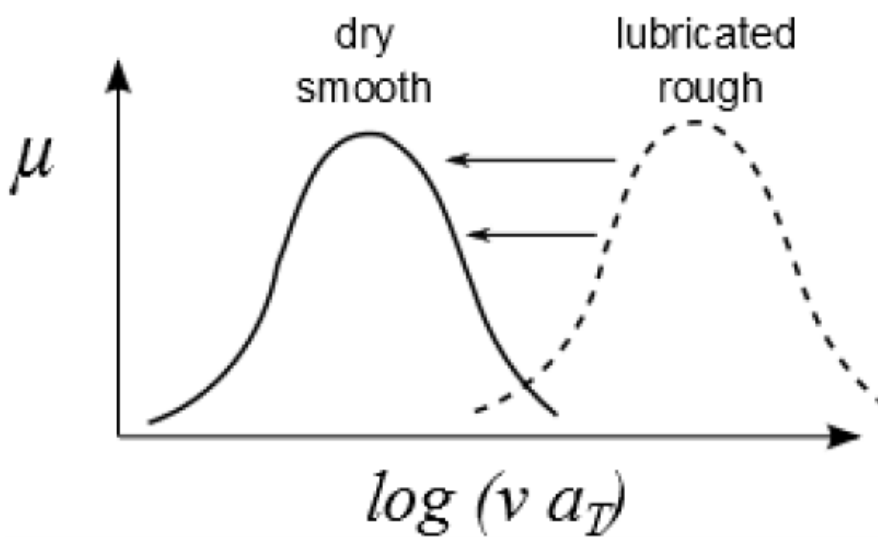


Figure 36. Comparison between dry friction on smooth surfaces and lubricated friction on rough surfaces, adapted from [90].



The following chapter consist a deeper description of hysteresis and adhesion and the corresponding analytical approaches to predict the two main friction contributions and to understand the complex friction behaviour under dry/wet condition.

### **2.6.1 Numerical models**

An overview of the numerical model approaches is given in this chapter as well as a summary of the continuum mechanics background. This will be necessary for the finite element formulation of solid mechanics and structural problems in order to provide an overview of the numerical models for rubber friction by using the finite element method. In particular, the fundamental balance principles is briefly discussed, as they need to be considered in all branches of the continuum mechanics, followed by an overview of the constitutive equations and finite element analysis working principles.

Basically the two approaches developed are single- and multiscale:

- Single scale approaches
  - Elastic or viscoelastic continuum on flat or rough surface without microscopic details
  - Viscoelastic continuum on rough surface with all surface details
  
- Multiscale approaches
  - Contact homogenization
  - Projection methods

The first category is composed by pure elastic or viscoelastic rubber models without modelling the complex contact interactions between the rubber and a flat or rough surface (without microscopic details). These models concentrate on the macroscopic modelling of rubber friction for the prediction for example of the contact pressures or temperatures. Furthermore, such models are also used to compare different rubber block geometries on the macroscopic length scale. A drawback regarding multiple rubber-surface combinations is that for such approaches a complex friction experiment is necessary to incorporate a friction law in the contact simulation. Thus, for slight changes in material or surface properties, a completely new measurement has to be performed. A prediction of the hysteretic contribution is thus not achievable.

Another way to model rubber friction applied in the present work is the direct modelling of the viscoelastic material properties and the involved rough surface with its details. Predictions and detailed studies of the contact interaction are possible with such approaches by using friction experiments for the validation of the model. Consequently, no experimental data from the friction experiments are necessary as a model input. The viscoelastic material properties are achieved through laboratory experiments. The rubber material is considered homogeneous in most numerical studies of rubber friction. An extension to complex heterogeneous rubber micro structures is possible and probably necessary for detailed wear and adhesion studies. Nevertheless, modelling the surface roughness with all asperity details makes a single scale calculation too expensive for today's computer technology. Therefore, complex contact interactions with rough surfaces can be modelled with

numerical multiscale approaches in an efficient way; in fact, the surface profile can be reproduced by a superposition of sinusoidal waves of different frequency and amplitude as shown in Figure 37:

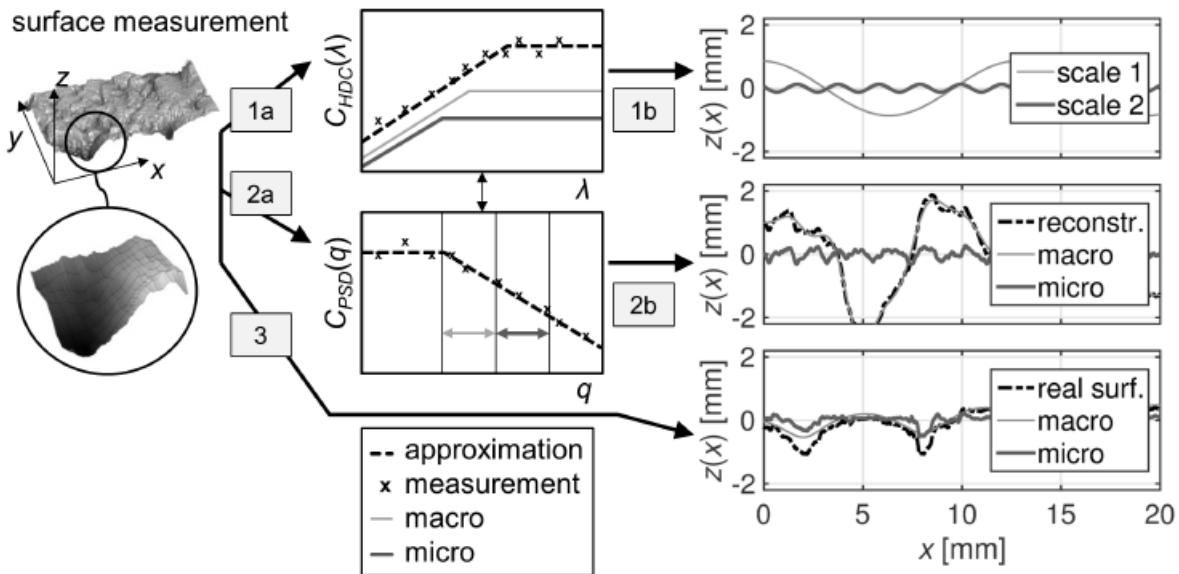


Figure 37. Three approaches for processing and decomposition of a rough surface measurement: 1) HDC-based approximation, 2) PSD-based reconstruction, 3) Direct filtering of the rough surface [78].

## 2.6.2 Hysteresis and adhesion friction

A rubber pressed against a rigid body tends to adapt to the interface contour. If sliding takes place, the rough surface will dynamically excite the layer of rubber that gets in contact with it. Since rubber is viscoelastic, each local deformation cycle is characterised by a respective hysteresis with a consequential loss of energy. For this reason, the deriving friction force is called hysteresis friction.

To have a better understanding of this mechanism, a single asperity should be taken into account. Consider Figure 38, where the asperity is moving at a defined speed relative to rubber, the section of material located in front is pressed and slides over the asperity. Since rubber is not perfectly elastic, it does not relax instantaneously when pressed into the surface cavities and therefore it can not push on the downstream surface as hard as it pushes on the upstream surface. This unsymmetrical pressure distribution, coming from the hysteretic nature of the rubber, results in friction forces even if the surfaces are lubricated and no adhesive interactions occur [91].

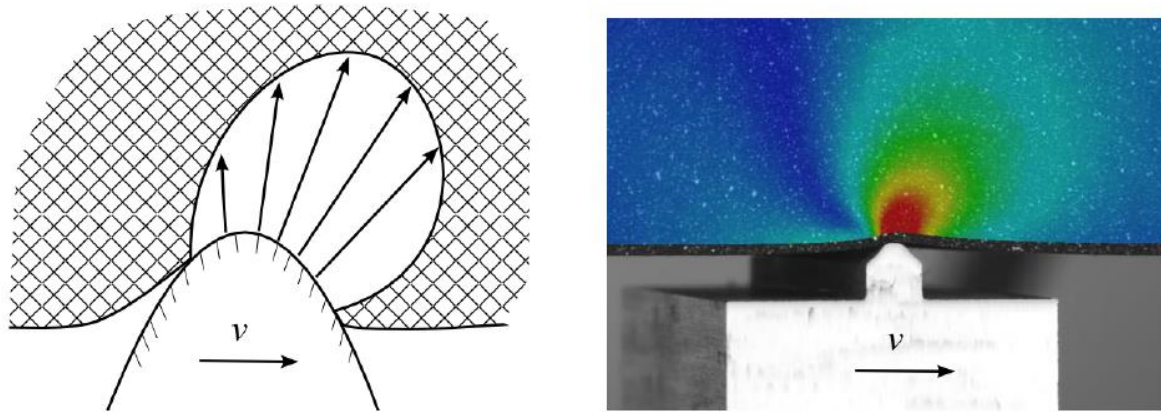


Figure 38. Concept of unsymmetrical pressure distribution generated by hysteresis friction (left) and deformation analysis performed by optical technique (right) [91].

As previously mentioned, Grosch carried out a fundamental study of the hysteresis friction in the 60's [90]. A relevant part of his studies focused on measuring the friction on a wavy glass surface. In this special case, each surface irregularity excites the rubber dynamically at a frequency related to the length of the wave. The correlation found between the velocity dependence of  $\mu$  and the frequency dependence of  $\tan \delta$ , [92] confirmed the viscoelastic nature of rubber friction (see Figure 39).

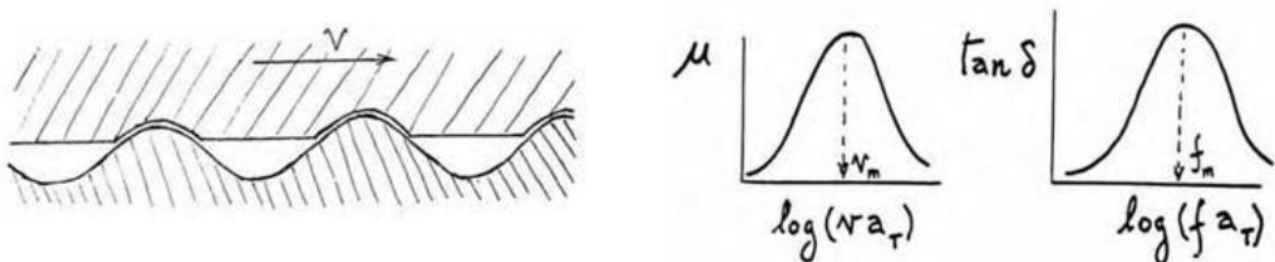


Figure 39. Sliding friction for a viscoelastic material over a sinusoidal surface with a qualitative comparison between friction master curve and  $\tan \delta$  master curve [92].

Another contribution called adhesion plays an important role in the friction phenomena. The previous arises from molecular interactions (i.e. Van der Waals forces) between rubber and substrate during the sliding process. The distribution of the contact patches is constantly renewed within the contact area, inducing a cyclic formation and breakage of the molecular bonds between polymer chains and surface asperities associated with dissipative effects.

The challenge is to determine how the level of adhesion and hysteresis can vary depending on the testing conditions (load, temperature, lubricant, speed).

The adhesion component dominates under dry condition and can be strongly reduced by lubricating the interface with liquids, for instance tensides as water plus small amount of soap. Indeed, a rough surface covered with a water soap mixture matches well [85] [93] [94] [95] with a pure hysteretic

response without the adhesive part since the low surface tension of the mixture lead to a separation of the rough surface and the rubber bulk.

In water condition a hysteresis contribution occur (on the hypothesis that is not changing from wet to dry condition), as well as a partial adhesion contribution ,“adhesion wet”, which appears when the lubricant squeezes out from the contact establishing dry contact patch rubber substrate. The lubricant dewets by the nucleation of dry patches. De Gennes, Roberts [96] [97] discovered that the lubricant film between the rubber and the substrate is unstable and may dewet by the nucleation and growth of a dry patch surrounded by a liquid rim that accumulates the expelled fluid. The expelled liquid is collected in a thick rim of fluid surrounding the formed dry zone. A representation of this scenario is shown in Figure 40.

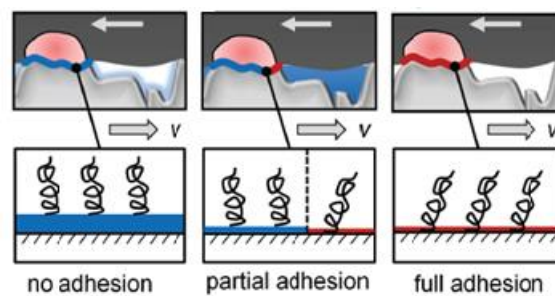


Figure 40. Level of adhesion on dry/wet conditions.

The dry patches phenomenon based on spreading coefficient  $S$  which is represents the energy balance of interfacial free energy  $\gamma_{ij}$  between substrate (F), rubber (R) and liquid (L), see Figure 41. Higher negative value reflects higher dry patches occurrence. The water condition shows significantly higher negative value, indicating higher dry patches in comparison to other lubricants like soap or water + soap.

$$S \triangleq \gamma_{RF} - (\gamma_{RL} + \gamma_{FL}) \quad (25)$$

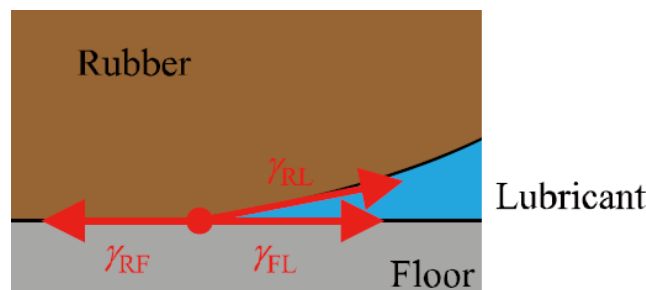


Figure 41. Energy balance of interfacial free energy between substrate rubber and liquid [98].

The actual contact condition tire/rough track reveals the level of hysteresis, adhesion and the linked dewetting process.

The tire/wet road contact area is usually divided into three zones as depicted in Figure 42:

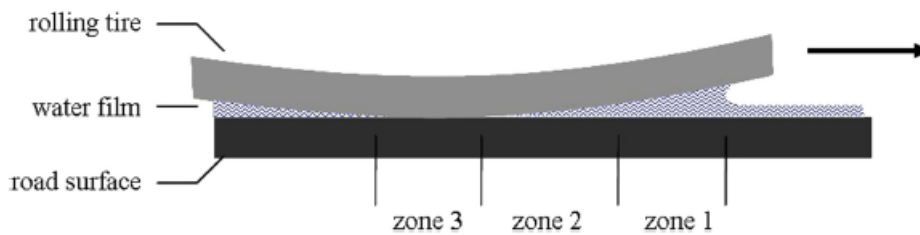


Figure 42. Tire/wet road contact area [99].

- in front of the tire (zone 1), water accumulates and tends to lift up the tire;
- in zone 2, the bulk water is evacuated and the water film becomes thin but it still prevents the contact between tire and road;
- in zone 3, contact is established between the tire and the road surface. Friction forces are generated in this zone.

The time to evacuate water decreases when the vehicle speed increases. Consequently, the size of zones 1 and 2 increase and consequently friction decreases. In the case where zone 1 occupies the whole contact area, contact between the tire and the road is lacking, this is the onset of aquaplaning. The above description is widely used for the development of tire/road friction models. However, there is still a vague knowledge about delubrication mechanisms in zone 3. Authors like Moore [99] talk about water evacuation by microasperities, but it is not clear whether the restored contact is dry enough to develop adhesion forces. In the contact area the macrotexture helps, jointly with the tire tread depth, to evacuate the bulk water in zone 1 (thickness of the order of millimeter). This surface drainage is possible thanks to the reservoirs created by the space between the aggregates. Once the bulk water is evacuated by the macrotexture, a thin water film (thickness of the order of tenth of millimeter or less) remains in zone 2 and, locally in zone 3, water ‘pockets’ at the summit of the asperities. The squeezing of these residual water films is only possible by high pressure exerted by angular asperities forming the microtexture. Friction forces are then generated by the interaction between the tire rubber and the road surface microtexture.

Relative slip between the tire and the road generates, in the presence of thin water films, hydrodynamic pressure, which rises rapidly on the upward slope of surface asperities and then drops to negative values on the downward slope (Figure 43 top).

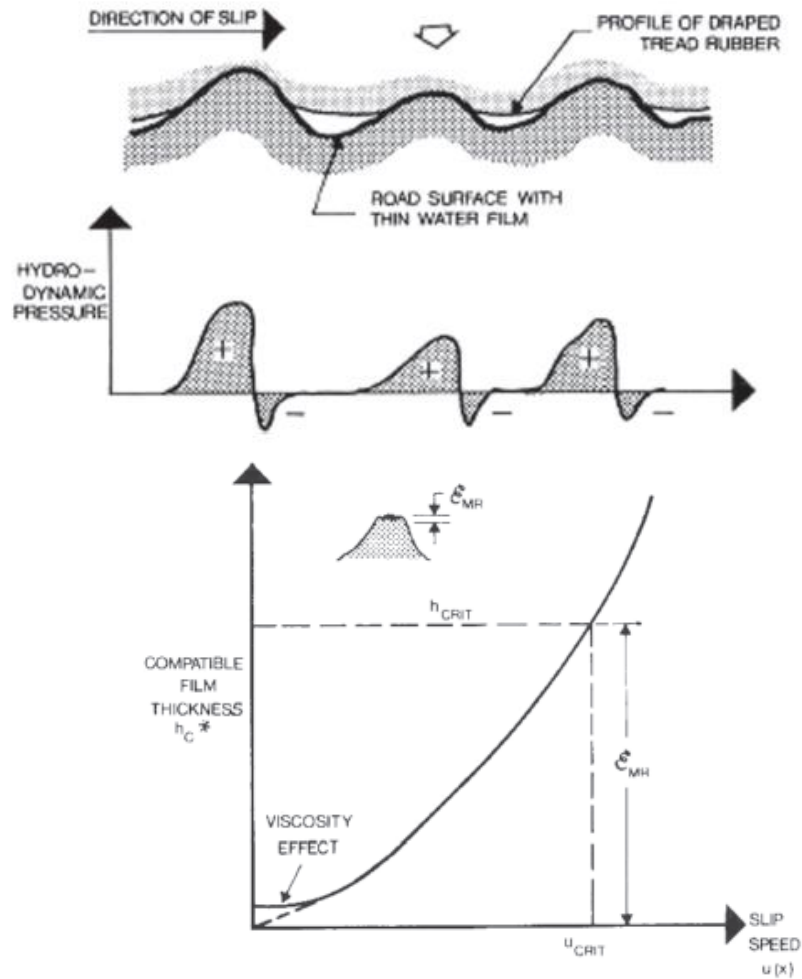


Figure 43. Generation of hydrodynamic pressure due to relative slip between the tire and the road (top) Variation of the water depth with slip speed (bottom) [99].

The result is an uplifting force which tends to separate the tire and the road. This mechanism generates a water depth  $h_c^*$  at the asperity summits which ensures equilibrium between hydrodynamic (due to the water film) and elastic (due to rubber deformation) forces acting on the tire tread. Modeling shows that  $h_c^*$  is greater for more rounded asperities and increases as the relative slip speed increases (Figure 43 bottom), and that the relative speed varies with position in the contact area and reaches a maximum value at the rearmost point of the traction zone (zone 3). Thus, “erosion” of the contact area also occurs from its rear part, in addition to bulk water intrusion from the front part; contact loss due to thin water film is usually referred to as viscoplaning.

Savkoo [100] in his theory also states the need of a minimum microtexture height to emerge from the water film. The same author adds that, due to the high viscosity related to the low thickness of the water film (few microns), microtexture also needs a good sharpness to break down the water film. Rohde [101] and later Taneerananon and Yandell [102] proved the approaching time between two parallel plates, which simulates the time needed for a tire tread element to sink in the water film and touch the road surface, decreases when one surface is rough and the decrease is more important for

triangular asperities compared with cylindrical asperities. These works highlight the fact that shape is another main characteristic of road surface microtexture.

Research studies carried out by Grosch showed that both micro-texture and macro-texture of the countersurface have a strong effect on the friction coefficient. In particular, referring to Figure 44, the micro-texture produces a higher grip level, especially at low sliding speed. This effect is even stronger in the case of wet friction, where the micro asperities produce a significant hysteresis and exert high pressure locally capable to break through the water film [103] [104] [105]. On the other hand, rougher macro-texture implies a better grip level at high sliding velocities.

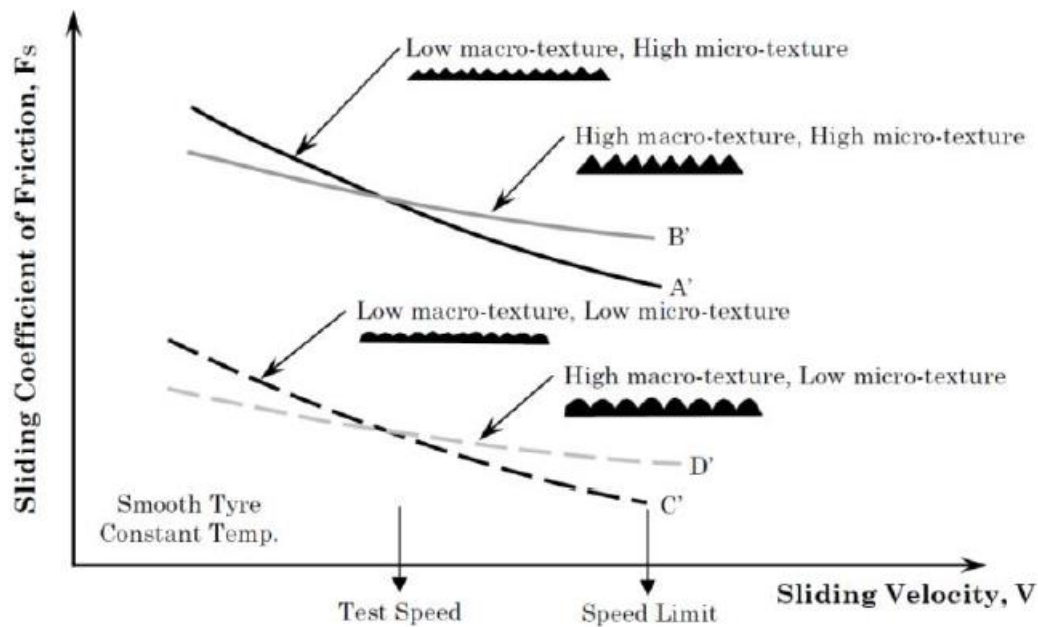


Figure 44. Effect of the micro-texture and macro-texture on the friction between rubber and rough substrates at different sliding speeds. Adapted from [106].

Finally, the recent works by Do et al. [107] provide a further insight into the variation of skid resistance with water depth, mainly for thicknesses of the order of tenth of millimetre using sandblasted aggregate mosaics (Figure 45a). These authors varied the microtexture level while maintaining the same macrotexture. The friction/water depth variation was obtained by measuring the friction coefficient at dry state and different wet states by spraying the surface with successive equal quantities of water. Figure 45(b) shows that without any microtexture (specimen S590-E0), the friction coefficient drops as soon as the surface is wetted. With microtexture (specimens S590-E1 to E3), the friction coefficient remains close to the dry value until the water depth reaches a critical value (between 0.1 and 0.2mm). Above this critical water depth, the friction coefficient drops drastically. Increasing the microtexture level (E1 to E3 respectively) also helps to maintain a higher friction coefficient.



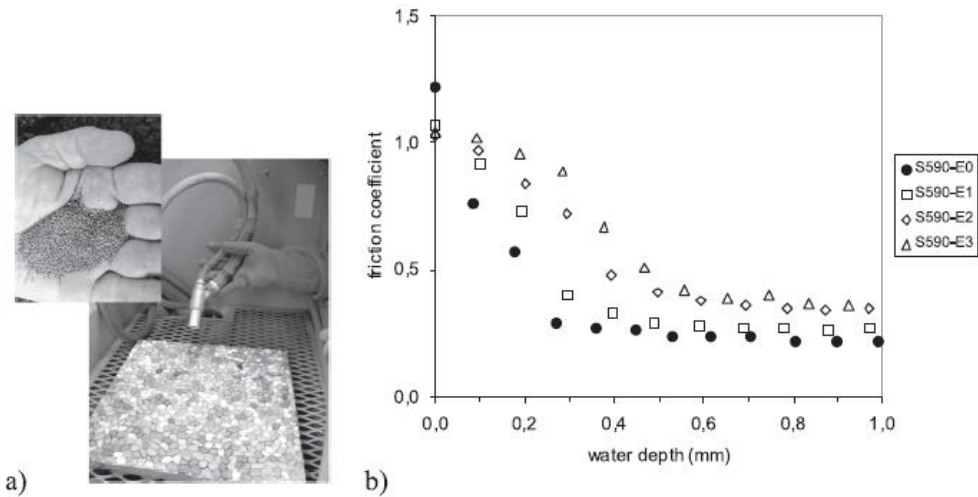


Figure 45. Variation of friction coefficient with water depth (a): sandblasting of the specimen surface; (b): comparison with/without microtexture) [107].

## 2.7 Modelling rubber friction

After an introduction to the mathematical descriptions of rough surfaces, a short overview and classification of the current analytical and numerical models for rubber friction is provided. The most relevant results of the pioneers work are summarized. The advantages and disadvantages of the methods are discussed in order to prove the necessity of a FEM multiscale approach for elastomer friction on rough surfaces, which will be introduced in chapter 4.3.

### 2.7.1 Surface roughness description

The road surfaces usually made of asphalt or concrete are rough over many length scales and exhibit the self-affine character of fractal surfaces. An overview of the fractal geometry is given in Mandelbrot (1983). An example of a rough road surface is given in Figure 46. Self-affine surfaces show statistical invariance under anisotropic dilation in a certain surface-wavelength ( $\lambda$ ) range ( $\lambda_{\min}$ – $\lambda_{\max}$ ). Accordingly, a rough surface shows the same statistical properties and morphology under a scaling  $\alpha$  in cross section direction and  $\alpha^H$  in the perpendicular direction. The so-called Hurst-exponent  $H$  is introduced as a measure of the surface irregularity and is linked to the fractal dimension by  $D = 3 - H$  for three-dimensional surfaces.

One way to describe mathematically the measured rough surfaces is to calculate the height difference correlation (HDC), see Figure 47a:

$$C_{HDC}(\lambda) = \langle (z(x + \lambda) - z(\lambda))^2 \rangle \quad (26)$$



This function evaluate the average  $\langle \dots \rangle$  square height difference of the height profile  $z(x)$  for different horizontal wavelengths  $\lambda$  in x-direction. For self-affine surfaces, the function  $C_{HDC}$  is described by the power law

$$C_{HDC}(\lambda) = \xi_{\perp}^2 \left( \frac{\lambda}{\xi_{\parallel}} \right)^{2H} \quad (27)$$

for  $\lambda < \xi_{\parallel}$  with  $2H$  representing the slope. The cutoff-point is defined by the values  $\xi_{\parallel}$  and  $\xi_{\perp}^2$  for a schematic example of a HDC function. Beyond the cutoff-point, the HDC shows a characteristic plateau for a rough surface since the height differences are determined by the surface envelope.

The description of a rough surface by the power spectral density (PSD) is in the context of the elastomer friction introduced in [108] [112] and reads

$$C_{PSD}(q) = \frac{1}{(2\pi)^2} \int \langle z(x)z(0) \rangle e^{-iq \cdot x} d^2x \quad (28)$$

with the spatial vector  $x$ , the wave vector  $q$ , and the mean height of the profile  $z(0)$ . Under the assumption that the statistical properties of the considered surface are translationally invariant and isotropic, the magnitude of the wave vector  $q = |q|$  used to evaluate  $C_{PSD}$ . A schematic example of a PSD function of a rough surface is given in Figure 47b. The PSD and HDC functions can be used equally to describe the characteristics of a self-affine rough surface.

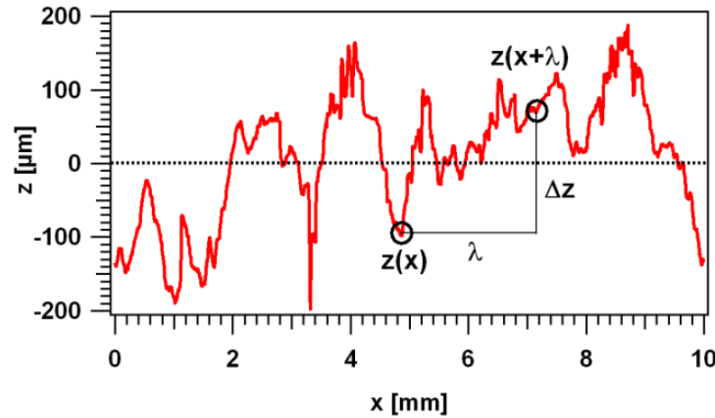


Figure 46. Roughness measurement of a granite surface by using white light interferometer.

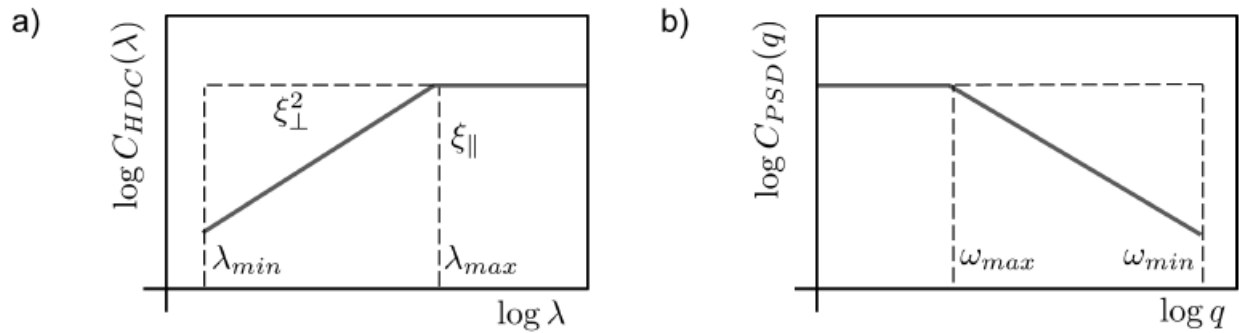


Figure 47. a) Exemplary schematic height difference correlation function (HDC) of a rough road surface measured. b) Exemplary schematic power spectral density function (PSD) of a rough road surface.

A general survey of the most important surface descriptors is given in Figure 48 of variety substrates:

Substrate	$z_{max}$ [ $\mu\text{m}$ ]	$\xi_{\perp}$ [ $\mu\text{m}$ ]	$\xi_{\parallel}$ [ $\mu\text{m}$ ]	$\lambda_2$ [ $\mu\text{m}$ ]	$D_{mak}$ -	$D_{mik}$ -	$\xi_{\parallel} / \xi_{\perp}$ -	$s$ -
Asphalt	800	430	1440	332	2.39	2.09	3	1.25
Granit	550	313	2490	93	2.37	2.13	8	1.25
Tile	26	13	270	-	2.31	-	21	1.25
Polished Steel	0.845	0.313	1.89	-	2.32	-	6	1.25
Coated Sheets	0.02	0.017	18	2.6	2.45	2.80	1059	1.61
Glass	0.005	0.0033	37	-	2.84	-	11212	1.37
Smooth Vul. Plate	0.05	0.035	43	2.7	2.64	2.53	1229	1.31
Fine Vul. Plate	0.3	0.172	13.3	1.0	2.39	2.45	77	1.54
Coarse Vul. Plate	2	1.76	35	14	2.53	2.17	20	1.26

Figure 48. Surface descriptors of relevant substrates [109].

Asphalt and granite are the coarsest materials, both in maximal heights and orthogonal descriptors, which correlate with the vertical standard deviation. Polished steel, glass and coated substrates on the other side are exceptionally smooth. Lateral descriptors tend to follow this classification from microscopic to macroscopic, Figure 49 displays this relationship. There is no exact proportionality, however, and the ratio of lateral and vertical cut-off lengths tells if the structures are rather sharp or blunt. The asphalt for example is despite of similar roughness sharper than granite, as the ratio in the table displays. Glass is extraordinarily blunt.

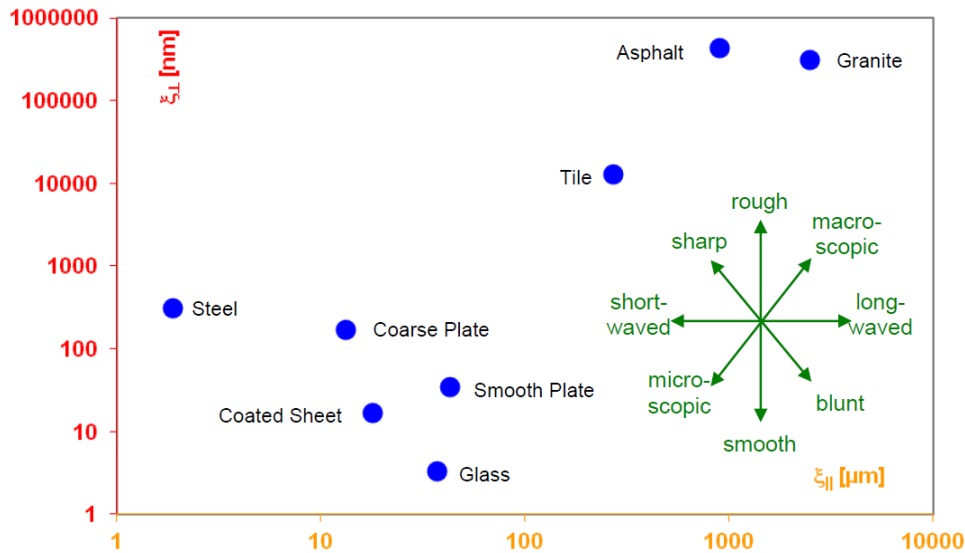


Figure 49. Orthogonal versus parallel cut-off lengths, showing a relation between vertical and lateral structures on fractal surfaces. The green arrows indicate the denotations of the directions [109].

## 2.7.2 Modeling in contact mechanics

To model physically how the rubber is perturbed by surface asperities, it is necessary to model the contact. It is widely known that the real area of contact between two rough surfaces is relatively small. Additionally, the fractal nature of rough surfaces has significant implications in the contact mechanics theories as any contact model must take a wide range of roughness scales into account. One of the earliest solid contact mechanic models was developed by H. Hertz (for whom the frequency unit ‘Hertz’ is named) in the 1880’s. Hertz assumed the surface roughness as smooth, elastic and based on spherical asperities. When two spheres are in contact, both will deform in accordance with their respective elastic moduli, and a localized stress field is occurred, which is a function of the sphere radius, elastic moduli and the force holding the surfaces in contact. An example of a Hertz contact between an elastic half-space with the modulus of elasticity and a sphere with the radius and a modulus is shown in Figure 50.

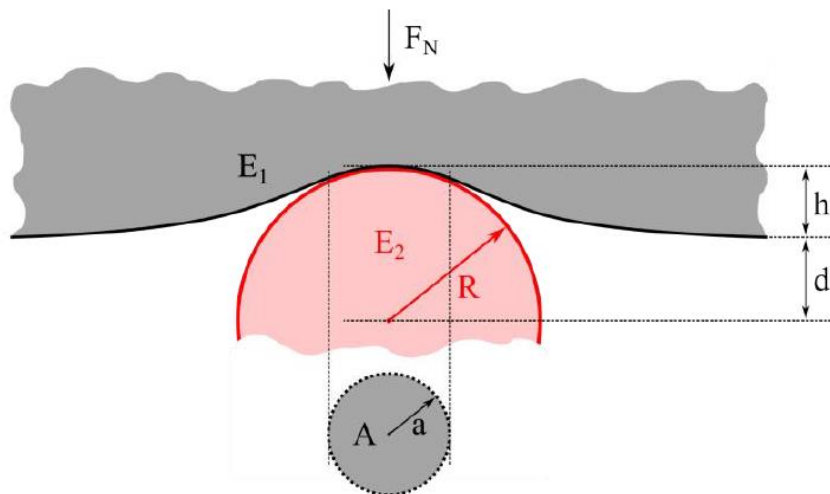


Figure 50. Representation of the Hertzian contact between a sphere of radius  $R$  and a plate with the resulting contact surface  $A$ . Reproduced from [41].

Considering the reduced modulus of elasticity  $E_r$  of the two bodies in contact

$$\frac{1}{E_r} = \frac{1 - \nu_1^2}{E_1} + \frac{1 - \nu_2^2}{E_2} \quad (29)$$

where  $\nu_1$  and  $\nu_2$  are the corresponding Poisson ratio of the bodies whereas the contact radius is equal

$$a = \left( \frac{3 F_N R}{4 E_r} \right)^{1/3} \quad (30)$$

as a function of the normal force  $F_N$ .

In the case of contacts between rubber and steel or asphalt reads  $E_r = E_1/(1 - \nu_1^2)$  since such rigid surfaces have a Young's modulus, which is considerably greater than the elastomer one. Considering the rubber incompressible  $\nu_1 = 0.5$  the penetration depth  $h$  can be calculated

$$h = R^{-1/3} \left( \frac{9 F_N}{16 E_1} \right)^{2/3} \quad (31)$$

and  $a^2 = R \cdot h$ , follows the penetration depth dependence of the normal force:

$$F_N = \frac{16}{9} E_1 \sqrt{R} h^3 \quad (32)$$

The following expression is obtained for the resulting real contact area  $A_c$

$$A_c = \pi a^2 = \pi R h \quad (33)$$

The contact surface therefore does not show a linear rather  $F_N^{2/3}$  load dependence. With the assumption that the friction force is proportional to the contact surface  $F_R \sim A_c$  the coefficient of friction decreases with increasing load [85].

Taking a closer look in the case of real surface, a defined roughness over a wide range of length scales is noticed. A further theory was presented by Greenwood & Williamson in 1966 [110]. The Hertz theory was extended including many Hertz contacts distributed according to a normalized distribution function rather than considering contacts on one level but. In other words, the asperities of roughness are approximated first by spheres with radius and randomly distributed in height. The boundary conditions for the individual contacts remain the same. A 2D section is shown in Figure 51.

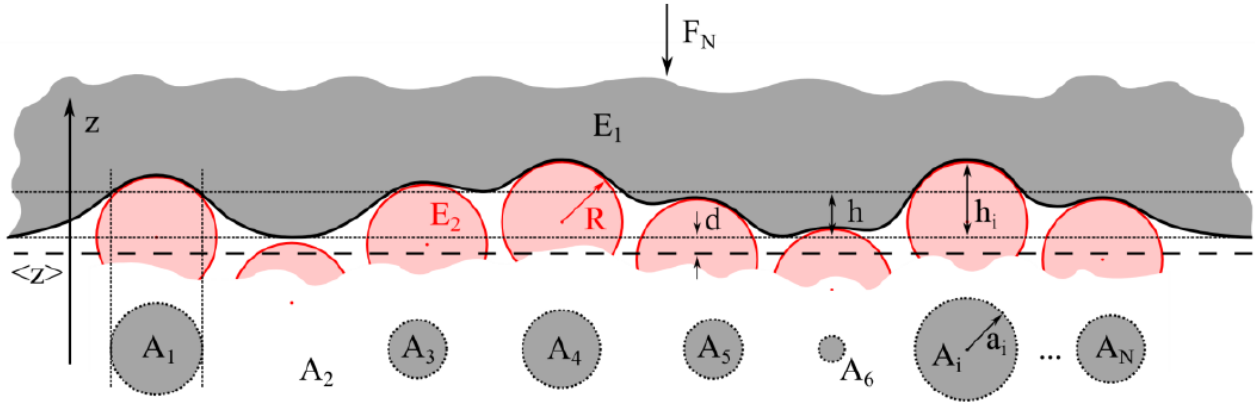


Figure 51. Representation of elastic contacts according to Greenwood & Williamson with the sphere radius  $R$  and the respective contact surfaces  $A_i$  [41].

### 2.7.3 Analytical friction model

Two analytical approaches for the description of rubber friction are the ones from Klüppel & Heinrich [108], Persson & Tosatti [111] and Persson [92]. The energy dissipation inside the rubber volume  $V_r$  during a certain time  $\Delta t$  originates the hysteretic friction and can be calculated by the product of stress  $\sigma$  and the time derivative of strain  $\dot{\epsilon}$ :

$$\Delta E_{diss} = \int_0^{\Delta t} \int_0^V \sigma \dot{\epsilon} dt dx^3 \quad (34)$$

Transformations of the equation lead to a description including the frequency-dependent loss modulus  $E''(\omega)$  of the rubber material and the power spectral density  $C_{PSD}(q)$  of the rough surface introduced in the previous subsection. Furthermore, the dissipated energy during the sliding interval  $T$  has to be equal to the product of the hysteretic friction force  $F_{hys}$  and the applied velocity  $v$ .

$$\frac{\Delta E_{diss}}{T} = F_{hys} v \quad (34)$$

Based on this equation and integrating over all excitation wavelengths, the equations of the hysteretic friction coefficient differ from the before mentioned approaches. In Klüppel & Heinrich,  $\mu_{hys}$  is calculated with the applied macroscopic pressure  $\sigma_0$  and the macroscopic velocity  $v$ :

$$\mu_{hys} = \frac{1}{2(2\pi)^2} \frac{\langle z_p \rangle}{\sigma_0 v} \int E''(\omega) \cdot S(\omega) d\omega \quad (35)$$

using a frequency-dependent description of the power spectral density  $S(\omega)$  based on the quantities  $(\xi_{||}, \xi_{\perp}^2, H)$  of the height difference correlation. The quantity  $\langle z_p \rangle$  represents the mean penetration depth of the rubber into the rough surface. Klüppel & Heinrich use an extension of the well-known

theory of Greenwood & Williamson [110] for self-affine surfaces to determine  $\langle z_p \rangle$ . A new experimental determination of this crucial contact parameter is depicted in chapter 5.2.

In contrast to the theory of Klüppel & Heinrich, Persson [92] uses a function  $P(q)$  describing the interaction of the rubber block and the road surface on each length scale, obtaining different results. The latest formulation for the coefficient of friction by Persson reads:

$$\mu_{hys} = \frac{1}{2} \int_{q_{min}}^{q_{max}} C_{PSD}(q) S(q) P(q) q^3 dq \int_0^{2\pi} \cos\Phi \frac{E^*(qv \cos\Phi, T_q)}{(1 - \nu^2)\sigma_0} d\phi \quad (36)$$

with the magnitude of the wave vector  $q$ , the reduction factor  $S(q)$ , the complex viscoelastic rubber modulus  $E^*$ , the Poisson ratio  $\nu$ , the surface angle  $\phi$  and the temperature  $T_q$ . The detailed theory for the incorporation of flash temperature effects can be found in Persson [112] [113] and Fortunato et al. [114].

In the case of a model sinusoidal surface, the equation (34) with one main wavelength can be simplified. The excitation induced in the rubber will be cyclic and the angular frequency is defined by  $\omega_0 = v/\lambda_0$ , with  $\lambda_0$  which corresponds to the sinusoidal wavelength. Assuming a linear viscoelastic behavior of rubber, the energy loss for each cycle is expressed by the following formula:

$$\Delta E_{diss} = \pi V E''(\omega, \varepsilon) \varepsilon^2 \quad (37)$$

where  $V$  is the deformed volume and  $E''$  is the loss modulus, which is in turn a function of the angular frequency  $\omega$  and the strain  $\varepsilon$ . Considering the sliding process over a multi asperity sinusoidal surface, the strain within the rubber sample will not be uniform. The material located near the contact interface is expected to undergo higher excitation compared with the material located in the bulk. Nevertheless, the continuous strain field can be discretized in several regions, each of them characterized by homogeneous strain level, as illustrated in Figure 52. Based on this assumption, considering the Eq. (36) it is possible to write a formula that estimates the hysteresis friction coefficient for a defined sliding velocity:

$$\mu_{hys} \cong \frac{\pi}{F_N \lambda_0} \sum_{i=1} V_{\varepsilon_i} E''(\varepsilon_i, \omega_0) \varepsilon_i^2 \quad (38)$$

where the dissipated energy is calculated as a sum of the contributions coming from the  $i_{th}$  volume  $V_{\varepsilon_i}$  in which the strain  $\varepsilon$  is assumed constant.

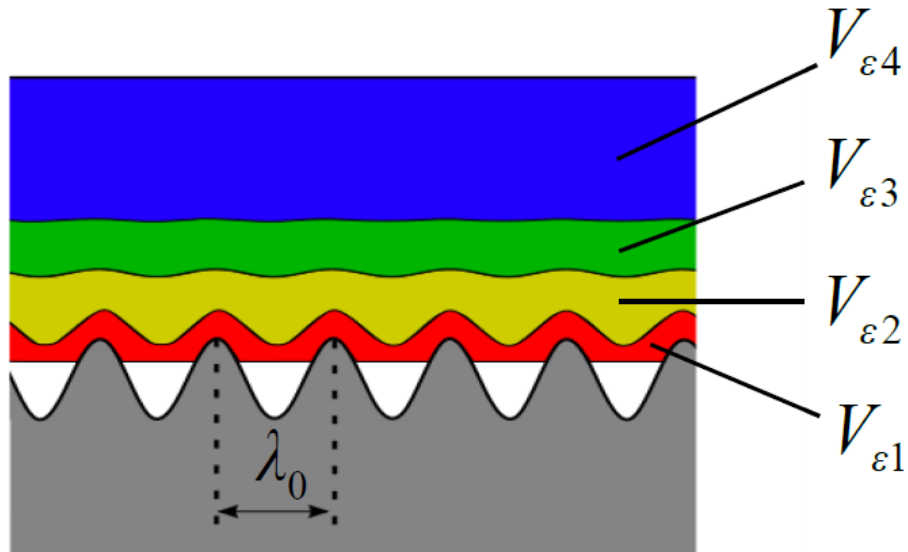


Figure 52. Discretization and homogenization of the strain field occurring in the rubber during the sliding over a sinusoidal substrate [91].

This approach is very important to quantify the contributions coming from the different deformed volumes. Indeed, the energy dissipation during sliding friction occurs in the thin rubber layer (less than 1 mm) close to the contact with the asperities of substrate, as it will be shown later in the results section.

Figure 53 shows an example based on an asperity that deforms an elastomer sample and slides relative to it. Higher deformation occurs near the contact leading to higher energy losses (see blue hysteresis), whereas the deformation decreases strongly further away from the contact (see red hysteresis).

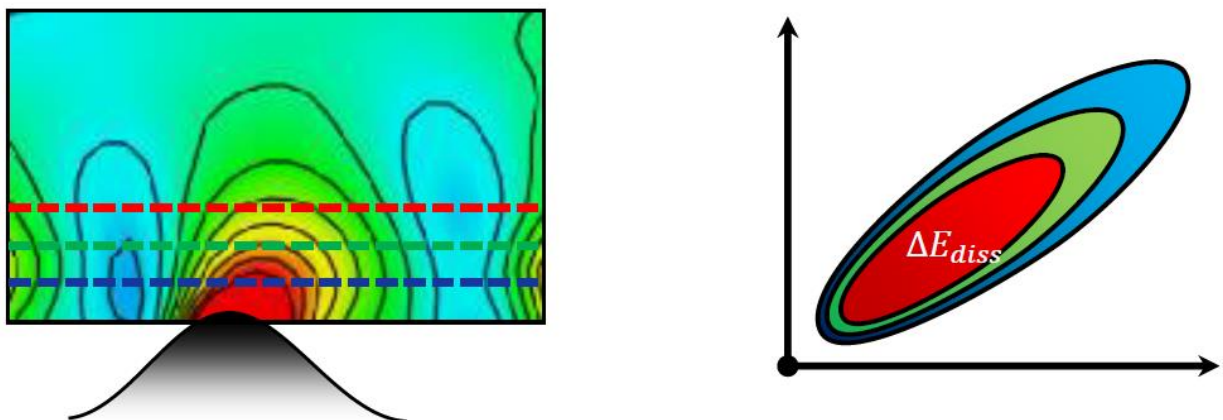


Figure 53. Representation of the deformation field and the resulting hysteresis loops along three planes with different distances from the rubber surface contacting the asperity [41].

The decrease refers approximately to an exponential function as depicted in Figure 54. Therefore, the actual strain amplitude is considered as an additional free parameter to optimize the prediction of the

hysteresis friction models. Accordingly, an important aspect is the strain dependency of the dynamic properties of filled compounds.

The deformed volume for high deformations is small while small deformations reflect a large deformed volume. The penetration depth and the viscoelastic contact conditions play an important role. With increasing sliding speed and the corresponding excitation frequency, the stiffness of material increases: the stiffer the material (and thus the penetration depth) the lower real contact surface. The dissipative portion increases until a maximum is reached, based on the increase of the loss module.

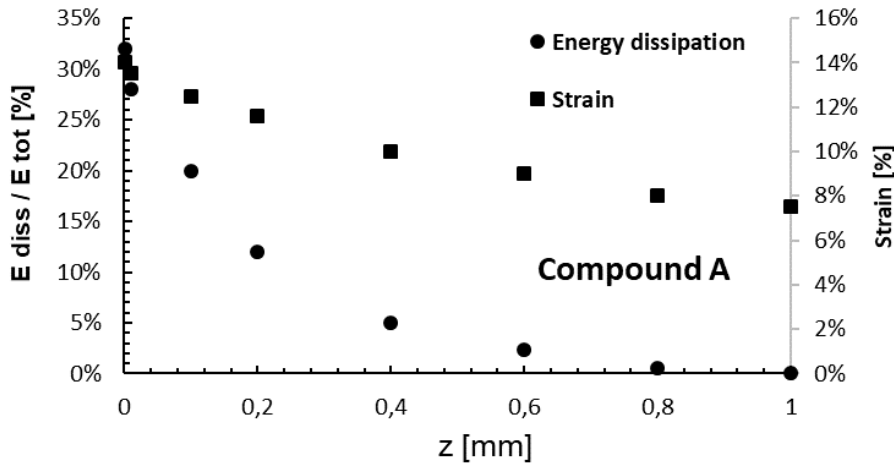


Figure 54. Distribution of the energy dissipation and strain along a vertical path  $z$  determined from FEA [115].

An additional important mechanism contributing to rubber friction is adhesion. The extensions of the friction theory including adhesive effects are presented in Persson [116], Persson et al. [105], Le Gal et al. [77] and Le Gal & Klüppel [85]. In Lorenz et al. [117], the adhesive contribution is modelled with the interfacial shear stress  $\tau_s$  and the contact area  $A_c = P(q_{max})A_0$ :

$$\mu_A = \frac{\tau_s A_c}{\sigma_0 A_0} = \frac{\tau_A}{\sigma_0} P(q_{max}) \quad (39)$$

Therefore, a crucial parameter is the interfacial shear strength. The physics of this term is difficult to describe and therefore a comprehensive explanation can be provided first in the case of a single asperity. When the body comes into the entrance zone, an adhering process occurs with the spherical asperity located at the trailing edge due to the attractive forces. This is followed by the deformation of the bulk material associated with the hysteresis friction. Finally, a breakage of the contact is observed at the leading edge, via a peeling-off process resulting in local energy dissipation. This mechanism is schematically illustrated in Figure 55. By overlapping a second wavelength on the asperity, it shows that peeling-off process occurs over the whole contact zone and not only at the



leading edge. Since real surfaces are rough over many length scales, the mechanisms described above are statistically distributed in the contact area. The formation and breakage of contact patches is expected to be controlled by the viscoelastic properties of the rubber as it corresponds to a mechanical stretching and relaxation process of polymer chains.

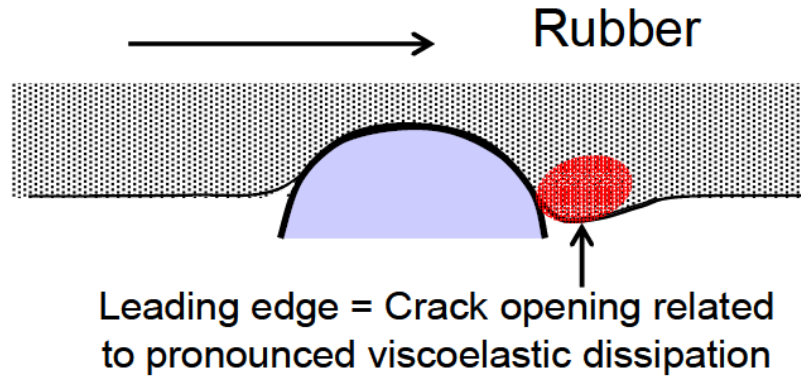


Figure 55. Schematic view of local peeling effects occurring during dry sliding friction [79].

The rate dependence of the peeling-off experiments between rubber-like materials and a blunt asperity can be taken into consideration via the introduction of an effective surface energy term  $\Delta\gamma_{eff}$  describing the viscoelastic nature of such processes [118].

At low rates of separation, the effective surface energy reaches a constant value corresponding to the static surface energy  $\Delta\gamma_0$ . By increasing the rate of separation,  $\Delta\gamma_{eff}$  goes through a modulus-like transition and follows a power law until a critical velocity  $v_c$ , which is assumed to depend on the nature of the polymer and the filler content (see Figure 56). The “step height” of the transition is given by the one observed during mechanical spectroscopy, e.g.  $\frac{E_\infty}{E_0}$  (dynamic modulus in glassy and rubbery state).

The surface energy  $\Delta\gamma$  is related to the true interfacial shear strength  $\tau_s$  where  $l_s$  is a typical length scale where such processes occur.

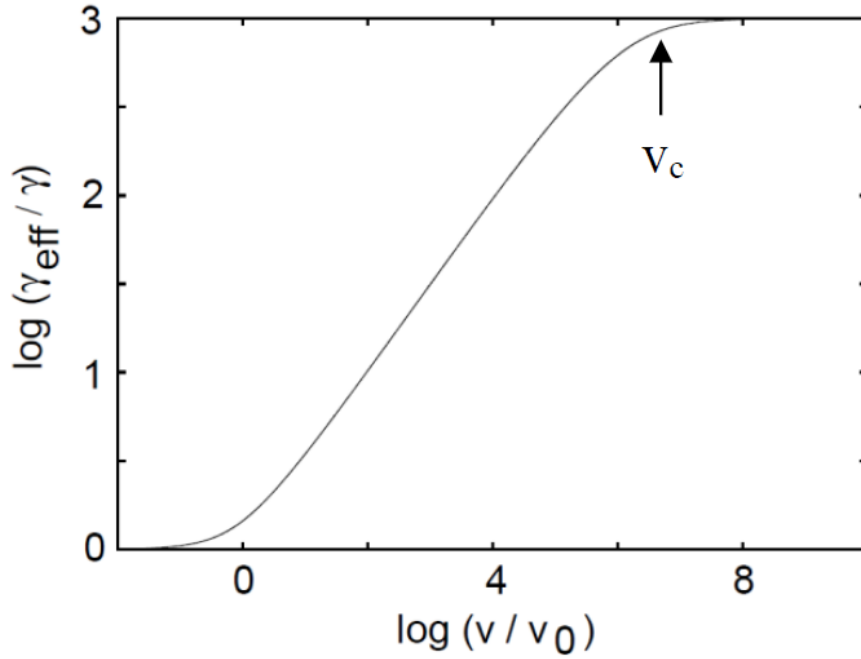


Figure 56. Dependence of the effective surface energy on the peeling rate or equivalently crack opening velocity from [119].

Based on it, an empirical formulation for the velocity dependence of the true interfacial shear strength  $\tau_s$  can be derived and is given by:

$$\tau_s = \tau_{s,0} \left( 1 + \frac{\frac{E_\infty}{E_0}}{\left(1 + \left(\frac{v_c}{v}\right)\right)^n} \right) \quad (40)$$

where  $n$  is a material dependent exponent,  $\tau_{s,0}$  is the interfacial shear strength in the limit of very low velocities,  $v_c$  is the critical velocity above which the true interfacial shear strength  $\tau_s$  is constant and  $\frac{E_\infty}{E_0}$  is the step height of the dynamic modulus between rubbery and glassy state. A numerical application of the true interfacial shear strength  $\tau_s$  is schematically presented in Figure 57.

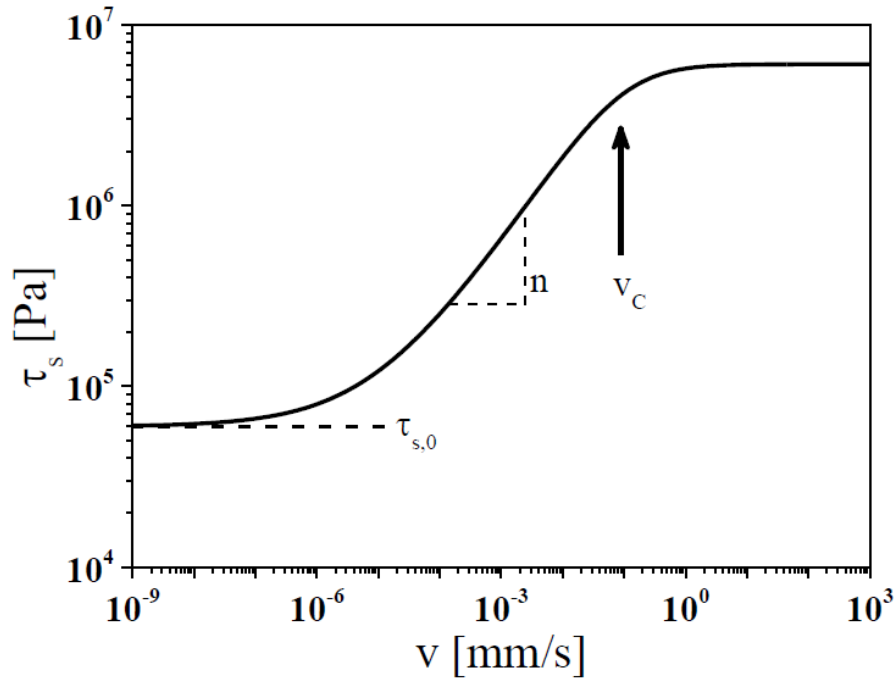


Figure 57. Shear stress in the contact as a function of the sliding speed according to the Eq. (41).

Combining the two analytical models for hysteresis and adhesion, a prediction of the dry friction can be estimated (see Figure 58).

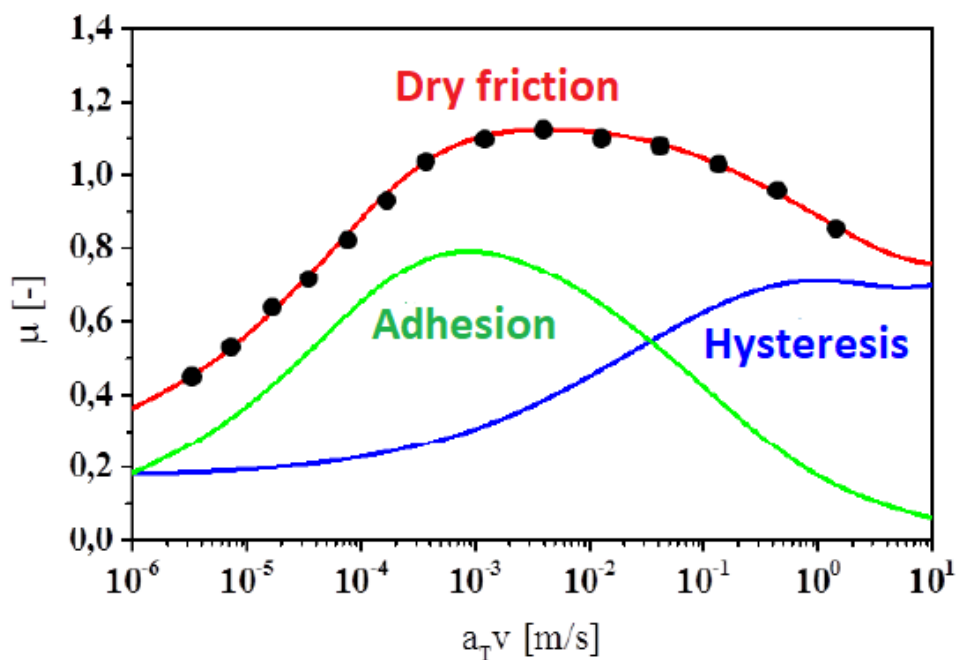


Figure 58. An example of the two friction contributions resulting from adhesion and hysteresis with the resulting friction curve under dry condition on a rough granite surface.

## 2.8 Continuum mechanics for finite element analysis

Three-dimensional thermomechanical problems can be described with a set of mathematical equations based on the theory of continuum mechanics. The kinematical relations together with an adequate strain measure are the basis for the description of the contact mechanisms. The universally valid balance equations provide a system of differential equations for the considered continua. Each material reacts differently to an applied load. Therefore, a proper constitutive law has to capture the relationship between independent variables (displacement, temperature) and dependent variables (e.g. stresses) for the considered material correctly. Fundamental introductions and further continuum mechanical aspects can be found in Altenbach [120], Chadwick [121], Haupt [122], Holzapfel [123], Marsden & Hughes [124], Ogden [125], Truesdell et al. [126]. To apply a solution with the finite element method, the weak formulations of the balance laws are stated in this paragraph.

### 2.8.1 Kinematics

This section introduces the fundamental quantities for a body undergoing large deformations. In a large deformation setting, it is necessary to distinguish between the initial and the current configuration. Following the common literature, capital letters are used for quantities defined in the initial configuration and small letters for quantities defined in the current configuration.

By definition, a solid body  $\mathcal{B}$  consists of a certain number of connected particles  $P$ . During a deformation process, no change for particles is assumed. The position vector of a particle or material point is denoted with  $\mathbf{X}$  in the initial configuration at time  $t = 0$  and with  $\mathbf{x}$  at the current configuration, see Figure 59. The used basis system of unit vectors  $\mathbf{E}_i, \mathbf{e}_i$  is denoted utilizing the Einstein summation convention for both configurations.

$$\mathbf{X} = X_i \mathbf{E}_i, \mathbf{x} = x_i \mathbf{e}_i \quad (41)$$

A common notation for the deformation process is given by the mapping operator  $\varphi$

$$\mathbf{x} = \varphi(\mathbf{X}, t) \quad (42)$$

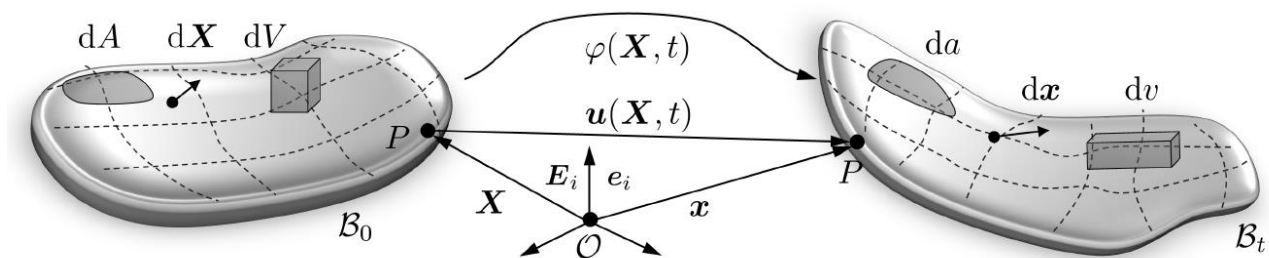


Figure 59. Kinematics of a solid body including surface, line and volume elements.

The displacement vector  $\mathbf{u}$  of a given point is the difference between the position in the current and the initial configuration

$$\mathbf{u}(X, t) = \mathbf{x}(X, t) - \mathbf{X} \quad (43)$$

The time derivative of the position vector describes the velocity  $\mathbf{v}$  and the second time derivative describes the acceleration  $\mathbf{a}$

$$\mathbf{v} = \frac{d\mathbf{u}}{dt} = \frac{d\mathbf{x}}{dt} = \dot{\mathbf{x}}, \quad \mathbf{a} = \frac{d^2\mathbf{x}}{dt^2} = \frac{d\mathbf{v}}{dt} = \dot{\mathbf{v}} = \ddot{\mathbf{x}} \quad (44)$$

The deformation gradient  $\mathbf{F}$  maps a line element from the initial configuration  $d\mathbf{X}$  to the current configuration  $d\mathbf{x}$  during a deformation process

$$d\mathbf{x} = \mathbf{F} \cdot d\mathbf{X}, \quad \mathbf{F} = \frac{\partial \mathbf{x}}{\partial \mathbf{X}} \quad (45)$$

From a physical point of view, no points are allowed to vanish or to appear suddenly. Thus, the inverse  $\mathbf{F}^{-1}$  mapping has to exist. This is ensured by a condition for the determinant

$$\det \mathbf{F} = J > 0 \quad (46)$$

This quantity is also called Jacobian  $J$ , mapping infinitesimal volume elements:

$$dv = JdV \quad (47)$$

After a transformation surface elements can be mapped with the so-called Nanson's formula

$$\mathbf{n} da = J\mathbf{F}^{-T} \cdot \mathbf{N} dA \quad (48)$$

with  $\mathbf{n}$ ,  $\mathbf{N}$  being the normal vector of the considered surface element in current and initial configuration. In order to describe deformations, strain measures have to be introduced. The deformation gradient is not suitable for this purpose since it also includes rigid body motions. To circumvent this drawback, the Green-Lagrange tensor  $\mathbf{E}$  and the Euler-Almansi tensor  $\mathbf{e}$  are defined in the following way

$$\mathbf{E} = \frac{1}{2}(\mathbf{C} - \mathbf{1}), \quad \mathbf{e} = \frac{1}{2}(\mathbf{1} - \mathbf{b}^{-1}) \quad (49)$$

with the right Cauchy-Green tensor  $\mathbf{C}$  in the initial configuration and the left Cauchy-Green tensor  $\mathbf{b}$  in the current configuration, given by the following equations:

$$\mathbf{C} = \mathbf{F}^T \cdot \mathbf{F}, \quad \mathbf{b} = \mathbf{F} \cdot \mathbf{F}^T \quad (50)$$

The time derivative of the deformation gradient  $\mathbf{F}$  is often called material deformation velocity gradient. A mapping to the current configuration leads to the spatial velocity gradient  $\mathbf{l}$  and its symmetric representation  $\mathbf{d}$

$$\dot{\mathbf{F}} = \frac{\partial \dot{\mathbf{x}}}{\partial \mathbf{X}} = \frac{\partial \mathbf{v}}{\partial \mathbf{X}}, \quad \mathbf{l} = \dot{\mathbf{F}} \cdot \mathbf{F}^{-1} = \frac{\partial \dot{\mathbf{x}}}{\partial \mathbf{x}}, \quad \mathbf{d} = \frac{1}{2}(\mathbf{l} + \mathbf{l}^T) \quad (51)$$

## 2.8.2 Basic balance equations

The first considered balance is the mass, also expressed by the density  $\rho$  integrated over the volume of a body. During a deformation process, the mass  $m$  remains constant and does not change in time for a closed system. This means that no mass is added to the system or removed from it.

$$\frac{d}{dt} m = \frac{d}{dt} \int_{\mathbf{B}_t} \rho \, dv = \frac{d}{dt} \int_{\mathbf{B}_0} \rho_0 \, dv = \frac{d}{dt} \int_{\mathbf{B}_0} \rho J \, dV = 0 \quad (52)$$

Based on Eq. (46) the equation can be reformulated in the initial configuration. The time derivative can be applied on the inner part of the integral, leading to

$$\dot{m} = \int_{\mathbf{B}_0} \frac{d}{dt}(\rho J) \, dV = \int_{\mathbf{B}_0} (\dot{\rho} + \rho \operatorname{div} \dot{\mathbf{x}}) J \, dV = \int_{\mathbf{B}_0} (\dot{\rho} + \rho \operatorname{div} \dot{\mathbf{x}}) \, dv = 0 \quad (53)$$

The local form of the continuity equation with the mass density field  $\rho = \rho(\mathbf{x}; t)$  can be written as

$$(\dot{\rho} + \rho \operatorname{div} \dot{\mathbf{x}}) = 0 \quad (54)$$

Another essential principle in the continuum mechanics is the balance of the linear momentum. The time derivative of the linear momentum  $\mathbf{L}$  of a body  $\mathbf{B}_t$  in the current configuration equals the sum of the applied external forces that gives the balance equation

$$\frac{d}{dt} \mathbf{L} = \frac{d}{dt} \int_{\mathbf{B}_t} \rho \dot{\mathbf{x}} \, dv = \int_{\mathbf{B}_t} \rho \mathbf{b} \, dv + \int_{\partial \mathbf{B}_t} \mathbf{t} \, da \quad (55)$$

The external forces include mass forces  $\mathbf{b}$  and surface tractions  $\mathbf{t}$ . The Cauchy theorem defines the traction as the product of the stress tensor  $\boldsymbol{\sigma}$  and the outward normal vector  $\mathbf{n}$ . With the use of the Gauss theorem the surface integral can be exchanged by a volume integral

$$\int_{\partial B_t} \mathbf{t} \, da = \int_{\partial B_t} \boldsymbol{\sigma} \cdot \mathbf{n} \, da = \int_{B_t} \operatorname{div} \boldsymbol{\sigma} \, dv \quad (56)$$

Equation (55) can be rewritten as

$$\int_{B_t} \operatorname{div} \boldsymbol{\sigma} \, dv + \int_{B_t} \rho \mathbf{b} \, dv = \int_{B_t} \rho \ddot{\mathbf{x}} \, dv \quad (57)$$

The local form for the balance of linear momentum for an arbitrary volume reads

$$\operatorname{div} \boldsymbol{\sigma} + \rho \mathbf{b} = \rho \ddot{\mathbf{x}} \quad (58)$$

with a vanishing inertia term  $\rho \ddot{\mathbf{x}} = \mathbf{0}$  for static problems.

The balance of angular momentum is formulated with respect to a fixed point  $\mathbf{x}_0$  as a reference point. Thus, the time derivative of angular momentum in the current configuration equals the sum of applied external moments

$$\frac{d}{dt} \mathbf{J} = \frac{d}{dt} \int_{B_t} (\mathbf{x} - \mathbf{x}_0) \times \rho \mathbf{v} \, dv = \int_{B_t} (\mathbf{x} - \mathbf{x}_0) \times \rho \mathbf{b} \, dv + \int_{\partial B_t} (\mathbf{x} - \mathbf{x}_0) \times \mathbf{t} \, da \quad (59)$$

Using the Gauss theorem, the conservation of mass and the balance of linear momentum prove that the Cauchy stress tensor has to be symmetric

$$\boldsymbol{\sigma} = \boldsymbol{\sigma}^T \quad (60)$$

Besides mechanical balances, the conservation of energy in a thermodynamic process is another important principle necessary to define. The law that postulates such principle is the first law of thermodynamics

$$\dot{E} = P + Q \quad (61)$$

This means that the change in time of the total energy  $E$  is equal to the sum of the mechanical power  $P$  of all external loads plus the heat supply  $Q$ . After several mathematical transformations the local form of the first law of thermodynamics can be obtained:

$$\rho \dot{u} = \boldsymbol{\sigma} \cdot \mathbf{d} + \rho r - \text{div } \mathbf{q} \quad (62)$$

Where  $\dot{u}$  is the time derivative of the internal energy  $u$ . The term  $\boldsymbol{\sigma} \cdot \mathbf{d}$  is called specific stress power, while the inner heat source  $r$  and the heat flux vector  $\mathbf{q}$  derive from the heat component. In this case the terms of Eq. (63) are zero, since neither heat is generated within the body nor external sources of heat are considered. Although in reality some heat development occurs during friction tests, all analysis have been carried out considering isothermal conditions, since the most important factor of the investigation was the pure mechanical behaviour.

Still in the thermodynamic context the entropy inequality law must be considered, as it describes the direction of an energy transfer process. In principle, the inequality is based on the second law of the thermodynamics, which states that heat flows always from the warmer to the colder region of a body and that mechanical energy can be transformed into heat by friction, but this can never be converted back into mechanical energy. It is convenient to introduce the Helmholtz energy  $\psi$ :

$$\psi = u - \zeta \theta \quad (63)$$

where  $\zeta$  denotes the entropy of the system and  $\theta$  is the absolute temperature. The Clausius-Duhem inequality can be then expressed as follows:

$$\boldsymbol{\sigma} \cdot \mathbf{d} - \rho \dot{u} + \theta \dot{\eta} - \frac{1}{\theta} \mathbf{q} \text{grad } \theta \geq 0 \quad (64)$$

The last term in Eq. (64) determines the entropy production by conduction heat. As already mentioned before, the present work does not consider any thermal effect, nevertheless the inequality is necessary to compute the energy dissipation due to viscoelastic losses and mechanical deformations.

In addition to the presented equations, a relation between stresses and displacements, based on the material properties, needs to be defined to perform a finite element analysis. This topic will be discussed in the following section.

## 2.9 Constitutive equations for filled rubber

Unlike in classical elastic materials like metals, it is still challenging to derive a general-purpose constitutive model for rubber, due to the nonlinear nature of the stress-strain behavior and the time dependent viscoelasticity. The rapid development of the computer and Finite Element Methods (FEM) programs offer the opportunity to solve equations capable to describe the complex mechanical behavior of several materials including rubber. Commercial FEM softwares, like ABAQUS have already included several material models, some of them can be adapted for rubber-like materials. Rate-dependent materials are often modeled in Finite Element Analysis (FEA) as a combination of hyperelasticity and viscoelasticity on frequency and time domain (visco-hyperelastic model). The



hyperelastic behavior is based on the invariant of continuum mechanics, while viscoelasticity is modeled through the Prony series (Generalized Maxwell model), each of these material models refers to various authors and scientific publications. Some of the new challenges are the implementation of material models able to describe stress softening effects like the Dynamic Flocculation model (DFM) and the Plagge model (PLM). An overview is provided in the following paragraphs.

## 2.9.1 Hyperelasticity: Invariant-based continuum mechanics treatments

Most continuum mechanics treatments of rubber elasticity begin with the fundamental basics of continuum mechanics for an isotropic, hyperelastic material, where the strain energy density is dependent on the stretch via one or more of the three stretch tensor invariants  $I_i$ :

$$I_1 = \lambda_1^2 + \lambda_2^2 + \lambda_3^2 \quad (65)$$

$$I_2 = \lambda_1^2 \lambda_2^2 + \lambda_2^2 \lambda_3^2 + \lambda_1^2 \lambda_3^2 \quad (66)$$

$$I_3 = \lambda_1^2 \lambda_2^2 \lambda_3^2 \quad (67)$$

where  $\lambda_1, \lambda_2, \lambda_3$  are the extension ratios in the three principal axis [127] [128].

The elastomer is approximated to be incompressible, thus  $I_3$  is taken to be constant and equal to 1 and does not contribute to the strain energy. As proposed by Rivlin [129] one general representation of  $W$  is given by,

$$W_R = \sum_{i,j=0}^{\infty} C_{ij} (I_1 - 3)^i (I_2 - 3)^j \quad (68)$$

where  $C_{ij}$  are the material parameters. When only the first term is retained, the following is obtained

$$W_{NH} = C_{10} (I_1 - 3) \quad (69)$$

also called the Neo-Hookean model.

By keeping the second term of Eq. (67), the equation first derived by Mooney is obtained

$$W_{MR} = C_{10} (I_1 - 3) + C_{01} (I_2 - 3) \quad (70)$$

This is the Mooney-Rivlin model. Mooney proposed Eq. (68) by determining an expression for the strain energy that would provide a constant modulus in shear (a modulus that did not depend on the shear strain). The model has some deficiencies. The Mooney-Rivlin model as well as Arruda-Boyce

[130] [131] can potentially grossly overestimate stresses at moderate to large deformations in different deformation states.

Working within the continuum mechanics framework of the strain energy function as proposed by Rivlin in Eq. (68), several investigators have used higher order terms of  $I_1$  and in some cases  $I_2$  to account for departure from neo-Hookean/Gaussian behaviour at large stretches. One model of this type is the Yeoh model [132].

$$W_Y = C_{10}(I_1 - 3) + C_{20}(I_1 - 3)^2 + C_{30}(I_1 - 3)^3 \quad (71)$$

As previously mentioned, the stress-strain formulation for the above presented models can be derived from the strain energy density function. The strain energy density can be interpreted as the area under the stress-strain curve. Thus, the stress-strain behavior can be determined from the differential of  $W$  with respect to the strain. Stress-strain curves are commonly studied through the following simplified tests: uniaxial, biaxial and pure shear or compression. In these cases, the computation of the invariants can be strongly simplified, given the correlation between the extension ratios in the three main directions. Therefore, the stress-strain formulations of the two models used in the present work (Neo-Hooke and Yeoh) can be calculated considering that:

- for uniaxial tension:  $\lambda_1 = \lambda$  and  $\lambda_2 = \lambda_3 = 1/\sqrt{\lambda}$
- for equi-biaxial tension:  $\lambda_1 = \lambda_2 = \lambda$  and  $\lambda_3 = 1/\lambda^2$ ;
- for pure shear:  $\lambda_1 = \lambda$ ,  $\lambda_2 = 1$  and  $\lambda_3 = \frac{1}{\lambda}$ ;

The nominal stress for the Neo-Hooke and Yeoh is reported on the Table 3 by considering Eq. (69) and Eq. (71) in the case of uniaxial tensile, pure shear and equi-biaxial tests:

Table 3. Nominal stress for three different strain modes (uniaxial, pure shear and equi-biaxial) in the case of New Hooke model and Yeoh models.

	New Hooke model	Yeoh model
Uniaxial	$\sigma = \frac{\partial W}{\partial \lambda} = 2C_{10}(\lambda - \frac{1}{\lambda^2})$	$\sigma = \frac{\partial W}{\partial \lambda} = 2[C_{10} + 2C_{20}(\lambda^2 + \frac{2}{\lambda} - 3) + 3C_{30}(\lambda^2 + \frac{2}{\lambda} - 3)^2](\lambda - \frac{1}{\lambda^2})$
Pure shear	$\sigma = \frac{\partial W}{\partial \lambda} = 2C_{10}(\lambda - \frac{1}{\lambda^3})$	$\sigma = \frac{\partial W}{\partial \lambda} = 2 \left[ C_{10} + 2C_{20}(\lambda^2 + \frac{1}{\lambda^2} - 2) + 3C_{30}(\lambda^2 + \frac{1}{\lambda^2} - 2)^2 \right] (\lambda - \frac{1}{\lambda^3})$
Equi-biaxial	$\sigma = \frac{\partial W}{\partial \lambda} = 2C_{10}(\lambda - \frac{1}{\lambda^5})$	$\sigma = \frac{\partial W}{\partial \lambda} = 2 \left[ C_{10} + 2C_{20}(2\lambda^2 + \frac{1}{\lambda^4} - 3) + 3C_{30}(2\lambda^2 + \frac{1}{\lambda^4} - 3)^2 \right] (\lambda - \frac{1}{\lambda^5})$

## 2.9.2 Derivation of finite linear viscoelasticity for numerical approach

To understand the constitutive equations governing the time-dependent behavior of polymers, implemented in ABAQUS, it is convenient to recall the viscoelastic theory from Mohammed [133][131].

Viscoelasticity assumes a homogeneous and isotropic material, as well as a separable time and strain dependent material behaviour [134]. The relaxation stress under a step strain loading history can be written as a product of a function of time,  $g(t)$  and a function of strain,  $\sigma_0(\varepsilon)$

$$\sigma(\varepsilon, t) = \sigma_0(\varepsilon)g(t) \quad (72)$$

The time function can be represented by the Prony Series [135]

$$g(t) = g_\infty + \sum_{i=1}^N g_i e^{(-\frac{t}{\eta_i})} \quad (73)$$

where  $t$  and  $\eta_i$  are time and relaxation time constants, respectively and  $g_i$  are dimensionless constants. The 1D equivalent of the Prony series in tension consists of a series of Maxwell elements connected in parallel with a spring is shown in Figure 60.

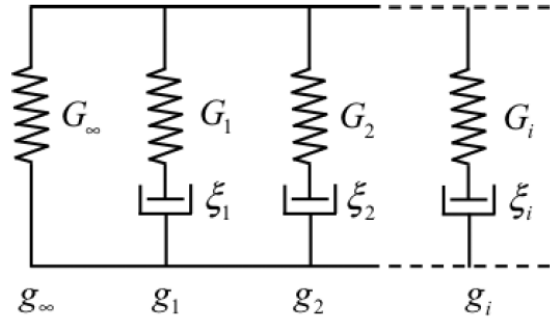


Figure 60. The Prony series representation.

Each  $g_i$  is defined as:

$$g_i = \frac{G_i}{G_0}, \quad g_\infty = \frac{G_\infty}{G_0} \quad (74)$$

where  $G_i$  is the modulus of the  $i$ th spring,  $G_\infty$  is the modulus of the infinite lone spring and  $G_0$  is the instantaneous modulus, given by  $\sum_{i=1}^N G_i + G_\infty = G_0$ . Therefore  $g_i$  is related to  $g_\infty$  through  $\sum_{i=1}^N g_i + g_\infty = 1$ . The function  $\sigma_0(\varepsilon)$  represents the instantaneous stress-strain relationship since and from Eq. (72). Note that is the long term or equilibrium stress-strain relationship as  $g(\infty) = g_\infty$  and  $\sigma(\varepsilon, \infty) = g_\infty \sigma_0(\varepsilon)$  from Eq. (72). This long term behaviour occurs physically as the dashpots relax the  $i$  springs in Figure 60 and only the  $g_\infty$  spring remains loaded.

Using the Leaderman form of the convolution integral, the total stress is given by the algebraic sum of the entire past loading history, with each stress component being independent of the loading history. In the limit of continuous strain history, the total stress at time  $t$  is therefore given by Williams [136].

$$\sigma(\varepsilon, t) = \int_0^t g(t-s) \frac{d\sigma_0(\varepsilon)}{ds} ds \quad (75)$$

where  $\sigma_0(\varepsilon)$  is the instantaneous true stress at strain  $\varepsilon$ . The function  $g(t-s)$  is described as:

$$g(t-s) = g_\infty + \sum_{i=1}^N g_i e^{(-\frac{t-s}{\eta_i})} \quad (76)$$

Therefore Eq. (75) becomes

$$\sigma(t) = \int_0^t [g_\infty + \sum_{i=1}^N g_i e^{(-\frac{t-s}{\eta_i})}] \frac{d\sigma_0(\varepsilon)}{ds} ds \quad (77)$$

The stress on the left-hand side is expressed in terms of  $t$  only, provided that the strain history  $\varepsilon(t)$  is known [135]. Therefore, we get:

$$\sigma(t) = g_\infty \sigma_0(t) + \sum_{i=1}^N g_i e^{(-\frac{t-s}{\eta_i})} \frac{d\sigma_0}{ds} ds = g_\infty \sigma_0(t) + \sum_{i=1}^N h_i(t) \quad (78)$$

$$\text{with } h_i(t) = \int_0^t g_i e^{(-\frac{t-s}{\eta_i})} \frac{d\sigma_0(s)}{ds} ds$$

The convolution integral in Eq. (78) is computed using a numerical algorithm based on finite time increments [137]. For a time interval  $(t_n, t_{n+1})$  and time step  $\Delta t = t_{n+1} - t_n$ , the exponential term in the integrand is written as:

$$e^{(-\frac{t_{n+1}}{\eta_i})} = e^{(-\frac{t_n}{\eta_i})} e^{(-\frac{\Delta t}{\eta_i})} \quad (79)$$

The term  $h_i$  at  $t_{n+1}$  can be separated into two components: The first component corresponds to deformation history during period  $0 \leq s \leq t_n$  while the second component corresponds to the period,  $t_n < s < t_{n+1}$ . Therefore:

$$h_i(t_{n+1}) = g_i \int_0^{t_{n+1}} e^{(-\frac{t_{n+1}-s}{\eta_i})} \frac{d\sigma_0(s)}{ds} ds \quad (80)$$

which gives

$$\sigma(t_{n+1}) = g_{\infty}\sigma_0(t_{n+1}) + \sum_{i=1}^N \left( e^{\left(\frac{-\Delta t}{\eta_i}\right)} h_i(t_n) + g_i \int_{t_n}^{t_{n+1}} e^{\left(\frac{-t_{n+1}-s}{\eta_i}\right)} \frac{d\sigma_0(s)}{ds} ds \right) \quad (81)$$

It is worth noting that in the newer version of the commercial finite element software, Abaqus version 6.9 (Abaqus 2010), an updated version of viscoelastic model has been introduced to replace the former Abaqus version 6.8 (Abaqus 2009). A modification is performed to (77) as follows:

$$\sigma(t) = \lambda(t) \int_0^t \left[ g_{\infty} + \sum_{i=1}^N g_i e^{\left(\frac{-t-s}{\eta_i}\right)} \right] \frac{dP_0(\varepsilon)}{ds} ds \quad (82)$$

Notice the difference where  $\sigma_0$  in Eq. (77) represents the true stress term, whereas  $P_0$  in Eq. (82) represents the nominal stress term. The stretch ratio,  $\lambda(t)$  is introduced in Eq. (82) to convert the nominal stress term in the integral into true stress term after integration. True stress and nominal stress are related through:

$$\sigma_0(t_n) = P_0(t_n) \cdot \lambda(t_n) \quad (83)$$

Eq. (82) is then evaluated using the same finite time increment algorithm as before, which finally yields:

$$\sigma(t_{n+1}) = g_{\infty}\sigma_0(t_{n+1}) + \lambda(t_{n+1}) \sum_{i=1}^N \left( e^{\left(\frac{-\Delta t}{\eta_i}\right)} h_i(t_n) + g_i \frac{1 - e^{\left(\frac{-\Delta t}{\eta_i}\right)}}{\frac{\Delta t}{\eta_i}} [P_0(t_{n+1}) - P_0(t_n)] \right) \quad (84)$$

The Eq. (84) expresses the viscoelastic model adopted by ABAQUS and is valid only in the case of small deformation.

### 2.9.3 Overview of the main rubber material models and its parameters identification

Rubbery material behavior in ABAQUS is represented by a stored energy function combined with a time-dependent function. Therefore, modeling a rubber compound means mostly finding the proper material parameters for the long term behavior, as well as for the time dependent behavior. Since the effectiveness of the calculations is directly related to the quality of the input material data, these need to be determined with the highest accuracy possible.

The material data can be generated by measuring the material under certain conditions in order to reproduce the load profile of the friction application and fit the resulting mechanical properties with a proper material model.

The material parameters were retrieved by making a separate fitting of the quasi static measurements (for the long term behaviour) and the dynamic mechanical master curves (for the time-dependent behaviour).

Concerning the quasi static measurements (low testing speed  $20 \div 80 \text{ mm/min}$ ) the elastomeric compounds show hysteretic behaviour, for this reason the middle line between the loading and unloading cycle was calculated to obtain the average stress-strain behaviour of the material.

Based on the Mullins effects for each measurement run, the fifth loading/unloading cycle was considered to take into account a stable mechanical behaviour. The procedure is illustrated in Figure 61.

The material parameter fitting consists in obtaining the optimum set of coefficients, for the selected hyperelastic model, this leads to the minimum error between the experimental and theoretical results for each strain mode (uniaxial, biaxial and pure shear) simultaneously.

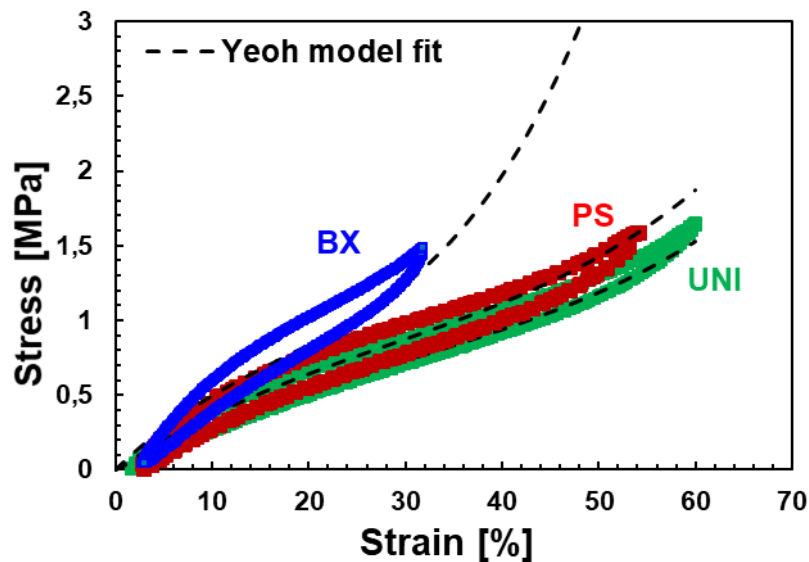


Figure 61. Example of the quasi-static behaviour extrapolation in different strain modes (uniaxial, pure shear and biaxial) for a filled SSBR rubber. Considering the Mullins effect, the 5th loading-unloading cycle was identified as reference cycle. The dashed middle lines reveal the fit of Yeoh hyperelastic model.

For the time-dependent behavior, the relaxation parameters can be defined by including in the data set creep or relaxation test and also a defined initial guess of the Prony parameters. The latter method was applied in the present work and the data set are fitted using external tool. The two approaches selected were:

(i) to fit dynamic test data such as viscoelastic moduli master curves  $G'$  and  $G''$  in the frequency domain up to the GHz region. The Prony series terms can be also calibrated using frequency-dependent test data. In this case, ABAQUS uses analytical expressions that relate the Prony series relaxation functions to the storage and loss moduli:

$$G'(\omega) = G_0 \left[ 1 - \sum_{i=1}^N g_i^p \right] + G_0 \sum_{i=1}^N \frac{g_i^p \tau_i^2 \omega^2}{1 + \tau_i^2 \omega^2} \quad (85)$$

$$G''(\omega) = G_0 \sum_{i=1}^N \frac{g_i^p \tau_i \omega}{1 + \tau_i^2 \omega^2} \quad (86)$$

For further details, a deeper explanation is described in chapter 2.5.1. The measured master curve constructed using a physical shifting procedure based on the time-temperature principle (TTS) was fitted with the Prony parameters (see Figure 62), carried out in Excel using the least squares method.

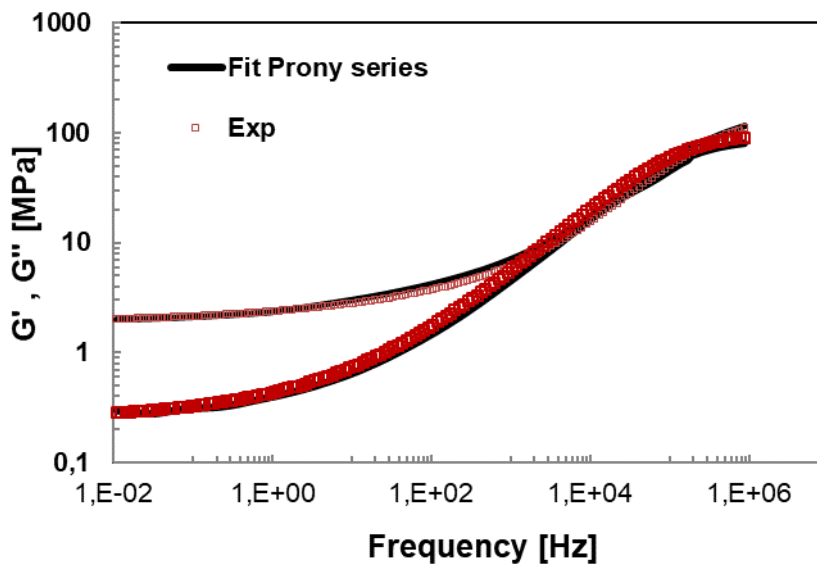


Figure 62. Fitting in the frequency domain between the Prony series and  $G'$ ,  $G''$  moduli master curve constructed by TTS principle from DMTA measurements for compound SSBR filled with 40 phr of carbon black. Reference temperature  $T = 20^\circ\text{C}$ ; shear strain level  $\gamma = 2.5\%$ .

(ii) to fit the stress relaxation curves at different strain level in case of uniaxial tension/compression modes

More in detail, to identify the material parameters the experiment consists in a multihysteresis test with dumbbells sample in uniaxial mode, where five multihysteresis loading-unloading cycles up to 60% in tension and -20% in compression (precondition) were performed to induce the breakage and recovery of the filler network. Afterwards, stress relaxation tests were carried out at different constant strain levels to include the strain amplitude dependency (Payne effect) as shown in Figure 63.

The measurement is repeated for several temperatures from  $-15^\circ\text{C}$  (very close to the glass transition of the rubber) up to  $60^\circ\text{C}$  to apply the time-temperature superposition principle.

The described experimental campaign captures the mechanical response of material at high strain and the history of deformation in the case of nonlinear highly filled compounds.

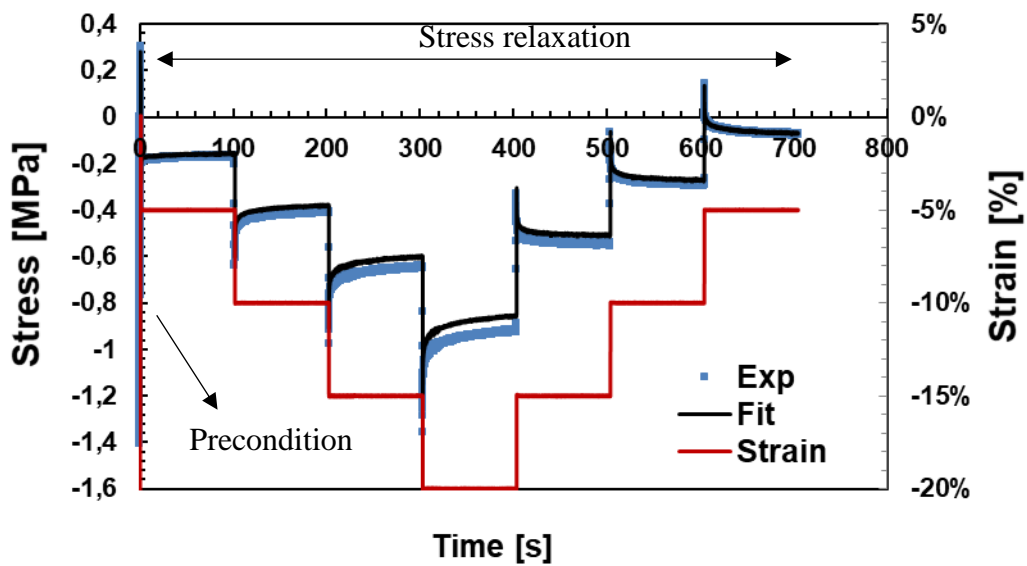


Figure 63. Fitting in the time domain (with the Prony series) of the stress relaxation measurements performed with dumbbells in uniaxial mode at different strain levels for compound SSBR filled with 80 phr of carbon black plus 30 phr of commercial oil. Temperature  $T= 20^{\circ}\text{C}$ .

The commercial product of SIMULIA called ISIGHT was used to calibrate and optimize the material parameters of the hyper-viscoelastic model according to the raw data experiment. An example of the set-up is represented in Figure 64.



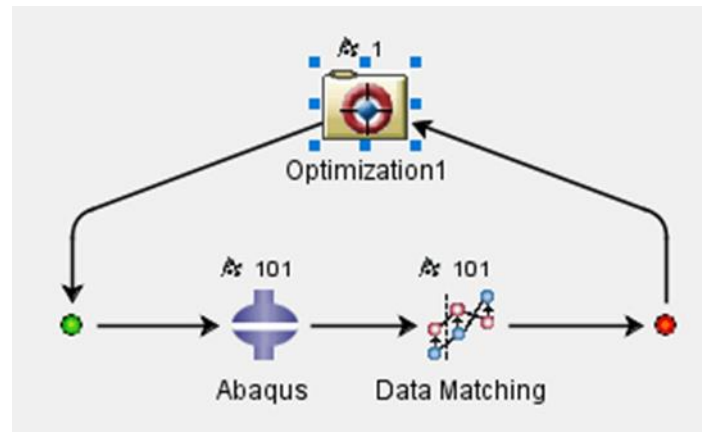


Figure 64. Iterative cycle performed with ISIGHT to minimize the error between the ABAQUS simulation and the experiment (Data Matching).

### *DFM (Dynamic Flocculation Model)*

The previous modelling approaches do not consider the stress softening effect. The permanent deformation combined with the stress-softening effects result in a complex mechanical behaviour. The modelling of such phenomena is still at an early stage. To relate the properties of rubber and filler a microstructure-based approach (dynamic flocculation model DFM [138]) can be used, where the material parameters are physical quantities, instead of mere fit parameters. The model is based on the hydrodynamic reinforcement of rubber elasticity (tube model) by stiff filler clusters. The deformation is concentrated at a smaller part of the total volume, resulting in an amplification of stress. Under stress, the clusters can break and become soft, leading to the deformation of larger parts of the volume and the related stress softening. The effect is expressed as an integral over the “surviving” section of the cluster size distribution. On the other hand, the cyclic breakdown and re-agglomeration of soft clusters causes hysteresis.

Filled elastomers also show a certain inelastic behaviour called setting. The corresponding stress contribution is modelled by a semi-empirical dependency with respect to the maximum deformation. Stress-strain measurements were carried out uniaxially in tension and compression using dumbbell specimens. The parameter fitting shows the model successfully describes the compression and tension-experiments. Generally, the parameters lie in a physically reasonable range. For the first time the hydrodynamic reinforcement is formulated by a reinforcement exponent. The DFM aims to capture the additional phenomena occurring in filled rubber: stress softening, increased hysteresis and permanent set. The polymer matrix is described by the non-affine tube model. The filler is assumed to interact with the polymer matrix in two different ways. Stiff filler clusters consisting of several aggregates increase the local strain by hydrodynamic amplification. If stress surpasses a cluster-dependent critical load, the cluster breaks apart into aggregates and has a greatly reduced amplifying effect. At low strains, the broken clusters are assumed to reaggregate into softer clusters, which do not amplify but take over the network stress. When stress gets large enough the soft clusters break as well, dissipating their energy. The latter process causes hysteresis. The free energy is defined as

the sum of an elastic contribution of the rubber matrix  $W_R$  given by the free energy density of the non-affine tube model and the contribution from the soft filler clusters  $W_A$ .

$$W_{DFM}(\varepsilon_\mu, \varepsilon_{\mu, \min/\max}) = (1 - \phi_{eff}) W_R(\varepsilon_\mu, \varepsilon_{\mu, \min/\max}) + \phi_{eff} W_A(\varepsilon_\mu, \varepsilon_{\mu, \min/\max}) \quad (87)$$

where  $\phi_{eff}$  is the effective filler volume fraction which is larger than the true filler volume fraction due to occluded rubber (see Figure 65). The  $\varepsilon_\mu, \varepsilon_{\mu, \min/\max} = \lambda_{\mu, \min/\max} - 1$  measure the maximum and minimum deformation in each direction of space  $\mu$ . Hydrodynamic strain amplification is implemented by assuming that the macroscopic stretch  $\lambda_\mu$  translates into an amplified microscopic stretch  $k_\mu$ :

$$\lambda_\mu = 1 + \varepsilon_\mu \quad \rightarrow \quad k_\mu = 1 + X_\mu \varepsilon_\mu \quad (88)$$

Via a hydrodynamic amplification factor  $X_\mu$  in direction  $\mu$ . The requirement of rubber incompressibility holds for macroscopic as well as microscopic stretches, such that  $\prod_\mu \lambda_\mu = \prod_\mu k_\mu = 1$ . This poses constraints on  $X_\mu$  that can be fulfilled by rewriting

$$k_\mu = \lambda_\mu^r \quad \text{with } r = \log(1 + X_{max} \varepsilon_f) / (1 + \varepsilon_f) \quad (89)$$

where  $X_{max}$  and  $\varepsilon_f$  refer to the respective values in the direction of maximum strain (in principal axes system). Additionally, it may induce discontinuities when the direction of maximum principal strain changes (e.g. in two sided shear experiments). The amplification factor  $X_{max}$  depends on the all time maximum and minimum strain, and on the details of the cluster structure within the network

$$X_{max} = 1 + c \phi_{eff}^{\frac{2}{3-d_f}} \left[ \int_0^{\xi_{1, \min}} x^{d_w - d_f} \phi(x) dx + \int_{\xi_{\min}}^{\infty} \phi(x) dx \right] \quad (90)$$

where  $c = 2.5$  is a constant motivated by the Einstein relation for spherical inclusions and  $\phi_{eff}$  is the effective filler volume fraction.

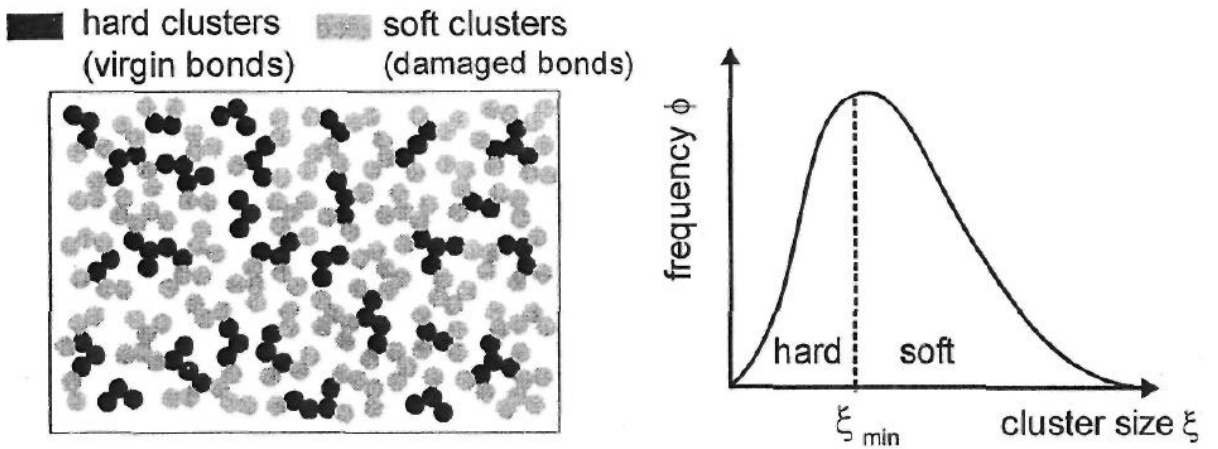


Figure 65. Cluster size distribution  $\phi(x)$  as defined. Black clusters have never been broken (called stiff or virgin clusters) and are assumed to amplify the material. grey clusters (called soft or broken) have already been broken and are responsible for hysteresis [138].

The latter is larger than the real filler volume fraction  $\phi$  mainly due to the rubber occluded from mechanical deformation. The quantities  $d_w \approx 3.1$  and  $d_f \approx 1.8$  are the anomalous diffusion coefficient and fractal dimension of filler clusters respectively.  $\xi_{min}$  is the size of the largest cluster which survived the maximum previous strain given in units of primary particle size. The cluster size distribution  $\phi(x)$  in Eq. (90) is chosen as a Smoluchowski type, because it reflects the outcome of cluster-cluster aggregation (CCA) occurring during carbon black flocculation inside the rubber matrix:

$$\phi(x) = \frac{4x}{x_0^2} \exp\left(-2\frac{x}{x_0}\right) \quad (91)$$

with  $x_0$  being the average cluster size. The distribution is displayed in Figure 65. Using Eq. (2.34) and approximating  $d_w - d_f \approx 1$  the integral in Eq. (90) can be carried out analytically. The size of the largest surviving cluster  $\xi_{1,min}$  is calculated via

$$\varepsilon_{\mu,min} = \frac{s_v}{\hat{\sigma}_{R,\mu}(\varepsilon_{\mu}, \varepsilon_{\mu,min/max})} \quad (92)$$

where  $s_v$  is the strength of virgin (never broken) filler-filler bonds which are assumed to consist of glassy polymer bridges. The denominator is the maximum relative stress the sample has ever experienced within its deformation history. The hysteresis is generated by the broken soft clusters, see Figure 65. The soft clusters are assumed to be in mechanical equilibrium with their elastic surrounding and correspondingly store energy. Upon stretching, soft clusters in the stretching direction  $\mu$  break down and dissipate the stored energy. During the sample relaxation these clusters reaggregate, while the lateral dimension is expanded and induces lateral cluster breaking. The integral boundaries  $x_{\mu}$  define the fraction of intact soft clusters. They are defined as

$$x_{\mu}(\varepsilon_{\mu}, \varepsilon_{\mu,min/max}) = \frac{s_d}{\hat{\sigma}_{R,\mu}(\varepsilon_{\mu}, \varepsilon_{\mu,min})} \quad (93)$$

The total energy is then expressed as

$$\sigma_v = (1 - \phi_{eff}) \sigma_{R,v}(k_v) + \phi_{eff} \sigma_{A,v} + \sigma_{set} \quad (94)$$

where  $\sigma_R$  is the first Piola-Kirchhoff stress derived from the free energy density of the non-affine tube model,  $\sigma_{A,v}$  is the soft clusters stress contribution in direction  $v$ . The stress was split into matrix- and filler contribution according to their contribution to total volume. Further details about the model are described in [138] [139]. An example of the application of such model to characterize the mechanical behaviour of rubber is reported in the case of a highly filled material in chapter 4.3.1.

### Plagge Model (PLM)

The Plagge model (PLM) is another material model able to reproduce complex mechanical response and stress softening effects, which depends on temperature, load history and deformation rate under dynamic condition. More specifically, the material relaxes under load and becomes softer. The degree of softening is a function of maximum load and time spent at the respective load level. Although this effect is well understood at low strains in terms of breakdown of the filler network, it remains an open question what occurs at high strains. Viscoelasticity is modeled by a modified Prony element according to the differential equation, which naturally generate Payne-effect like behavior and can be used to represent viscoelastic data obtained at strains outside the linear regime.

$$\dot{S}_v^* = -\frac{1}{\tau_0} \exp\left(\frac{1}{\sigma_c} \|S_v\|\right) S_v + S_{el}^* \quad (95)$$

where  $S_{el}$  denotes deviatoric elastic Cauchy stress and  $S_v$  is the corresponding viscoelastic contribution. The operator  $*$  indicates the Zaremba-Jaumann rate and  $\|\cdot\|$  is the Frobenius norm. The relaxation time reduces, when the viscoelastic stress contribution surpasses  $\sigma_c$ . The micromechanical model focuses on the time- and load dependent breakdown of rubber-filler structure to explain the softening. The model is based on the assumption of a microscopically heterogeneous material with different strain-amplified rubber-filler domains. The free energy density  $W_X$  of the model is simplified to contain only elementary mathematical functions.

$$\begin{aligned} W_X = \frac{1}{2} \frac{1}{(X_{min} + C)^{1-x} - (X_{max} + C)^{1-x}} & \left[ \frac{G_c \tilde{I}_1 + 4G_e \tilde{I}^*}{\chi - 2} ((C + X_{min})^{1-x} \right. \\ & (C + (\chi - 1)X_{min}) - (C + X_{max})^{1-x} (C + (\chi - 1)X_{max})) \\ & \left. + G_c n^2 (\chi - 1) \tilde{I}_1^{x-1} (C \tilde{I}_1 + n)^{-x} \log\left(\frac{\tilde{I}_1 X_{min} - n}{\tilde{I}_1 X_{max} - n}\right) \right] \end{aligned} \quad (96)$$

The maximum amplification factor of the system is assumed to decrease according to a simple differential equation, whose relaxation time is reduced when the local load surpasses a critical value. It is shown that the formalism automatically generates logarithmic stress relaxation as observed in the experiments performed at different temperatures and deformation states. Moreover, a similar approach is used to create nonlinear Prony elements, which describes Payne-effect like behavior and may be used to represent the viscoelastic data obtained at strains beyond the linear regime. For further details of the constitutive material model refer to Plagge et al. [140]. Chapter 4.3.1 reports an example of the model feasibility to reproduce the mechanical behaviour of highly filler material under dynamic load condition (high strain and frequency).

## 2.9.4 Finite Element Analysis: fundamental concepts of contact mechanics

The present chapter describes the general framework of finite elements. The finite element method (FEM) is selected to solve friction problems in order to capture the hysteresis friction contribution. Commercial packages are used mainly ABAQUS. A limitation of computer programming is necessary to implement material models and post processing algorithms.

The analysis is based on the finite element methods (FEM) which consists in breaking down a real object into a large number of finite elements, usually triangular or rectangular in shape for two dimensional models. Mathematical equations are solved by the FEA software to predict the behavior of each element. More in detail, the set of elements constitutes the mesh on which the analysis is performed. Each node of the mesh can move in various directions, specifically translation or rotation, which are known as the degrees of freedom (DOF). The range of DOF can be defined by applying boundary conditions to the nodes, like loads or displacements constraint, see Figure 66. In the mechanical analysis the mesh deformation is calculated thanks to a force displacement equation given by [141]:

$$[K]\{U\} = \{F\} \quad (97)$$

where  $[K]$  is a square matrix or stiffness matrix derived from the models geometry and material properties,  $\{U\}$  and  $\{F\}$  are the vectors of nodal displacements and the vector of applied forces, respectively. When the displacements are applied, the unknown forces can be calculated, in the case that forces are applied, the above relationship can be inverted to calculate the unknown displacements using non-linear Newton solver. The FEA software is then capable to solve the equation for each node of the system and reconstruct the body deformation. The more the elements the higher will be the accuracy of the solution, however an extreme complex model can have unreasonable computational costs. For this reason, simplifications are done using symmetries of the body in order that the model can be reduced from three to two dimensions.

In this case plane stress or plane strain analysis can be performed. The plane stress is used when the model has one dimension negligible when compared to the other two dimensions and the loads are in plane with the body. The plane strain is used when the body is long and both geometry and loadings do not vary significantly along the longitudinal direction.

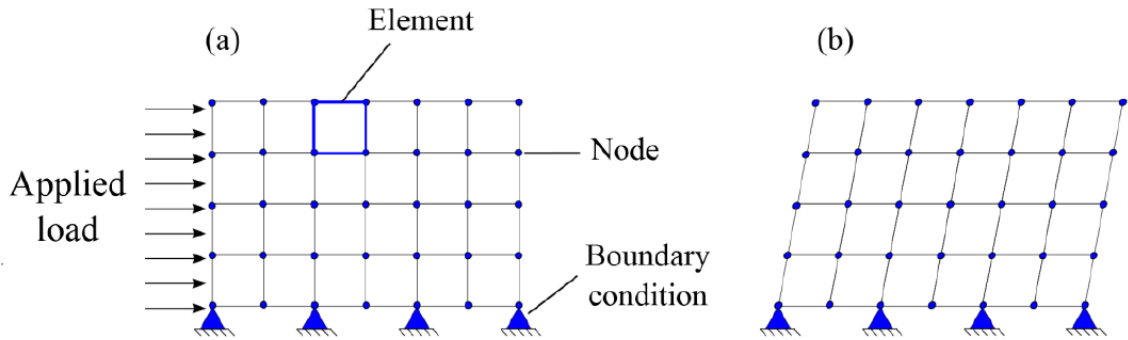


Figure 66. Example of a two dimensional mesh consisting of joined elements (a) and deformed mesh after analysis (b).

A friction simulation requires that an interaction exists between the two bodies. ABAQUS has many possibilities to simulate contact interactions. The most suitable contact formulation for the friction between the rubber and a rigid substrate, is the surface-to-surface and finite sliding formulation. The first step is to define the contact pair surfaces, identified as the master and slave surfaces. Each contact element consists of a slave node (red) and of the master surface (blue) onto which it projects, i.e. the closest master surface (Figure 67).

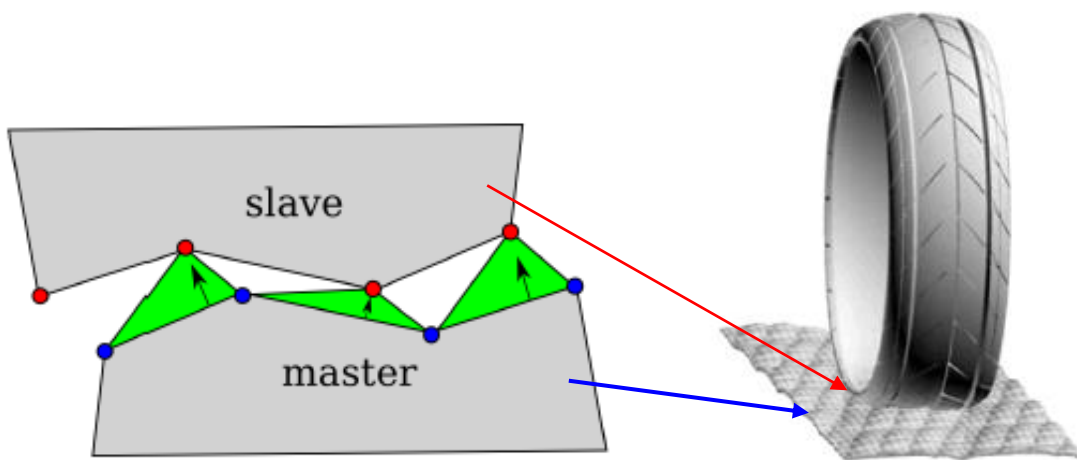


Figure 67. Surface to surface and finite sliding formulation as contact formulation.

Generally, the master surface has to be chosen as the surface of the stiffer body, which in this case reflects the substrate, while the slave surface represents the rubber [142]. Afterwards, the contact needs to be established between the bodies.

Generally contact is split into normal and tangential contact. Normal contact can be formulated as a geometrical constraint, which describes the non-penetration condition of two bodies in contact. This is the known as Signorini contact description, which models the non-penetrability  $g_n > 0$  and non-adhesion  $\sigma_n \leq 0$  of the bodies in contact with the following relations

$$g_n \sigma_n = 0, g_n > 0, \sigma_n \leq 0, \sigma_n = \sigma \cdot n \quad (98)$$

For contact it holds that  $g_n = 0$  and  $\sigma_n < 0$ , where  $g_n$  is the gap distance and  $\sigma_n$  is the normal pressure (see Figure 68).

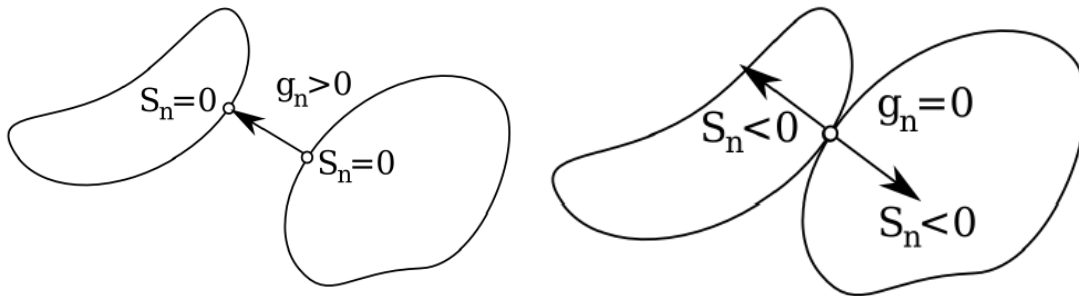


Figure 68. Normal contact formulation (Signorini contact description).

In the case a gap is present between the bodies the pressure is equal to zero. This can be formulated as:  $g_n \geq 0$ ;  $\sigma_n \leq 0$ ;  $g_n \sigma_n = 0$ . This formulation states that only compressive forces can be transmitted if there is contact (no adhesion) and forms the basis of contact problems.

In addition to the normal contact, tangential contact needs to be defined in the FEA code. ABAQUS calculates the tangential behavior in a contact interaction using the local tangent directions as reference orientation. The response in the tangential direction can be modelled in several ways. Mainly a distinction between the interaction with or without friction is made. Friction means that the nodes of the master and slave surfaces are hold together as long as a certain magnitude of shear stress is reached. Above this critical shear stress, the sliding of surfaces starts as a function of the contact pressure between the surfaces. The Coulomb's friction condition reads (see Figure 69).

$$|\dot{g}_t|(\sigma_t + \mu \sigma_n) = 0; |\sigma_t| \leq -\mu \sigma_n; \dot{g}_t = |\dot{g}_t| \frac{\sigma_t}{|\sigma_t|}, \sigma_t = \sigma \cdot t \quad (99)$$

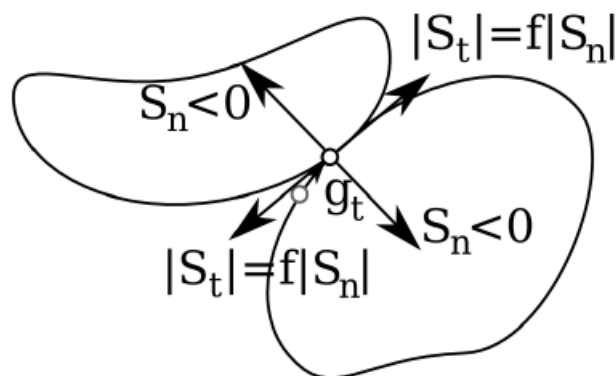


Figure 69. Coulomb friction formulation.

In the present work, frictionless simulation are performed in order to capture the hysteresis friction induced by the surface asperities, which results in the viscoelastic energy dissipation whenever rubber slides on a rough substrate. In dry condition, the hysteresis contribution is enhanced with the adhesion contribution. Therefore, an artificial tangential friction can be added as input in the simulation to reproduce adhesion and to compare it (see 2.6.1 and 4. chapters) with the dry friction measurements.

A more complex approach used in Wagner is the Mortar discretization [143], which reveals a proper contact stress distribution within the contact at large deformations and slip. However, the implementation is very complicated and shows stability problem for curved surfaces.



# 3. Experimental methods and materials

This chapter introduces the materials, experimental equipments and techniques adopted to carry out the investigation. The first part consists of a description of the rubber compounds, followed by an insight of the rubber physical mechanisms and equipment features.

In the case of tribological measurements, the samples consisted of various types of rubber, prepared according to the experimental purpose. Reproducibility and cleanliness were considered. Samples and substrates were cleaned residue free with isopropanol before and during the experiment to remove possible abrasion particles.

The sample preparation consisted of several steps:

1. Mixing a batch of the filled elastomer including carbon black and special ingredients
2. Vulcanization to fulfil the cross-linking
3. Shaping the samples to fit the experimental setup

The matrix samples were composed of rubber. Depending on the type of elastomer, various materials were formulated. The amount of rubber is the gauge to which the other components are scaled: the fraction of elastomer is always set to 100 phr (“*per hundred rubber*”), and the rest of the ingredients relate to weight percent compared to the rubber. Those additional substances grant different advantages such as increased mechanical stability for fillers like carbon black, better control of the cross-linking process and stability against aging as well as sun rays, plus softeners and dyes. Only pure rubber types (chapter 2) were used, no blends.

## 3.1 Rubber materials selection

Eight rubber compounds were used for the investigation and can be grouped in two categories (see Table 4 and Table 5). One group characterized by simpler mechanical behaviour based on polymer and lower filler content (40 phr), the second group consisted of highly non linear mechanical properties characterized by polymers filled with higher filler content and commercial oil.

Table 4. Chemical composition and glass transition temperature of the rubber used for the investigation. T<sub>g</sub> evaluated by DSC.

Name	styrene (%)	Mooney viscosity (%)	T <sub>g</sub>	Uses	Characteristics
Nipol NS 616	21	62	-23°C	Tires, vibration insulators	Best performance for silica application. Well-balanced between wet skid resistance and resilience.
Nipol NS 612	15	62	-55°C		Best performance for silica application. Low styrene type for all-season tires.

Two different styrene-butadiene rubbers (hereinafter referred to as H & L), based on different glass transition temperature, were chosen and mixed with 40 phr carbon black (N339).

A lower amount of filler (H-CB40 and L-CB40) was adopted to have a material characterized by reduced non-linearity, withstanding at the same time multiple friction tests without excessive abrasion as the first group of compounds.

A second group of compounds (H-CB80, L-CB80, H-Si80 and L-Si80) was formulated by adding more filler content and different types of filler, thus enhancing mechanical non-linearity and showing different friction behaviours.

The general composition of the first and second compound groups are illustrated in Table 5.

Table 5. Formulation of the second compound group.

Ingredient (phr)	H-CB40	L-CB40	H-CB80	L-CB80	H-Si80	L-Si80
S-SBR (Nipol NS 616)	100	-	100	-	100	-
S-SBR (Nipol NS 612)	-	100	-	100	-	100
Carbon black (N339)	40	40	80	80	-	-
Ultrasil Evonik U7000GR	-	-	-	-	80	80
Silane Evonik Si-69	-	-	-	-	6,4	6,4
Vivatec oil	-	-	30	30	30	30
Stearic Acid	1	1	1,5	1,5	1,5	1,5
Zn Oxide	3	3	3	3	3	3
Sulfur	1,5	1,5	1,5	1,5	1,5	1,5
CBS	2	2	2	2	1,6	1,6
DPG	-	-	-	-	2,0	2,0
6PPD	1,9	1,9	1,9	1,9	1,9	1,9

## 3.2 Mixing and vulcanization

The compounds were mixed by using an internal mixer from Werner & Pfleiderer (GK 1.5E), see Figure 70. The mixer fill level was 75% to achieve the highest shear forces possible and thus improve the dispersion. The starting temperature was approximately 70°C and the initial speed of the rotors was set to 40 rpm. In the further mixing process, the speed was adapted to the maximum specified temperature. This was set between 100°C and 140°C, depending on the mixture. The ingredients of the compounds were added to the internal mixer in several steps to ensure the best dispersion possible of the fillers in the polymer matrix.



Figure 70. Representation of the internal mixer (left) and the rolling mill (right) for the production of the mixtures.

In-situ silanization was also carried out in the case of mixtures filled with silica. During mixing, the silane (Si-69) was added to the silica mixture and a reaction between the silane and the silica was forced at a mixing temperature of 140°C. This also contributed to a better distribution of the silane on the surface of the silica. Figure 71 shows a mixing curve of an elastomer filled with silica. In comparison to the mixture filled with carbon black an additional step (3) is required for the silanization.

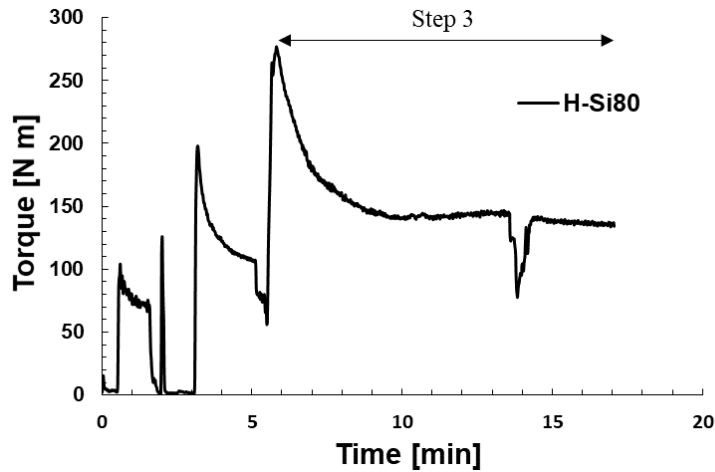


Figure 71. Representation of the mixing curve in the case of silica-filled compound.

In the case of the compounds vulcanization, a specific vulcanization time has to be specified. The “Vulcameter curves” were determined by using Monsanto rheometers MDR 2000E, this is shown in Figure 72 (a). The resulting torque over the measurement time for a silica compound is shown as an example in Figure 72 (b).

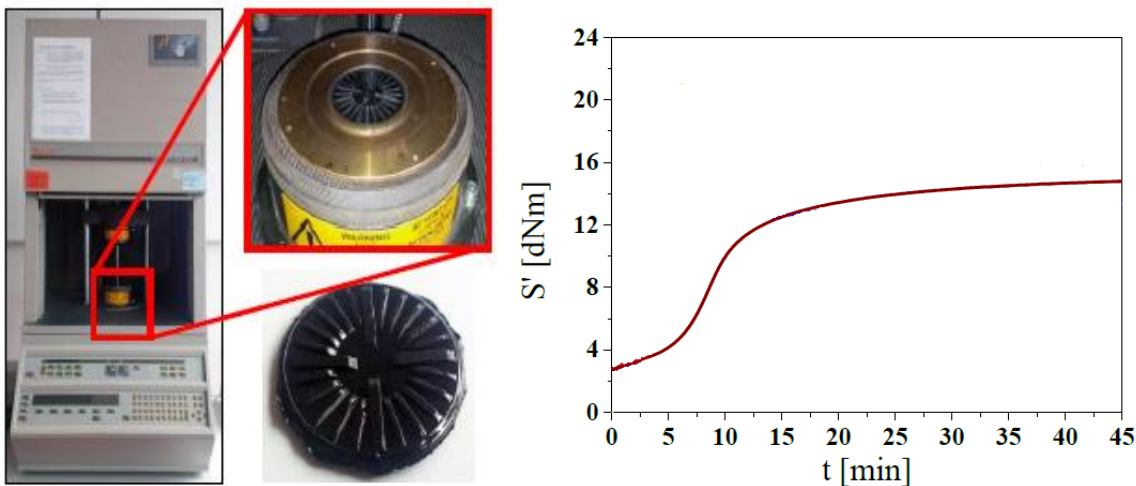


Figure 72. Representation of the vulcameter equipment (a) and the measured vulcameter curve for H-Si80 (b).

In the SBR compounds the torque at the beginning rises slightly due to filler flocculation. The forces, which have an entropic origin, ensure the agglomeration of the filler clusters into a filler network. After an incubation period, the cross-linking of the polymer matrix dominates and the torque increases

strongly until reaching a maximum or a plateau value. Different reference times ( $t_{90\%}$ ) were used for the vulcanization of the mixtures. The vulcanization parameters are listed in Table 6.

Table 6. Vulcanization parameters for the production of the test specimens.

Compound	Vulcanization time	$t_{90\%}$	T vulcanization
H-CB40	$t_{90\%} + 1 \text{ min per 1mm}$ sample thickness	8,2 min	160°C
L-CB40		7,2 min	
H-CB80		12,1 min	
L-CB80		13,4 min	
H-Si80		24,8 min	
L-Si80		23,1 min	

The test specimens of different geometry were produced with a heating press at 280 bar. The press (Rucks Maschinenbau KV 207.00) is shown in Figure 73.



Figure 73. Heating press used for the vulcanization process of the compounds.

### 3.3 Quasi-static stress-strain measurement

The quasi-static tests were used to determine the stress strain behaviour in different strain modes (uniaxial, pure shear, equibiaxial) with a Zwick universal testing machine. Generally the measured magnitudes are expressed as stress (force per unit of cross sectional area) and strain (deformation referred to the initial dimension). The term “quasi-static” was applied to distinguish this group of tests from the dynamic or cyclic tests. In the first one, the deformation time is higher than the time required for the molecular network to respond to an applied stress. Therefore, these tests allow the estimation of the material stiffness with almost no viscoelastic behaviour. This peculiarity is very important to determine a proper material model such as in the case of the Finite Element methods.

The uniaxial test was performed using the dumbbell specimen stretched along its axial direction (see Figure 74). The tensile samples were cut from the vulcanized 2 mm thickness sheet, according to the geometry reported in the ISO 37 norm [144].

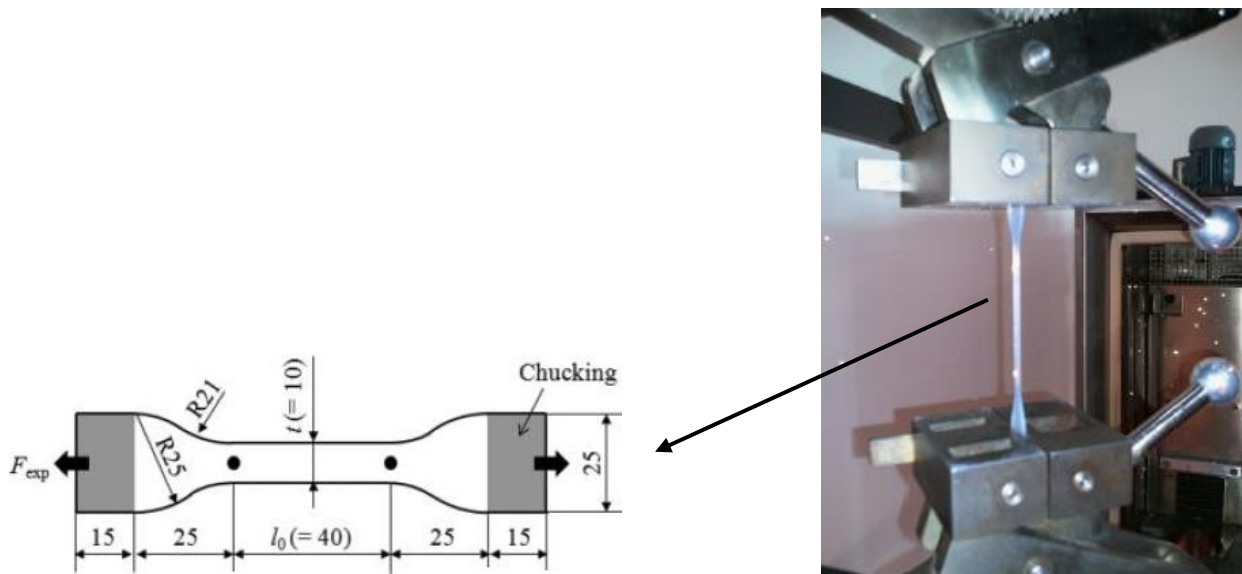


Figure 74. Multihysteresis test in uniaxial mode with dumbbell specimen.

The pure shear test condition is obtained with a strip test piece stretched perpendicular to its length as shown in Figure 75. The strip thickness must be small compared with its width, and the width must be smaller than its length of a factor 10, as suggested by the norm BS 903-5. Therefore, a vulcanized strip of 200 mm x 20 mm x 2 mm was used for the investigation.



Figure 75. Multihysteresis test in shear mode.



Biaxial tests were carried out to determine the most amount of data possible as an input to the finite element programs. Currently there is no ISO standard for such test, nevertheless the British standard BS903-5 for finite element analysis on rubber outlines an approach based on the equi-biaxial stretching of a flat sheet. The biaxial straining rig has two members to which the specimen is attached by gripping links. The two members slide past each other when a force is applied by the crossbars, hence stretching the specimen in two directions, as illustrated in Figure 76. The roller bearings installed on the grippers ensure the pull force remains normal to the edges during the test.



Figure 76. Equi-biaxial test performed in the Zwick machine.

The deformation is evaluated considering the optical extensometer, which follows the marks on the sample with a light beam to avoid the distortion of the clamped zone.

### 3.4 Dynamic mechanical analysis

The dynamic Mechanical Analysis (DMA), also called Dynamic Mechanical Thermal Analysis (DMTA), is an important test method for measuring and characterizing material behavior under dynamic deformation conditions. The measured values are easily reproducible and it allows the detection of the smallest deviations in the frequency or temperature-dependent curves. The ARES equipment of the company Rheometric Scientific<sup>TM</sup> was used (see Figure 77).

Strip samples with the size 30mm x 10mm x 2mm (HxWxD) were used as test specimens, these were prepared from a vulcanized 2mm plate.

A harmonic torsion excitation with a defined deflection amplitude was applied to the test specimens, the resulting forces were measured, this type of measurement is also called "deformation-controlled". In the case of force-controlled measurement, a set force acts on the specimen and the resulting deformation change is measured. The test conditions were kept as constant as possible to obtain consistent results of the tested compounds. An excitation frequency of 1Hz and a deformation amplitude of 0.1% at ARES were selected as measurements at a fixed frequency and variation of the temperature (also called temperature sweeps). An infinitesimally small preload of approximately 1N was set in order to avoid "bulging" of the samples during heating or cooling. The temperature was successively increased from -60°C to 60°C with a ramp of 5K/min and the data were recorded in 1K steps. In addition, temperature- and frequency-dependent measurements were carried out to generate viscoelastic master curves and thus extend the measurable spectrum of properties (see section 2.5.2.1). The frequency varied from 0.01 Hz to 10 Hz, recording 9 points per decade. The dynamic-mechanical data generated were converted into a master curve by applying the time-temperature superposition principle.

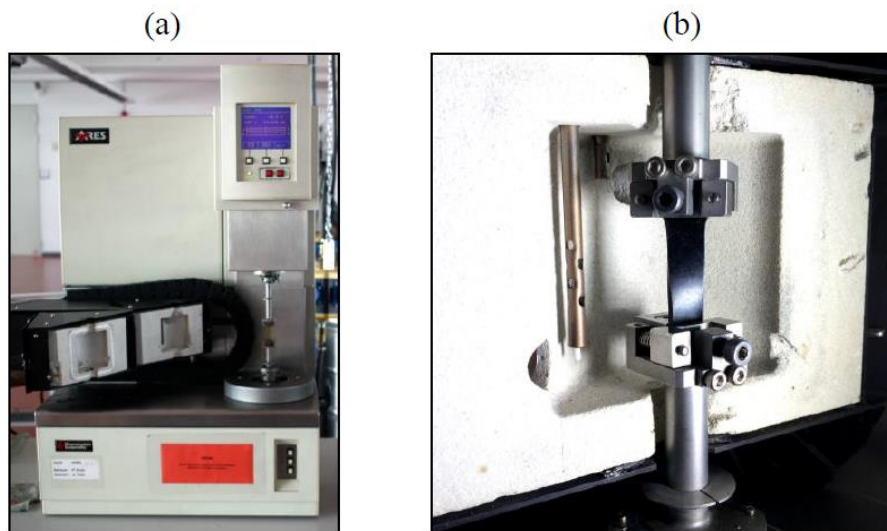


Figure 77. ARES equipment of the company Rheometric Scientific TM (a) and the open thermal chamber with a clamped rubber sample (b).

Strain sweep tests up to 10% at room temperature were performed using 1 Hz as excitation frequency, to measure the dependence of the loss modulus on the strain amplitude.

For the validation of the material model, frequency sweep tests were performed in compression using another dynamic mechanical machine called the Eplexor Gabo 500N, which based on the same principle of the ARES. Contrary to the ARES, this machine is characterized by an electromagnetic shaker, which can apply longitudinal dynamic excitations. This allows to make tension and compression tests besides shear tests. Hence, it was possible to perform frequency sweep tests on a prism shaped rubber specimen in compression under force control as well as to extrapolate the hysteresis stress-strain loops.



### 3.5 Friction measurements

Two different equipments were available for the friction tests. The measurements were made with two linear tribometers (LFT, linear friction tester), the features are shown below.

The second friction machine was selected in order to achieve higher sliding speeds (up to 1,5m/s) and to set up the indentation measurement as explained in chapter 3.1.8. Since these machines are prototypes, the proper measurement of the friction forces has to be ensured.

The DIK friction equipment is a linear tribometer, built up by the University of Hanover at the Institute for Machine Design and Tribology. A schematic representation of the measurement device is shown in Figure 78.

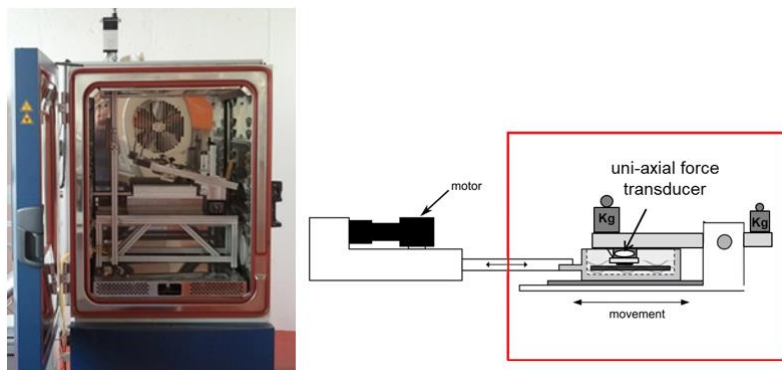


Figure 78. Schematic representation of the first DIK friction equipment.

The first tribometer achieves wide temperature ranges between  $-40^{\circ}\text{C}$  and  $100^{\circ}\text{C}$ , at high loads up to 10 bar at  $0.0005\text{ m}^2$  nominal sample surface and speeds between  $0.005\text{ mm/s}$  and  $300\text{ mm/s}$ . The mounting of the counter surface is very flexible, therefore the experiments can be carried out on rough asphalt and steel surfaces.

The second tribometer was built up by Coesfeld. A schematic representation of the machine is shown in Figure 79.

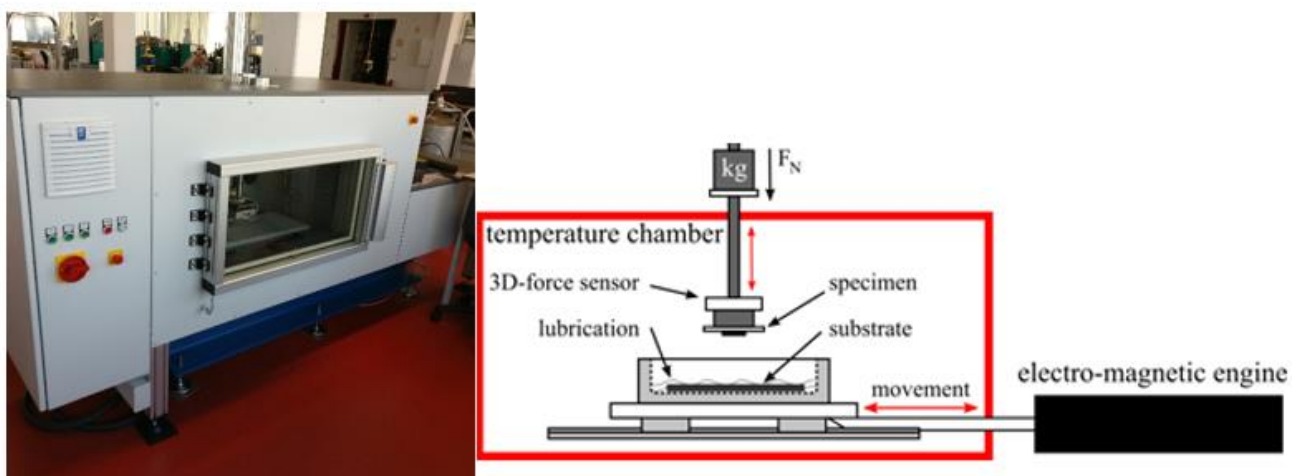


Figure 79. Schematic representation of the second DIK friction equipment.

This equipment achieves higher speeds (bidirectional) up to 2 m/s in comparison to the first tribometer and normal loads from 0.1 bar to 5 bar. The measurements are possible over a broad temperature range (-20°C... +120°C). The sample was placed in contact with the substrate while a force transducer records the friction forces generated when the relative motion between the two friction partners occurs. The sample was connected to the force transducer and is pressed against the substrate thanks to weights applied on the rotating shaft installed to the static part of the machine. The shaft can freely rotate in order that the sample can follow the surfaces asperities. The normal load is applied by a dead weight system.

A typical friction measurement at different sliding speeds is qualitatively described in Figure 80a. The friction test was performed two times for each sliding speed (forward and backwards). A pause of 10 s between the different sliding speeds was observed to avoid the heating of rubber sample that occurs especially at high sliding speeds.

A magnification in the case of sliding speed of 10 mm/s is shown in Figure 80b. During the first step (1) of the test, the sample is sticking on the surfaces and the friction forces raise until the shear stresses are high enough to reach the sliding regime. During the rubber sliding a scatter of the force is generally observed due to vibrations and surface irregularities (2). When the motion ends (3), the sample relaxes slowly back to its initial condition. The friction coefficient can be calculated by dividing the average friction force measured during the pure sliding regime to the normal load. The temperature can be controlled thanks to a climate chamber, where the whole friction machine is installed.

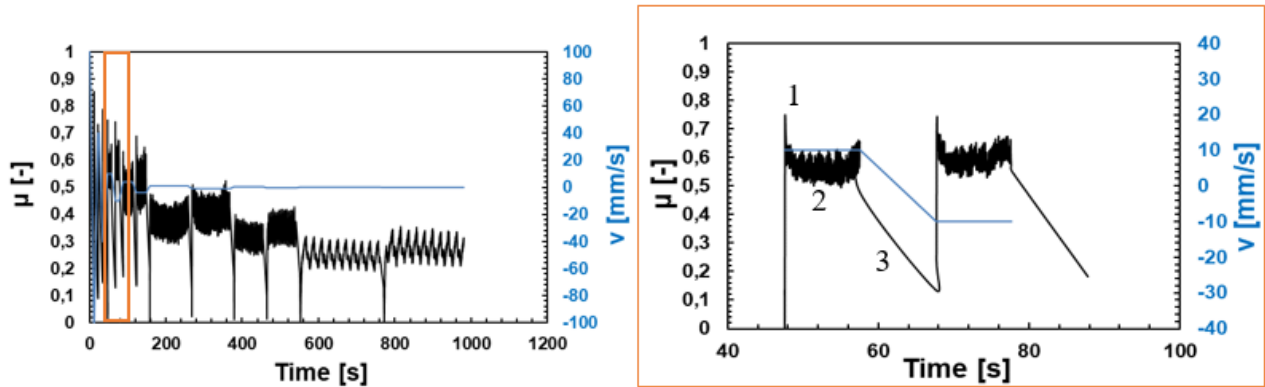


Figure 80. An example of the friction measurement on sinusoidal substrate at different sliding speeds (a) and the corresponding magnification for  $v=10$ mm/s (b).

Before each friction measurement the samples were preconditioned to ensure a stable friction process. The speed was 10 mm/s and the sliding distance corresponded to approximately 2 meters. An example is shown in Figure 81 for a load of 0.26 MPa. The mean value of the resulting friction coefficient ( $\mu$  average) is determined for each cycle (a run forward and backwards). Stable dynamic friction values are reached after 5-6 cycles at  $T=20^\circ\text{C}$  whereas major number of cycles are required to get a stable condition at lower temperatures ( $T=0^\circ\text{C}$ ).

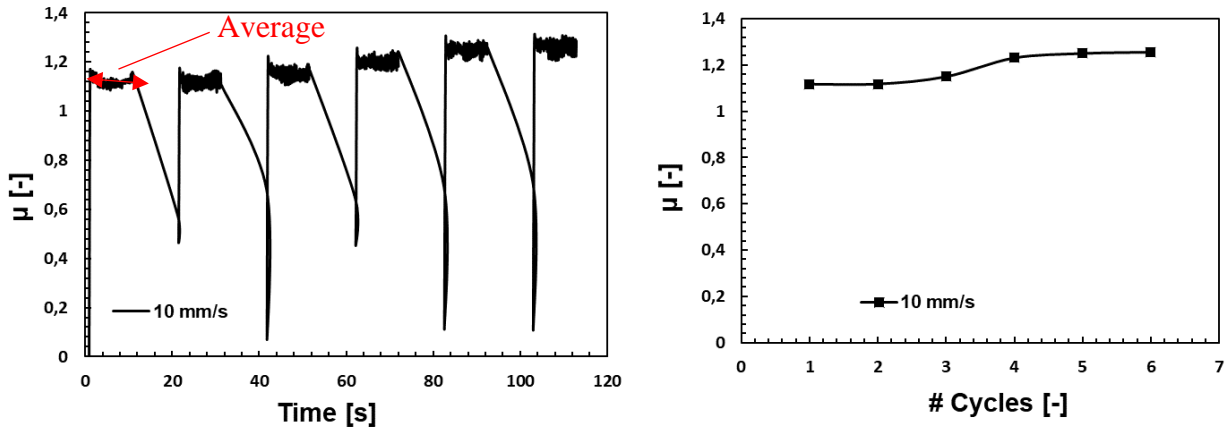


Figure 81. Representation of the friction precondition (6 cycles at 10 mm/s) of rubber sample on rough sinusoidal substrate.

### 3.5.1 Substrates

Various substrates of different roughness were used for the friction tests. Aluminium sinusoidal multi-indenters with different roughness, granites and asphalt surfaces were used for the investigations on rubber compounds described in chapter 3.1, the four types of surfaces are shown in Figure 82. In particular, different multi-asperity indenters were used with a wavelength  $\lambda$  and height  $h$  of 2 millimeters, as well as different radius  $R$  at the top of asperities and micro-roughness (Figure 83). The granite surface was finely bush-hammered and showed a homogeneous distribution of the surface.



Figure 82. Types of substrates used for the friction investigation.

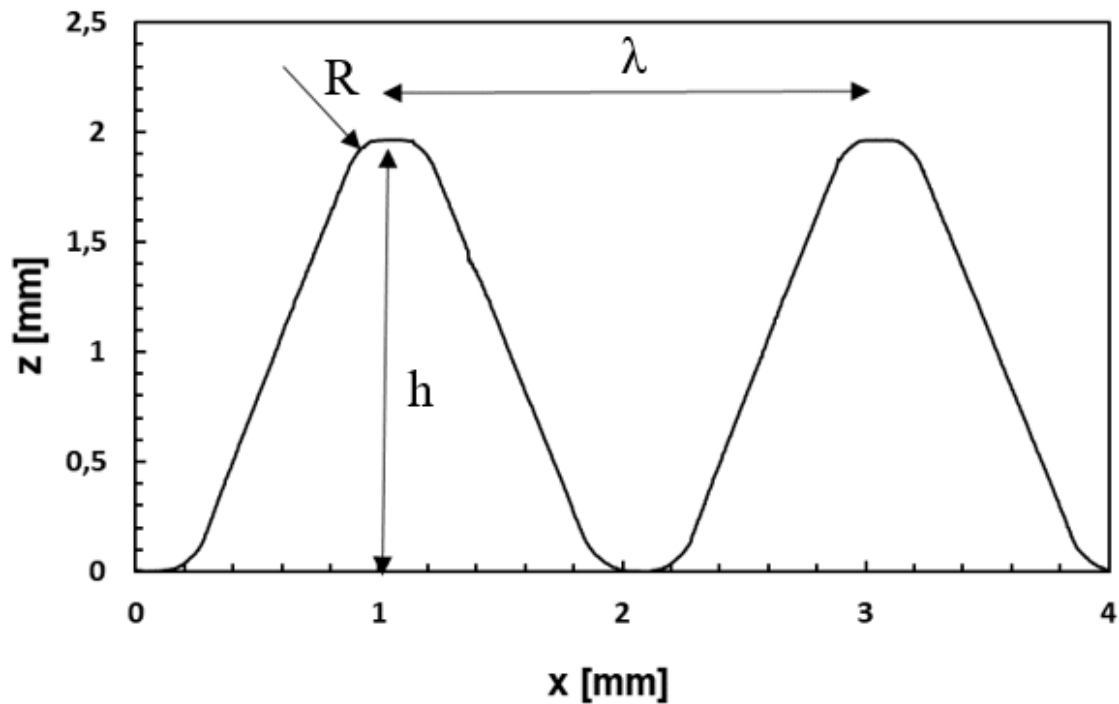


Figure 83. 2D sketch of the sinusoidal multi-indenter substrate used in this research.

The ratio  $h/\lambda$  and the radius of the asperities define the level of local rubber deformation and consequently the viscoelastic response of the material according to the Payne effect.

### 3.5.2 Measurement of the roughness

Two equipments were used to characterize the surface roughness, one optical device based on white light interferometry (see Figure 84) as well as a confocal scan microscope (see Figure 85). The MicroProf® is equipped with a particular sensor FRT CWL based on a patented method, which uses the chromatic aberration (in principle the wavelength dependent refractive index) of optical lenses. This measuring method can be described as follows: the sample is illuminated by focusing a white light while a xy table is moving in order that the profile or surfaces can be analyzed. The focused light – in contrast to the unfocused components of the beam - will be optimally reflected after meeting a surface. Afterwards, it goes into a miniaturized spectrometer via the same lens through a glass fiber cable. A passive lens with larger chromatic aberration fans out the white light vertically in different colored focal points. The wavelength of the reflected light is matched with a calibration table and reveals the resulting distance between the sensor and the sample. The measuring range of 300 $\mu$ m and an accuracy of 0.1 $\mu$ m were used for the roughness measurements.

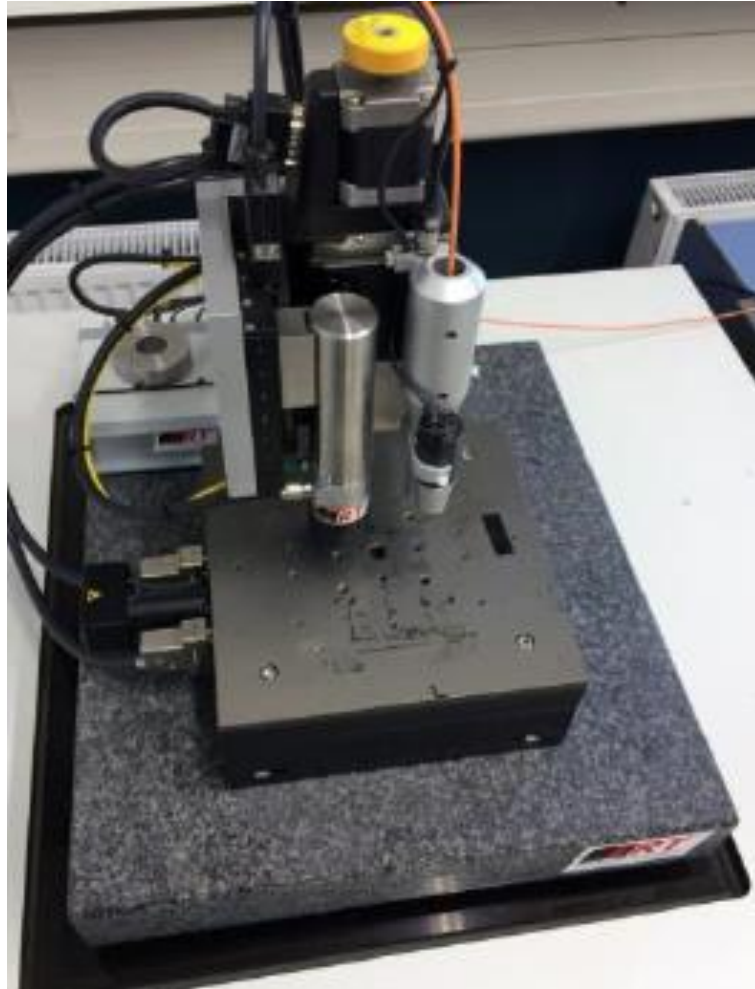


Figure 84. Representation of the white light interferometer of the company FRT GmbH.

Another device from KEYENCE was used to get an automatic roughness profile by performing 3D scanning of the surface. The equipment incorporates two light sources, a white light to gather color and a laser source to scan the surface of an object and collect detailed height information. As the microscope observes a surface, the laser is scanned in the XYZ directions to collect data throughout the entirety of the specified range. The result is a high-resolution, large depth-of-field, color image with a nanometer-level height resolution for getting accurate profile and roughness measurements. This equipment is able to combine a lot of the functionality of an optical microscope, scanning electron microscope, and surface roughness gauge, still maintain the ease-of-use of an optical microscope.



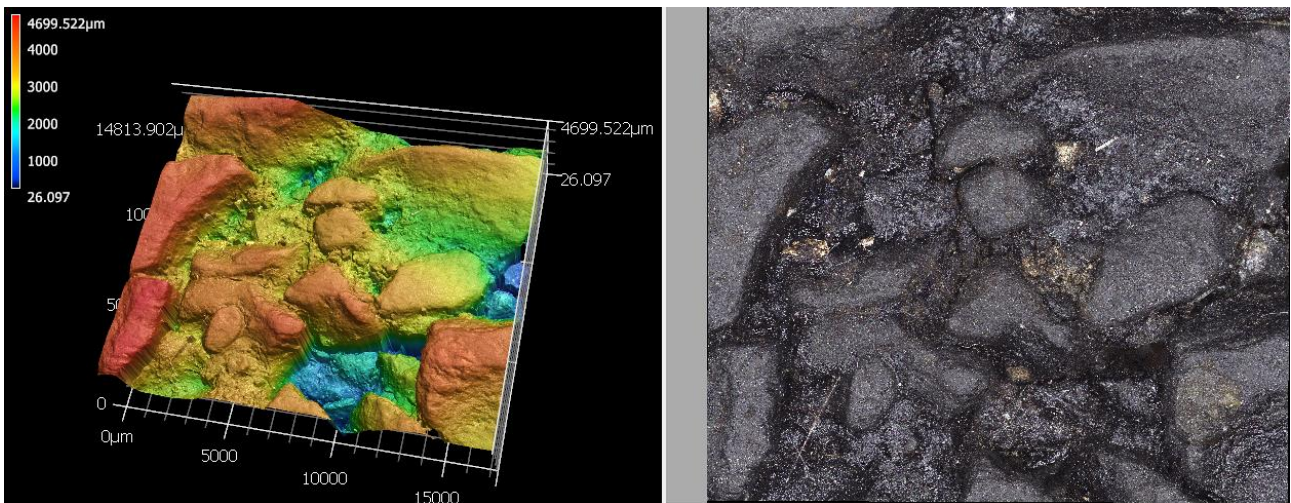


Figure 85. Description of 3D laser scanning microscope (top) and an example of asphalt surface analysis (bottom).

### 3.6 Indentation measurement by laser displacement sensor

A laser displacement sensor (LK-052K from Keyence) is used to determine the depth of the rubber indentation  $z_p$  with respect to the reference plane, originated from the relaxation of a rubber block into cavities of the counter surface (substrate). The laser beam of the sensor goes through a pinhole, located exactly between two asperities, drilled vertically through the substrate to observe the bottom of the rubber sample and thus to detect the indentation during friction measurement. The reference plane is defined on the top of asperities. A schematic description is depicted in Figure 86. Static and dynamic indentation is measured by detecting the distance in relation to the reference plane.

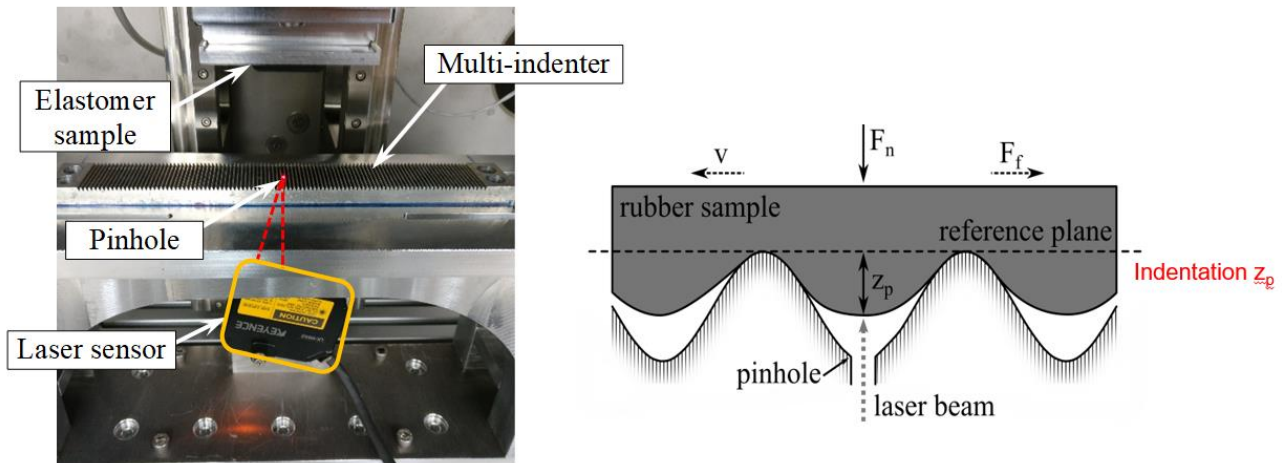


Figure 86. Schematic description of the rubber indentation measurement into sinusoidal model substrate measured by a laser sensor (left). The measured indentation  $z_p$  is indicated (right) [145].

### 3.7 Thermographic measurement

A thermographic camera was used to take images from the thermal radiation of the bodies. The operating principle is that each body, with a temperature above the absolute zero ( $-273.15^{\circ}\text{C} = 0$  Kelvin), emits an electromagnetic radiation from its surface, which is proportional to its intrinsic temperature.

A part of this intrinsic radiation is an infrared radiation, which can be used to measure the temperature of the body. This radiation penetrates the atmosphere and with the help of a lens (input optics) can be focused on a detector element generating an electrical signal proportional to the radiation. The signal is amplified and is transformed into an output signal using digital signal processing, which reflects the object temperature.

This technique was used to investigate the temperature increase (heat build-up HBU) induced in the sample due to frictional heating (see Figure 87) – energy dissipation which is converted in heat in the hot spot of the contact rubber substrate – and during biaxial measurement (compression  $F_z$  plus shear deformations  $F_x$ , see Figure 88) performed with MTS (Mechanical Test Machine). The measurements were carried out using the VarioTHERM camera from InfraTec® and the image analysis was performed with the IRBIS plus v2.2 software.

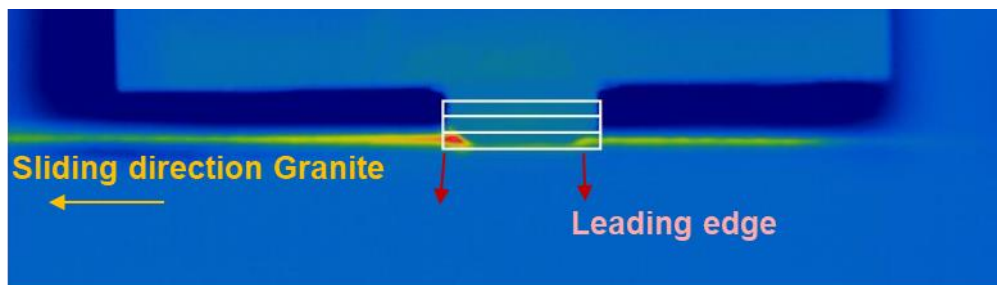
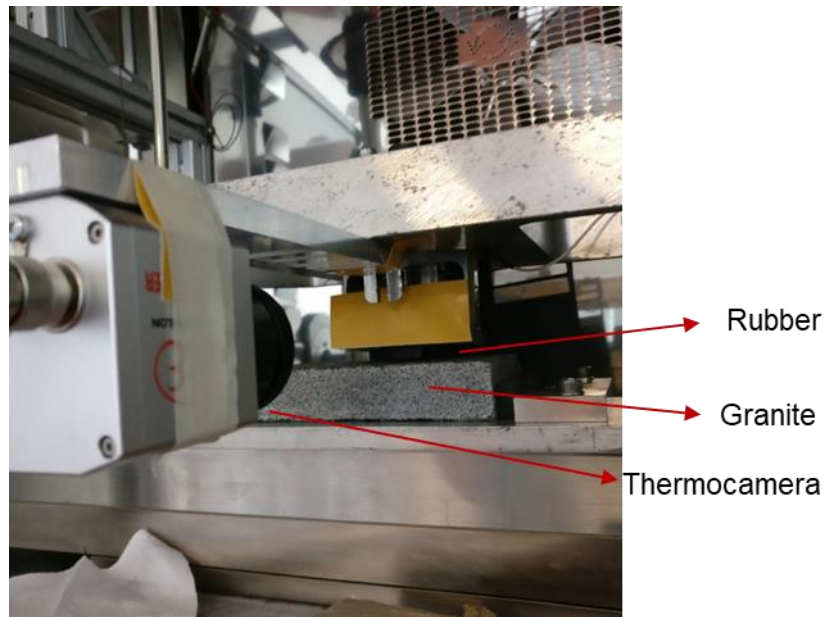


Figure 87. Set up of the infrared camera (top). Heat build-up outcome due to the rubber friction on granite surface (bottom).

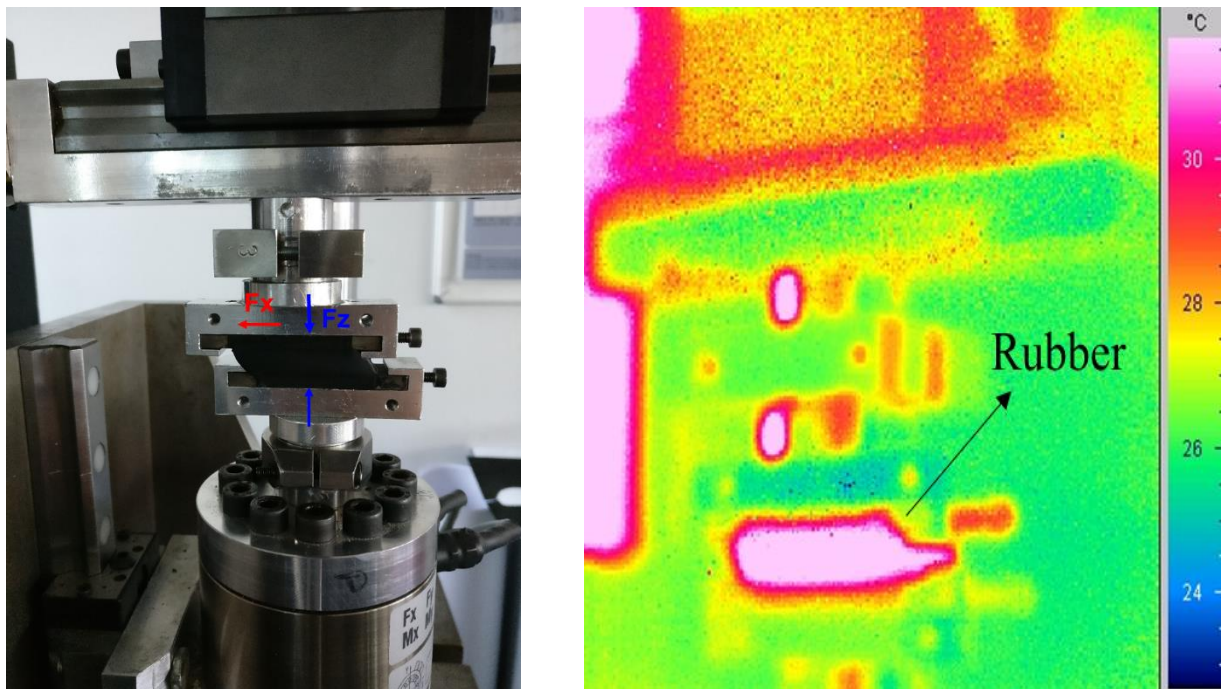


Figure 88. Biaxial measurement carried out with MTS equipment (left) and corresponding rubber temperature increase detected by infrared camera (right).



### 3.8 Contact angle measurement

Contact angle (CA) measurements were carried out to characterize the wettability of solid technical surfaces. The Contact angle is the experimentally observed angle on the liquid side between the tangent to the solid surface and the tangent to the liquid-gaseous interface at the contact line among the three phases. The point of intersection between tangent lines is denoted as the contact point (Figure 89).

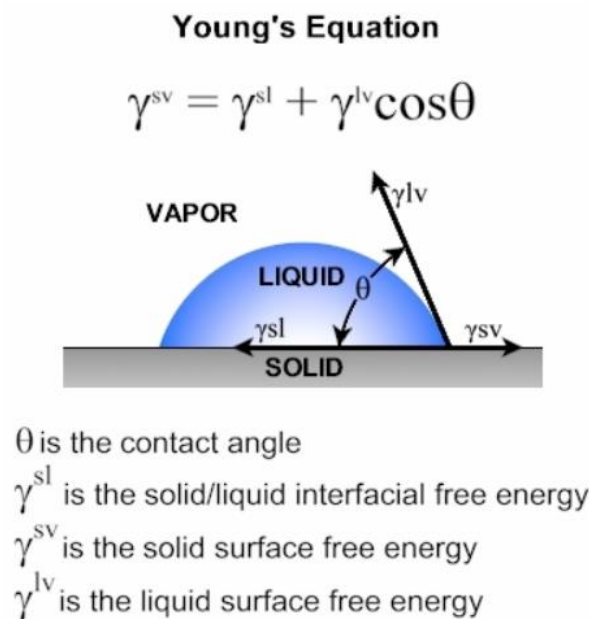


Figure 89. Definition of contact angle according the well-known Young equation [146].

Contact angles are sensitive to many factors, e.g. surface geometry, roughness, contamination and deformation of polymer surfaces [29-30]. There is a lack of contact angle data for the mostly used materials, which could serve as reference source. Contact angles, measured for an observed system, can not be regarded as unique values. Therefore, several method are developed for CA measurement. The sessile drop method is frequently used, since it is the most convenient method. However, other contact angle measurement methods such as the captive bubble and the Wilhelmy plate are available [147].

The measurement allows to capture an image of a liquid droplet that sits on a solid (sessile drop) and subsequently to analyse it with a software. The evaluation of the grey scale values of the recorded image allows the detection of the base line (contact between droplet and solid) and the drop outline. The easiest method to determine the right and left contact angle is to apply tangents at the intersections of the drop outline and the baseline. The tangent method in the *SCA 20 software of DataPhysics Instruments* additionally offers four automatic methods as well a manual one to evaluate the contact angle.

The automatic method consists of a contour line which is fitted to the drop outline based on a mathematical equation. The latter describes a circle when using the height/width method, an ellipse when using the ellipse method and a higher-order polynomial when using the polynomial method.

In contrast to these purely mathematically motivated fits, the fourth automatic method, also called Young-Laplace method, considers the droplet's physical properties. The image scale, the local gravity acceleration, the densities of the liquid and the surrounding medium have to be defined. The Young-Laplace method yields the most reliable results, especially for large contact angles and big drops. However, the Young-Laplace method always obtains a common contact angle for the left and right intersection with the base line because the calculation assumes a symmetric drop.

Another used method is the measurement of the dynamic contact angle. Surface and interfacial tensions are measured with a dynamic contact angle measuring instrument and tensiometer of the DCAT series. For this purpose, the weight of a liquid lamella that forms when a measuring body is wetted is being measured. Accordingly, the most important part of a tensiometer is a highly precise balance to which the measuring bodies are being attached. A vessel with the liquid of interest is placed under the balance on a height-adjustable table (see Figure 90).

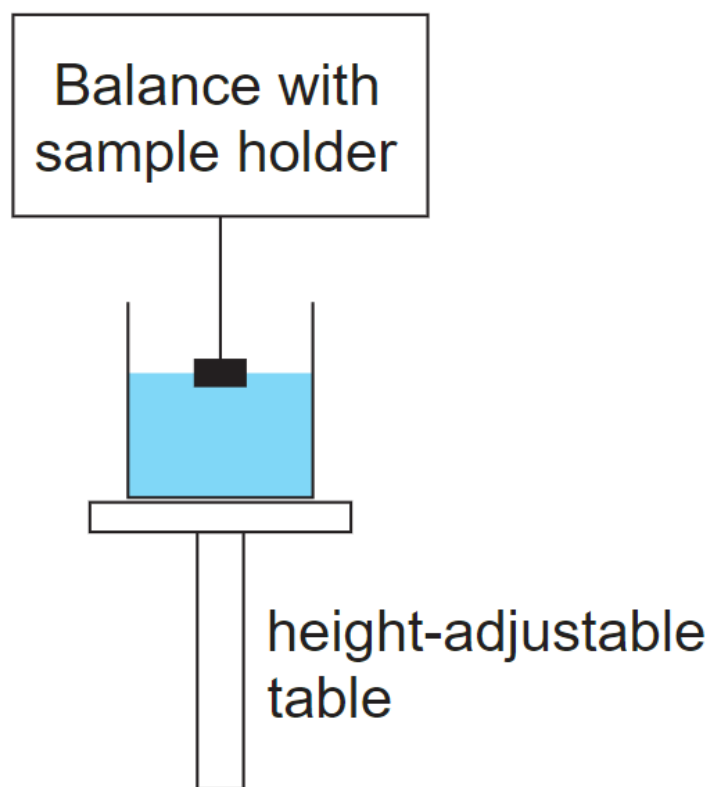


Figure 90. Schematic setup of tensiometer.

At the three-phase contact line a tension force  $F_{\text{tens}}$  acts tangentially to the liquid surface. It can be split into a force parallel and a force perpendicular to the undisturbed liquid surface.

The most common method to measure the surface/interfacial tension is the Wilhelmy plate method. A Wilhelmy plate is a thin, generally rectangular plate made of iridium-platinum with a few centimetres in length and height. The material is chosen because of good wetting when contacting a

liquid. In this case a lamella snaps on whose shape is determined by the interfacial tension of the liquid. The volume and hence the weight of the formed lamella depends on the wetted length  $L = 2 \cdot b + 2 \cdot l$  of the Wilhelmy plate.

$$\begin{aligned} F_{\perp} &= F_{tens} \cos \theta_c \\ F_{\parallel} &= F_{tens} \sin \theta_c \end{aligned} \quad (100)$$

The balance, located in z-direction, only feels the perpendicular part of the tension force, which matches the gravitational force  $F_G$  of the formed lamella. The gravitational force of the measuring body is irrelevant since the balance of the tensiometer is tared with an attached measuring body at the beginning of a measurement. With the definition of the surface tension, the Wilhelmy equation is obtained as:

$$\sigma = \frac{F_{tens}}{L} = \frac{F_{\perp}}{L \cos \theta_c} = \frac{F_G}{L \cos \theta_c} \quad (101)$$

Assuming the Wilhelmy plate is completely wetted (contact angle  $0^\circ$ ) the equation simplifies ( $\cos(0^\circ)=1$ ), this enables a direct determination of the surface tension knowing the plate dimensions and the measured gravitational force.

Concerning the “dynamic modified Wilhelmy method”, advancing and receding contact angles can be determined on solid samples with defined geometry. This method has several advantages compared to the conventional optical methods like the sessile drop method.

The measurement of a contact angle is reduced to measuring the weight and length of a specimen, which is achieved by high accuracy and reproducibility [148] [149] [150]. Furthermore, the measured force concerning any given depth of immersion is already an averaged value. This automatically gives a more accurate contact angle value showing the property of the entire sample [151] [152], the roughness and chemical heterogeneity. Additionally the graphs of the Wilhelmy balance method are useful to study the contact angle hysteresis at different wetting speeds. In fact, the conventional Wilhelmy method, by which the surface tension of the liquids is determined, has been modified (see Figure 91) in a way that a test specimen with defined dimensions was used instead of a DIN-standardized and roughened platinum plate [153]. Before dipping the sample in a liquid test, the surface tension of the solvents has to be determined by the Wilhelmy Pt-Ir-Plate. The DCAT 11 (Data Physics Instruments GmbH) was used to perform the wetting experiments.

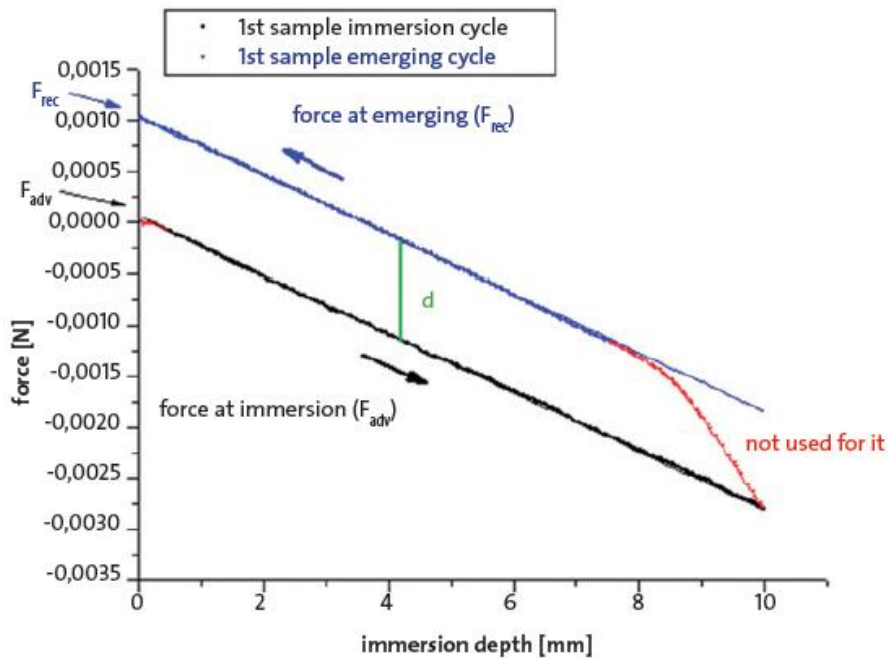
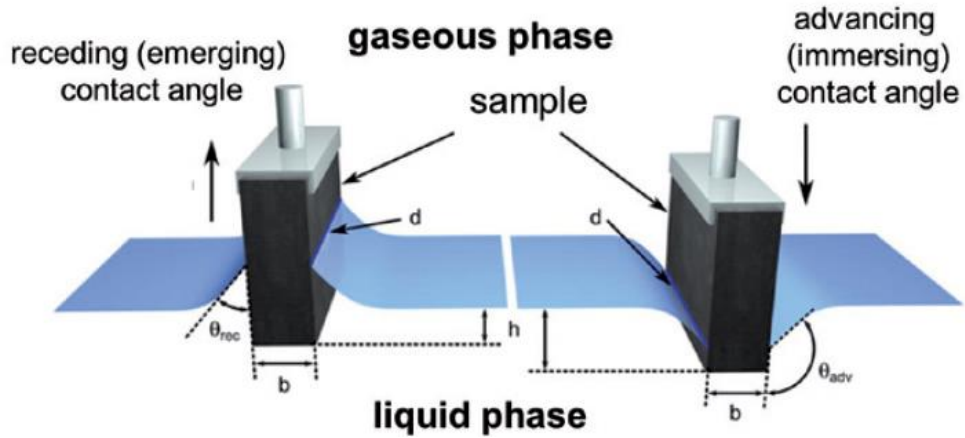


Figure 91. (a) Schematic representation of the immersing and the emerging cycles to determine the advancing and receding contact angles of the modified Wilhelmy balance technique [154]. (b) An example of the modified Wilhelmy balance technique is depicted showing the immersion and emerging cycles of a SBR-sample.

After balancing the weight force ( $mg=0$ ), the test specimen is immersed in the particular test liquid and emerged. The forces  $F_{adv}$  and  $F_{rec}$  (see Eqs. (100)) are measured as a function of the immersion depth  $h$ .  $V=h b d$  is the volume and  $l=2(b+d)$  is the wetted length of the test specimen, and  $\gamma_{lv}$  designates the surface tension and  $\rho_{lv}$  the density of the solvent.

$$F_{adv} = l\gamma_{lv}\cos\theta_{adv} - V\rho_{lv} + mg \quad (102)$$

$$F_{rec} = l\gamma_{lv}\cos\theta_{rec} - V\rho_{lv} + mg \quad (103)$$

The buoyancy force  $F_b = V\rho g$  can be eliminated from the recorded force-distance diagrams by doing a linear regression to the immersion depth zero. If the sum of buoyancy and weight force is equal to zero, the resulting force corresponds to the wetting force. Hence, the corresponding measured forces  $F_{adv}$  and  $F_{rec}$  and the resulting contact angles  $\theta_{adv}$  and  $\theta_{rec}$  can be calculated are obtained separately for the extrapolation of  $h$  to 0 (i.e.  $V=0$ ) [155].

$$\theta_{adv/rec} = \arccos\left(\frac{F_{adv/rec}(h=0)}{l\gamma_{lv}}\right) \quad (104)$$

Figure 91 shows a plot from the immersion and emerging SBR-sample as well as the calculation of the mean contact angle [156], [157]. Before using the samples have to be cleaned with isopropanol. The preparation of the samples is explained in [157].

The difference between advancing and receding contact angle is the contact angle hysteresis which can not be correlated with the ideal contact angle based on current knowledge. However, the measurement of these angles is extremely important since the contact angle hysteresis is a measure of the non-ideality of the solid surface. Contact angle hysteresis may be considered as a rough indication of the degree of drop adhesion on a solid surface, since in many cases the larger the contact angle hysteresis, the stronger is the drop adhesion. It was figured out that the nanometric holes in a monolayer can be detected through the measurement of the contact angle hysteresis.

# 4. Results and discussion

## 4.1 Friction measurement on rough substrate

The first stage of this research investigates the friction interaction of rubber compounds sliding over a sinusoidal aluminum multi-indenter with wavelength and height of 2 millimetres in order to understand the contact mechanism and validate the friction theory such as the rubber hysteresis (Figure 83). Several factors such as filler, surface, load, lubricant and sliding velocity influence the contact mechanics.

In dry condition occur mainly two contributions: (i) hysteresis contribution, originated from the energy dissipation of the rubber induced by the substrate roughness and (ii) dry adhesion which arises from the molecular interactions between rubber and substrate. The cohesion component that describes the wear process at the interface, is negligible in a first approximation since the present research focuses on low macroscopic velocities.

$$\mu_{DRY,tot} = \mu_{Hys} + \mu_{dry,adh} \quad (105)$$

In wet conditions occur a hysteresis contribution (based on the hypothesis it does not change from wet to dry condition), a viscous contribution that depends on the viscosity of the fluid and the nature of contact and finally a partial adhesion contribution, called adhesion wet contribution. The latter appears when the lubricant squeezes out at the interface establishing direct contact rubber substrate.

$$\mu_{WET,tot} = \mu_{Hys} + \mu_{adh,wet} \quad (106)$$

Taking into account intrinsic parameters such as temperature, speed and load, the complex friction phenomena was split in the following topics. On one side it was investigated the contact mechanics based on the interaction substrate / roughness / rubber properties combined with the rubber geometry. It was also studied the rubber indentation and relaxation in the substrate, both induced by the roughness, followed by the thermal effect (also called heat build-up) occurring locally in the contact, especially at dry high-speed conditions. On the other side, the contact mechanism was examined from a physical-chemical point of view based on the affinity of substrate/rubber and lubricant.

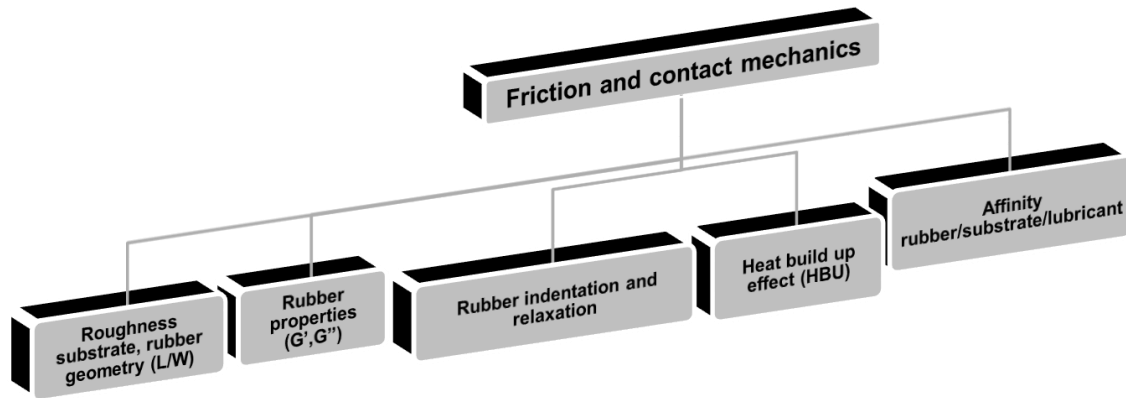


Figure 92. Problem solving of the friction behaviour.

The blocks in Figure 92 were described one at a time to quantify their effect on the hysteresis and adhesion friction. Basically, two approaches were used for the friction prediction in this work: FEM for the hysteresis contribution and an analytical model for the adhesion one.

First, the role played by the substrate (roughness and type) and lubricant were studied. Figure 93 depicts the friction behaviour of compounds on dry and lubricated (water, water+soap5% and pure soap, see Figure 94) sinusoidal multi-indenter.

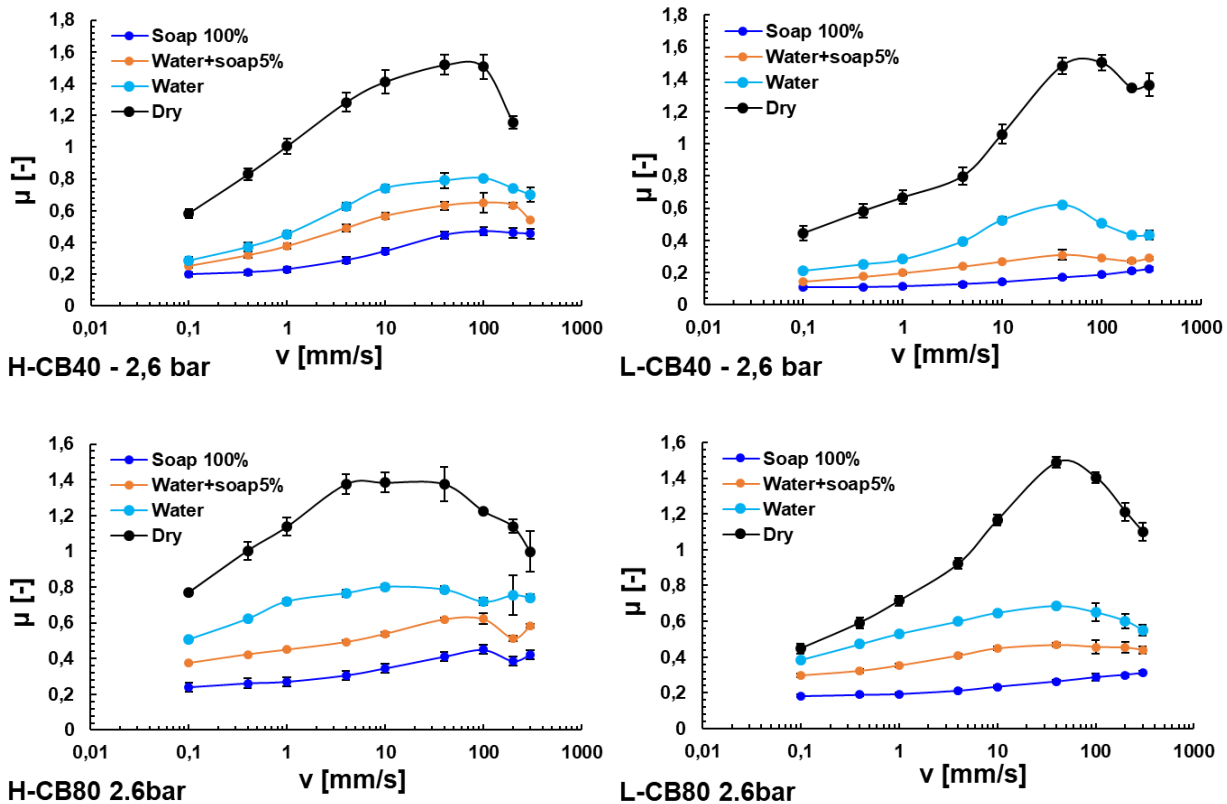


Figure 93. Friction coefficient of the model compounds sliding over the dry and lubricated 2 mm multi-indenter. Values measured at 20°C and 2.6 bar nominal contact pressure.

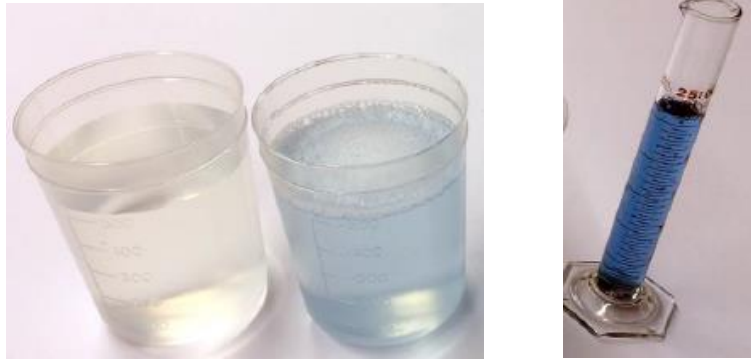


Figure 94. Overview of the different lubricant/liquid used over a substrate during friction tests: water, water+soap5% and pure soap.

According to the literature [77] [79] [41] the rough surface covered with a soap water mixture matches with the pure hysteretic response since the low surface tension of mixture leads to a separation of the rough surface and the rubber bulk minimizing the adhesive effects. Indeed the soap condition tends to mask the smallest length scales of the substrate due to the high viscosity of the lubricant.

In the case of water+soap5% condition the compounds H-CB40 and H-CB80 portray lower variation of the friction coefficients compared with the compounds L-CB40 and L-CB80 (Figure 95).

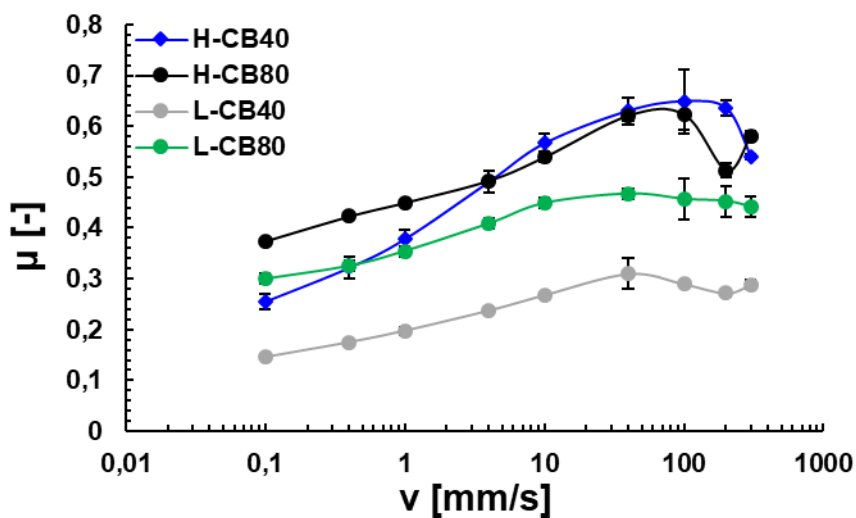


Figure 95. Hysteresis friction coefficient of the model compounds sliding over the 2 mm multi-indenter. Values measured at 20°C and 2.6 bar nominal contact pressure.

Such different friction behavior among the compounds can be explained on the basis of the correlation between hysteresis friction and the viscoelastic properties of materials. Considering the velocity from 0.1 to 300 mm/s and only the macroscopic wavelength of the substrate, the main excitation frequency induced by the indenters into the rubber, can be estimated as the ratio between the velocity and the asperity wavelength ( $f=v/\lambda$ ). This concept is proved considering the friction coefficient crossover between H-CB40 and H-CB80 samples occurring at a sliding speed of 4mm/s. The contact radius calculated from the Hertz contact theory (see Eq. (30)) is equal to  $\sim 0,11$ mm in a first approximation. If the viscoelastic master curves of Figure 96 are taken into account within the corresponding frequency range (0.05 to 150 Hz), it can be observed the crossover of the curves at the excitation



frequency  $f \sim 10/0,11 \sim 91$  Hz and therefore a qualitative correlation between loss factor  $\tan \delta$  and friction coefficient  $\mu$ .

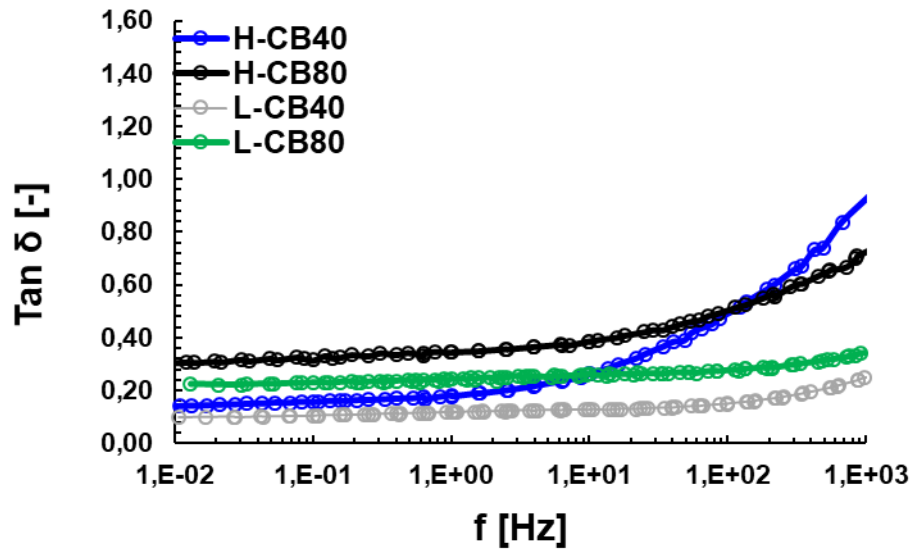


Figure 96. Cut out of  $\tan \delta$  master curves from 0.1 Hz to 1000 Hz. Original master curves are shown in Figure 106.

However, since real surfaces such as granite and asphalt exhibit roughness length scales over many decades, there will be a wide band of perturbing frequencies, all of which contribute to the viscoelastic rubber friction.

Therefore, two different pavers (fine and rough granites) are selected in this work, depicted in Figure 97. Granite surfaces were selected because they furnish stable dynamic friction values.



Figure 97. Rough substrates used for the investigation: fine granite paver (left side), rough granite paver (right side).

The height difference correlation (HDC) function was evaluated for both surfaces and reported in Figure 98. The chart shows that the surface on the right is rougher.

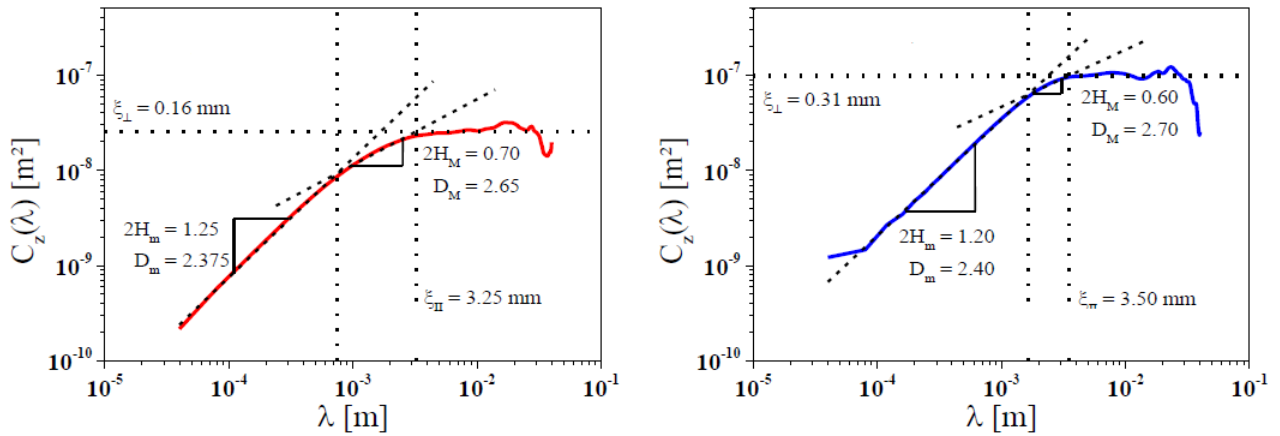
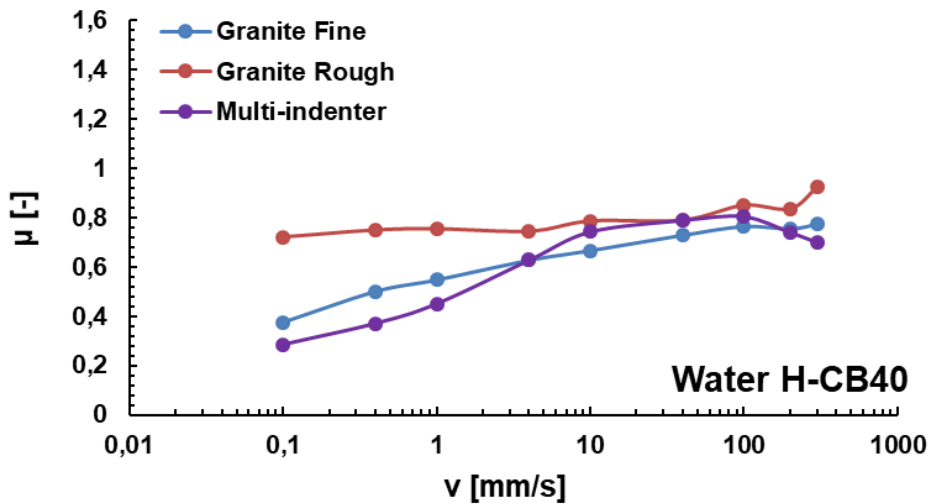
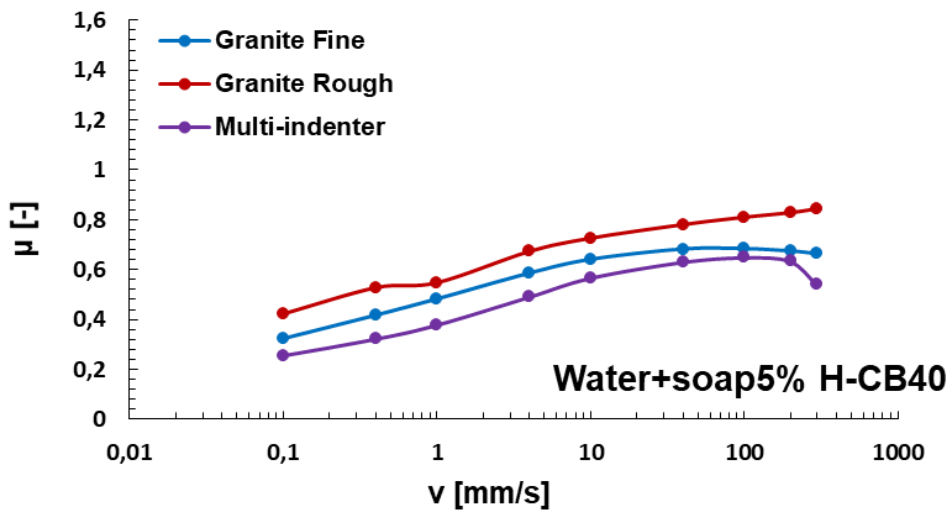


Figure 98. Height difference correlation (HDC) functions for the granite substrates (left: fine and right: rough) selected.

The results of the granite experiments are shown in Figure 99, the results of the multi-indenter substrate are also included as a comparison.



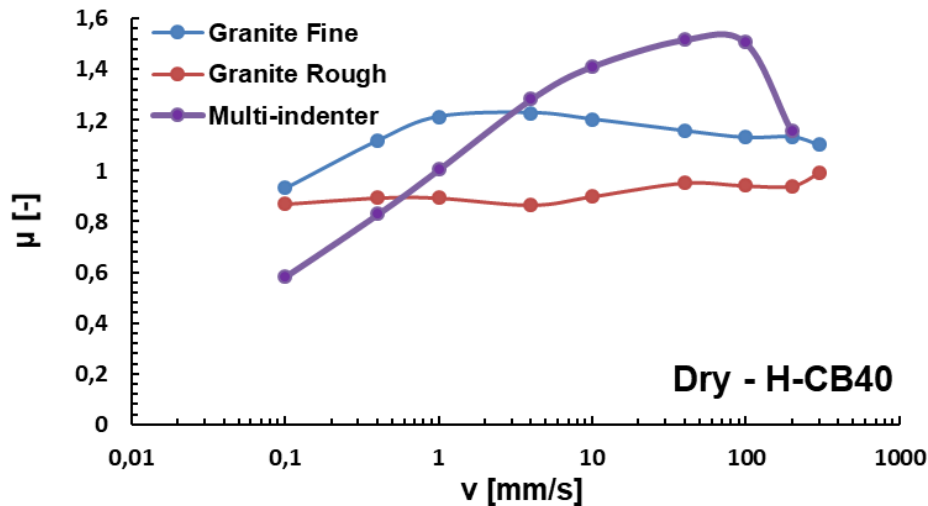


Figure 99. Comparison of the friction behaviour (exp.) between three different rough substrates for H-CB40.  $T=20^{\circ}\text{C}$  and  $p=0.26\text{MPa}$ .

Considering the hysteresis component of the Figure 99 (water+soap5% condition), a higher friction was observed for rough granite in comparison to fine granite and multi-indenter. This reflects the friction contribution resulting from the multiscales roughness. The trend in water and dry condition did not show a clear tendency unlike water+soap because of the occurrence of adhesion, which decreases for rougher surface (lower real contact area for rough granite in comparison to fine granite).

The following chapter describes a multiscale FEM approach, which was developed to estimate the hysteresis contribution depending on the roughness of the length scales and consequently on a wide band of perturbing frequencies.

## 4.2 Mechanical behaviour

The compounds, selected for the investigation were tested under both quasi-static and dynamic conditions. The first type of measurement describes the long term behavior of the material, which are necessary for the identification of material parameter in the case of FEA (sec. 2.9). The dynamic mechanical tests provide a description of the viscoelastic material behavior, which is relevant for the friction prediction.

### 4.2.1 Quasi static analysis

The quasi-static measurements were carried out in uniaxial, pure shear and biaxial deformation modes for the compounds filled with carbon black and silica (see Figure 100). The stress-strain behavior of the materials differ significantly from each other. To simplify the legend, the symbols L and H are used referring to the glass transition temperature of compounds ( $L \rightarrow T_g = -55^{\circ}\text{C}$ ,  $H \rightarrow T_g = -20^{\circ}\text{C}$ ). CB and Si indicate carbon black and silica respectively followed by the content of filler expressed in phr

(i.e. 40 or 80). The following table illustrates the strain amplitudes selected which describes an exhaustive mechanical characterization.

Table 7. Strain amplitudes and speed rates of the quasi-static tests selected for each strain mode.

	1° Ampl.	2° Ampl	3° Ampl	4° Ampl	5° Ampl	6° Ampl	speed rate
Uniaxial	5%	15%	35%	60%	100%	150%	20 mm/min
Pure shear	4,363%	13,177%	31,3%	54,66%	93,18%	142,49%	20 mm/min
Biaxial	2,518%	7,602%	18,1%	31,9%	55,4%	86,65%	80 mm/min

The strain amplitudes of the uniaxial mode together with the equi-biaxial and the pure shear ones are calculated in order to reflect the same strain energy density maximum. To facilitate the reading only the graphs about H-CB80 mechanical characterization are shown in the following chapter whereas the rest is reported in the appendix. An example of the quasi-static characterization of the material is portrayed in Figure 100.

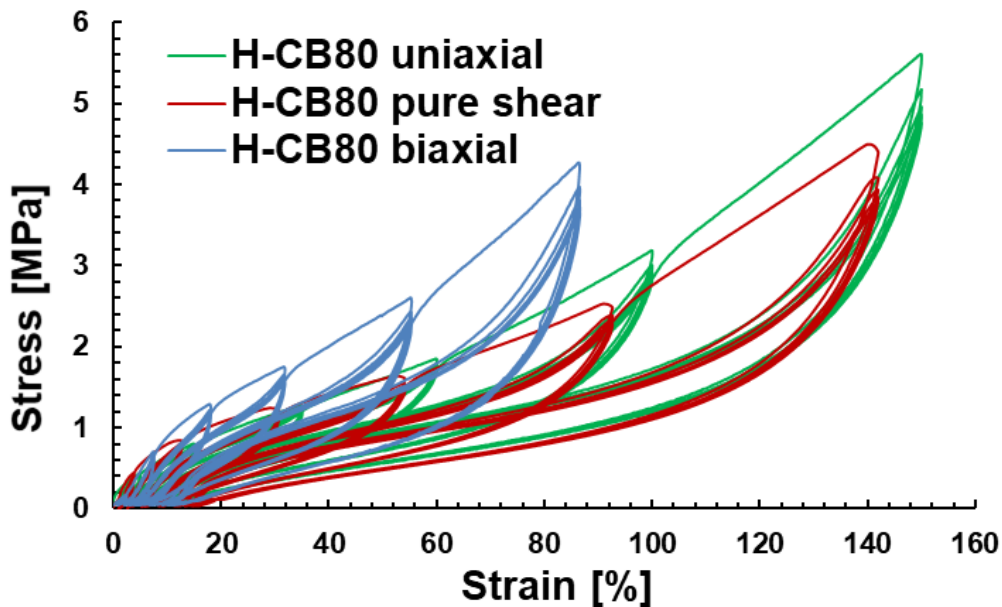


Figure 100. Stress-strain curves on uniaxial, pure shear and equi-biaxial quasi-static modes test for H-CB80 material. T=20°C and crossbar speed 20 mm/min for uniaxial and pure shear test and 80 mm/min for biaxial one.

Samples H-CB40 and L-CB40 showed softer behaviour, smaller hysteresis and less pronounced stress softening in comparison with H-CB80 and L-CB80 because of the lower filler content. Furthermore, compounds with the polymer NS612 (L) showed stiffer behaviour and less hysteresis at T=20°C in

comparison to the polymer NS616 (H). In Figure 101 is considered the type of filler: the silica filled compounds exhibited softer behaviour (lower slope of the loading unloading hysteresis loops) and less hysteresis loss in comparison to carbon black filler.

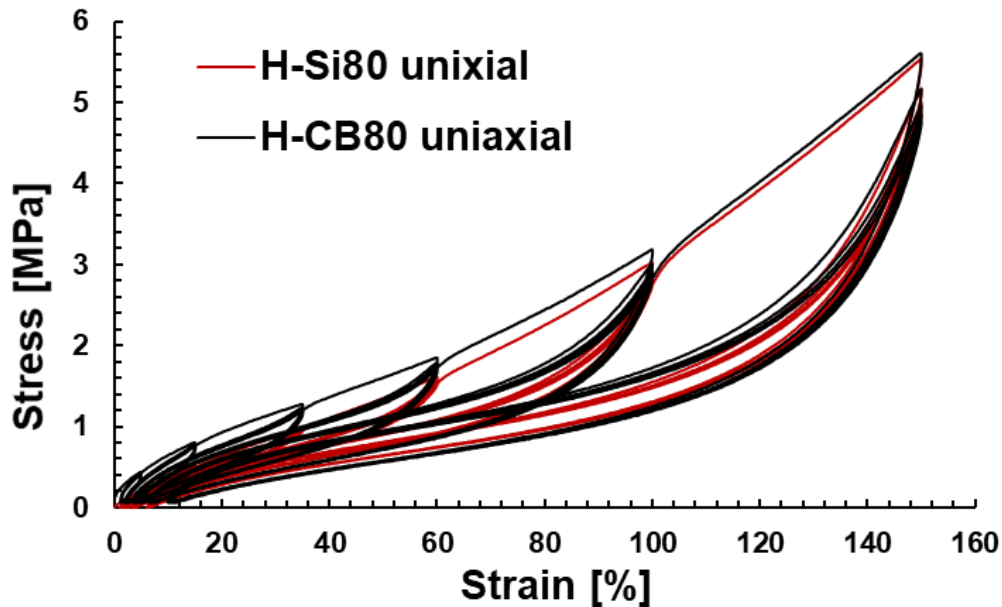


Figure 101. Stress-strain curves on uniaxial mode for silica and carbon black filled compounds.

#### 4.2.2 Dynamic mechanical analysis

As already mentioned in the previous sections, the properties of a rubbery material are strongly dependent on the excitation frequency and temperature. One of the most common methods to extrapolate the dynamic behaviour is the construction of the master curve through the WLF Eq. (15), this was applied in the present work. For more details, see sec. 2.5.2.

The isothermal measured curves of  $\tan \delta$  were shifted along the frequency axis until they overlap. To get a proper master curve, the shifting factor  $a_T$  was applied to the small strain amplitude measurements (0.1 %) where the material exhibits a linear behavior, and afterwards adjusted until they can fit a WLF based equation. Viscoelastic master curves were constructed by using a physical motivated shifting procedure varying the frequency from 0.1 Hz to 10 Hz and temperature from -60°C to 60°C for the compounds with “lower” glass transition temperature (L system) and -30°C and 60°C for H system compounds (high glass transition temperature).

Considering the horizontal and vertical shift factor, an example of the measurement and the corresponding master curve construction is shown in Figure 102. The coefficients  $C_1$  and  $C_2$  were obtained from the WLF fitting, see Figure 103. These were used to shift the  $G'$  and  $G''$  curves in case of larger strain amplitude measurements (2.5 %).

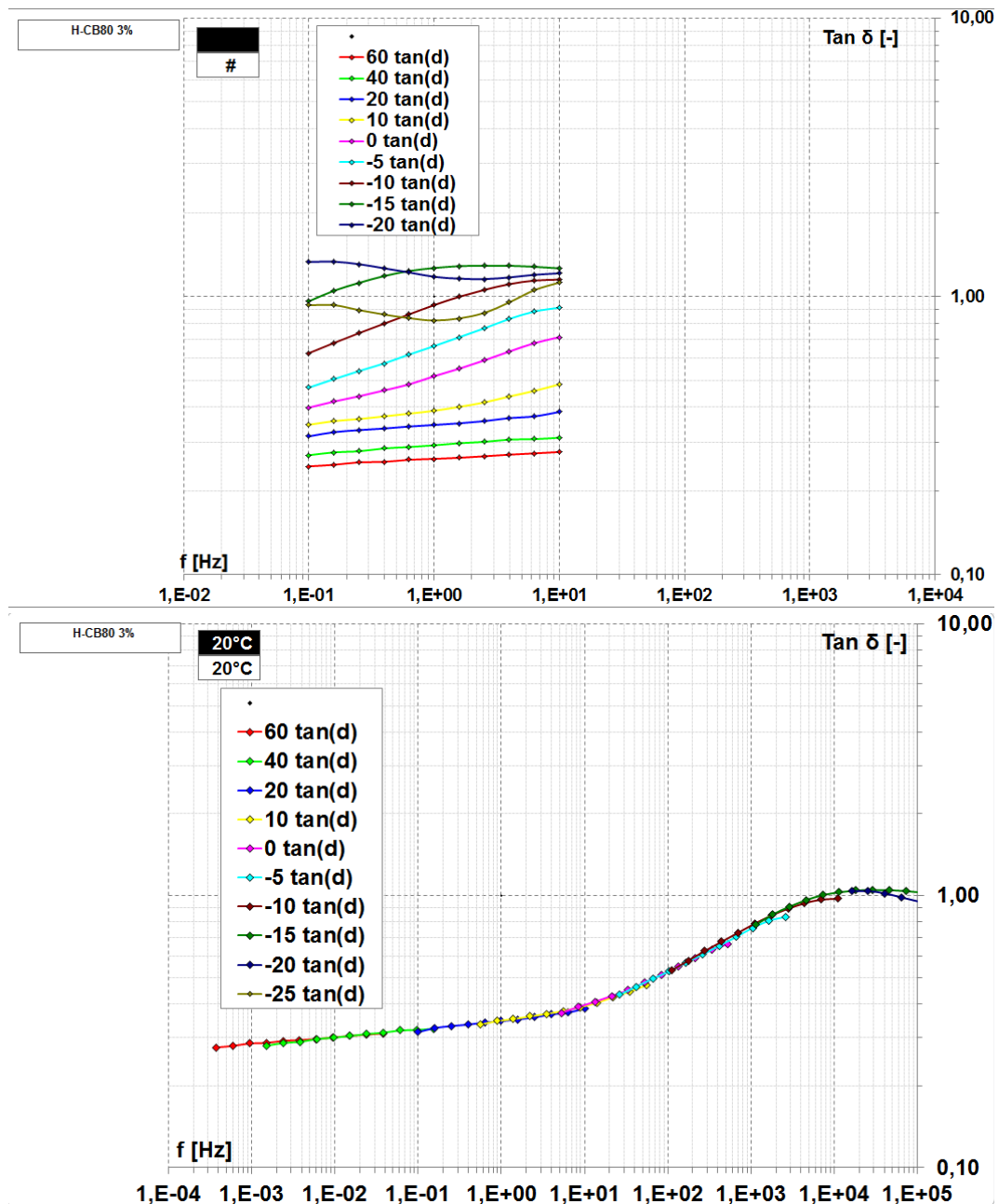


Figure 102. Master curve construction of  $\tan\delta$  for the compound H-CB80 using the WLF principle at 20°C reference temperature. Measurement conditions: 0.01 to 10 Hz; +60°C to -25°C; 2,5% strain.

The horizontal shift factor  $a_T$  used during the dynamic mechanical analysis was not influenced by the filler content, e.g. the master curve procedure based on the horizontal shift factors should be applied in the same way, regardless the elastomer is filled or not. The corresponding coefficients  $C_1$  and  $C_2$  calculated for the carbon black compounds are listed in Table 8.

A vertical shifting was required afterwards for high filled systems to compensate the gap between high temperature branches, caused by the presence of a filler network. The modulus decrease is not identical whether the storage or the loss modulus are considered suggesting the occurrence of two distinct thermally activated mechanisms. Consequently, the vertical shift factors were separately applied to each modulus. An example of H-CB80 is depicted in Figure 104. The left side of the curve

(high temperatures) corresponds to the activation regime where isothermal segments are vertically shifted with respect to the reference temperature. Thereby, an Arrhenius dependence of the vertical shift factors was found and physically interpreted as a thermally activated processes with a probability of occurrence equal to  $e^{(-E_a/RT)}$ , where  $E_a$  and  $R$  are the activation energy and the gas constant respectively. When approaching the glass transition, the thermally activated processes are frozen and vertical shift factors tend to zero since the chain mobility is progressively reduced in the bulk material. The temperature dependent vertical shift factors is physically interpreted as the activation energy of the glassy polymer bridges, in the vicinity of nanoscopic gaps between adjacent filler particles. By applying the same procedure to the dynamic storage modulus, a unique master curve was constructed over a wide range of frequency.

The evaluated activation energy is physically related to the thermal activation of the filler-filler bonds. Table 9 shows the energy activation for compounds filled with carbon black and silica. The activation energy associated with  $G'$  is related to an Arrhenius behaviour of the filler-filler bonds force in a virgin state, while the activation energy of  $G''$  corresponds to the softer filler-filler bonds force in a damaged state, resulting from stress induced breakdown and re-aggregation of the bonds during cyclic deformations. This represents an explanation of the temperature dependency of the stress softening effect as well as the filler induced hysteresis up to large strain. The activation energies obtained from the vertical shifting procedure at 2.5% strain amplitude provided reasonable simulations for the stress-strain cycles between 5% and 100% strain [158]. These results indicate that the larger activation energies found for very small strain amplitudes are possibly related to a dispersion effect of the bond structures, e.g. a fraction of weaker filler-filler bonds which break initially at small deformations.

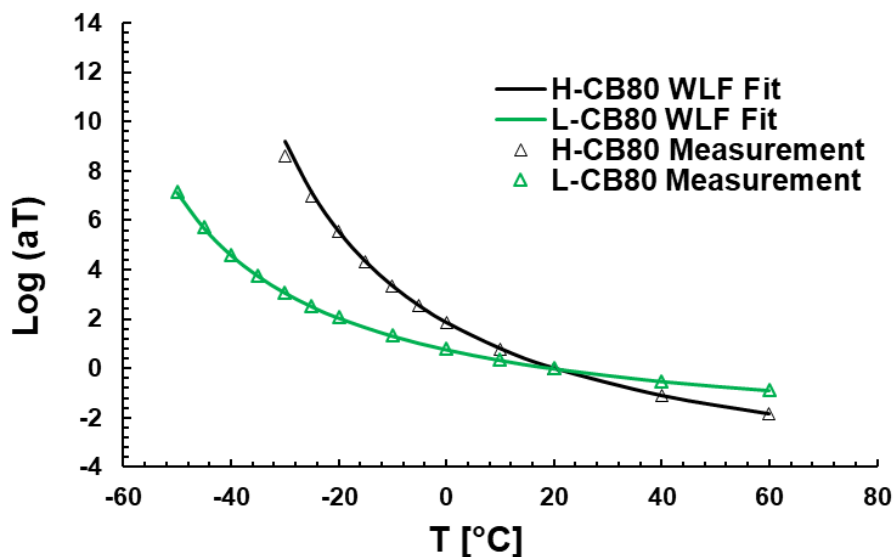


Figure 103. Fitting between the shifting factors applied to the compounds H-CB80 and L-CB80 measured at 0.1 % strain.



Table 8. Coefficient used for the WLF principle considering a reference temperature of 20°C.

Compound	$C_1$	$C_2 [^{\circ}C]$
H-CB40	4,87	70,25
L-CB40	3,58	106,9
H-CB80	5,61	80,42
L-CB80	3,11	100,42
H-Si80	8,39	97,63

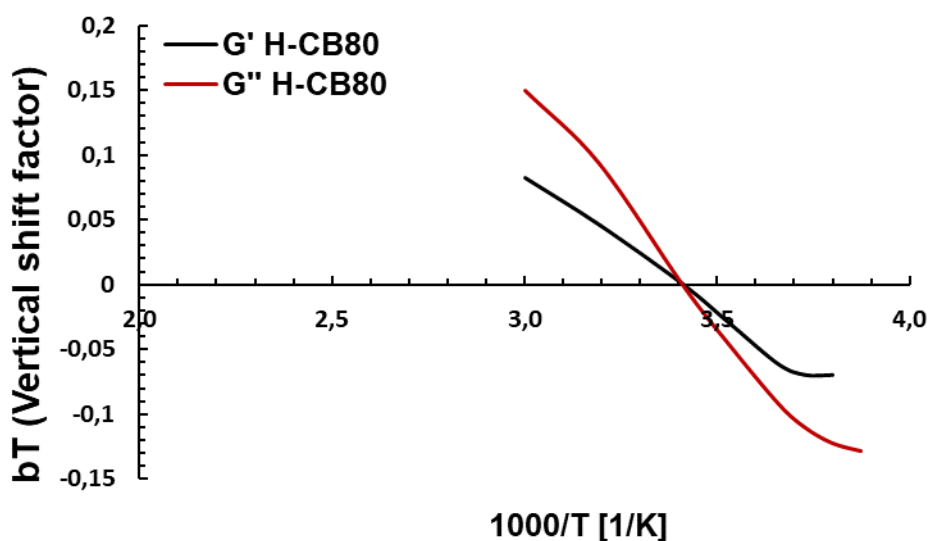


Figure 104. Application of vertical shift factor  $b_T$  function of temperature for H-CB80.

Table 9. Apparent activation energy for different elastomer systems and strain amplitude of 2.5%.

	$E_{a, G'}$ [kJ/mol]	$E_{a, G''}$ [kJ/mol]
H-CB40	2,34	5,39
H-CB80	3,92	6,86
H-Si80	1,07	4,31

The compounds filled with silica revealed lower activation energy. The filler-filler bonds explain this trend, since the thermal activation of the glassy polymer bridges is expected to be affected by the interaction strength between the polymer and filler surface. The silica particles are in both cases chemically coupled with a silane agent to achieve a strong bonding between the polymer chains and the filler particle. This implies that the polymer-filler coupling is based on single "contact points",



corresponding to the spatial location of the silane cross-links. On the contrary, the interaction between the carbon black and the bulk polymer is dispersive and therefore composed by an adsorbed layer of polymer chains with modified dynamics in the vicinity of the filler particle.

In this case, the interface is distributed over the carbon black surface implying that a large amount of polymer chains is involved in the bonding process. Consequently, the required energy to activate thermally the immobilized polymer layers around and between adjacent filler particles is higher for the carbon black filled composites. This leads to the conclusion that during dynamic-mechanical deformations, the silica systems are dynamically softer than the carbon black systems. This aspect is crucial for the friction behaviour and it was confirmed in the indentation experiment as explained in sec. 4.4.

The viscoelastic master curves of  $G'$  and  $\tan \delta$  of the model compounds are plotted in Figure 105 and Figure 106, respectively.

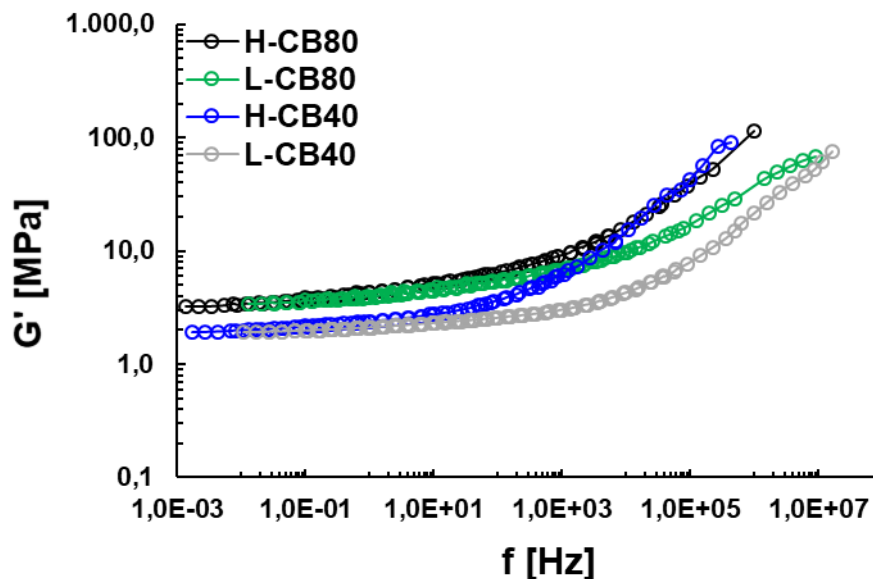


Figure 105. Storage modulus master curves of the model compounds for 20°C reference temperature, 2.5% strain.

The lower glass transition temperature  $T_g$  of the compounds L-CB40 and L-CB80 reveals a shifting of the glass transition to higher frequency compared with the compounds H-CB40 and H-CB80. L-CB40 exhibits a loss modulus shifted towards higher frequency compared to H-CB40, therefore a different material interaction is expected with the macro-micro roughness and consequently a different hysteresis friction.

By adding more filler (e.g. from H-CB40 to H-CB80) the moduli  $G'$  increases at high temperature, corresponding to low frequency range, contrary to the high frequency range where occurs a less effect of the filler amount in the material stiffness.

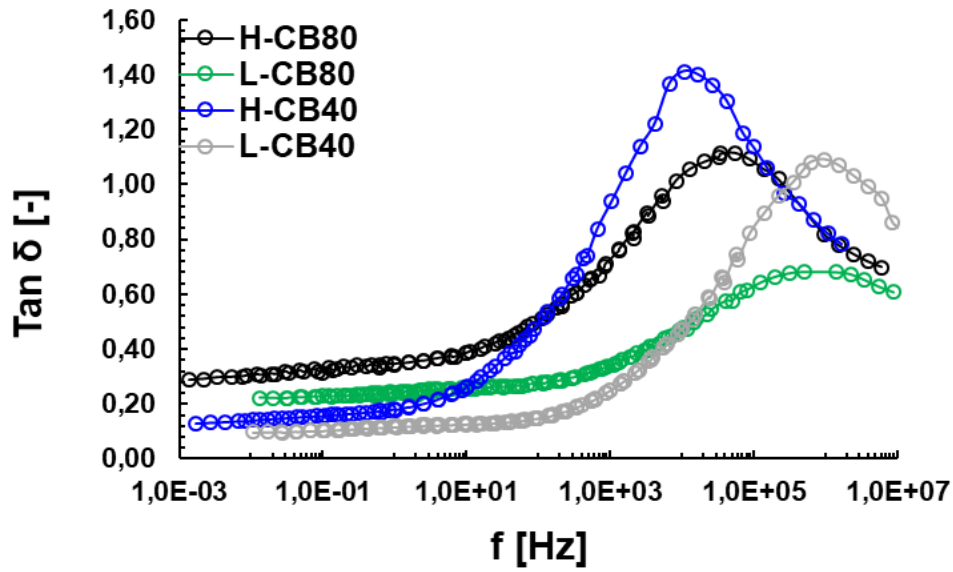
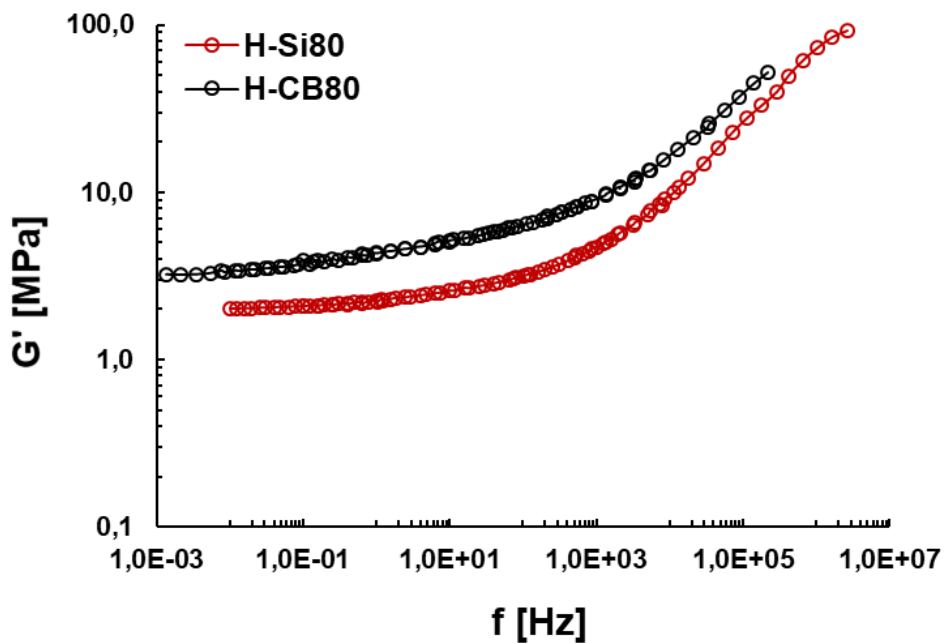


Figure 106. Loss factor master curves of the model compounds for 20°C reference temperature, 2.5 % strain.

The frequency of the maximum of  $\tan \delta = G''/G'$  did not change with the filler content. The maximum decreases strongly when the filler is added based on the fact that  $G''$  remains constant while  $G'$  increases. The viscoelastic properties were also influenced by the significant presence of the oil (30phr) in the case of H-CB80, L-CB80 and H-Si80. Figure 107 displays a comparison of the viscoelastic properties between the silica and carbon black systems.



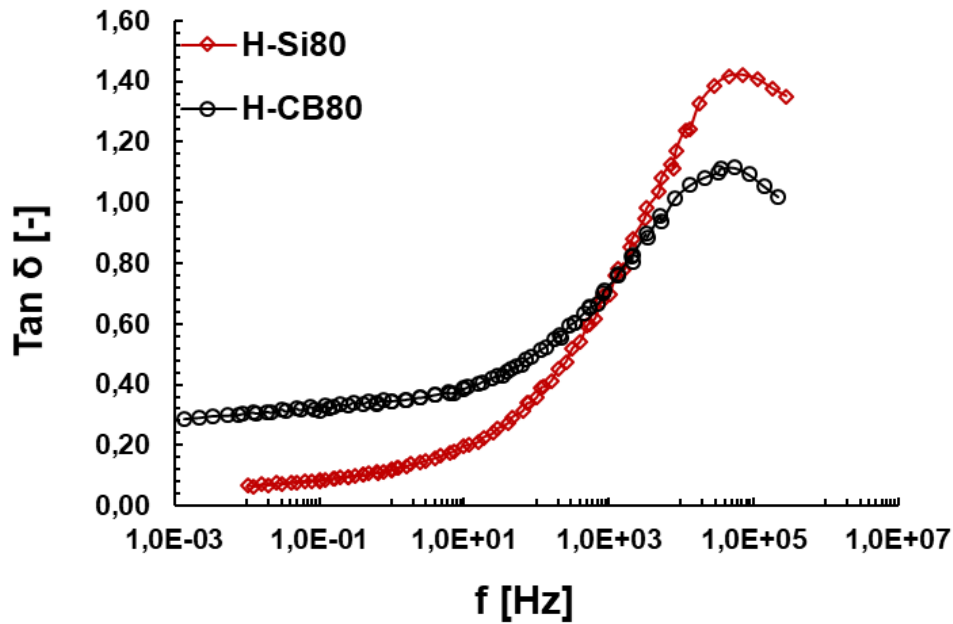


Figure 107. Comparison between storage modulus and loss factor master curves of silica and carbon black system compounds for 20°C reference temperature and 2.5 % strain.

The interpretation of the temperature-induced vertical displacement factors and the resulting apparent activation energy is caused by the interaction between the filler particles and the glassy polymer bridges. This means that the temperature dependence of the polymer bridges is low in case of silica system due to the silica polymer connection through the silane.

In the carbon black systems the polymer chains are adsorbed directly on the carbon black surface and are immobilized. The layer thickness of the adsorbed polymer chains is more strongly thermally activated.

The addition of filler significantly improves the rubber mechanical properties via a reinforcement mechanism but introduces at the same time a non-linear dependency upon the dynamic strain amplitude, generally denoted as Payne effect. Typically, the dynamic mechanical moduli exhibit a linear behavior only for small amplitude (< 0.1 %). The Payne effect, described in sec. 2.4.4, takes place for larger strains.

In Figure 108 is depicted the strain sweep test performed for the compounds H-CB80 and H-CB40 representing an example of moduli variation as a function of the strain. The difference between the materials results from the amount of carbon black in the two recipes. Similar consideration was found for the L compound system.

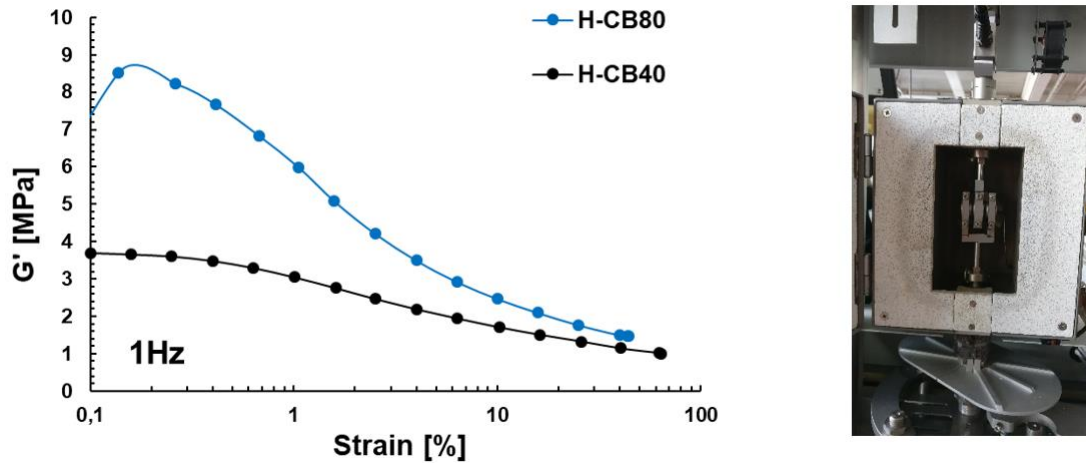


Figure 108.  $G'$  as a function of strain amplitude for compound H-CB80 and H-CB40 (left). Measurement carried out at room temperature and 1 Hz excitation frequency in double shear mode (right).

## 4.3 Finite element analysis for the hysteresis friction

As already mentioned the hysteresis contribution originates from the internal energy dissipation and it depends on the material excitation induced by the roughness of the track that occurs over a wide range of length scales. Therefore, a FEM approach was developed to study the contact mechanisms of rubber substrate and to estimate the contribution of each length scale on the hysteresis. Afterwards, the simulation results were compared with the friction experiment.

### 4.3.1 Material modelling

In the case of dynamic problems like sliding friction, the time dependent mechanical behavior of viscoelastic materials has a crucial impact on the accuracy of the FEM solution. A good material modelling is necessary to get an accurate friction prediction. In the present work, a linear viscoelastic material model based on the generalized Maxwell model was adopted (more details in sec. 0). The material parameters were determined fitting the mechanical behaviour of both quasi-static and dynamic tests (time and frequency domain). In particular, the stress-strain curves were measured under quasi-static conditions in three different strain modes. To skip the Mullins effect, the 5<sup>th</sup> cycle was selected and then the middle line of the hysteresis load/unload cycle was calculated as a reference for the characterization of the long-term material behaviour. In the appendix the fitting curves (with Yeoh model) were reported in the case of compounds H-CB40 and L-CB40. The fitting was optimized up to a maximum strain level of 60% ( $4^\circ$  amplitude), which matches with the maximum local strain expected during the sliding friction process. Several material models are used including New Hooke and Arruda Boyce. Yeoh model reveals the minimal error between the hyperelastic theory and the experiment in different strain modes (uniaxial, pure shear and biaxial see Table 7), despite the Neo-Hooke model in most cases turned out to be quite accurate. In case of the Yeoh model, the following parameters were used for H-CB40 and L-CB40 respectively:  $C_{10} = 0.580$ ,  $C_{20} = 0.0525$ ,  $C_{30} = 0.174$ ;  $C_{10} = 0.709$ ,  $C_{20} = -0.0879$ ,  $C_{30} = 0.0885$ . The compounds H-CB80 and L-

CB80 showed highly non-linear mechanical behaviour (i.e. higher stress softening and permanent set) and less accuracy of the fitting (Figure 109). The corresponding values are presented in Table 10.

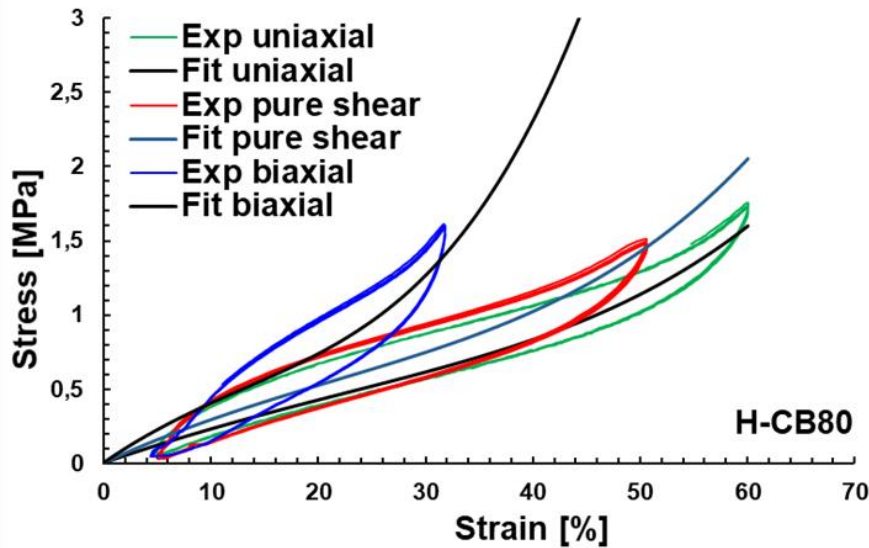


Figure 109. Fitting of the Yeoh model for the compound H-CB80 with the stress-strain curves measured in uniaxial, biaxial and pure shear at 20°C.

The highly filled materials exhibit higher stiffness (see the slope of the hysteresis cyclic loading-unloading loops) and hysteresis loss (area enclosed by the loading and unloading curves in the stress vs strain curve).

Table 10. Hyperelastic parameters (Yeoh model) for the compounds used in the investigation.

Compound	$C_{10}$	$C_{20}$	$C_{30}$
H-CB40	0.580	0.0525	0.174
L-CB40	0.709	-0.0879	0.0885
H-CB80	0.6188	-0.01639	0.1363
L-CB80	0.6330	-0.09482	0.1555

Figure 110 reports an example of the application of Dynamic Flocculation Model (DFM) to characterize the quasi-static mechanical behaviour of highly filled rubber (H-CB80). The model revealed its ability to catch hysteresis and stress softening effect in comparison to the standard hyperelastic model. This approach represents an interesting outlook of the rubber material modelling and friction simulations, which explains the effects of the deformation history on friction and wear behaviour and provides an improvement of the friction coefficient prediction in comparison with standard fitting methods. It is recommended in future work the implementation of the model in the FEM software.

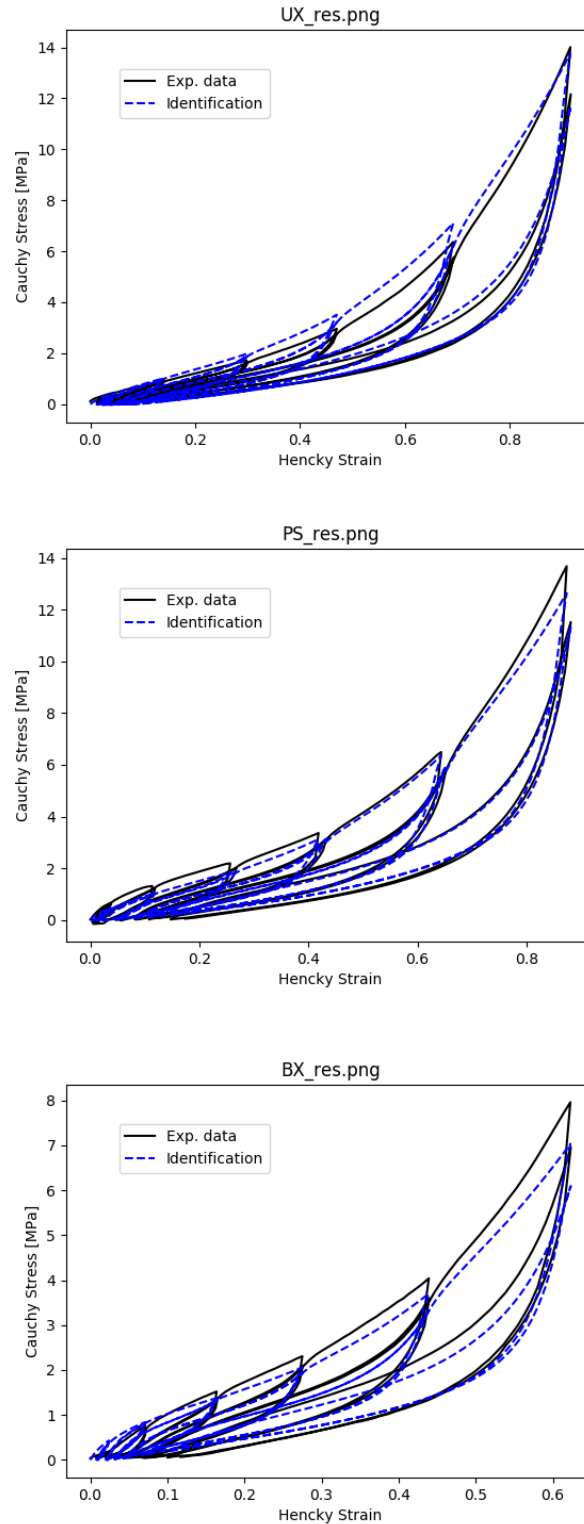


Figure 110. Uniaxial, pure shear and equi-biaxial multihysteresis measurements and corresponding fit with DFM model by considering a single set of parameters for the three strain modes,  $T = 20^{\circ}\text{C}$ , H-CB80.

Although the quasi-static behavior is relevant to capture the compound stiffness, the part which has the main influence on the friction behaviour, is the viscoelastic one. Based on the formulations

described in the theoretical section 2.9.3., it was determined the time-dependent behavior with the Prony series fitting of the dynamic moduli master curve in the frequency and time domains. This material characterization method was used for the friction simulation in ABAQUS. The fitting of the master curve was performed at high strain (2.5% strain) according to the limit of the testing equipment (ARES). The fit of the dynamic master curve in case of different compounds is shown in Figure 111. Depending on the compound, between 20 to 30 Maxwell elements were used for the fitting. The values of  $g_i$  and  $\tau_i$  are listed in the appendix (Table 18).

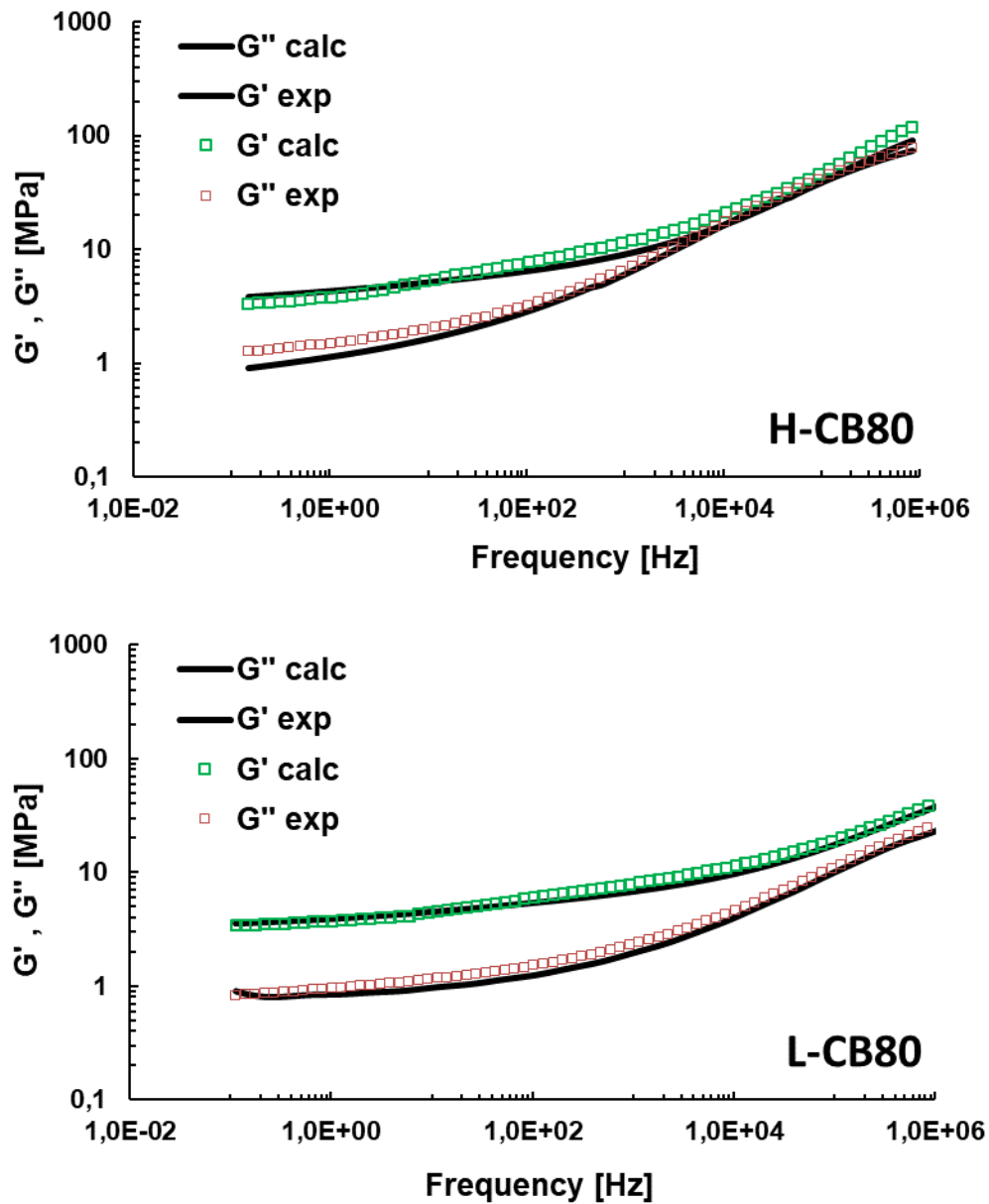


Figure 111. Comparison between the fitting Prony series and  $G'$ ,  $G''$  master curves for different compounds in the frequency domain. Reference temperature  $T=20^{\circ}\text{C}$ ; strain level  $\gamma=2.5\%$ .

The fitting showed a good prediction of the viscoelastic magnitudes  $G'$  and  $G''$  for the simpler mechanical materials (H-CB40 and L-CB40) whereas the fitting errors increased for highly filled compounds due to non-linear mechanical behaviour, especially at high strains (filler-induced stress softening).

A crosscheck between the strain response measured by a dynamic test equipment and the one simulated by FEM was performed to verify that the material models implemented in ABAQUS could reproduce the real material behaviour. More in detail, a rubber cube of 10 x 10 x 10 mm was tested under compression mode using Eplexor Gabo with 20 N preload and 30 N peak-to-peak dynamic load at different frequencies (1, 10 and 100 Hz see Figure 112). Afterwards, the measured stress-strain response of the material subjected to different deformations during the frequency sweep was compared with the FEM calculation.

Besides providing information about the accuracy of the material model, these simple tests allow better understanding of the complex mechanical behavior of rubbery materials and to reproduce similar load conditions expected in the friction experiment (see section 2.7.3).

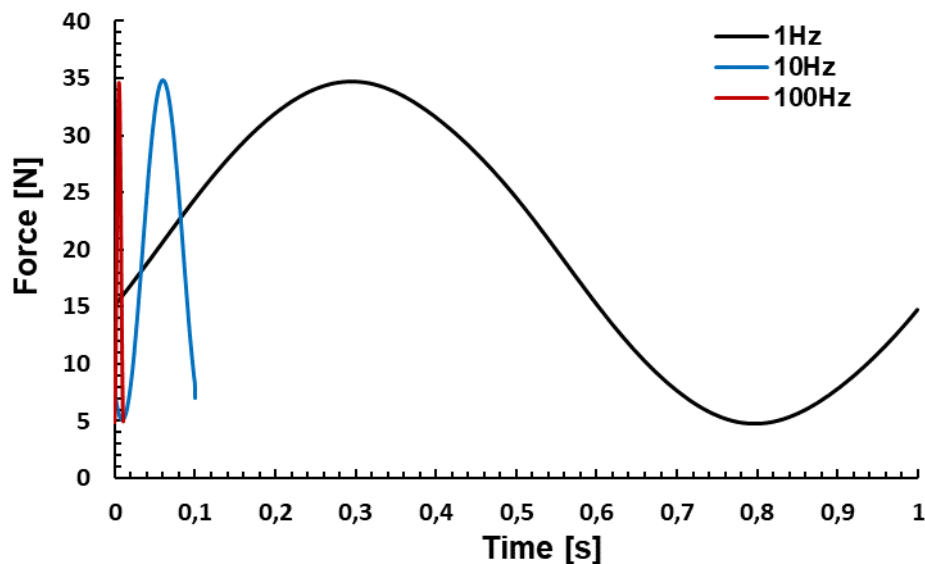


Figure 112. Dynamic test conditions (force control) given in input for GABO measurement. An example is illustrated for L-CB80.

Taking into account that all samples were subjected to the same dynamic load, the inclination angle of the loop (see Figure 113) represents the material stiffness while the region enclosed by the loop corresponds to the hysteresis loss. By increasing the excitation frequency, the stiffness response of the material increases as well as the hysteresis loss (according to the viscoelastic properties of the material  $G'$  and  $G''$ ).



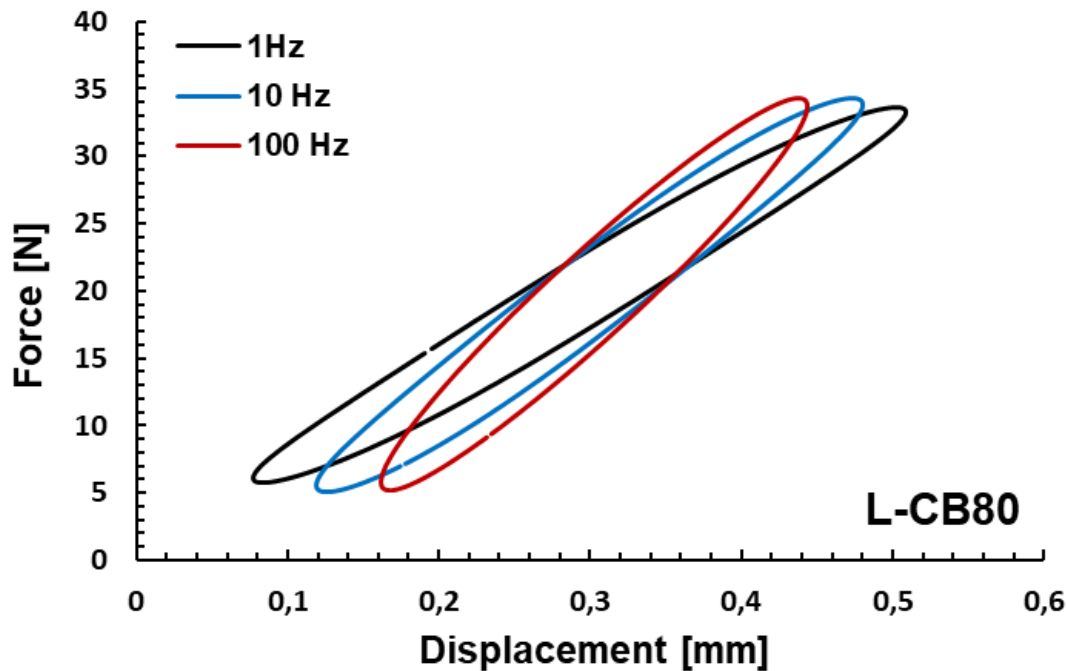
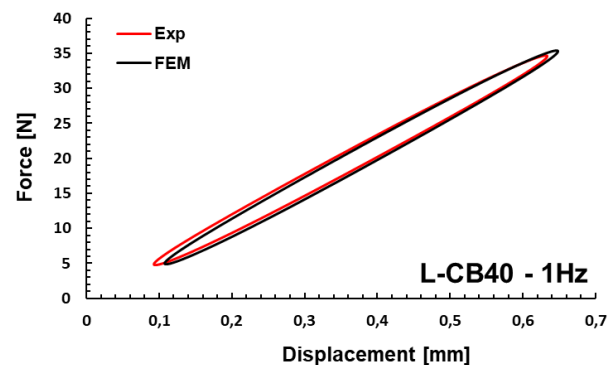
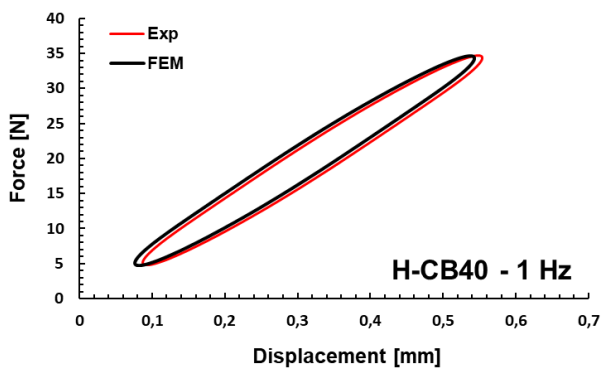


Figure 113. Force vs displacement response of the material L-CB80 under compression mode using Eplexor Gabo with 20 N preload and 30 N peak-to-peak dynamic load at different frequencies.

This means that, at 1 Hz of excitation frequency and 20°C of temperature, the samples H-CB40 showed lower stiffness and energy dissipation in comparison to the sample H-CB80 as expected (see the corresponding hysteresis loops in Figure 114). The experiment was simulated in ABAQUS to check the response of the material model used.

The standard modelling approach consists to adopt Yeoh model for long term behaviour and the Prony series model for the dynamic moduli master curves (frequency domain) representing the time dependent behaviour. The prediction showed a good agreement with the experiment results for materials with lower content of filler (H-CB40 and L-CB40) but a worst forecast in case of complex mechanical behaviour (H-CB80 and L-CB80).



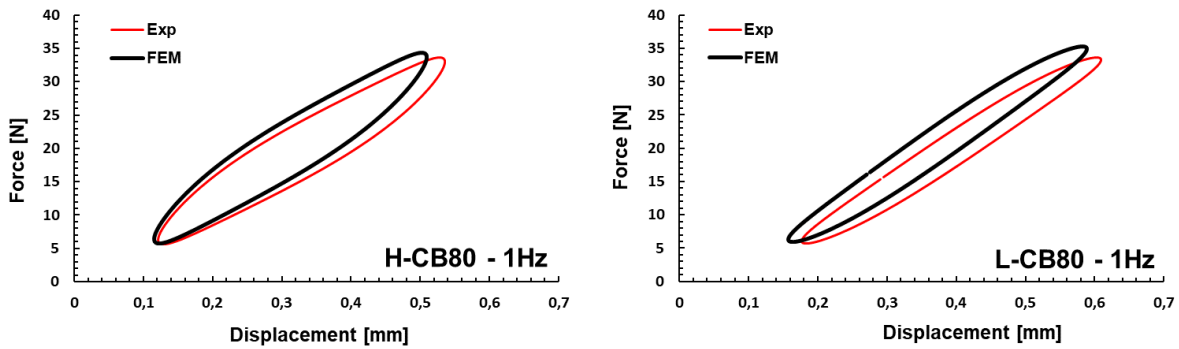


Figure 114. Force vs displacement response of the investigated materials (H-CB40, L-CB40, H-CB80 and L-CB80) and corresponding comparison with FEM simulation (standard approach).

Due to the inaccurate estimation, a new approach was selected to model viscoelasticity for the aforementioned complex materials (H-CB80 and L-CB80) in order to capture the mechanical behaviour at large strain and its dependence on temperature, frequency and history of deformation. Therefore, the Prony series parameters were adjusted considering the “new modelling approach” (fitting in the time domain) described in section 2.9.3. More in detail, the experiment to identify the material parameters consists of a multihysteresis test with dumbbells in uniaxial mode. First, five multihysteresis loading-unloading cycles up to 60% in tension and up to -20% in compression (precondition) were performed to induce the breakage and the recovery of filler network. Second, the stress relaxation tests at different constant strain levels were carried out. The measurement was repeated for several temperatures from  $-15^{\circ}\text{C}$ , very close to the glass transition of the rubber, up to  $60^{\circ}\text{C}$  in order to apply the time temperature superposition principle.

Figure 115 displays the fitting with the new modelling approach in the time domain based on the generalized Maxwell model applied to the aforementioned measurement procedure (at high strain).

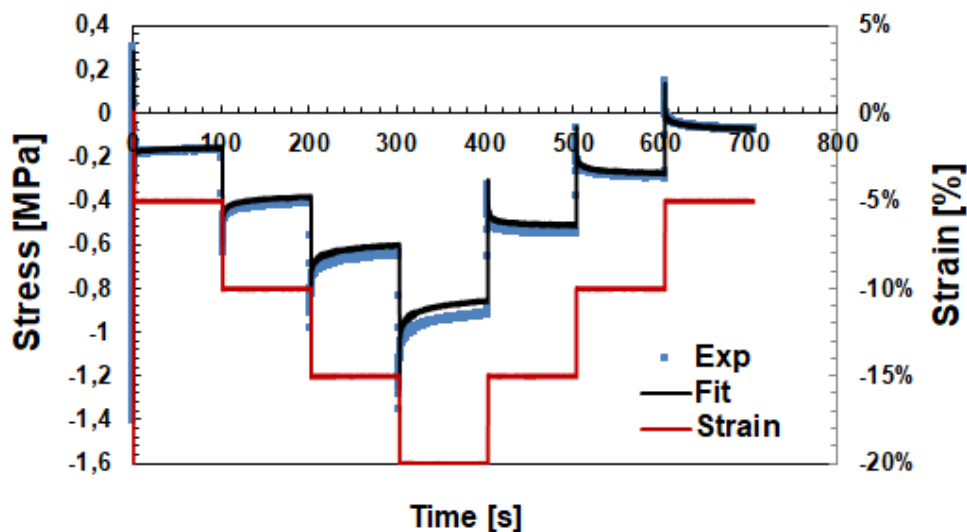


Figure 115. Fitting of the model in the time domain for H-CB80 at  $T=20^{\circ}\text{C}$ .

Afterwards, a second crosscheck was made between the experimental strain response and the one simulated by FEM with the updated model parameters (new modelling approach in the time domain) as portrayed in Figure 116.

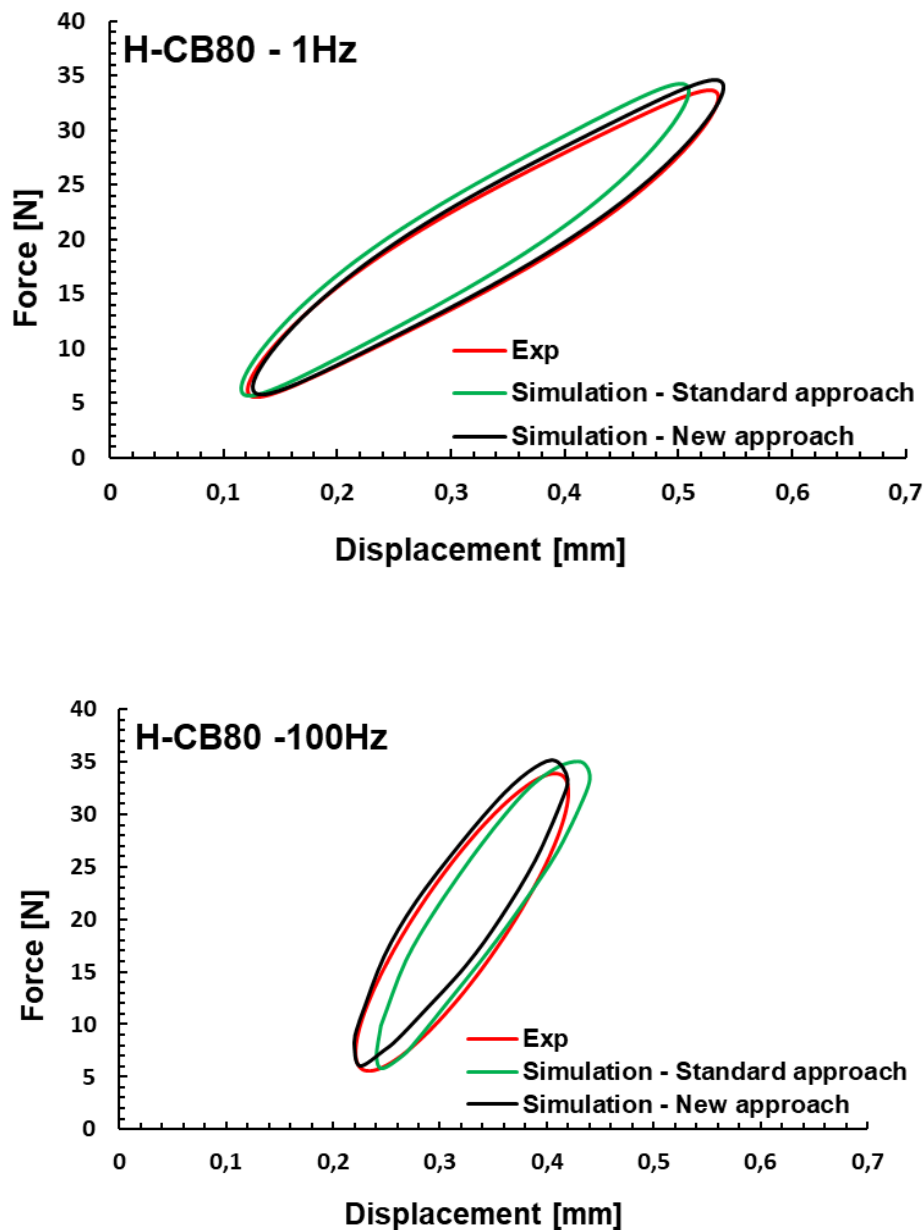


Figure 116. Comparison between the dynamic test (exp. depicted in red) and simulations (standard and new modelling approach depicted in green and black respectively) at different frequencies (a-1Hz; b-100Hz).

The experimental campaign with dumbbells in the uniaxial mode based on stress relaxation tests at different strain levels in tension and compression, captured the material response at high strain considering the history of deformation, this is recommended especially in case of highly filled compounds. This set of material parameters (see Table 18 reported in appendix) reveal a better prediction of the stiffness and energy dissipation in comparison to the previous set of parameters

(standard approach). Therefore, the new approach was considered as a material model reference to determine the prediction of the hysteresis friction reported in the following chapters.

The resulting stiffness and energy dissipation (hysteresis loss) of the two approaches were calculated from the force-displacement curves depicted in Figure 116. A comparison of the error estimation between the experiment and the simulation results is depicted in Figure 117. Besides of this mistake, it is also important to keep in mind that a linear viscoelastic model may not be adequate to predict the behaviour of rubber materials in every condition.

The material model predicts well the material behaviour with a maximum relative error less than 10% for stiffness and energy dissipation even in case of the materials with high content of filler. The fitting was less accurate at high frequency due to a more complex mechanical behaviour of the material (high strain and frequency). Similar results were obtained for “LTg” (lower glass transition temperature) material system. However, within the selected testing condition the error (less than 10%-15%) is acceptable.

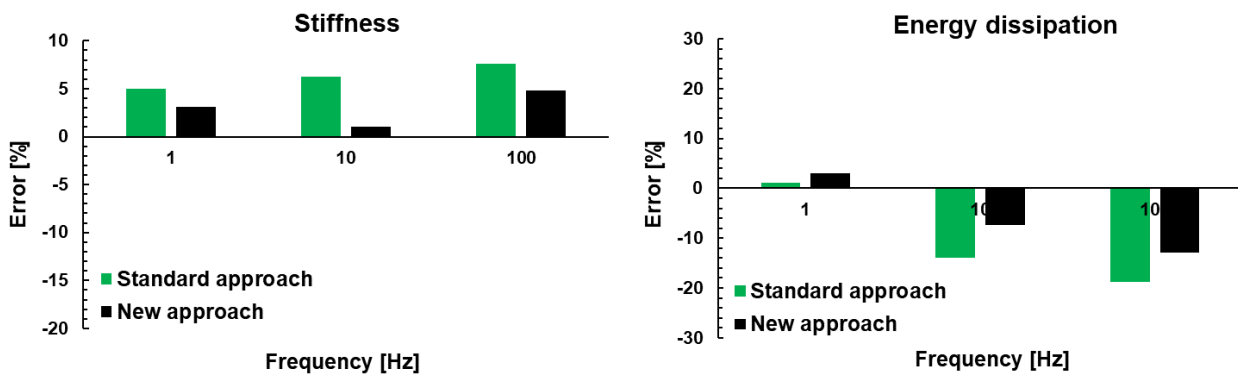


Figure 117. Error between the experiment (dynamic test in compression mode) and simulation predictions for complex mechanical material like H-CB80 at different excitation frequencies.

Another way to characterize the long term and time behaviour is the Plagge model (“PLM”) as described in chapter 2.9.3. An example regarding the potential of such model to reproduce the mechanical behaviour of highly filler material under dynamic conditions is reported below. The measurement was carried out in uniaxial tension-compression mode with a mechanical universal testing machine (MTS) with dumbbells sample. The test was composed by two stages, first the sample was held under the average strain of 5% for 60 seconds, second a frequency strain sweep was carried out (see Table 11).

Table 11. Frequency strain sweep to test the prediction capability of the Plagge model.

Temperature	Frequency	Dynamic strain	Average strain
20°C	1,10, 100 Hz	1%,2%,5%,10%,20%	5%

The material parameters were identified through a fitting procedure and afterwards passed to the ABAQUS FEM simulation via a subroutine (see Tab. 5). The same nomenclature of the Plagge et al. publication [140] was used.

Table 12. Material parameters of the the Plagge model in the case of uniaxial dynamic compression test of H-CB80 material.

Material parameters	
$G_C$ [MPa]	1.032
$G_e$ [MPa]	0.247
$\phi$	0.572
$\tau_0$ [s]	5.651
$\chi$	2.296
$n$	8.731
$\sigma_C$ [MPa]	0.078
$C$	1.110
$c_1$	0.586
$c_2$	7.80
$X_{max,0}$	500
$\gamma$	1.11
$K$ [MPa]	2500
$\beta$	4
$\alpha$	0.001
$T_0$ [K]	296

A rubber cube  $1 \times 1 \times 1 \text{ mm}^3$  was selected in the FEM model instead of the dumbbells geometry based on the assumption of a uniform strain distribution in the sample during uniaxial dynamic compression test. The experimental strain was given as input (see Figure 118 top), afterwards the measured Cauchy stress was compared with the simulated one extrapolated from FEM (see Figure 118 bottom).

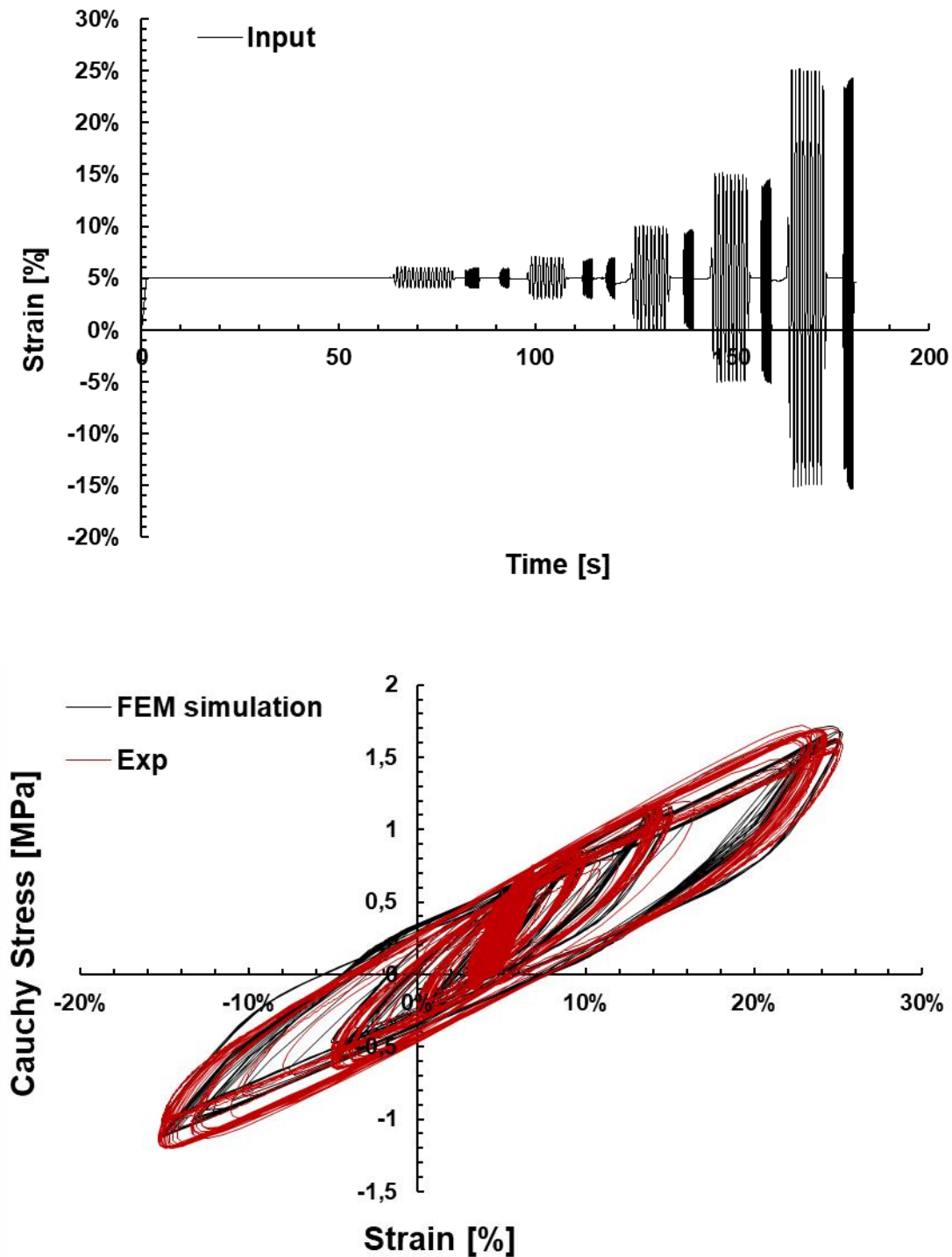


Figure 118. Strain input signal (top) of uniaxial dynamic compression test and the comparison between experimental stress and the simulated one (bottom). H-CB80, T=20°C.

The model showed good capability to catch the complex mechanical behaviour beyond the linear regime under quasi-static and dynamic conditions. The feasibility of the Plagge model was tested to reproduce the energy dissipation and stiffness of the rubber cube tested under compression mode using Eplexor Gabo at different frequencies (1, 10 and 100 Hz) as shown previously in the case of other material models. A subroutine based on the Plagge model was implemented in ABAQUS, the comparison between the experimental and simulated hysteresis loop is reported in Figure 119. The model showed promising results and could be used in the FEM friction simulations for future works.

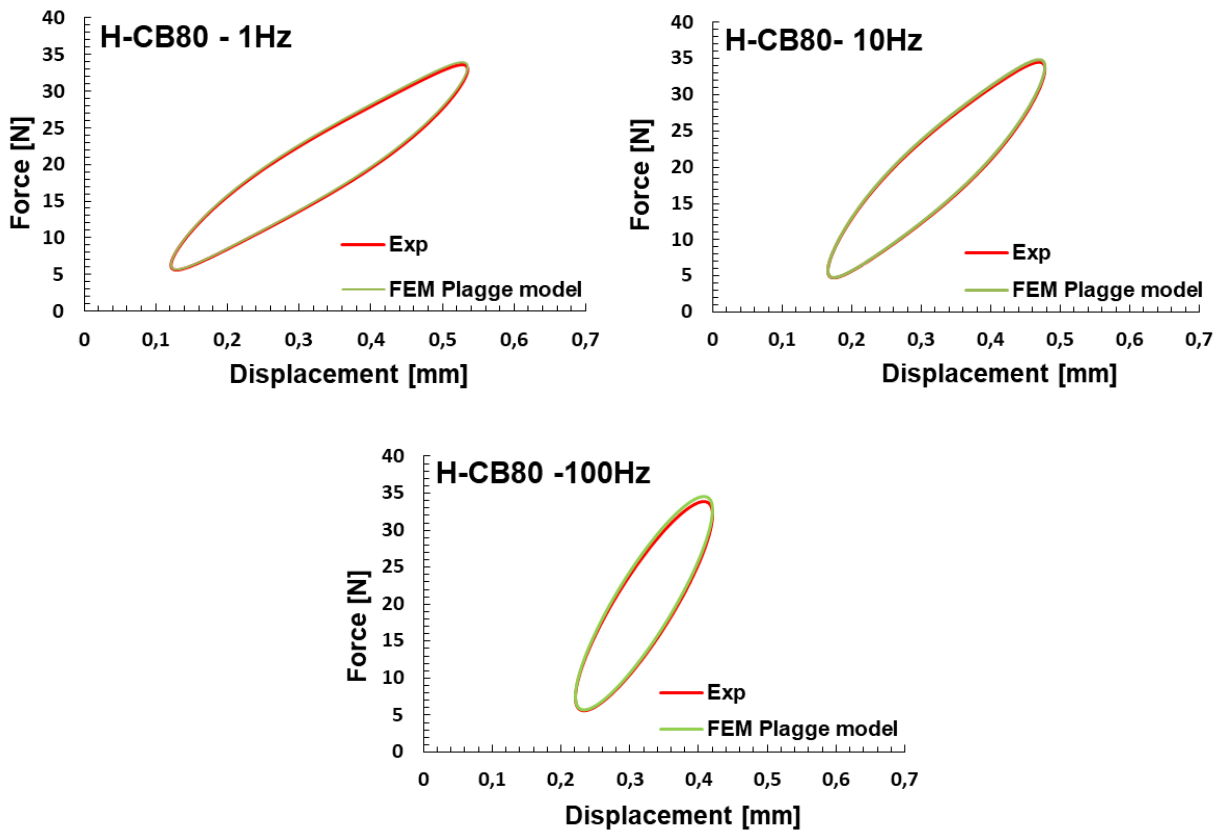


Figure 119. Comparison between the dynamic test (exp. depicted in red) and the simulations (Plagge model depicted in green) at different frequencies (a-1Hz; b-10Hz; c-100Hz).

### 4.3.2 Simulation results for model surfaces

FEM simulations were performed in a commercial software named ABAQUS to reproduce friction experiments and to investigate the hysteresis as a result of the pulsating forces induced by the surface asperities and the contribution generated from each substrate length scale. For this purpose a 2D FEM model was developed, based on the measurement set-up features for model surfaces. In particular, the multi indenter, used as substrate for the friction tests, was modelled as an analytical rigid body, reproducing the same geometry of the manufactured component. The rubber specimen was modelled as a deformable viscoelastic material, consisting of plain stress solid quadratic quadrilateral elements of type CPS8R (Figure 120). The friction problem was designed in two steps: first, the sample was pushed against the indenter with the same pressure applied in case of the experiment. Second, the substrate was horizontally moved at a constant velocity and the sample was set free to move only in the vertical direction. The normal load was constantly acting as a boundary condition on the rubber specimen. In order to isolate the hysteretic contribution, a frictionless interaction was set between the two surfaces in contact. The simulation was performed under isothermal conditions, without taking into consideration a possible heat generation induced by energy dissipation within the sample.

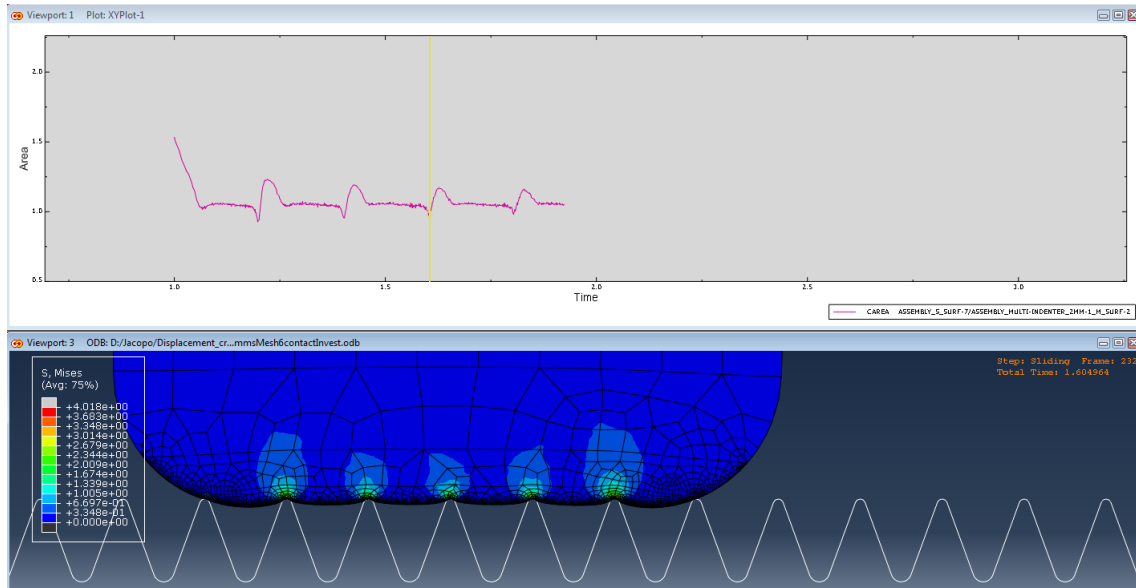


Figure 120. Sketch of the 2D FEM model, with a magnification near the contact substrate-rubber, used to calculate the friction values for the multi-indenter FEM. An example of the real contact area during sliding over time (top) and the stress distribution along the rubber block (bottom) is depicted.

It is important to remark that the tangential interactions are not active between the sliding surfaces, thus the friction value comes from the counteraction exerted by the viscoelastic matrix when it is pushed by the asperities. The hysteretic friction coefficient was determined based on energetic considerations. In the case of sinusoidal multi-indenter Eq. (107) allows to calculate  $\mu_H$  by considering the dissipated energy and the sliding distance, more precisely, the number of indentations:

$$\mu_H = \frac{1}{F_N} \frac{E_{diss}}{n\lambda_0} = \frac{1}{60N} \frac{580mJ}{13 * 2mm} = 0.3717 \quad (107)$$

The friction coefficient was calculated for different velocities and model compounds and afterwards, compared with the measurements. First, the FEM estimation of each roughness length scale (macro + micro) contribution of the sinusoidal multi-indenter was done, followed by the superposition of the aforementioned contribution. Finally a comparison of the results with the experiment was performed. The substrate profile was defined as the superposition of two sinusoidal waves (see Figure 121 macro:  $h=2mm$ ,  $\lambda=2mm$ ,  $R=210 \mu m$  and micro:  $h=8\mu m$ ,  $\lambda=20 \mu m$ ).

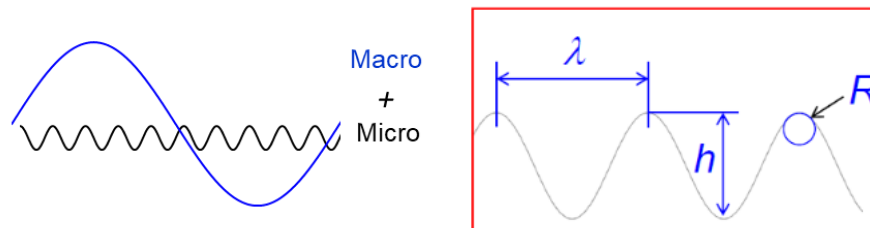


Figure 121. Multi-indenter sinusoidal profile represented as a superposition of two sinusoidal waves (macro+micro).



Figure 122 depicts the result of the FEM simulation and the corresponding comparison with the experiment for compounds H-CB40 and L-CB40.

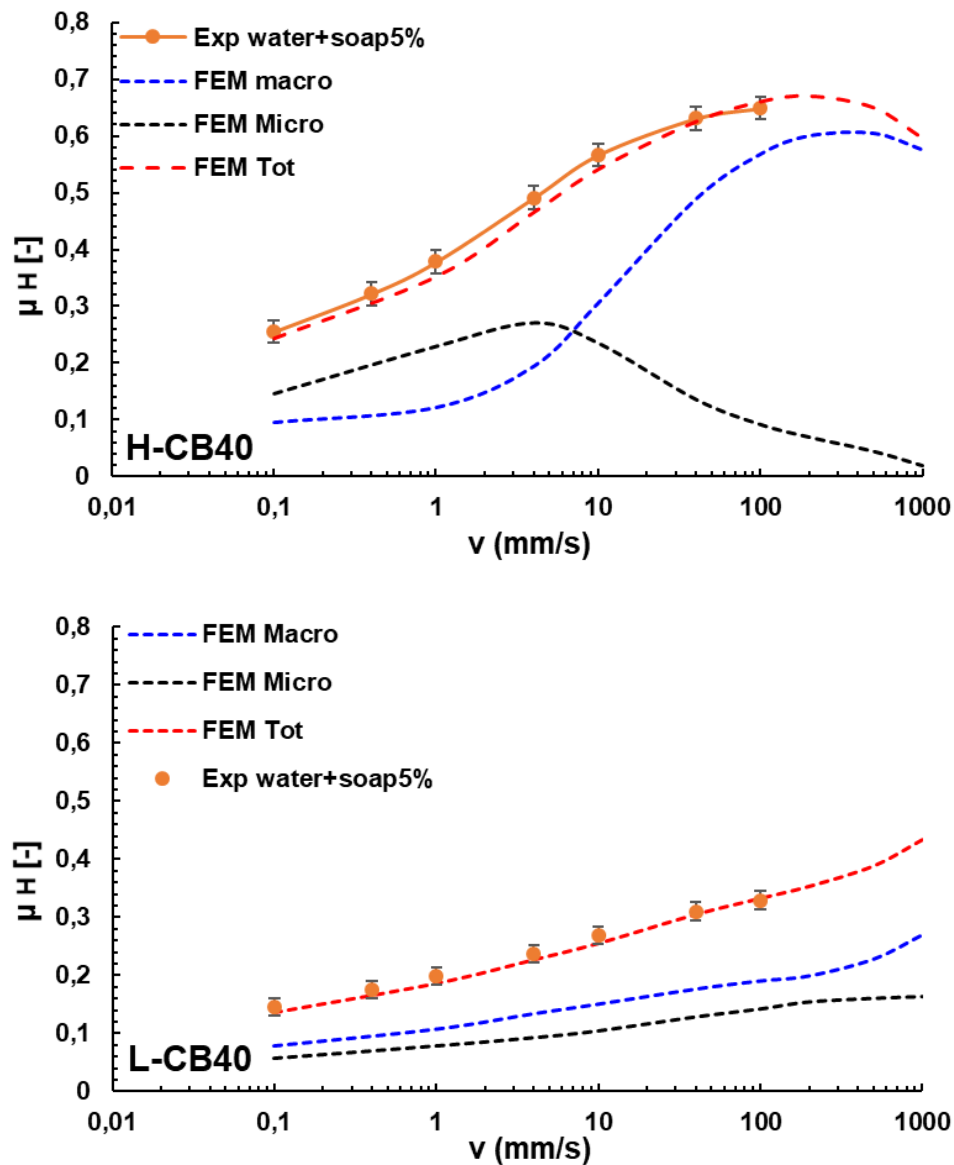


Figure 122. Comparison between the measured friction and FEM simulation hysteresis friction for compound H-CB40 (top) and L-CB40 (bottom) at 20°C and 0.26MPa nominal pressure. Multi-indenter 2mm used as substrate.

The total hysteresis contribution was obtained through the superposition of two length scales, a macro one with a wavelength of 2mm and a micro one with a wavelength of 20  $\mu\text{m}$  depicted in blue and black respectively. The graphs below displays the hysteretic simulation results for low content of carbon black on the left and high content of filler on the right.

The macrotexture is in general dominant compared to the microtexture, however, the latter plays a relevant role at low speeds ( $<10\text{mm/s}$ ) and is responsible for high local strains contributing significantly to the global response. The FEM simulations confirm the hysteresis friction is matching over a broad range of sliding speeds with the experimental condition water plus a small amount of soap as confirmed in the analytical models [77] [41]. The lubricant used in the friction tests, composed

of water and a small amount of soap, permits to isolate quite well the hysteresis contribution. The low surface tension of the lubricant mixture leads to a separation of the rough surface and rubber bulk to eliminate the adhesion contribution.

H-CB40 showed higher friction values and a hysteresis peaks in comparison to L-CB40 since the testing temperature is  $T=20^{\circ}\text{C}$ , this results reflect the behaviour of the loss modulus  $G''$ . To capture the hysteresis peak even for L-CB40, a lower temperature (i.e.  $2^{\circ}\text{C}$ ) must be measured, in other words, shifting the viscoelastic master curve towards lower temperatures (higher frequencies) (Figure 123).

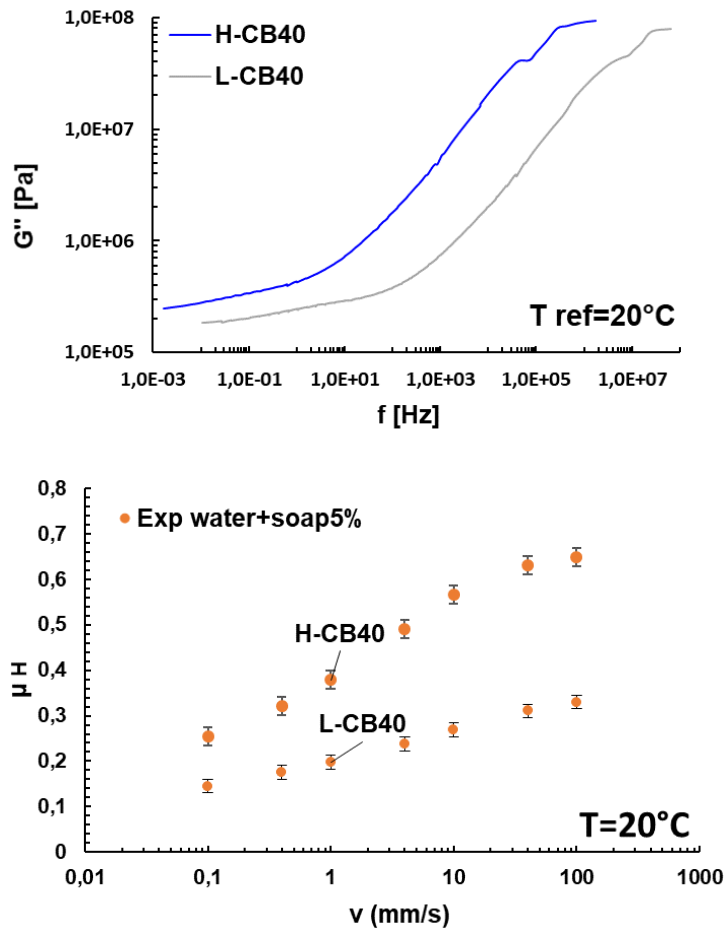


Figure 123. Loss modulus  $G''$  master curve at  $T=20^{\circ}\text{C}$  for H-CB40 and L-CB40 and the corresponding friction test on multi-indenter.

Figure 124 reports the simulation results for highly filled materials. First, the standard approach (Yeoh+Prony frequency domain at low strain 2.5%, see Figure 109 and Figure 111) was adopted for the parameters identification in case of low filled compound (H-CB40 and L-CB40). Second, the approach based on Yeoh+Prony time domain at high strain (see Figure 115) was used due to the mismatch of the experimental friction values obtained with the first approach in case of high filled materials (L-CB80 and H-CB80).

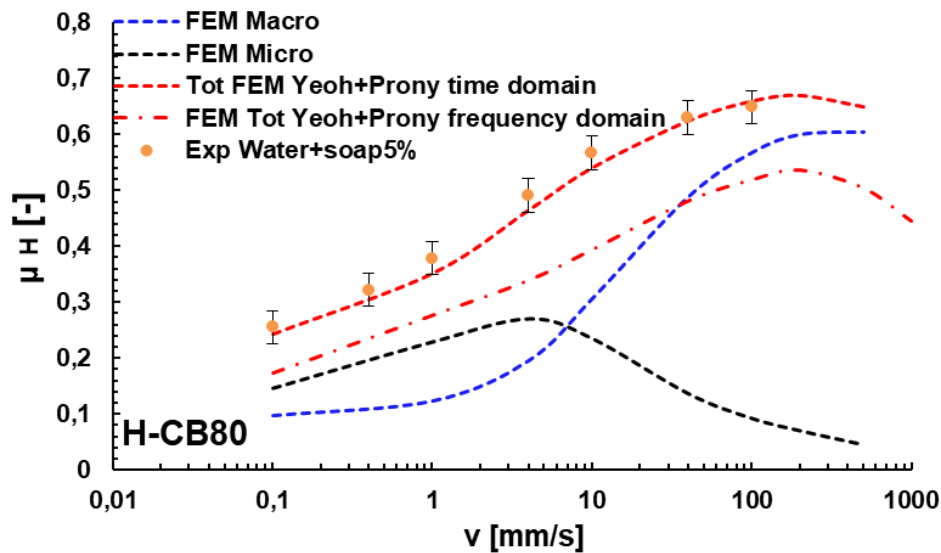


Figure 124. Comparison between the measured friction and FEM simulations hysteresis friction (two approaches) for compound H-CB80 at 20°C and 0.26 MPa nominal pressure. Multi-indenter substrate.

The second set of material parameters (characterization in the time domain) showed better prediction of the friction experiment campaign since the reproduction of the material mechanical response is more accurate at high strains, similar to the deformation levels occurring locally in the friction contact substrate/rubber.

Therefore, the same approach was adopted to model the viscoelasticity of the highly filled compound L-CB80. The friction simulation result is shown in Figure 125.

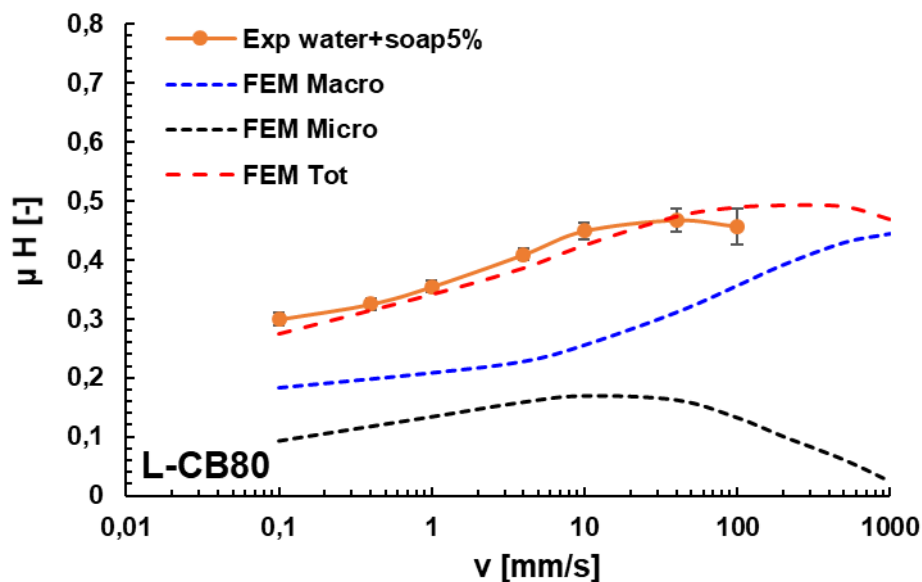


Figure 125. Comparison between the measured friction and FEM simulation hysteresis friction for compound L-CB80 at 20°C and 0.26 MPa nominal pressure. Multi-indenter substrate.

Low speeds were chosen to minimize the friction heating. Such result demonstrates that FEM analysis is a good tool to describe the phenomenology of the friction interaction to estimate the individual

contribution of each length scale. Nevertheless, a realistic estimation of the friction properties for every kind of rubber compound is still challenging and strong dependent to many other variables such deformation rate and history of deformation.

### 4.3.3 Simulation results for real rough surfaces

Based on the agreement shown in the previous section between FEM simulations and friction measurements over sinusoidal surfaces, FEM simulations were also performed for rough surfaces and compared to the lubricated friction test (water plus soap mixture). The accuracy of the FEM simulations was validated in the case of complex surface textures. For this purpose, the same model used for sinusoidal surfaces was adopted by considering a rough profile as a rigid substrate. The surface profile of the complex textures was imported in ABAQUS by using the raw data points measured with the white light interferometer microscopy instead of the CAD design used in the case of model surface (see Figure 126).

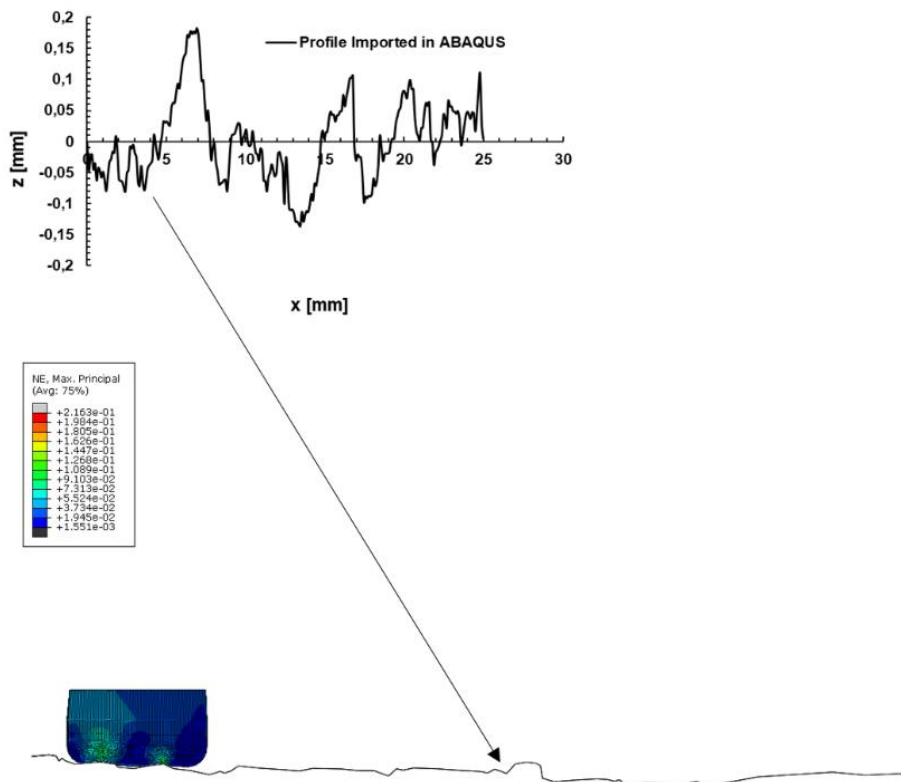


Figure 126. Magnification of the granite profile measured by white light interferometer imported in ABAQUS software for the FEM simulation (up). Visualization of the deformation occurring in the sample on different length scales. Compound H-CB40 sliding at 100 mm/s over the fine granite (bottom).

The investigation on the model sinusoidal surfaces showed that hysteresis friction was strongly affected by the roughness spectra of the substrate where the rubber is sliding. In particular, the more scales are present, the more affected was the resulting friction curve. The white light measurements were performed by using a lateral resolution of 0.5  $\mu\text{m}$  and a vertical one of 0.2  $\mu\text{m}$ . A profile in the middle of the sliding zone was selected as a representation of the surface. 2D FEM simulations were

performed using a representative line scan of the substrate with a two-dimensional approach. The deformation level and the resulting hysteresis occur on different length scales during the rubber sliding on these surfaces, an example is illustrated in Figure 126 for compound H-CB40 in case of the fine granite surface at 100 mm/s. In case of compound H-CB40 the hysteresis friction coefficient was calculated in the ABAQUS environment for both rough surfaces (fine and rough). The same compound was tested on dry, water and water+soap5% granite with the linear friction equipment at 0.26MPa nominal pressure and 20°C temperature. Figure 127 compares the 2D FEM simulations for fine and rough granites with the experiment data. A good prediction of pure hysteresis friction was achieved.

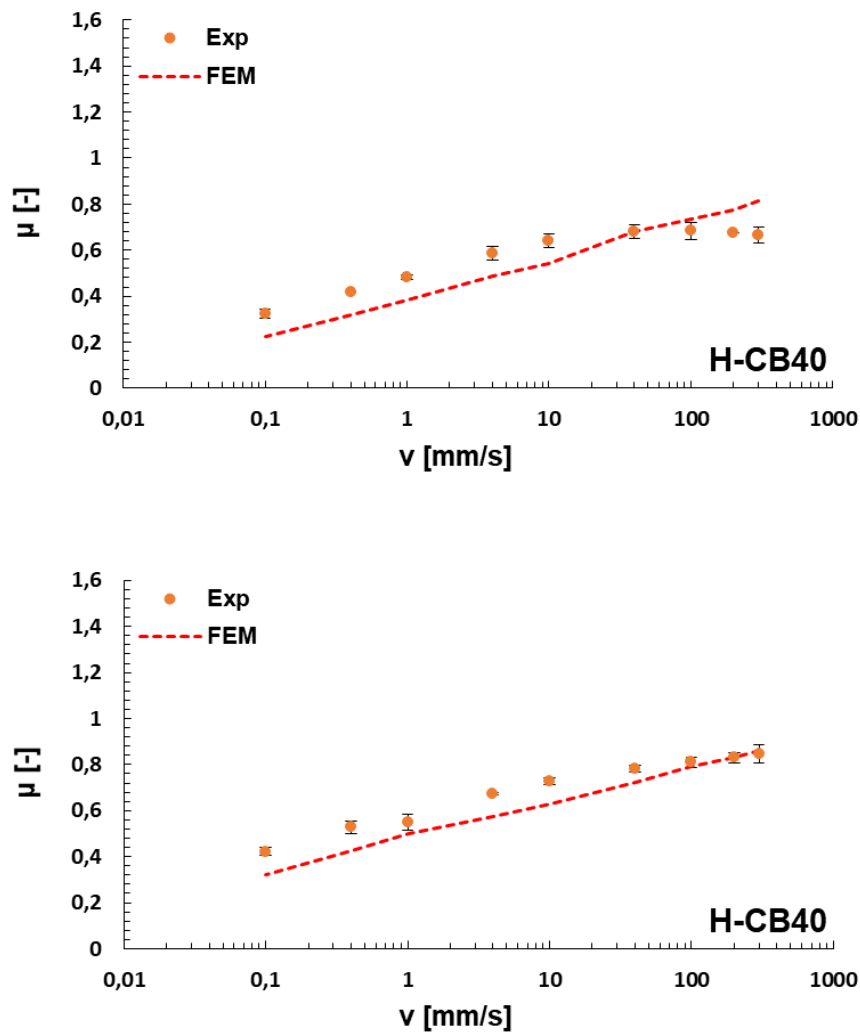


Figure 127. Comparison between the measured friction (water+soap5%) and FEM simulation hysteresis friction for compound H-CB40 for fine granite (top) and rough granite (bottom) at 20°C and 0.26MPa nominal pressure.

### 4.3.4 Dependence of the friction on rubber geometry

Another important purpose of this research was to optimize the friction coefficient concerning the rubber geometry and material properties. This section explains how the dynamic contact mechanics affect the friction on a rough substrate. The roughness was kept constant (fine granite surface), the rubber geometry and properties were systematically varied.

Several factors were investigated to figure out the combined effects of the geometry and material that occur in wet and dry friction. An overview of the geometrical factors studied is displayed in Figure 128.

- Systematic variation of the ratio length/width ( $L/W$ ) of the rubber block keeping constant the nominal area  $A_0$  and the radius  $R_{\text{sample}}$  in the rubber edges (Figure 128).
- The geometry effect was combined with different material stiffness  $G'$ , loss modulus  $G''$  and Mullins effect.
- The occurrence of the thermal effect during sliding friction (the so-called heat build-up, HBU) was investigated.

The height of the sample is set constant because the hysteresis contribution comes from the ultimate rubber layer in contact with the substrate, which is less than 1 millimeter.

The study of the first geometry effect at the rubber corner sample called edge effect, is depicted below. Friction tests were carried out in water+soap5%, water and dry conditions by considering two samples which have the same nominal area, one with radius in the corner equal to  $R_{\text{sample}}=2.5$  mm, and the other one without radius ( $R=0$ ) that reflects a sharp edge (see Figure 128).

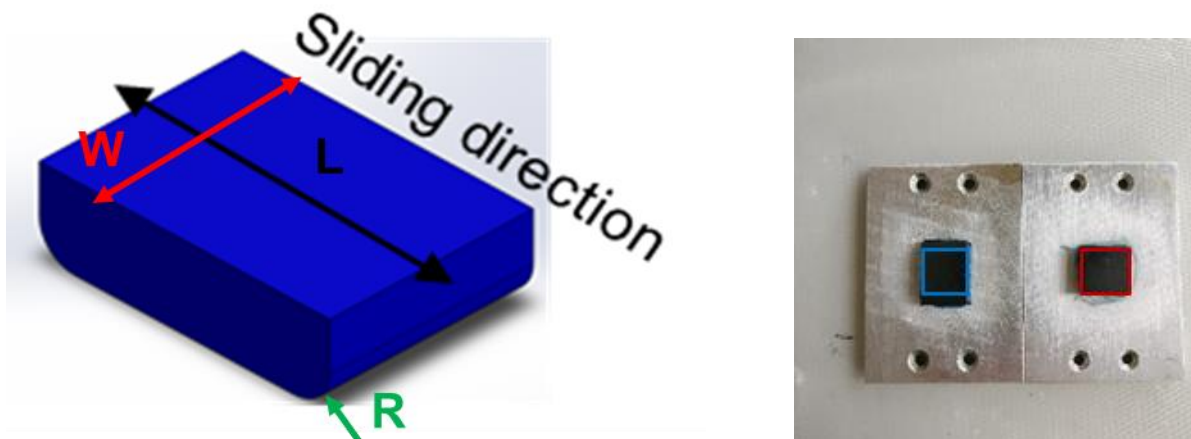


Figure 128. Selection of two rubber geometries for the friction investigation: with/without radius  $R_{\text{sample}}$  at the sample edges.

The results are illustrated in Figure 129. In dry and lubricated conditions higher friction was obtained in the case of sample with radius since the higher real contact area (peel back effect suppressed in the case of sample with radius, see Figure 130) and more uniform pressure distribution (the parts of the rubber surface with high contact pressure are trimmed back, since the contact pressure at those points will diminish).

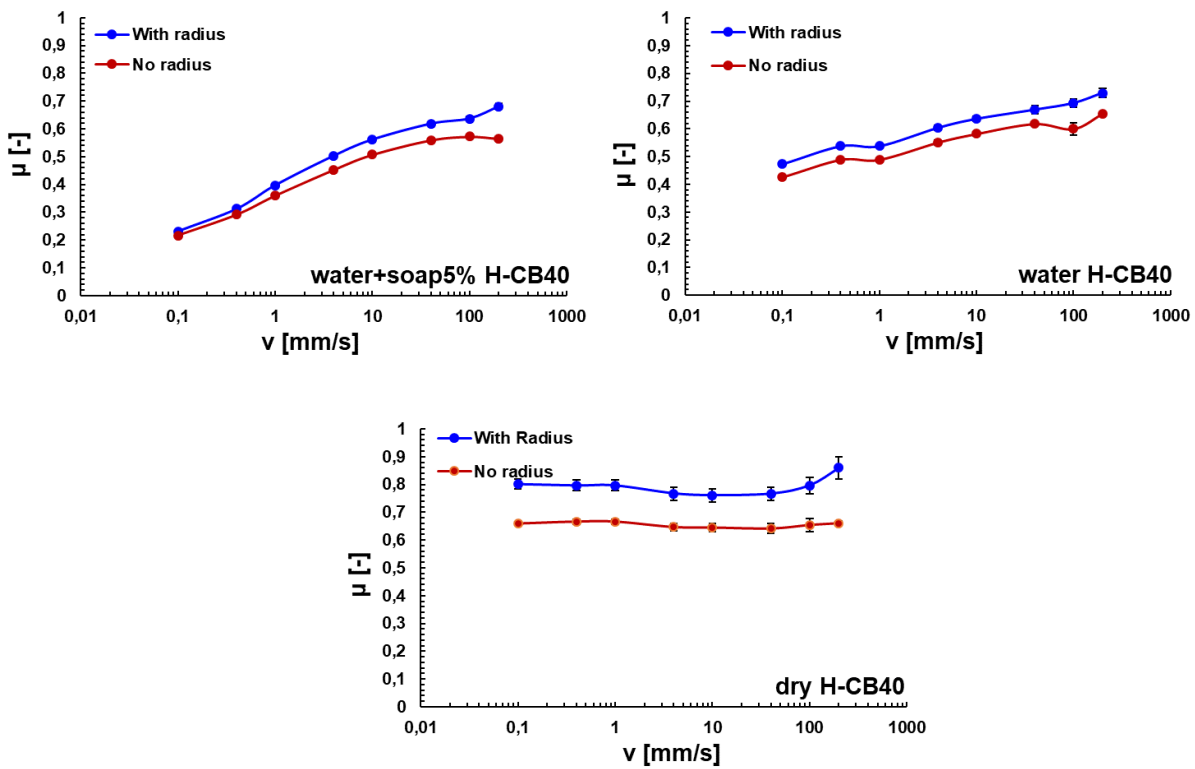


Figure 129. Friction test campaign considering two rubber sample geometries: with/without radius ( $R=0$ ) at the sample edges.  $T=20^{\circ}\text{C}$  and  $p=0.26\text{MPa}$ .

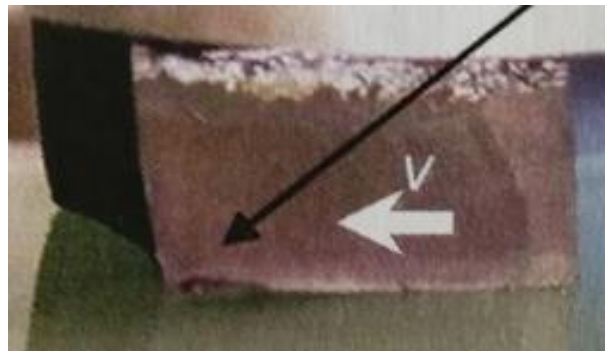


Figure 130. Peel back effect at the block edges in the case of geometry without radius, which suffers consequently, a decrease of contact area. Results in agreement with [159].

The  $\Delta\mu = \frac{\mu_{with R} - \mu_{no R}}{\mu_{with R}}$  value between the two different geometries and materials (H-CB40 and H-CB80) is reported in Figure 131.

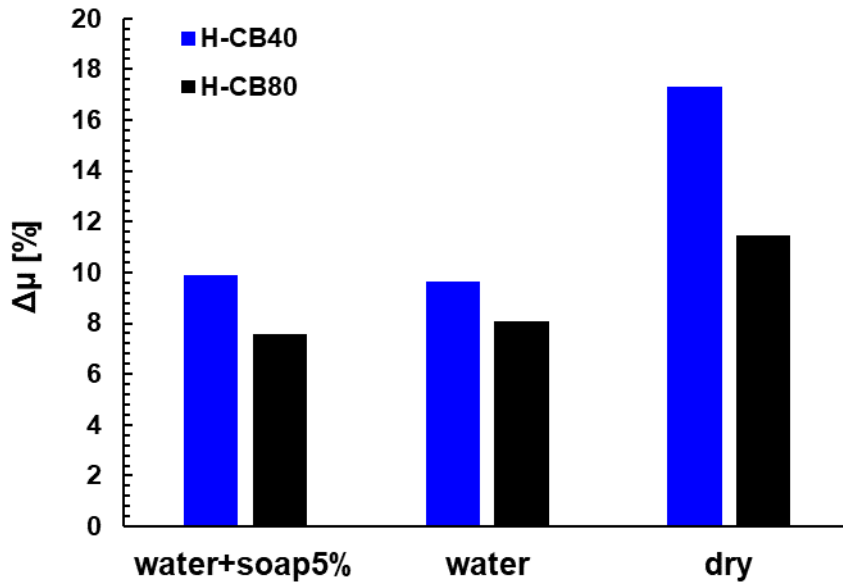


Figure 131. Calculation of  $\Delta\mu$  between with/without radius at the rubber edges on water+soap5%, water and dry conditions for H-CB40 and H-CB80.  $v=10\text{mm/s}$  and  $p=0.26\text{ MPa}$ .

The edge effect is almost constant in the lubricated condition (wat+soap5% and water) but increases significantly under dry condition and is more pronounced for softer material (H-CB40). The second geometry rubber effect referred to the ratio between the length  $L$  and width  $W$  was studied. The sample geometry with three different ratios  $L/W$  from 0.5 to 3.7 is depicted in Figure 132. Friction tests were performed on fine granite for water+soap5% condition, in order to get a condition close to pure hysteresis. The same rubber sample was used for the water and dry friction test (see Figure 133).

The friction coefficient decreased with the ratio  $L/W$  for the sliding speed range investigated in the case of water+soap5% since the edge effect reduced with  $L/W$ . Water and dry conditions did not show a clear trend due to the occurrence of adhesion and temperature effects as explained later on.

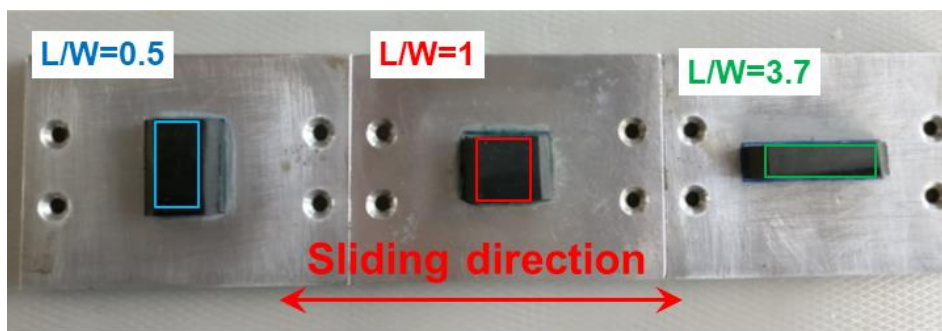


Figure 132. Selection of the three geometries: left:  $L/W=0.5$ ; middle:  $L/W=1$ ; right:  $L/W=3.7$ .



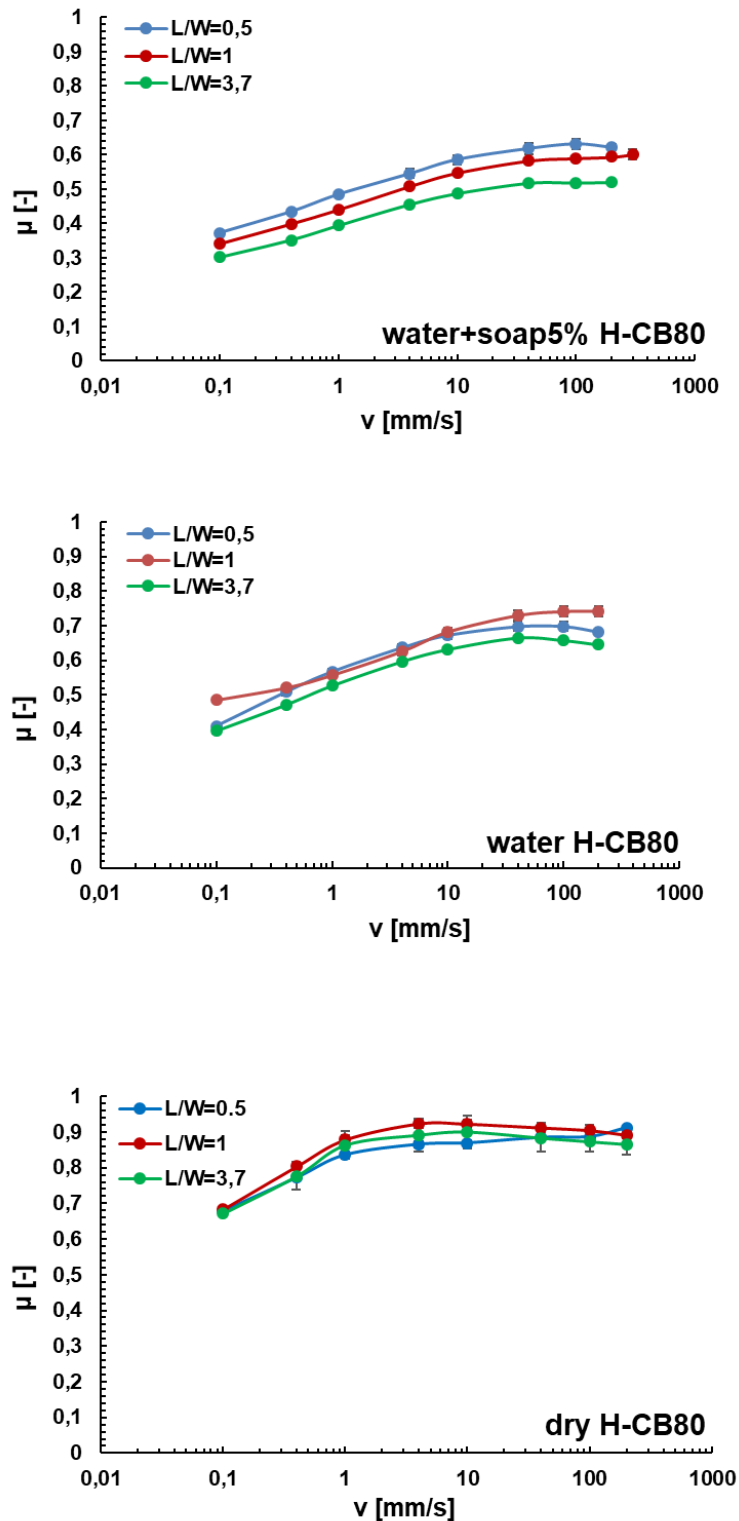


Figure 133. Friction test campaign on wet (top and middle)/dry (bottom) fine granite in the case of different rubber block geometries. H-CB80,  $T=20^{\circ}\text{C}$ ,  $p=0.26\text{MPa}$ .

By applying higher nominal forces, higher friction was obtained by decreasing  $L/W$  in the case of water+soap5%, nevertheless the geometry effect was less pronounced with the nominal pressure as depicted in Figure 134.

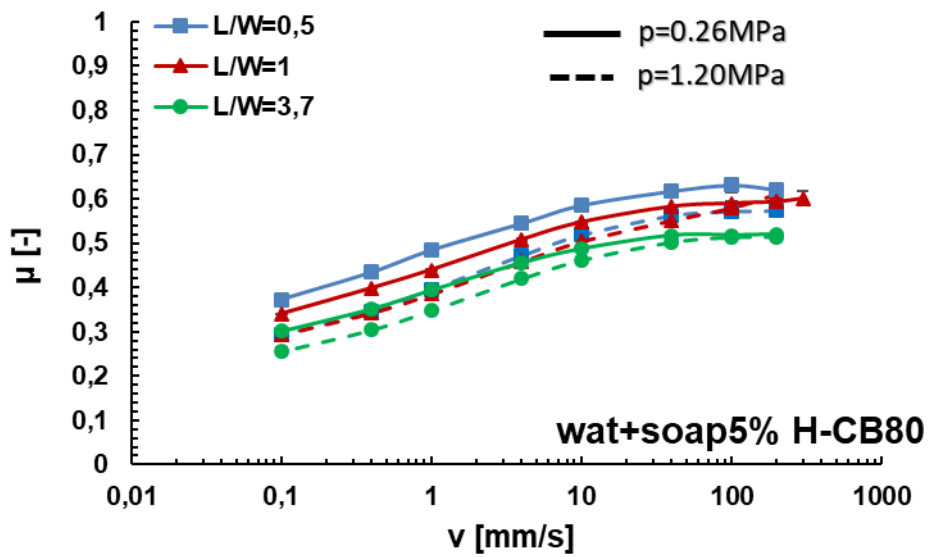


Figure 134. Pressure dependence of friction on water+soap5% fine granite in the case of different rubber block geometries. H-CB80, T=20°C.

Therefore, the presented mechanism was investigated through 3d FEM friction simulations by considering the material H-CB80 in different ratios L/W. The set-up is shown in Figure 135. The rubber was modelled as a 3d deformable-body whereas the 2d granite surface was imported from CAD software.

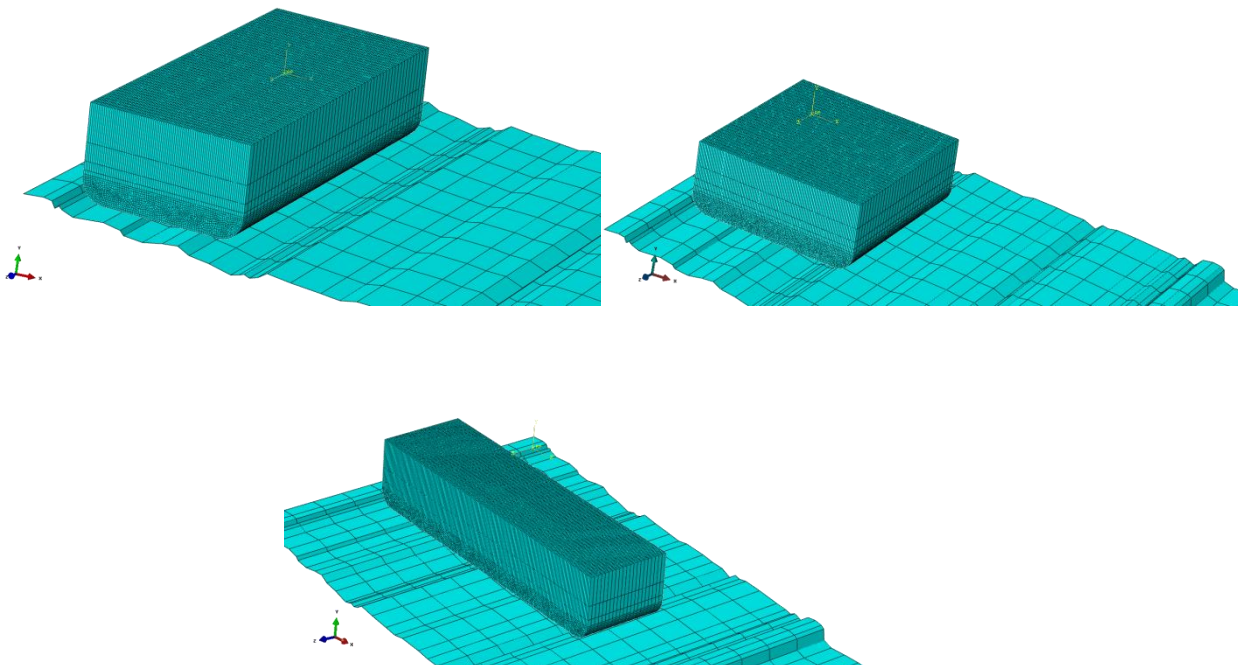


Figure 135. 3D FEM set up: three different rubber block geometries (deformable body) sliding on granite (2D rigid body).

The simulations confirmed the increment of friction by reducing the ratio L/W due to higher energy dissipation coming from the rubber edges while they go in contact with the asperities as depicted in Figure 136 for H-CB40 and H-CB80.

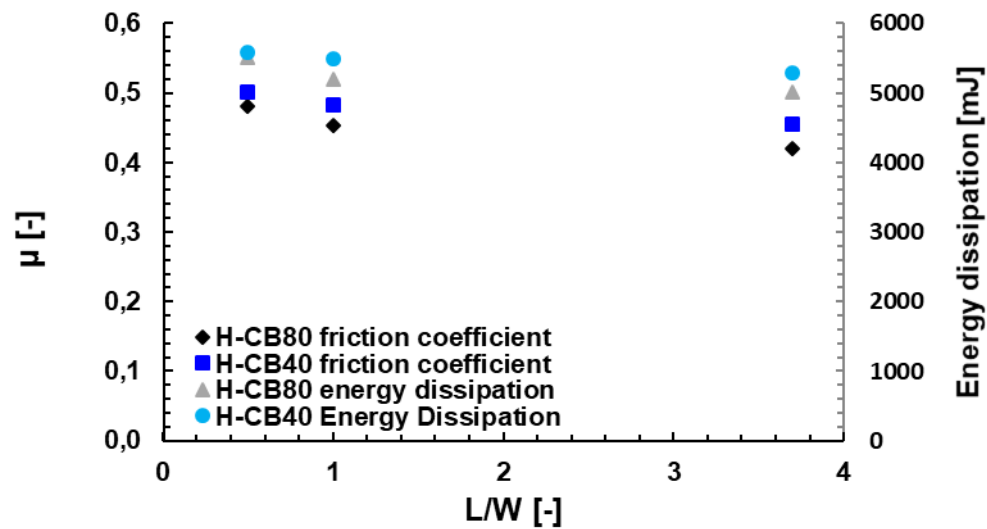


Figure 136. L/W dependence of the simulated friction coefficient (primary axis) and the energy dissipation (secondary axis) for H-CB40 and H-CB80 materials.

The result can be explained by considering the rubber block splits in three sections leading, trailing and middle as reported in Figure 137. The leading edge is the part of rubber that hits the road first as the tire slides (or rotates) whereas the trailing edge is the last part of the footprint coming in contact with the road surface.

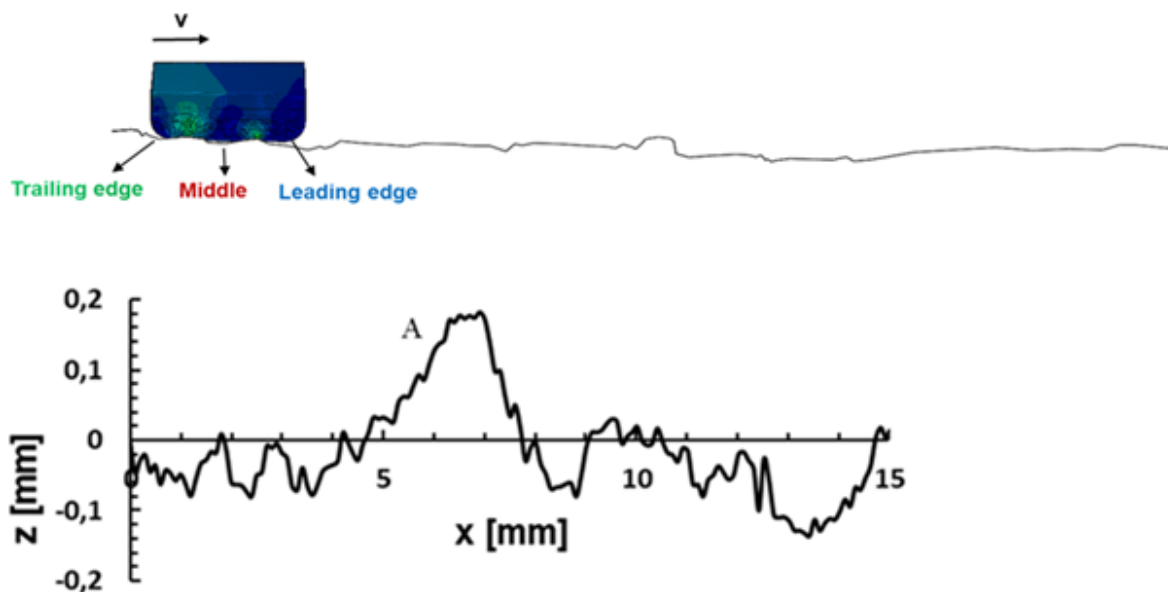


Figure 137. 2D front view of 3D FEM sliding friction simulation. A split of the rubber block in three volume sections are considered: Leading edge, middle and trailing edge (up). Substrate profile of the fine granite imported in ABAQUS for the FEM simulation. The macro and micro asperities are responsible for the high local deformation of the rubber induced by dynamic contact process (bottom).

The energy dissipated due to viscoelasticity was extrapolated in the three aforementioned sections from the field output in the ABAQUS software (the so-called CENER in  $\text{mJ}/\text{mm}^3$ ), as portrayed in Figure 138. Furthermore, the energy dissipated in the leading edge normalized to the total energy dissipated (sum of the three-volume sections) was higher in the case of  $L/W=0.5$  geometry due to a prominent edge effect which produces higher hysteresis.

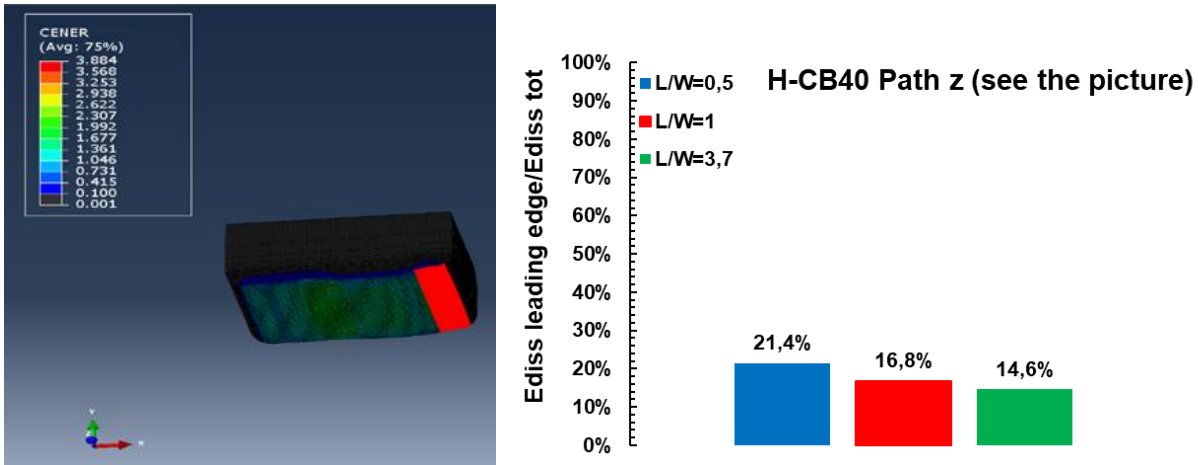


Figure 138. Energy dissipated by viscoelasticity (CENER) extrapolated from ABAQUS in the ultimate layer of rubber in contact with the road surface in the case of  $L/W=3,7$  geometry (left). Energy dissipated in the leading edge normalized to the total energy dissipated, that is sum of leading edge, middle, trailing edge in the case of the three rubber block geometries selected ( $L/W=0,5$ ,  $L/W=1$ ,  $L/W=3,7$ ) (right). Material: H-CB40  $T=20^\circ\text{C}$ , substrate: fine granite, sliding speed  $v=10\text{mm/s}$ .

In fact, the hysteresis friction is a result of two frequency dependence effects: (i) hysteresis ( $G''$ ) and (ii) indentation volume  $V$ , which is inversely proportional to the stiffness of rubber ( $V \sim \frac{1}{G'}$ ). Therefore, materials with different viscoelastic properties were selected to investigate the combined geometrical and rubber properties (see Figure 139).

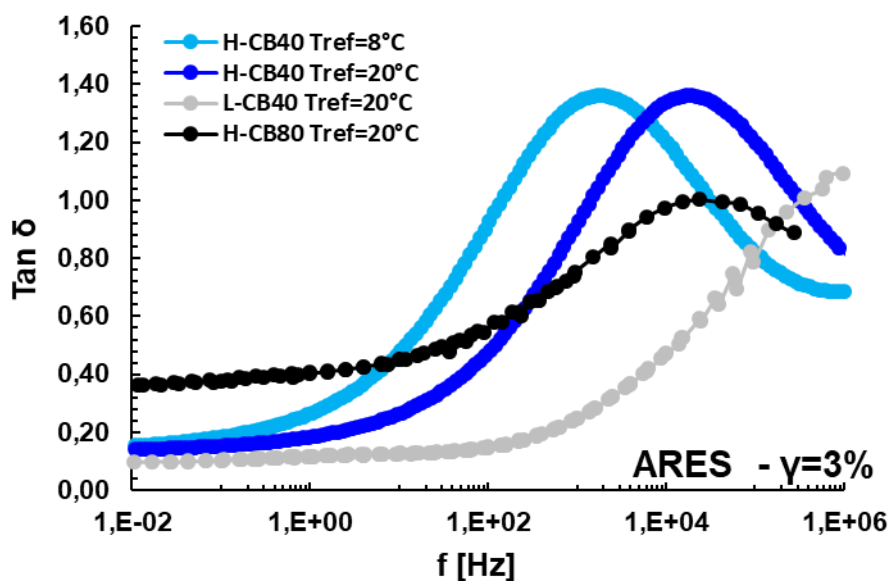


Figure 139. Viscoelastic master curve of loss factor ( $\tan \delta$ ) of the materials selected for the rubber design investigation.

The relationship between the average strain (estimated by FEM), induced by the roughness profile, and the energy dissipation is depicted in Figure 140. Indeed, the hysteresis friction is produced by the energy dissipation, which is quadratically proportional to the strain induced by the road asperities. Taking a look at the blue curve in Figure 140, the peak of strain at the sliding time 2.15 seconds highlights a high deformation of the rubber induced by the asperity, named A in Figure 137, and consequently a relevant contribution to the energy dissipation of the leading edge. Afterwards, the middle section (at around  $t=2,2$  seconds) and the trailing section (at  $t=2,25$  seconds) collide with the asperity A, which induces local strain and the corresponding energy dissipation.

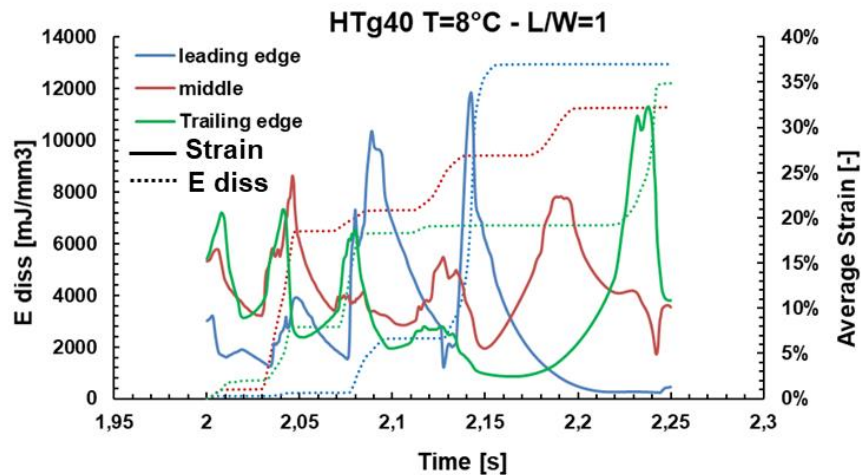


Figure 140. Energy dissipation and local average strain estimated by FEM, which occur in the above sections of rubber block during sliding friction in the case of H-CB40 ( $T_{ref}=8^{\circ}\text{C}$ ).

The local strain occurring at the leading edge is plotted in Figure 141 for H-CB40 with a reference temperature of  $8^{\circ}\text{C}$ . The geometry  $L/W=0,5$  showed the largest strain as evidence of the highest edge effect in the case of short and wide geometry.

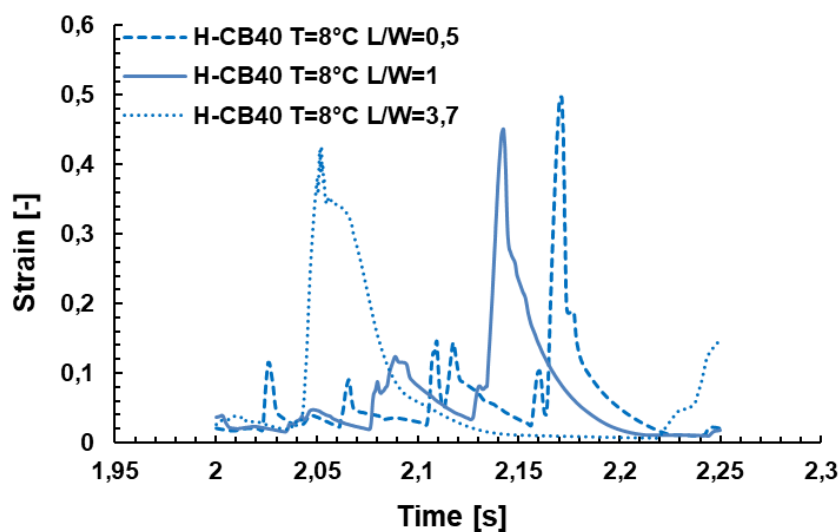


Figure 141. Nominal strain in the rubber leading edge for H-CB40 over sliding time in the case of the three selected rubber geometries.

Once the mechanism of dynamic contact road/rubber was understood, the friction simulations with the geometry  $L/W=1$  were repeated for different test conditions, i.e. sliding speeds (see Figure 142) and other materials (see Figure 143), to study and confirm their effect on the friction behaviour.

The leading and trailing edges showed a similar contribution on the energy dissipation, only shifted in the sliding time, at low velocities (10mm/s) whereas the energy dissipation resulting from the leading edge became predominant compared to the trailing edge (less contact with the asperity in this region) at high sliding speed. Hence, the high excitation frequency in case of high sliding speed changes strongly the dynamic mechanical contact rubber/road asperities and in turn the actual viscoelastic properties ( $G'$  and  $G''$ ).

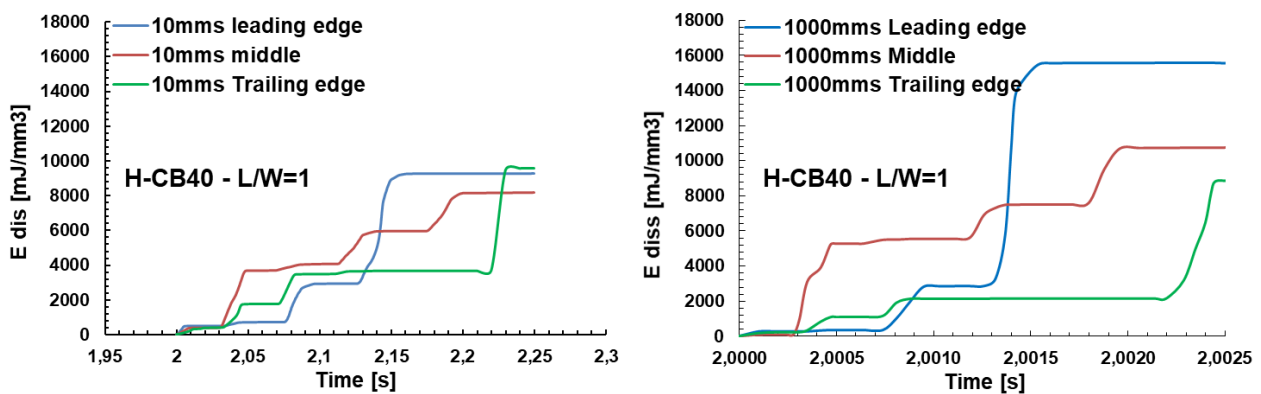


Figure 142. Comparison of the energy dissipated by leading, middle and trailing sections for low ( $v=10\text{mm/s}$  left) and high sliding speed ( $1000\text{ mm/s}$  right) in the case of H-CB40.  $L/W=1$ ,  $p=0.26\text{ MPa}$ .

Figure 143 summarizes the combined viscoelastic and geometrical effects.

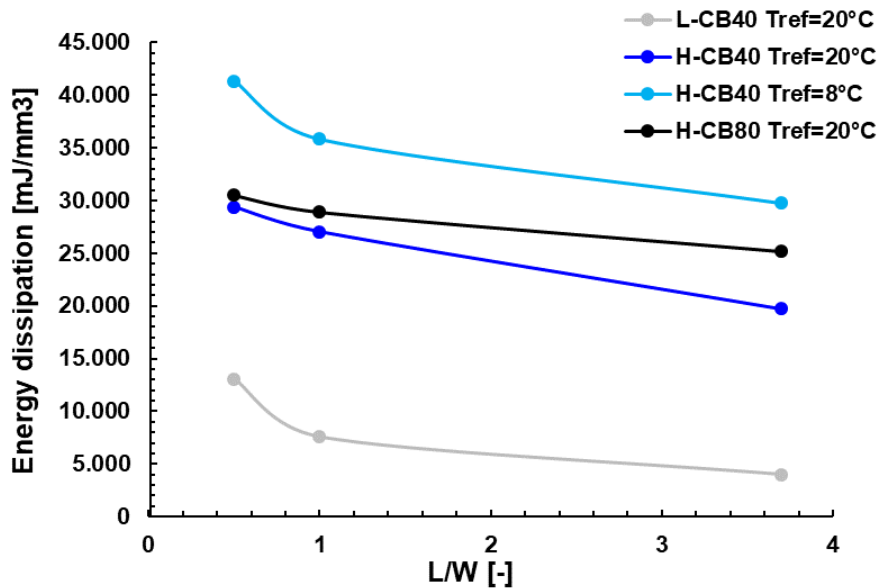


Figure 143. Energy dissipation induced by granite asperities by combining materials and geometry properties ( $L/W$ ).  $v=10\text{mm/s}$ ,  $p=0.26\text{MPa}$ .

The energy dissipation  $E_{\text{diss}}$  decreased with  $L/W$  for all materials because of the increase of the edge effect as described before. Furthermore, it was found this additional energy dissipation coming from the edges varied with the viscoelastic properties (selected from the master curve at the corresponding excitation frequency) also referred to the factor  $\frac{G''}{G^*} \gamma^2$  (where  $\gamma$  indicates the average shear strain) which is proportional to the energy dissipation. The higher the factor, the higher the edge effect will be (see Figure 144).

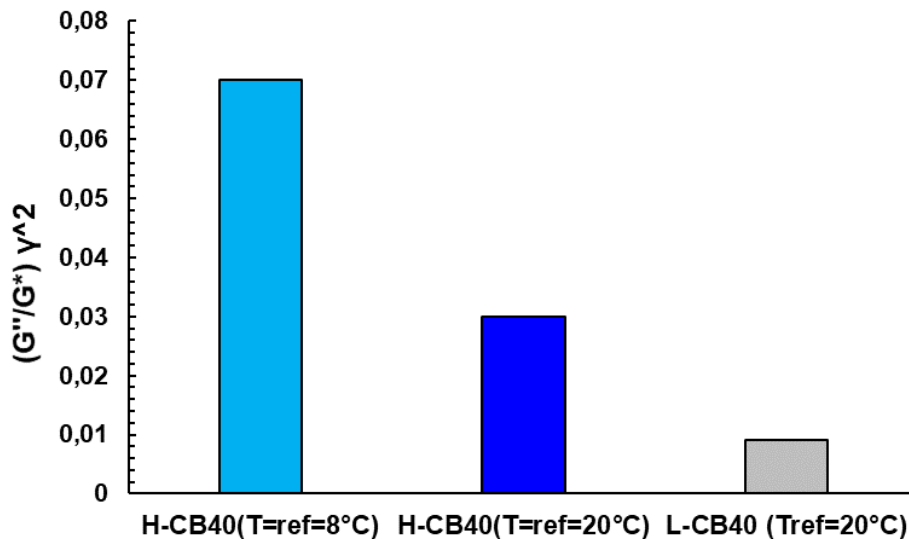


Figure 144. Estimation of the viscoelastic factor proportional to the energy dissipation extrapolated from the viscoelastic master curve of materials at  $f=v/\lambda=10\text{mm/s} / 100\mu\text{m}=100\text{Hz}$ .

Once the hysteresis induced by the different rubber geometries was investigated, wear and hysteresis loss tyre consideration follows.

Taking into account the tread blocks on the rear tyre, it is normal for the leading edges of them to wear more than the trailing edge. This is due to the way the tread blocks flex as power is transmitted through the tyre, driving the bike forward. Considering the front tyre may notice a similar pattern however reversed, as it transmits braking forces in the opposite direction.

Furthermore, a long, narrow contact patch ( $L/W=3,7$ ) will encounter fewer asperities per unit distance traveled than a short, wide one ( $L/W=0,5$ ) of the same total area (see Figure 145) and hence will generate proportionately less rolling resistance.

Suppose the contact patch of the first tyre has width  $2b$ . When it rolls a distance  $x$ , say, the total area of tyre tread that is squeezed against the road surface is  $2bx$ . Given a uniform density of asperities per unit area of the road, the energy loss is proportional to the area that is compressed, in other words, it is proportional to  $2bx$ . Considering a second tyre, whose contact patch is half the width of the first, but twice the length, where the total contact area and the average contact pressure are unchanged. In this given case, the area of the fresh tyre coming into contact with the road for every metre of travel is now half its previous value, at just  $bx$ , and therefore the tread hysteresis loss is halved too.



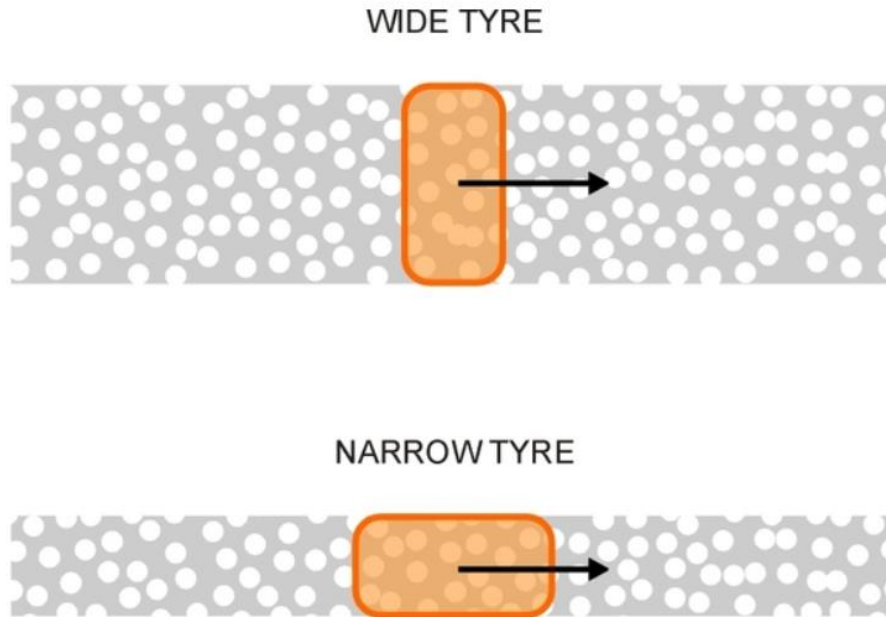


Figure 145. Asperities encountered by the contact patch in the case of narrow or wide tyres.

## 4.4 Investigation of rubber indentation and relaxation on dry substrate

Referring to the problem solving diagram block in Figure 92, the rubber relaxation and indentation block is examined in this chapter. The results of this topic have been published [145].

The focus of the chapter is to get a closer look at the contact between the rubber block and a rough surface to gain a better understanding of the static and dynamic friction problems, to validate the FEM simulation reported in the previous chapter and to validate the contact theories as well.

Contact parameters are crucial in the estimation of the two main friction contributions hysteresis and adhesion.

The Klüppel & Heinrich hysteresis equation [108] describes the hysteresis friction based on a frequency-dependent description of the power spectral density and a multi-scale indentation mechanism.

In fact, the hysteresis friction depends on the factor  $\langle \delta \rangle \equiv V/A_0 = b \cdot \langle z_p \rangle$ , defined as the mean layer thickness of the exciting rubber volume  $V$ , assumed to increase linearly with the mean penetration depth  $\langle z_p \rangle$  of the asperities into the elastomer sample, scaled with a free parameter  $b$  (see Figure 146).



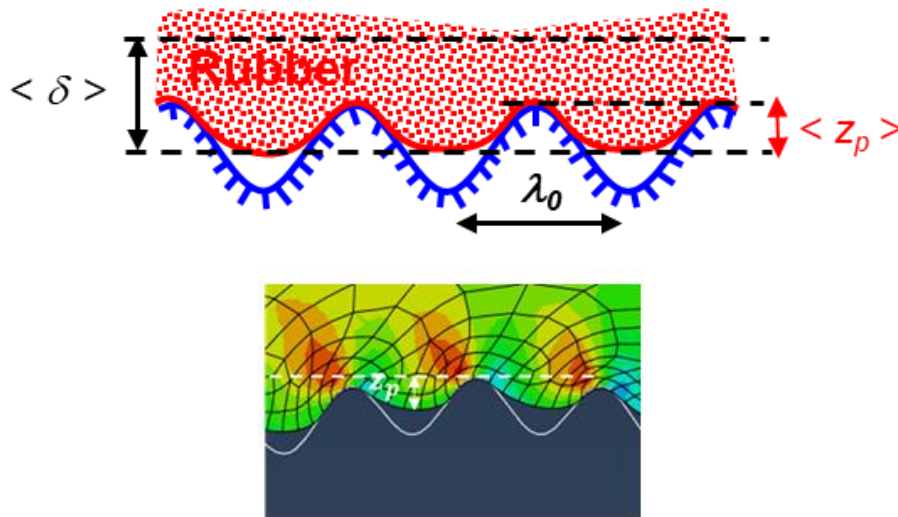


Figure 146. Representation of a crucial contact parameter for the friction: mean penetration depth  $\langle z_p \rangle$ .

Furthermore, an additional important mechanism is adhesion, which depends on the real contact area  $A_c$ .

These crucial contact parameters estimated by the current contact models and FEM simulations can deviate from the experiment due to geometric and material nonlinearities arising in the rubber behaviour. It is still challenging to treat such topic especially through an experimental point of view. Currently, no experimental techniques are available to determine real contact conditions. Therefore, a new experimental technique in the linear friction equipment was designed based on laser distance measurements to determine the relaxation process originating during the rubber deformation and the depth of rubber indentation  $z_p$  into the substrate cavities [145].

Figure 147 depicts the set-up of the experimental technique. A laser sensor was placed below a substrate (multi-indenter with a wavelength of 2 mm in this case). The laser beam goes through a pinhole (drilled through the substrate) located exactly between two asperities to observe the bottom of the rubber sample and thus detect the static and dynamic indentation originating from the relaxation of a rubber block into substrate cavities (during sliding friction).

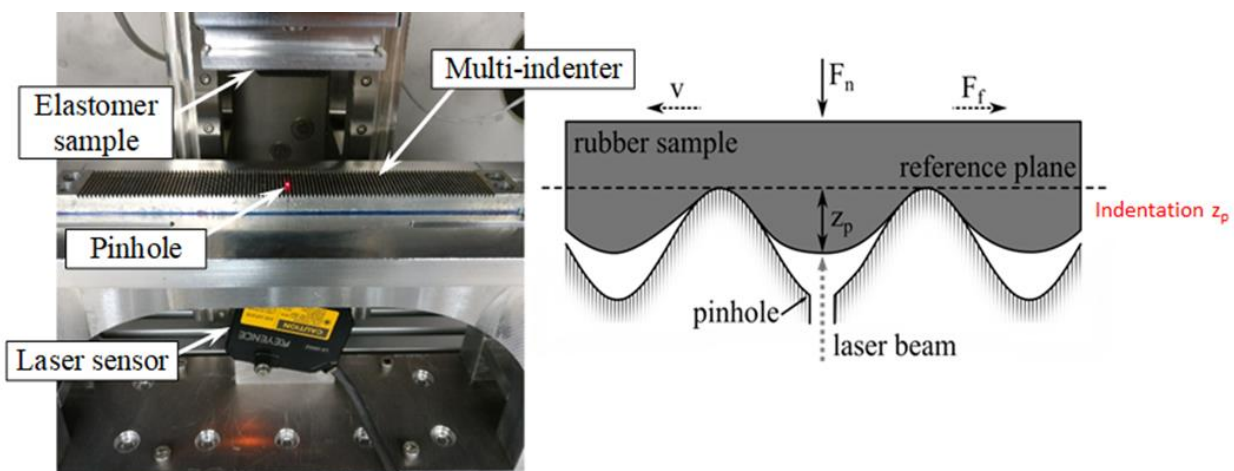


Figure 147. Sketch of the indentation measurement (left). Schematic description of the rubber indentation into one cavity measured by a laser sensor. The measured indentation  $z_p$  is indicated (right) [145].

The reference plane (also referred as the zero level of indentation) was defined on the top of asperities. Static and dynamic indentation were measured by evaluating the distance to the reference plane. Finally, the experimental results were compared with the frictionless simulations modelled in the FEM system ABAQUS in order to validate it.

#### 4.4.1 Static indentation

First, the rubber indentation  $z_p$  into the cavities was measured by applying different normal loads from  $p = 0.19\text{MPa}$  to  $p = 0.57\text{MPa}$  over 90 seconds. The load dependency was detected by the laser sensor, which measured the resulting gap. The experiment was carried out twice for each load step, the first cycle was named virgin cycle. An example of the laser measurement is depicted in Figure 148 for compound H-CB40 and showed negative increase of the indentation depth  $z_p$  when the load is applied, which means a higher indentation of the rubber material into the cavities of the substrate over load time.

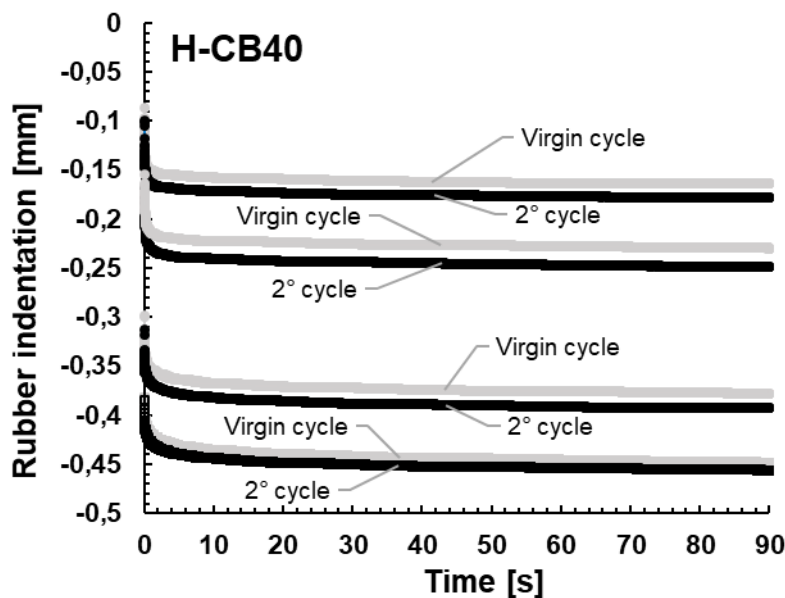


Figure 148. Static rubber indentation of compound H-CB40 measured by laser sensor on multi-indenter substrate.  $T=20^{\circ}\text{C}$ .

Hence, the indentation showed a time dependency due to material relaxation. After the first deformation, a softening of the rubber material took place and the indentation strongly increased for the second cycle. This effect was more pronounced for the higher content of filler. As a comparison, the indentation depth after 90 seconds of relaxation time for compounds L-CB40 and H-CB80 is depicted in Figure 149. Compound L-CB40 with lower filler content showed almost linear load dependence and a slight increase after the virgin cycle. In contrast, H-CB80 revealed a stronger nonlinear load behaviour and softening due to higher filler fraction. Furthermore, the indentation  $z_p$  converged at the maximum load for both cycles (virgin and second), revealing that  $z_p$  is also depending on the deformation history of the sample. This can be attributed to the mechanical behaviour of elastomeric materials like stress-strain measurements, which are shown in Figure 150.

Stiffer behaviour reflected a lower indentation while a higher permanent set induced stronger differences between the virgin and second cycle at lower loads.

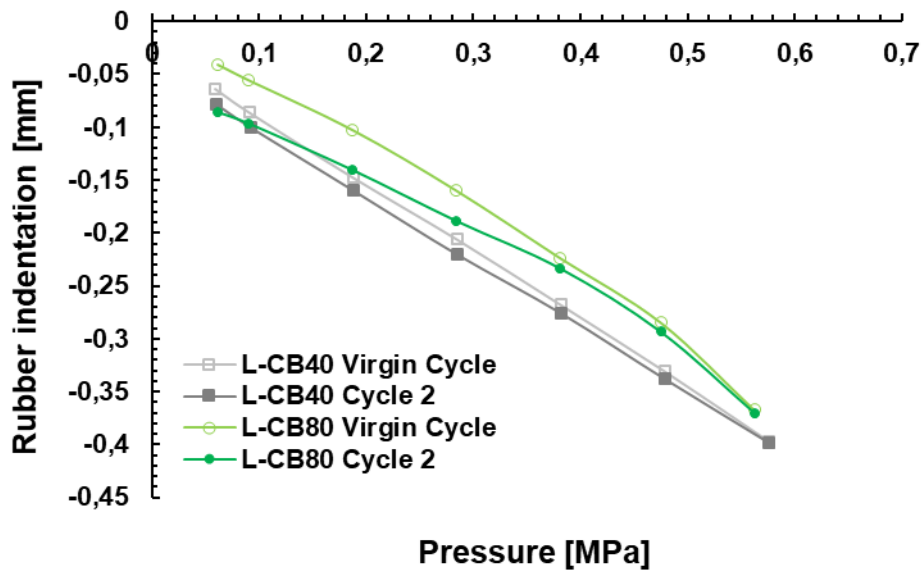


Figure 149. Load dependence of the indentation for compounds L-CB40 and L-CB80 on multi-indenter substrate after a load time of 90 seconds.

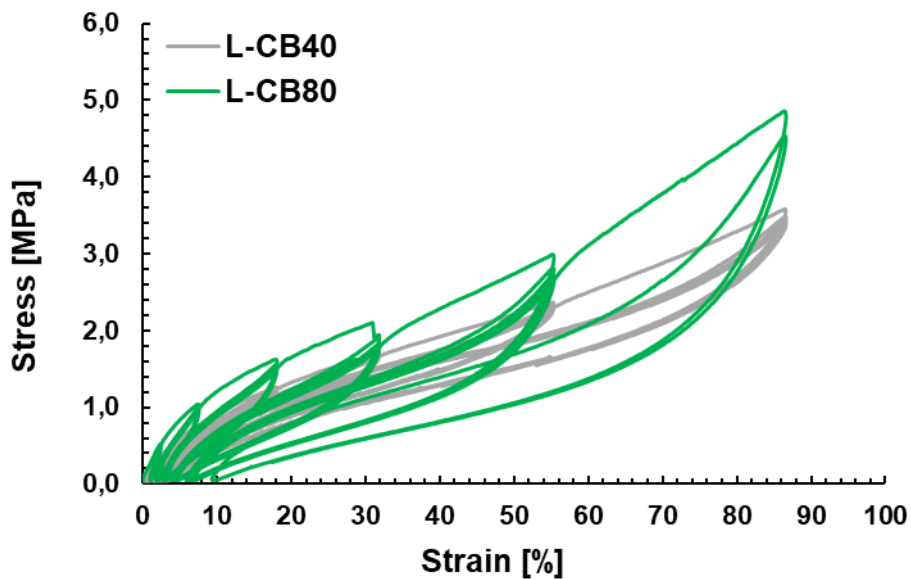


Figure 150. Multihysteresis measurements in biaxial mode of compounds L-CB40 and L-CB80.

Figure 151 evidences the analogy between the indentation curve and the stiffness  $G'$  measured during a strain sweep with Gabo equipment. Virgin and second cycles converged to the maximum shear strain applied. In other words, the history of deformation (i.e. precondition) affects the viscoelastic properties and consequently the indentation.

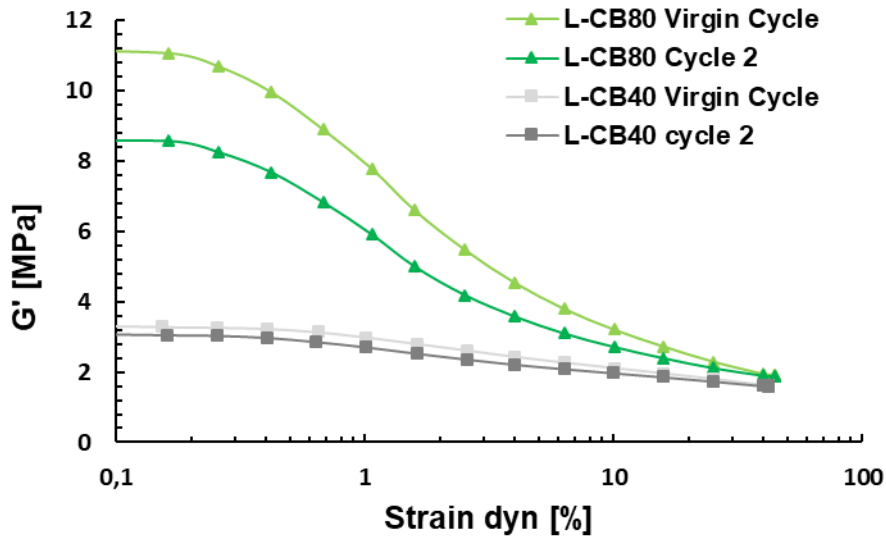


Figure 151. Stiffness  $G'$  as a function of the shear strain at frequency 1Hz in the case of L-CB80 and L-CB40.

Furthermore, the effect of the filler system on the relaxation and indentation level was investigated. The static indentation reflected the mechanical behaviour of the material, also referred to its stress-strain response in quasi-static condition (see Figure 152).

Silica compound showed softer behaviour, lower permanent set and non-linear mechanical behaviour as well due to the presence of silane<sup>69</sup>, which reduces the Payne effect. This resulted in a lower indentation level, non-linear load dependence of indentation and difference between virgin and second cycle indentation curves in comparison to H-CB80 as reported in Figure 153.

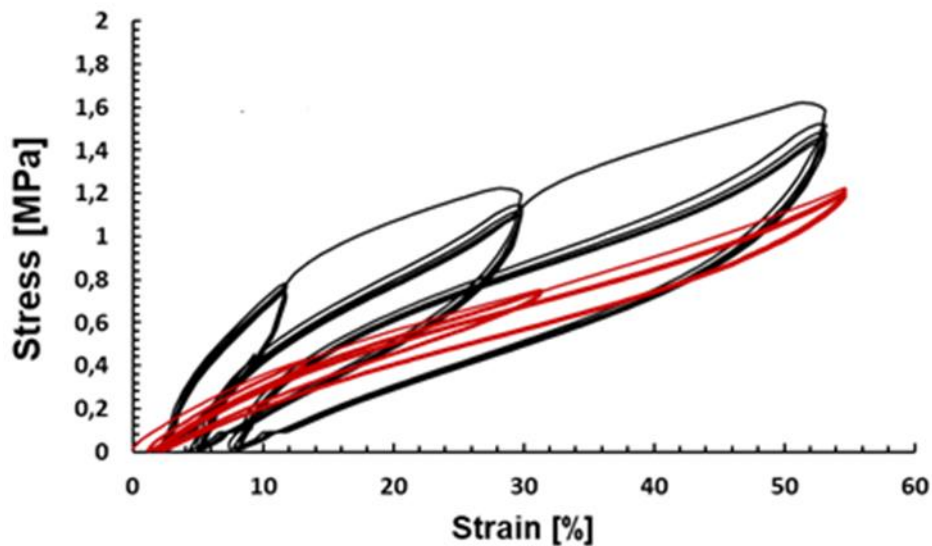


Figure 152. Stress strain measurement in biaxial mode in the case of H-CB80 (black) and H-Si80 (red).

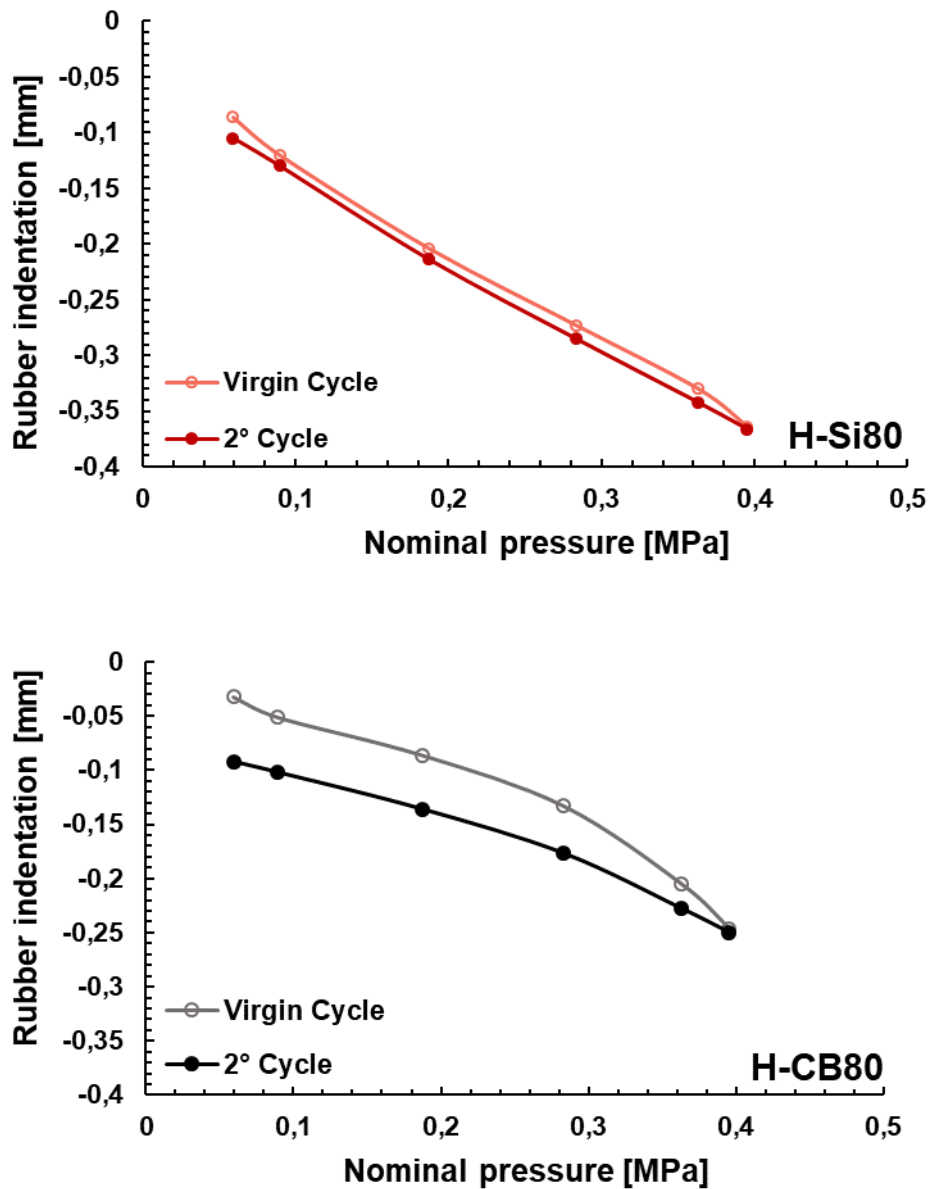


Figure 153. Load dependence of the indentation in the multi-indenter for compounds H-Si80 (top) and H-CB80 (bottom).  $T=2^{\circ}\text{C}$ .

Silica compound (H-Si80) showed steeper and deeper relaxation into the substrate cavities in comparison to the carbon black compound (H-CB80) as illustrated in Figure 154.

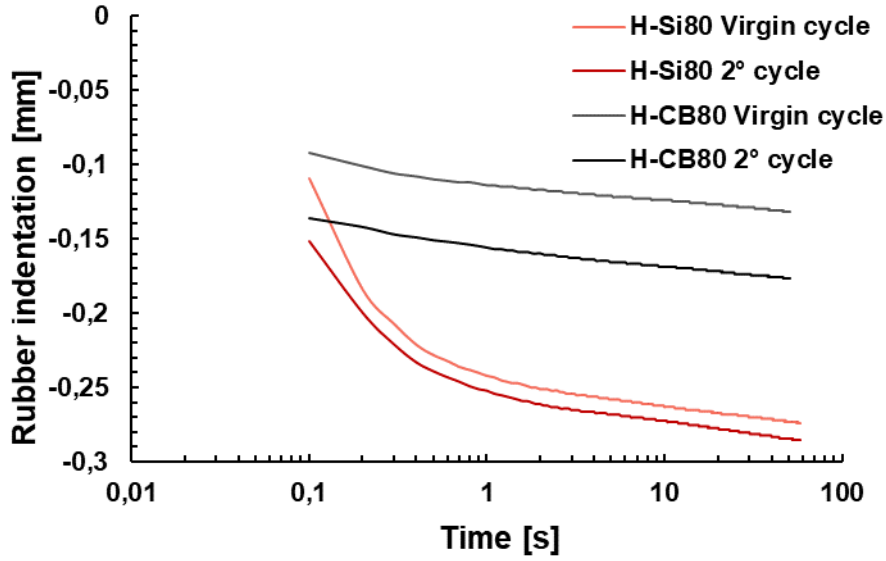


Figure 154. Static rubber indentation vs time in the case of H-Si80 and H-CB80 on multi-indenter.  $p=0.28\text{MPa}$ ,  $T=20^\circ\text{C}$ .

The experimental indentation curves (virgin cycle in this case) are fitted in Figure 156 considering three Maxwell elements based on the Eq. (108) and the nomenclature in Figure 155.

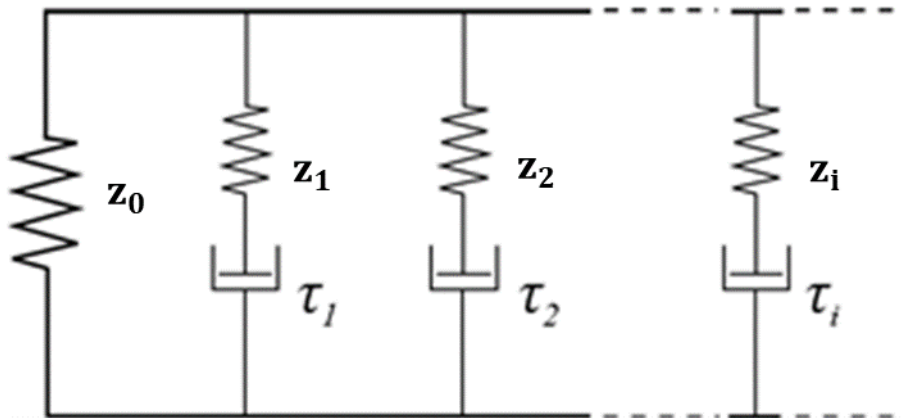


Figure 155. Visualization of the Maxwell model to represent viscoelastic behaviour during indentation test.

$$z(t) = z_0 + \sum_{i=1}^N z_i e^{-\left(\frac{t}{\tau_i}\right)} \quad (108)$$

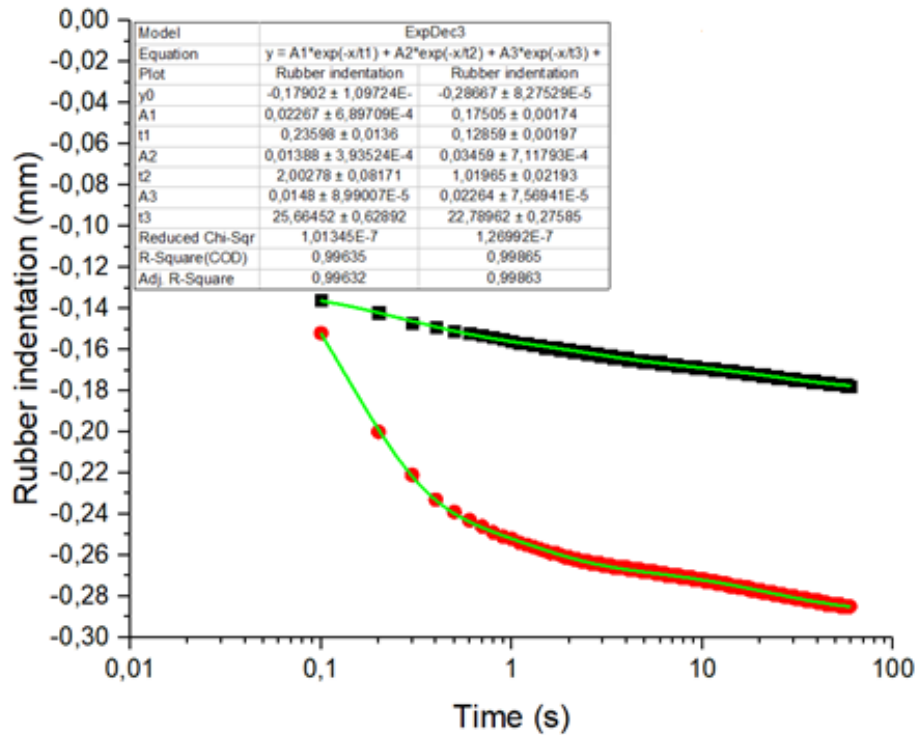


Figure 156. Static rubber indentation vs time for H-CB80 (black) and H-Si80 (red) and corresponding fit (green) by considering the Maxwell model.

The Table 13 reported the fitting parameters  $z_i$  and the relaxation times  $\tau_i$  in the case of silica and carbon black compounds.

Table 13. List of parameters of the Maxwell elements to fit the experimental static indentations.

Maxwell element	H-CB80	H-Si80
$z_0$	-0.179	-0.287
$z_1$	0.02267	0.175
$z_2$	0.01388	0.0346
$z_3$	0.0148	0.0226
$\tau_1$	0.236	0.129
$\tau_2$	2.003	1.020
$\tau_3$	25.665	22.790

The  $z_i$  values were higher in the case of silica compound implying a softer behaviour whereas lower relaxation times  $\tau_i$  revealed a faster relaxation.

## 4.4.2 Dynamic indentation

In this chapter, the dynamic indentation is investigated which means the contact mechanism when a rubber block moves relative to the substrate. The measurements at dynamic conditions were performed by varying load and speed in two steps with a defined test setup. An example for 10 mm/s is shown in Figure 157 for H-CB40 material.

In the first step, the load was applied for 180 seconds. As a result, the elastomeric material relaxes until an equilibrium state as previously described. In the second step, the substrate was moved keeping the sample under load. Observing the indentation curve, a slight peak appeared after the beginning, which can be attributed to a peeling effect at the leading edge. This caused a bulge and the indentation depth increased, the effect might depend on the rubber type, temperature and rate of separation. After the initial increase, the indentation depth decreased strongly and showed a periodical response with a time step corresponding to the sinusoidal wavelength of the substrate topology divided by the velocity. In case of 10 mm/s the indentation from static to dynamic condition decreased in average approximately 28% since the sample lifts up and consequently exhibits smaller contact under dynamic condition. Furthermore, the second measurement with the same sample showed good repeatability proving the consistency of the new experiment technique developed.

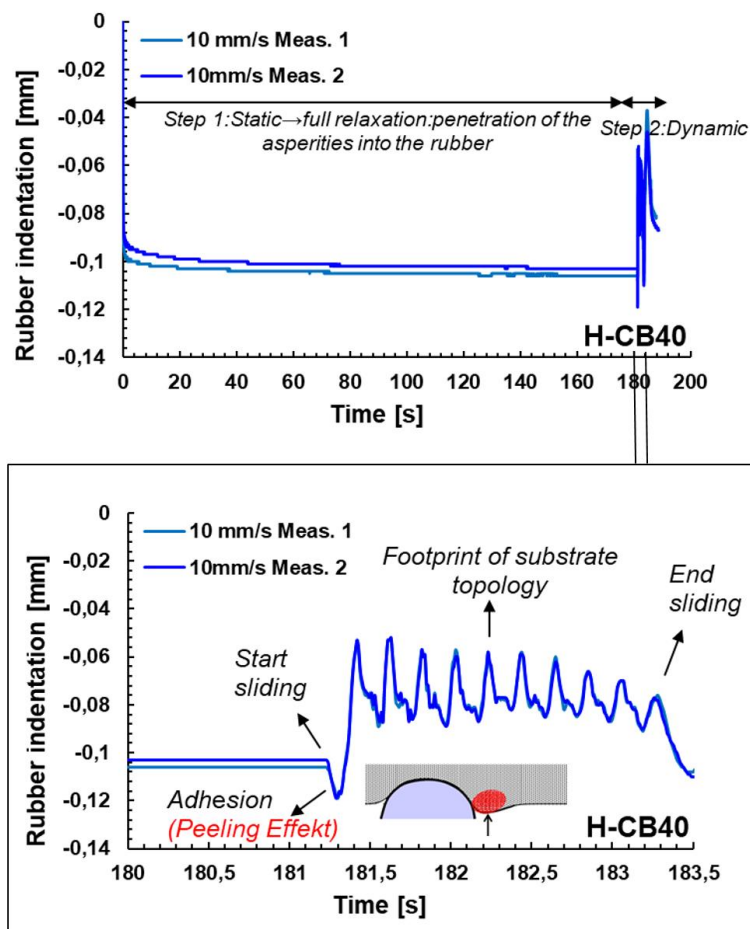


Figure 157. Static and dynamic indentation (top) and corresponding magnification of the second step (bottom) for compound H-CB40 at  $v=10\text{mm/s}$  and  $p=0.14\text{MPa}$  [145].



Figure 158 depicts the rubber indentation measured by the laser sensor over a sliding distance of 20 mm. The indentation level reduced with speed as the time for the elastomer to enter the cavities of the substrate reduced. Either this is caused by the higher stiffness or by the shorter contact time at high velocities preventing the rubber from establishing intense contact and in turn large true contact areas as found in the literature. Furthermore, the amplitude of the sinusoidal cycles reduced with speed for the previously explained reason. The values resulting from the dynamic indentation were estimated by the average of sinusoidal cycles, which occurred during the dynamic indentation for three different pressures and sliding speeds between 0.1 mm/s and 50 mm/s. The results are shown in Figure 159.

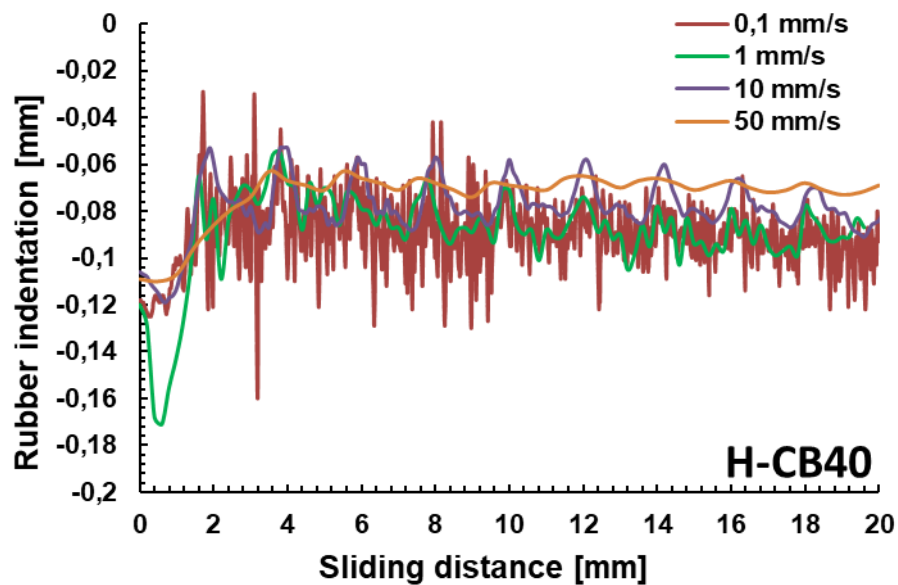


Figure 158. Dynamic rubber indentation over the sliding distance for H-CB40 in the case of multi-indenter.  $T=20^{\circ}\text{C}$ ,  $p=0.14\text{MPa}$ .

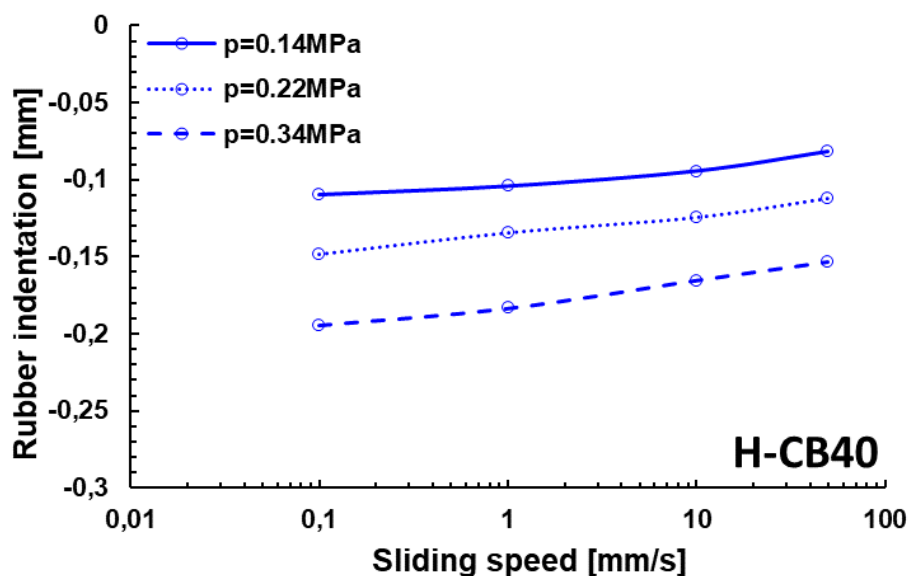


Figure 159. Load and sliding speed dependence of the dynamic rubber indentation in the case of multi-indenter for H-CB40.  $T=20^{\circ}\text{C}$ .

The comparison of the load and speed dependence of rubber indentation in the case of L-CB40 and L-CB80 is shown in Figure 160. The indentation reduced with sliding speed. This based on the consideration that the main excitation frequency rose up by increasing the sliding speed according to the equation  $f=v/\lambda$ , where  $v$  and  $\lambda$  are the sliding speed and substrate wavelength respectively, hence an increase occurred in the stiffness  $G'$ , which was extrapolated from the viscoelastic moduli master curve. Therefore, the indentation decreased with the speed. In summary, an analogy was established between the dynamic rubber indentation and the frequency-dependent stiffness  $G'$  master curve constructed by the dynamic mechanical analysis (DMA). The reader should compare Figure 160 and Figure 161. The lower dynamic stiffness of compound L-CB80 compared to L-CB40 implied lower indentation due to higher content of filler (in the excitation frequency range induced by the asperities).

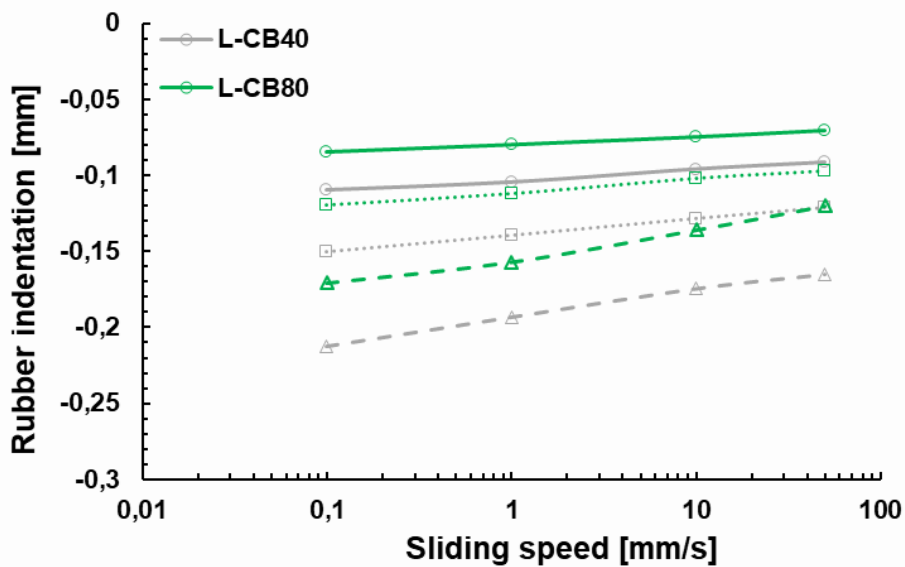


Figure 160. Load ( $p=0.14\text{MPa}$  (o),  $p=0.22\text{MPa}$  (□)  $p=0.34\text{MPa}$  (Δ)) and sliding speed dependence of the dynamic rubber indentation in the case of multi-indenter for L-CB40 and L-CB80.  $T=20^\circ\text{C}$ .

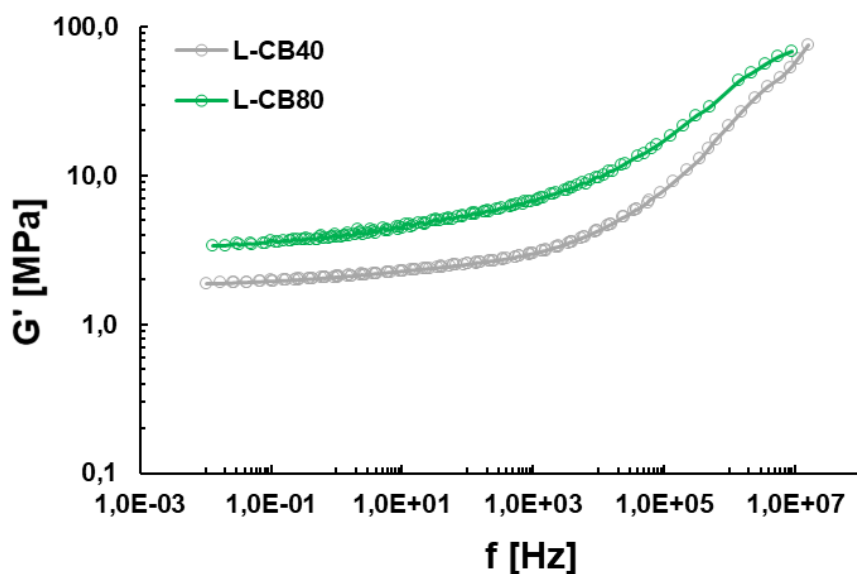


Figure 161. Storage modulus  $G'$  master curves of the L-CB40 and L-CB80 materials for reference temperature of  $20^\circ\text{C}$ , 2.5% strain.

### 4.4.3 Validation of the FEM model through indentation experiments

Considering the viscoelastic material model used for the friction simulation (see the section 4.3.2) an accompanying simulation was setup in ABAQUS to study the indentation experiment and to validate the FEM simulations.

The simulation results were compared with the static indentation experiment presented in the previous section.

First, the simulated static indentation pressure dependence is shown for low and high content of carbon black (L-CB40 and L-CB80) in Figure 162. The virgin cycle was simulated in ABAQUS.

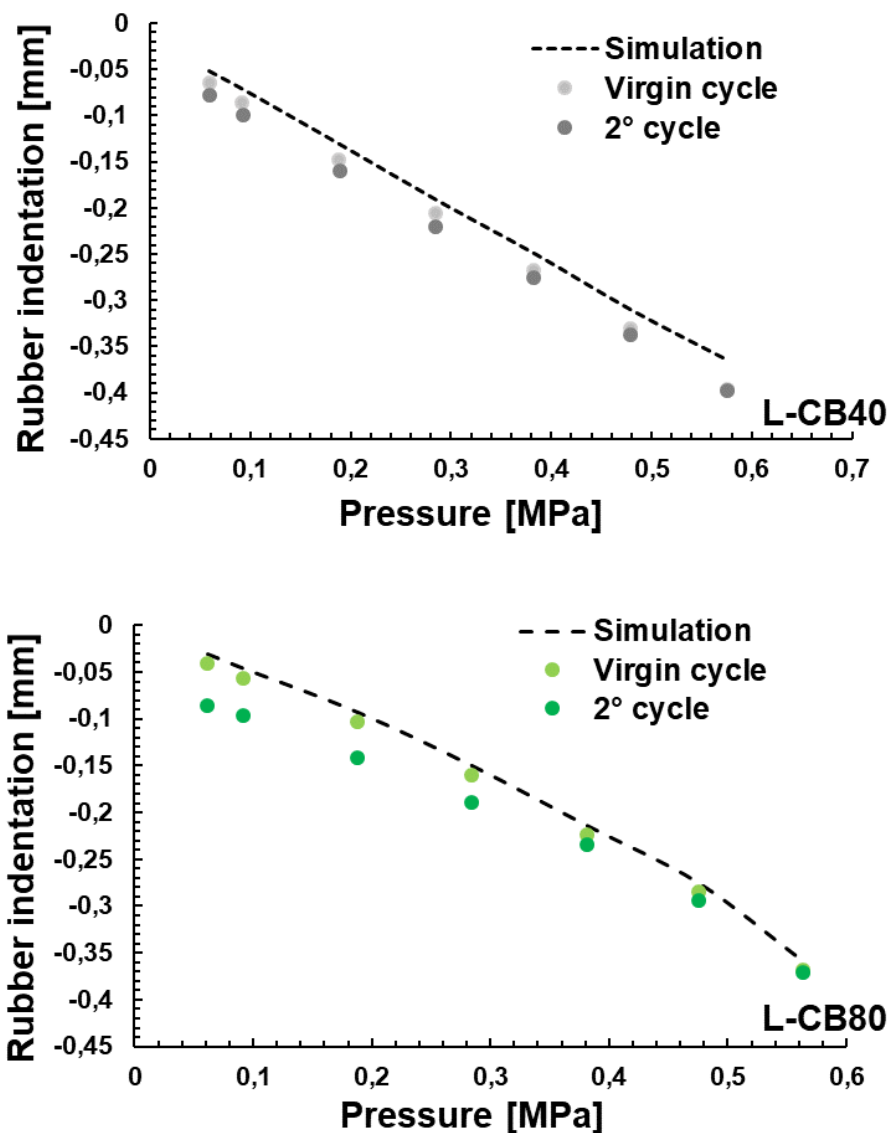


Figure 162. Comparison between the static experimental indentation (symbol  $\circ$ ) and FEM simulation (dashed line) in the case of multi-indenter substrate for L-CB40 (top) and L-CB80 (bottom).  $T=20^{\circ}\text{C}$  [145].

The prediction of the indentation over a wide range of pressures close to the tire applications was accurate. Second, the dynamic indentation during sliding friction was compared with the experimental one (measured by the laser sensor).

The simulation was composed of two steps as in the experiment. In the first step, the load was applied for 60 seconds until the elastomeric material fully relaxed in an equilibrium state. In the second step, the substrate was moved to the left direction with different constant sliding speeds keeping the sample under load. The dynamic indentation was detected from the right side of the rubber block to the left one (see the reference point A as an example in Figure 163).

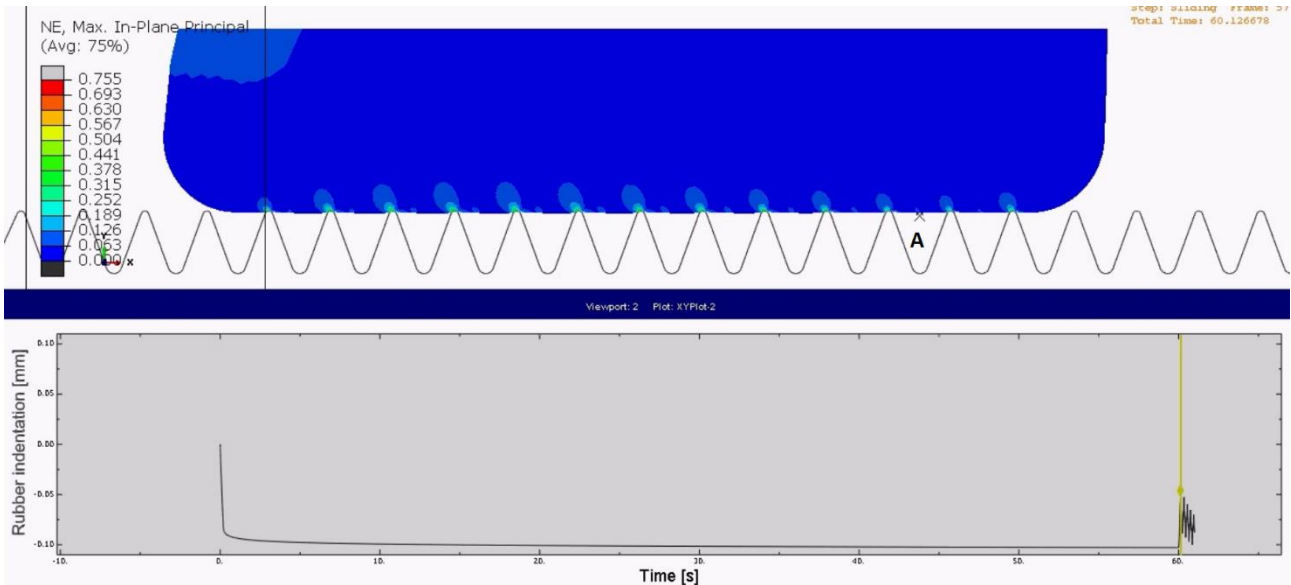
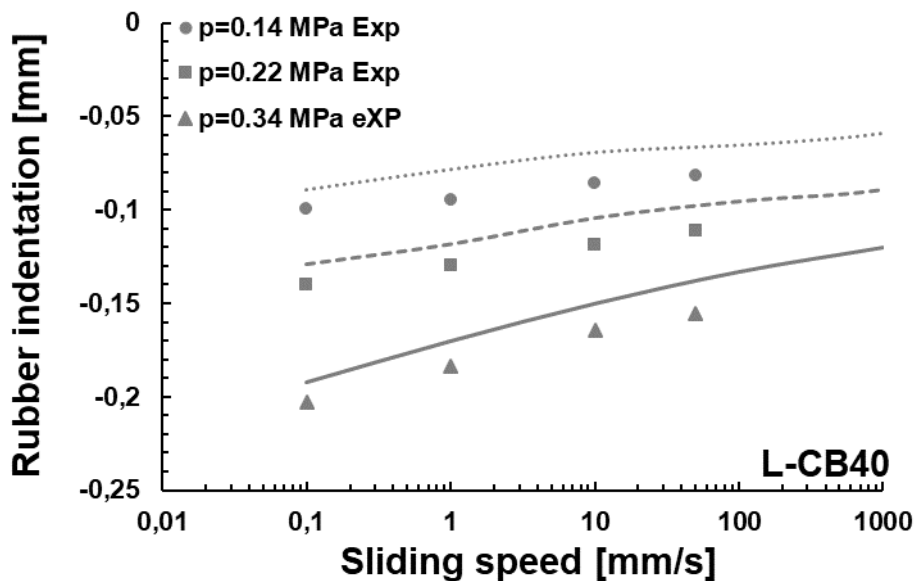


Figure 163. Double view (strain distribution and indentation vs time) of the rubber block indentation during sliding frictionless simulation based on two steps: static and dynamic [145].

The dynamic indentation revealed the local strain level induced by the rough track and dynamic stiffness of the rubber material. The simulated dynamic indentation was calculated by the average of the sinusoidal cycles induced by the substrate topology during the second step, see an example in case of two materials in Figure 164.



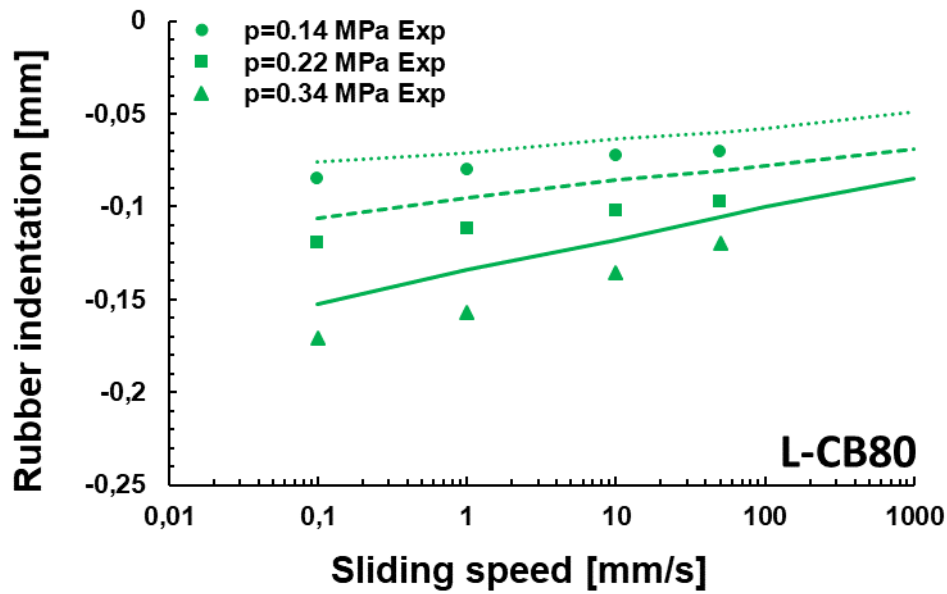
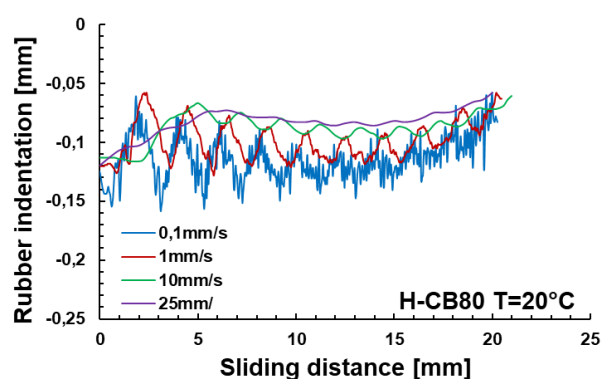
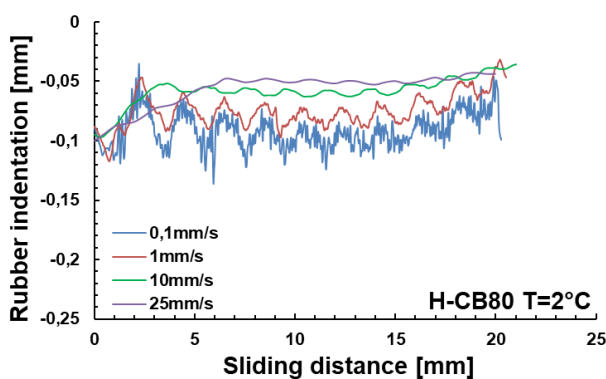


Figure 164. Comparison between the experimental dynamic indentation (symbol) and the simulated one (lines) by depending sliding speed and nominal pressure in the case of L-CB40 and L-CB80 compounds.  $T=20^{\circ}\text{C}$ .

A good prediction of dynamic contact condition was achieved with a slight underestimation due to the lack of adhesion effects, which were not considered in the FEM simulations of this research.

#### 4.4.4 Indentation master curve

In this section, the temperature dependence of the indentation was examined. The contact conditions are strongly affected by the mechanical behaviour of the material which depends on temperature. The indentation measurements were performed at  $2^{\circ}\text{C}$ ,  $20^{\circ}\text{C}$  and  $45^{\circ}\text{C}$  on the multi-indenter surface. The temperature of  $50^{\circ}\text{C}$  represents the maximum temperature measurable with the laser sensor used in this work. Figure 165 depicts the temperature dependence of the dynamic indentation over the sliding distance in the case of four different sliding speeds. Based on the material stiffness dependence with the temperature, a softer behaviour of material occurred by increasing the temperature. The same test set-up was adopted as previously described.



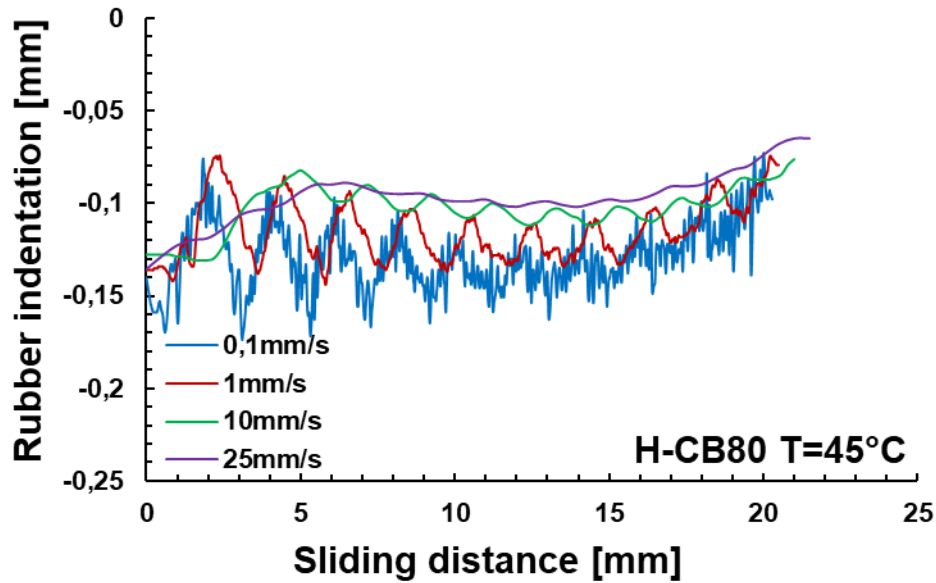


Figure 165. Temperature dependence (2, 20 and 45°C) of the dynamic indentation over the sliding distance in the case of H-CB80 and multi-indenter.  $p=0.22\text{MPa}$ .

Figure 166 depicts the speed dependence of the rubber indentation in the case of three temperatures, the calculations based on the average of the sinusoidal cycles depicted in the previous figure.

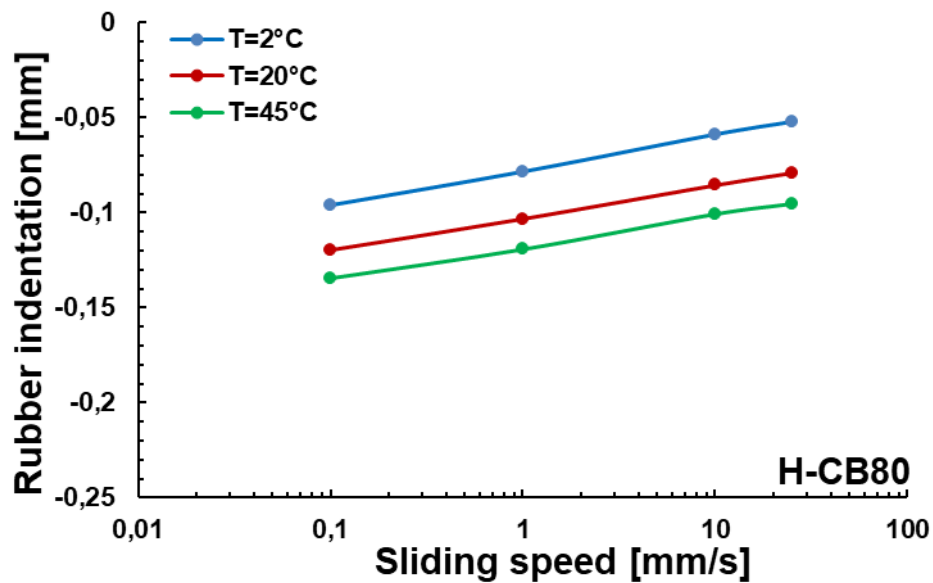


Figure 166. Temperature and sliding speed dependence of the rubber indentation in the case of H-CB80 and multi-indenter.  $p=0.22\text{MPa}$ .

This implied a correlation between the dynamic indentation and the frequency-temperature dependence of the stiffness  $G'$  as reported in Figure 167.

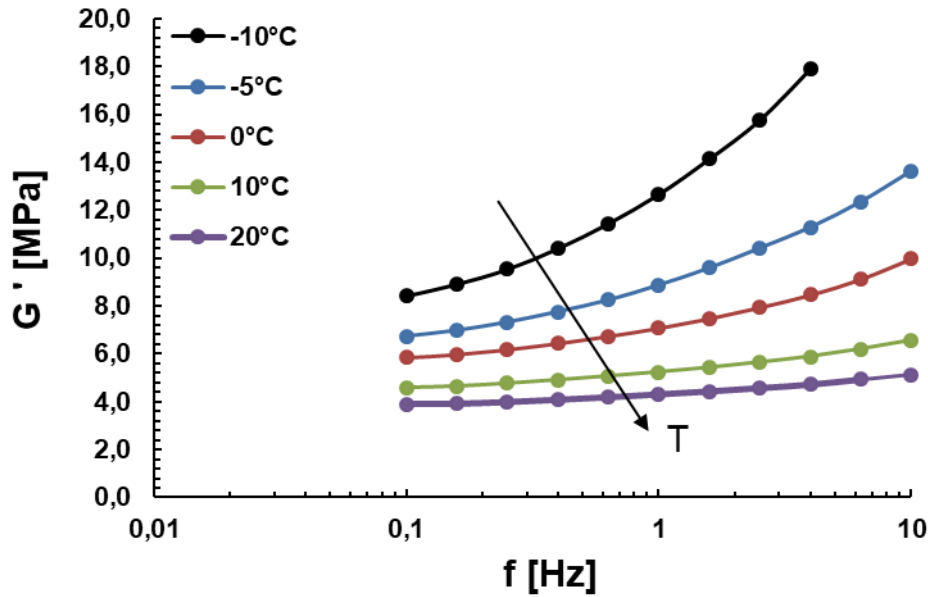


Figure 167. Frequency-temperature sweep carried out with the ARES equipment in the case of H-CB80. The stiffness  $G'$  in shear mode ( $\gamma=3\%$ ) is shown.

Lower indentation was observed by reducing the temperature due to the stiffer behaviour of the material. Besides, the amplitude of the sinusoidal cycles decreased with the temperature.

The time-temperature superposition TTS principle was applied to construct an indentation master curve similar to the one formulated for the stiffness  $G'$  (see chapter 2.5.2). The horizontal shift factor  $a_T$  was applied from the measurements with ARES equipment for the compound H-CB80 (see Figure 103) followed by the vertical shift factor  $b_T$  (see Figure 104) power the value  $-2/3$  because of the dependence between the indentation  $h$  and the rubber modulus  $E$  according to the Hertz theory (Eq. (31)).

$$h = \frac{a^2}{R} = \sqrt[3]{\frac{9}{16} \frac{F^2}{RE^2}} \propto E^{-\frac{2}{3}}$$

$$E(T_2) = b_T E(T_1) \quad (109)$$

$$\Rightarrow h(T_2) = \left(b_T^{-\frac{2}{3}}\right) \left(E(T_1)^{-\frac{2}{3}}\right)$$

Finally, the indentation master curve can be constructed as portrayed in Figure 168.

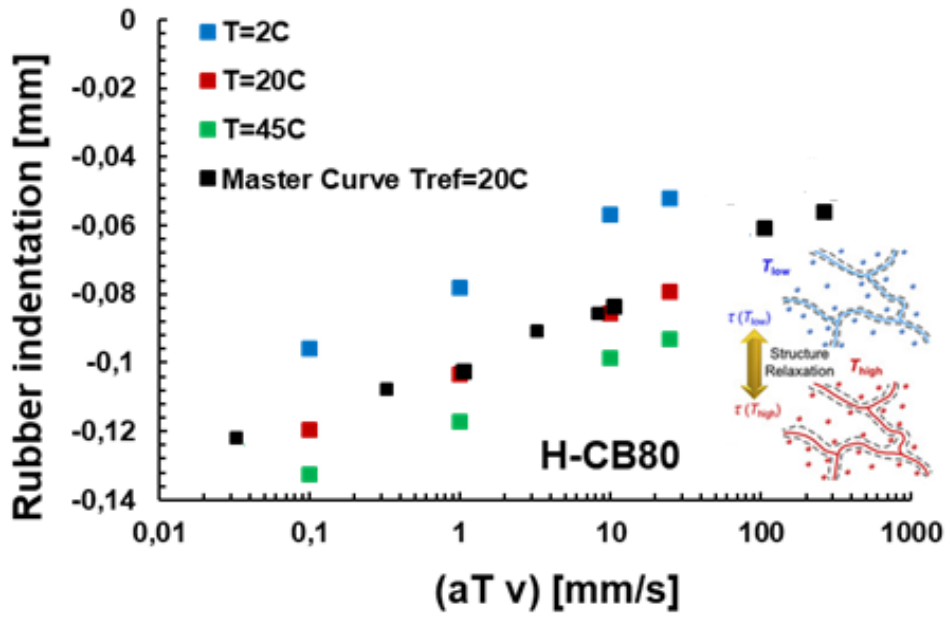
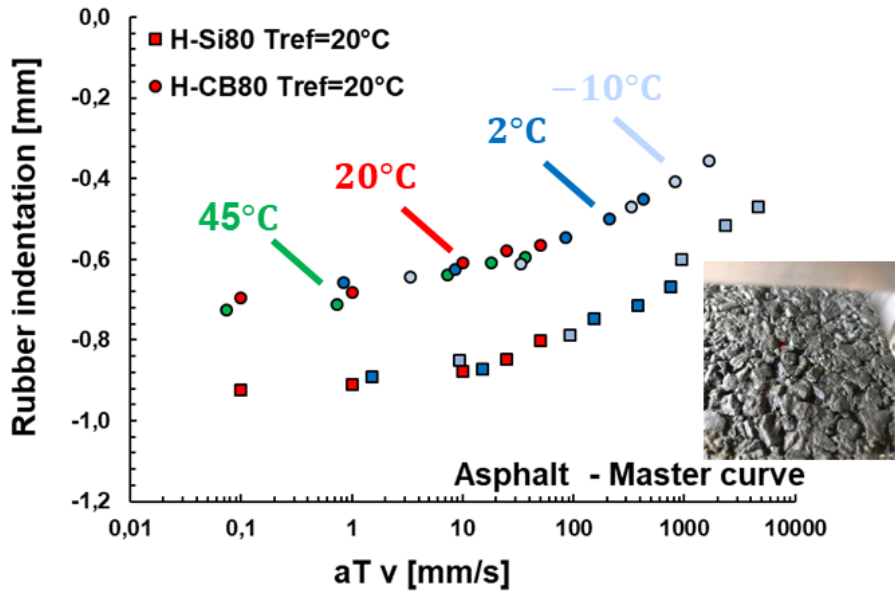


Figure 168. Indentation master curve ( $T_{ref}=20^{\circ}\text{C}$ ) in the case of H-CB80 and multi-indenter ( $p=0.22\text{MPa}$ ). Horizontal shift factor  $a_T$  and vertical one  $b_T$  are used to shift the curves.

The same procedure was applied to determine the indentation master curve for silica compound and an asphalt surface. The filler (top: silica versus carbon black compounds) and substrate (bottom: model-indenter versus asphalt) dependence of the indentation are provided in Figure 169.





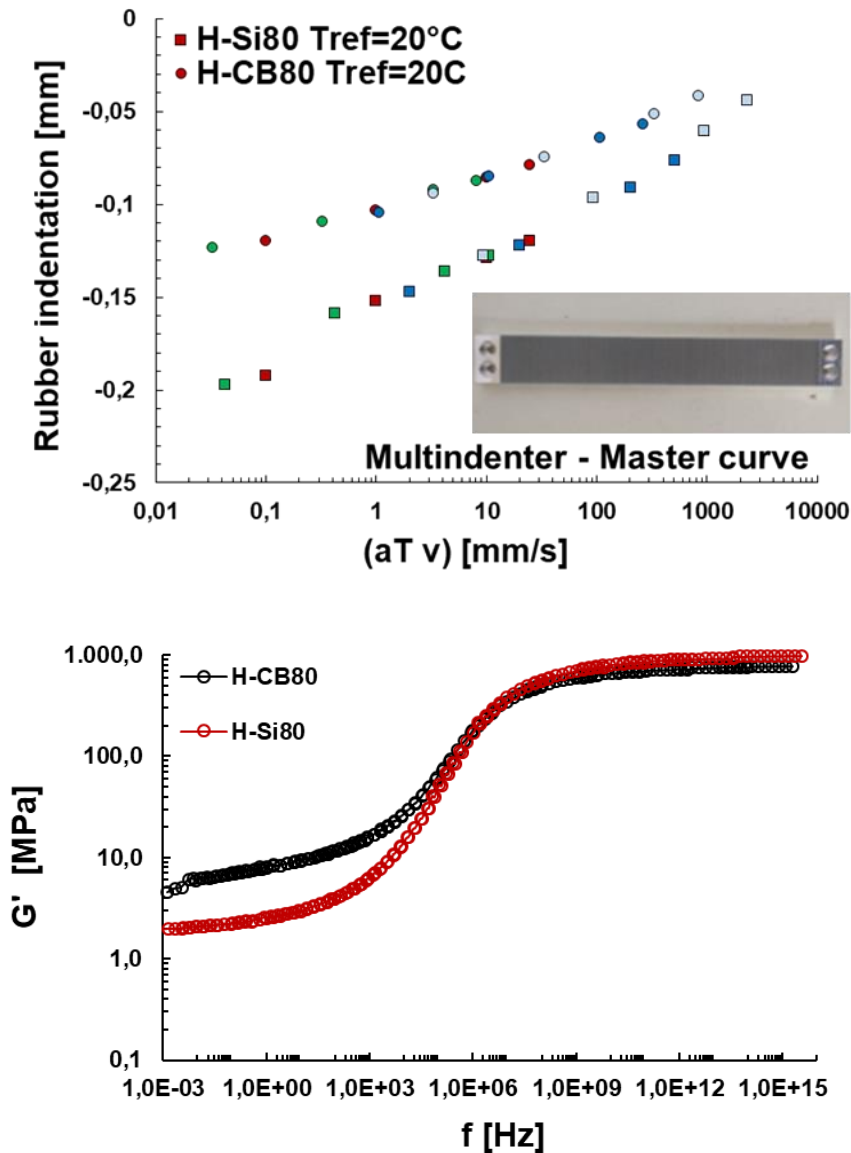


Figure 169. Indentation (top) and stiffness  $G'$  (bottom) master curve at  $T_{ref}=20^{\circ}\text{C}$  in the case of H-Si80 and H-CB80. Multi-indenter and asphalt surfaces.  $p=0.22\text{MPa}$ .

Silica compound shows a softer behaviour for both substrates in comparison to carbon black compounds. This confirmed a good correlation with the viscoelastic moduli master curve. Furthermore, the indentation presented more velocity dependence for silica compound in analogy with the frequency dependence of  $G'$ .

## 4.5 Numerical simulation of adhesion friction

As mentioned before, the hysteresis contribution matches well with the experimental condition water+soap whereas under water and dry conditions the adhesion occurs as well. The grip reduces strongly from dry to wet condition due to the presence of a lubricant. Consequently, it is still challenging to estimate the adhesion level, especially in water condition. In the current section, the

estimation of the adhesion contribution in dry and wet conditions, as well as its main parameters were done by studying the nature of the contact from a physical and chemical point of view.

### 4.5.1 Dry friction

The transition from wet to dry friction was interpreted in terms of adhesion since the specific experimental conditions hinder the occurrence of additional effects associated with fluid viscosity or interfacial heat generation during the sliding process. Physically-based considerations of adhesion friction generally involve the periodic formation and breakage of molecular bonds between polymer chains and a substrate during the sliding process. As a result, the rubber adhesion exhibits viscoelastic features with characteristic length scales below the micrometer range revealing that molecular mechanisms play a role.

The adhesion is strongly dependent on the real contact surface between the rubber and substrate (see Eq. 38), which depends on material (stiffness of the material, nature of polymer) and affinity of the system lubricant/rubber and substrate. The present work proposes a multi-scale formulation of the dynamic contact problems for rubbery materials sliding over rough surfaces. Thereby, the hysteresis friction and the contact parameters like real contact area are determined through FEM simulation (see Figure 120) while the modelling of adhesion includes the velocity dependent interfacial shear strength describing the kinetics of peeling effects at the interface.

The corresponding physical mechanisms fundamentally differ from the length scale at which they occur, even if both friction components are governed by the material viscoelastic response during the sliding process. In the following, the relevance of adhesion concepts is systematically investigated, in particular the simulated real contact area and the interfacial shear strength concerning material and surface effects.

A hybrid model was introduced based on the consideration that hysteresis and full adhesion occur under dry condition. Pure hysteresis, induced by substrate roughness, was estimated by FEM as shown above (i.e. Figure 122) whereas the adhesion was estimated by the analytical model [93] which involves the shear strength (Figure 170) and real contact area extrapolated from FEM (Figure 171). A calculation of the analytical model parameters is reported below for H-CB40 material.

$$\mu_{Adh}^{Dry} = \frac{\tau_s A_c}{\sigma_0 A_0} \quad (110)$$

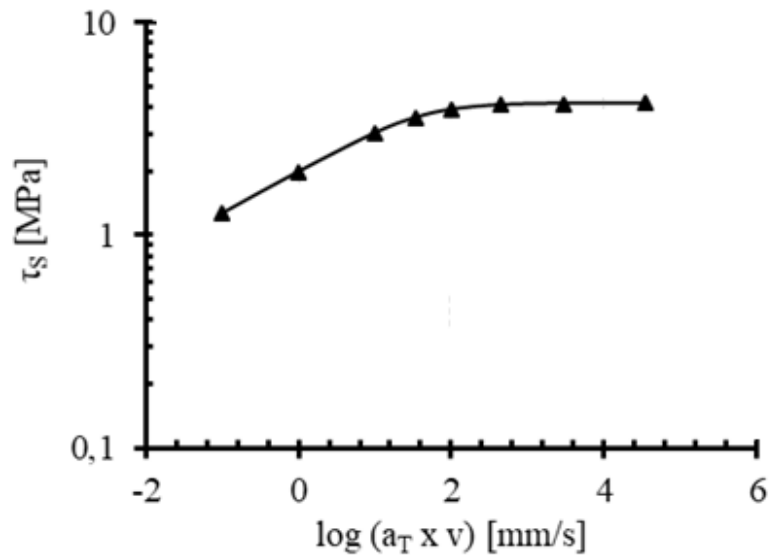


Figure 170. Dependence of the shear strength with the velocity for H-CB40.

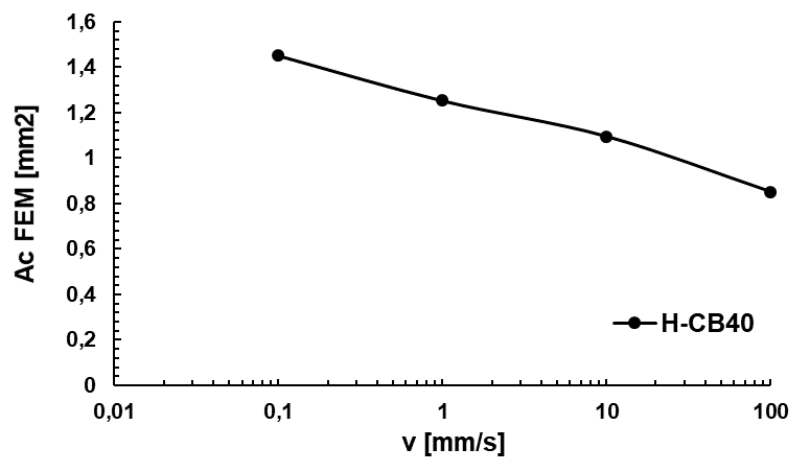


Figure 171. Real contact area of H-CB40 calculated by FEM in the case of multi-indenter at  $T=20^\circ\text{C}$  and  $p=0.26\text{MPa}$ .

The adhesion component decreases at the high sliding speed due to the increase of the dynamic stiffness of the material with the velocity.

This confirms that the level of adhesion friction for filled S-SBR is primarily governed by the real contact area, which was found to be significantly larger for lower amount of carbon black. Similar consideration can be done when silica and carbon black systems are compared revealing higher adhesion for a silica system. The glass transition temperature was strongly influenced by the level of dry friction at constant filler content as well (see Figure 172 L-CB40 vs H-CB40).

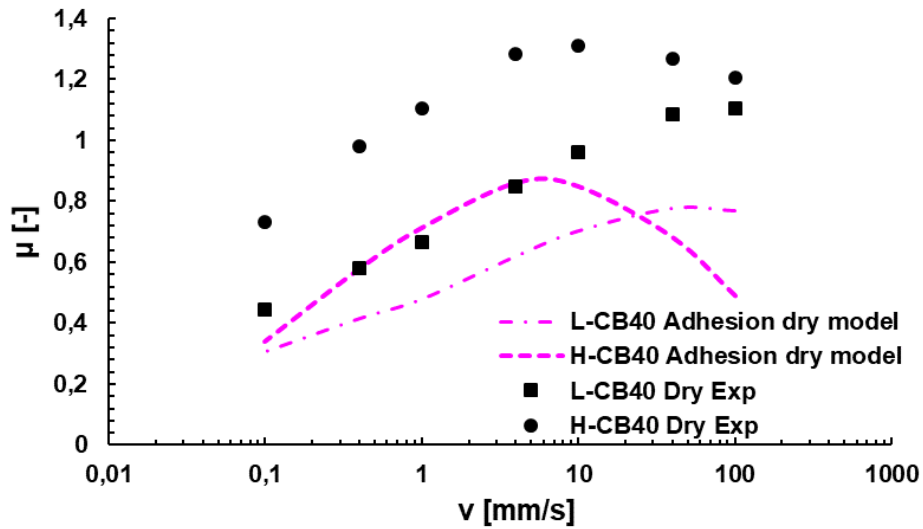


Figure 172. Comparison of the adhesion friction calculated with an analytical model and the dry friction (exp.) between L-CB40 and H-CB40 compounds.

The peak of the adhesion was found around 4 mm/s for HTg system whereas the peak for LTg system is shifted at higher speeds according to the lower glass transition temperature of the compound.

#### 4.5.2 Water friction

This chapter considers the second (viscoelastic properties) and fifth blocks (affinity substrate/rubber and lubricant) reported in the problem-solving diagram in Figure 92. An important challenge for tire manufacturers is the prediction of grip in water condition. The grip reduces strongly from dry to wet conditions due to the presence of lubricant, which prevents full contact between road and tyre. Different cases can occur during wet friction based on the contact condition (Figure 173).

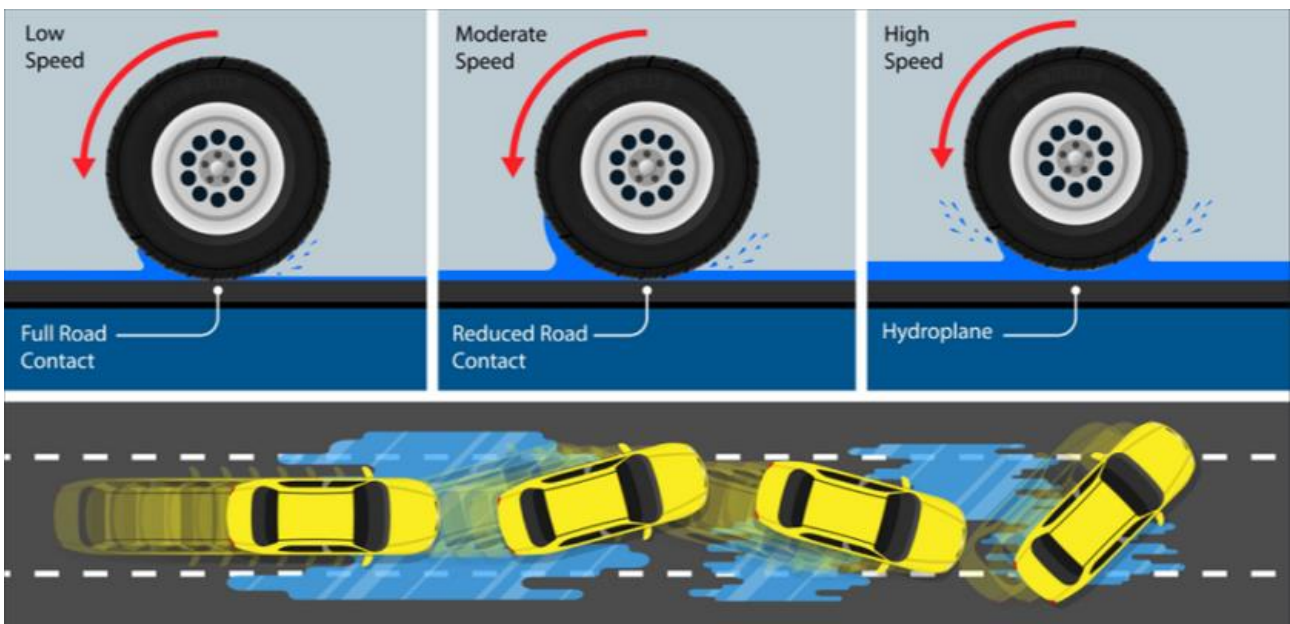


Figure 173. Possible contact conditions occurring during water friction.

In real life application three different scenarios can occur: direct contact, partial contact or no contact between substrate and rubber (aquaplaning), depending on several factors such as sliding speed, tread design, tyre size and depth, pressure and the road surface. Aquaplaning occurs when water builds up in front of the tyres faster than the weight of the vehicle can displace it.

As a result, the water pressure pushes under the tyre creating a thin layer of water between rubber and road surface. The thin layer of water is the difference between the tyre (gripping the road) and the car losing completely the contact and sliding out of control. The deeper the water, the faster the speed, therefore it is more likely for aquaplaning to happen, preventing to brake or steer (further details are depicted in section 2.6.1).

In this work, it is assumed that in water condition occurs a hysteresis contribution (with the hypothesis that is not changing from wet to dry condition) and a partial adhesion contribution, called adhesion wet contribution, which appears when the lubricant squeezes out establishing direct contact between rubber and substrate. The lubricant dewets in water condition by the nucleation of dry patches establishing a dry contact between the bodies.

The dry patches phenomenon based on the spreading coefficient  $S$  (see Eq. (25)) which defines the energy balance of the interfacial free energy between substrate, rubber and liquid. A higher negative value reveals the higher occurrence of dry patches. The dispersive and polar components of the surface free energy for the liquids (water, water+soap5% and soap), rubber and substrate (aluminium multi-indenter) were calculated from contact angle measurement.

Figure 174 depicts the result of the contact angle measurements of rubbers obtained considering three different standard liquids (L) with defined properties, see Table 14: water (very polar), ethylene glycol (EG, slightly polar) and diiodomethane (DME, less polar).

Table 14. Polar and dispersion components of the selected surface tension liquids.

<b>Surface tension</b>	<b>Water</b>	<b>EG</b>	<b>DME</b>
Polar	50.2	16	20.4
Dispersion	22.6	33.6	32.8
<b>Total</b>	72.8	54.0	48.8

First, the surface free energy of rubber (R) compounds was calculated by applying the OWRK (Owens, Wendt, Rabel, Kaelble) method.

$$\frac{\cos(\vartheta) + 1}{2} \frac{\gamma_L}{\gamma_{L,d}} = \sqrt{\gamma_{R,p}} \frac{\sqrt{\gamma_{L,p}}}{\sqrt{\gamma_{L,d}}} + \sqrt{\gamma_{R,d}} \quad (111)$$

$$y = mx + c$$

The linear equation was solved uniquely (based on the known values of  $\gamma_L$ ). The variables m and c represent the polar and dispersion components of the rubber respectively.

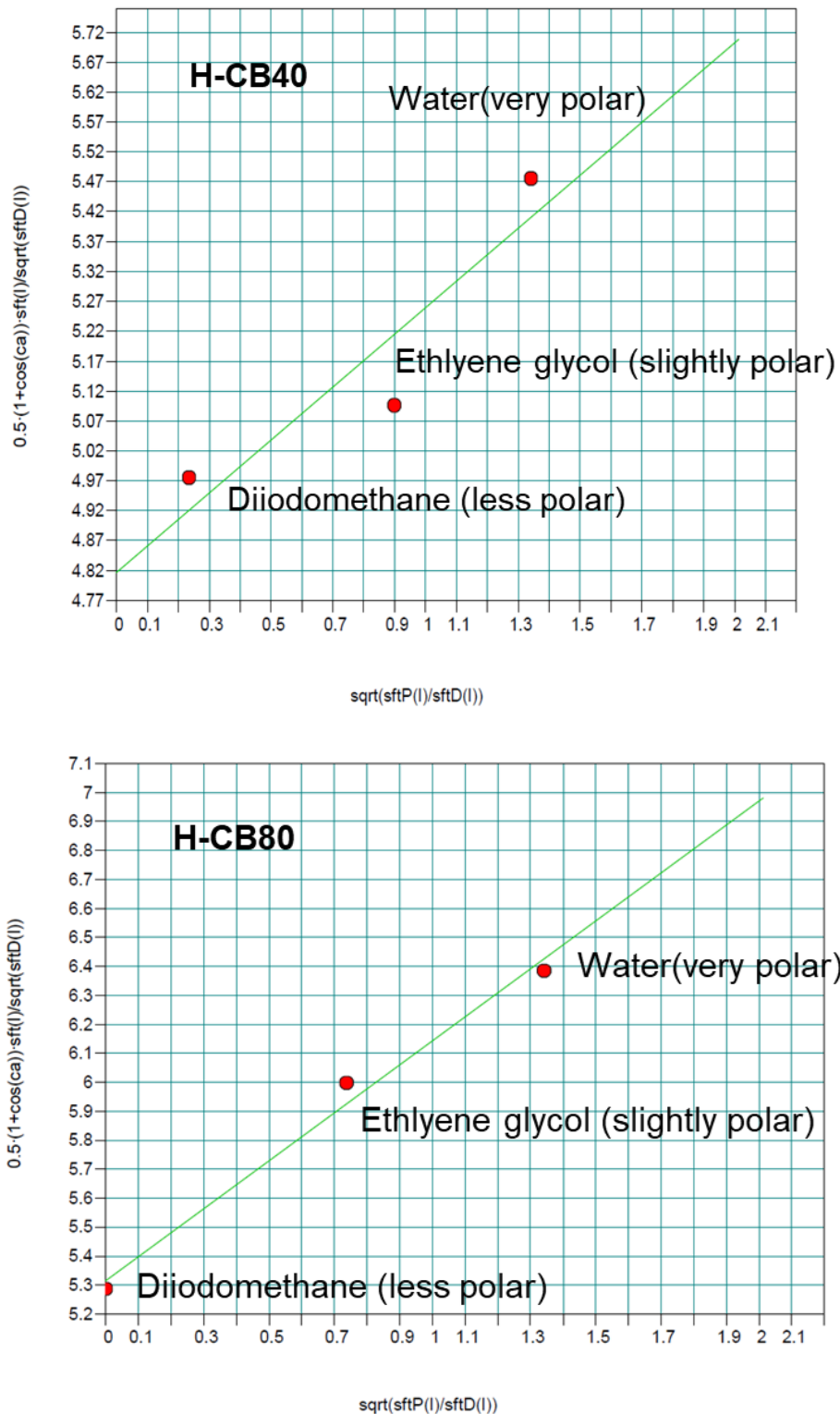


Figure 174. Calculation of the surface free energy (dispersion and polar components) for H-CB40 and H-CB80.

Second, the interfacial surface free energy components  $\gamma_{ij}$  (see Eq. (111)) of the friction system was determined to calculate the spreading coefficient.

$$\gamma_{ij} = \left( \sqrt{\gamma_i^d} - \sqrt{\gamma_j^d} \right)^2 + \left( \sqrt{\gamma_i^p} - \sqrt{\gamma_j^p} \right)^2 \quad (112)$$

Table 15 and Table 16 portrays the interfacial surface free energies  $\gamma_{RL}$ ,  $\gamma_{RF}$  and  $\gamma_{FL}$  where R, L and F represent rubber, liquid and substrate respectively.

Table 15. Interfacial surface free energies  $\gamma_{RL}$ ,  $\gamma_{RF}$  and  $\gamma_{FL}$  in mN/m by considering H-CB40 as rubber, aluminium multi-indenter as substrate and water, water+soap5% and soap as liquids.

	$\gamma_{RL}$	$\gamma_{RF}$	$\gamma_{FL}$
Water	12,379	5,904	35,405
Water+soap5%	4,460		20,440
Soap	3,805		19,013

Table 16. Interfacial surface free energies  $\gamma_{RL}$ ,  $\gamma_{RF}$  and  $\gamma_{FL}$  in mN/m by considering H-CB80 as rubber, aluminium multi-indenter as substrate and water, water+soap5% and soap as liquids.

	$\gamma_{RL}$	$\gamma_{RF}$	$\gamma_{FL}$
Water	12,656	7,693	35,405
Water+soap5%	3,081		20,440
Soap	3,113		19,013

Third, the spreading coefficient was calculated (Figure 175) according the Eq. (23). The spreading coefficient was selected as a physical parameters to evaluate the occurrence of dewetting phenomena.

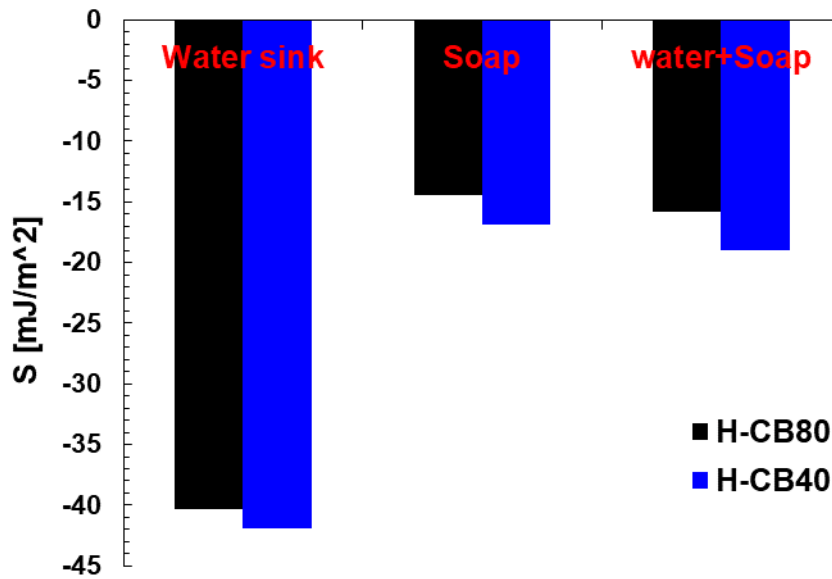


Figure 175. Spreading coefficient  $S$  by considering the liquids water, water+soap5% and soap in the case of multi-indenter and two different rubbers (H-CB40, H-CB80).

Negative values of the spreading coefficient  $S$  reveals an incomplete wetting whereas  $S > 0$  reflects complete wetting (Figure 176).  $S$  showed significantly negative value in the case of water which reflects a dewetting transition occurring in the asperity contact regions (dry asperity contact). In other words, the liquid film between the rubber and the substrate dewets with a certain dewetting speed  $v_d$  leading to the nucleation of dry patches establishing a direct contact rubber-substrate. This confirms the spreading coefficient is a key parameter to describe the wetting behaviour. Water condition showed a pronounced negative value of the spreading coefficient, therefore higher dry patches occurrence in comparison to the other lubricants as soap or water+soap5%.

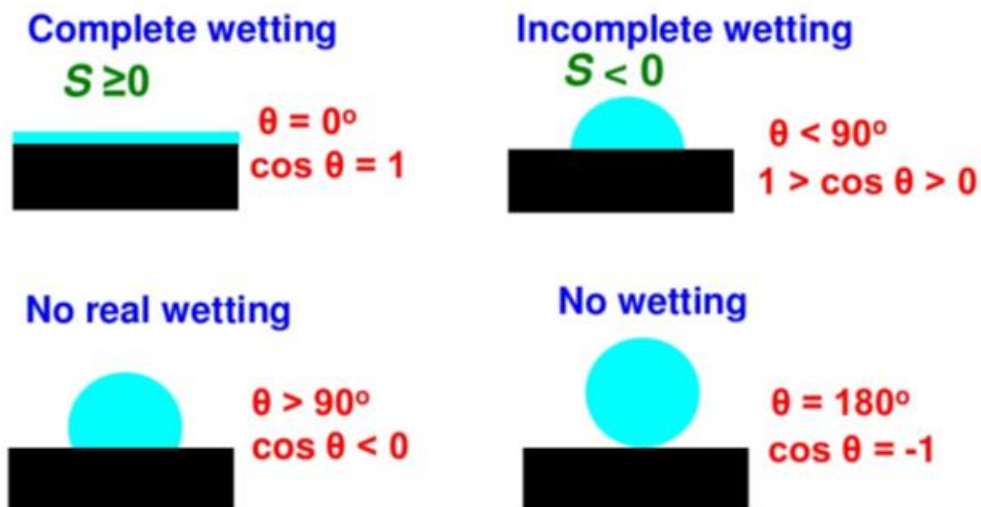


Figure 176. Different wettability occurrences according the affinity between lubricant and counter surface reflecting different spreading coefficient values.



Once rubber has a partial real contact with the substrate under water condition, the real contact area gets increased due to the dewetting effect. The latter effect based on the dewetting speed which is proportional to the spreading coefficient and inversely proportional to the viscosity of the liquid  $\eta$ , modulus of rubber  $E$  and minimum film thickness  $h_{min}$  [97] [96] [160] [161].

$$v_d = \frac{S^2}{h_{min} \eta E'} \quad (113)$$

The squeeze-out effect of the water increases with the dewetting speed and the dewetting phenomenon depends on sliding speed as illustrated in Figure 177.

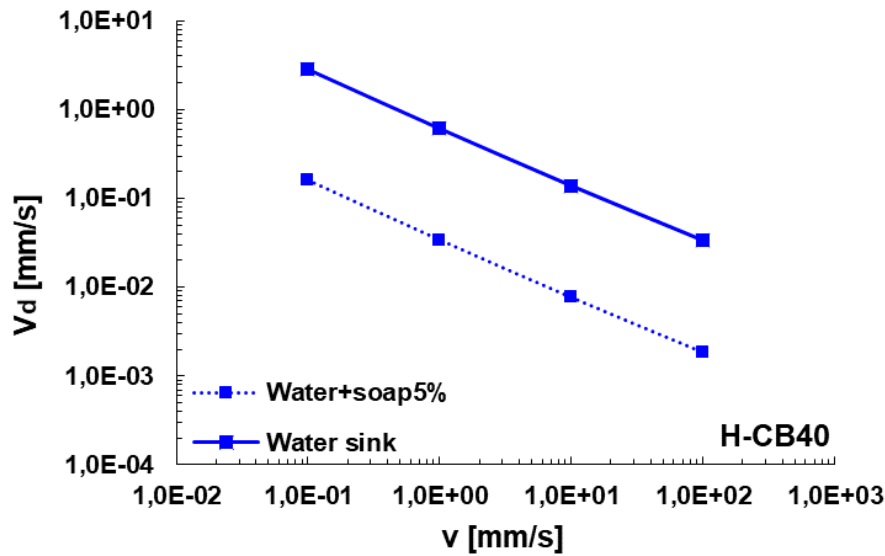


Figure 177. Dependence of the dewetting speed with the sliding speed in the case of water and water+soap5% conditions.

The dewetting speed increased from water+soap5% to water condition which confirms higher occurrence of dry patches in water condition. The minimum film thickness  $h_{min}$  is calculated according Hamrock and Dowson [162] which takes not into account the substrate roughness,  $E'$  is extrapolated from the viscoelastic master curve at the excitation frequency ( $f=v/\lambda$ ) induced by the substrate asperities. Based on the results above reported, it was assumed the hysteresis friction is enhanced with a partial adhesion friction in water condition where the water is wiped away. This was estimated through an alpha parameter  $\alpha$  (Eq. (114)), it varies between 0 and 1 and quantify the level of adhesion in the water. An example for the materials H-CB40 and H-CB80 is portrayed in Figure 178.

$$0 < \alpha = \frac{\mu_{Adh}^{water}}{\mu_{Adh}^{dry}} = \frac{\mu_{exp}^{water} - \mu_{Hyst}^{FEM}}{\mu_{Adh}^{dry}} < 1 \quad (114)$$

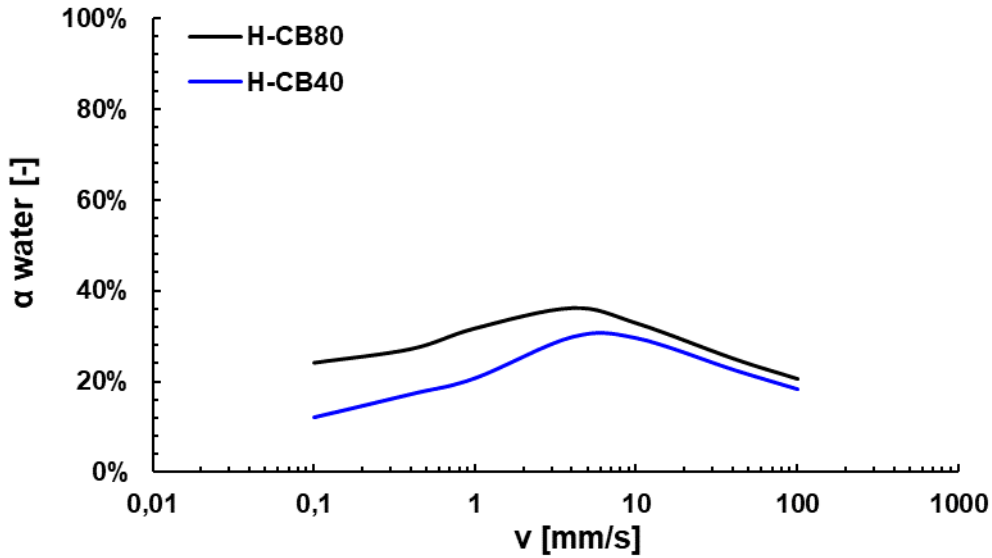


Figure 178. Estimation of the adhesion level in water condition through alpha parameter for H-CB40 and H-CB80 in the case of multindenter.

The estimated values were around 10% and 35% depending on the sliding speed and decrease for large speeds because of the reducing time for the water to squeeze out of the contact. H-CB80 showed higher dry patches occurrence at lower speeds, less than 10mm/s, due to higher local pressure. This is caused by the lower real contact area (see Figure 179) which induces higher dewetting compared to H-CB40. The grip condition and local pressure allow the tyre to cut better the water layer in the case of H-CB80.

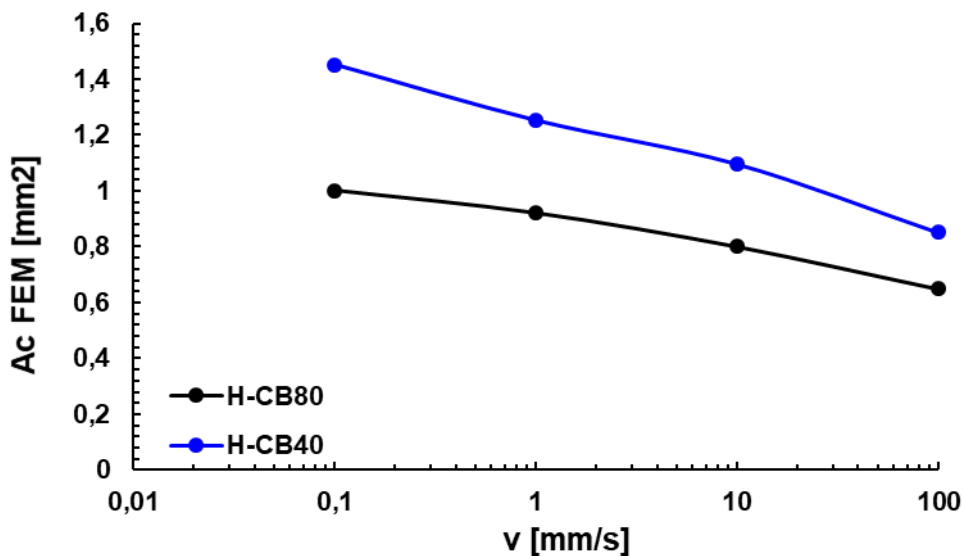


Figure 179. Calculation of the real contact area for compounds H-CB40 and H-CB80 in the case of multi-indenter.

The water friction consists of hysteresis and an adhesive interaction due to the occurrence of dry patches, the latter depends on the wettability of the system. The most influential parameters are the stiffness of rubber, viscosity of liquid and spreading coefficient (therefore the interfacial free energy of rubber/substrate and liquid).

Figure 180 shows the level of adhesion in wet multi-indenter and fine granite surfaces estimated through the parameter  $\alpha$ . The fine granite surface showed a flatter trend with the sliding speed in comparison to the multi-indenter reflecting a different topology of the countersurface (macro and micro length scales). The macro texture is responsible of the water evacuation from the contact especially at higher speeds. The micro texture favours through its sharpness the breakdown of the water at low speed due to higher local pressure. The affinity of the system rubber / surface / liquid influences the water grip as previously discussed.

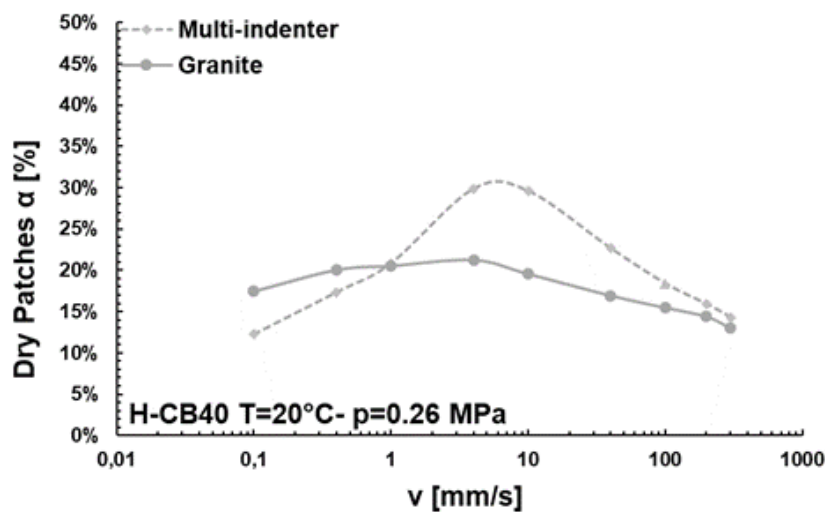


Figure 180. Occurrence of the dry patches ( $\alpha$ ) effect in water condition for multi-indenter and fine granite.

## 4.6 Thermal effect investigation

In this chapter, the thermal effect, also called heat build-up (HBU), is investigated. According to the contact condition, the friction behaviour varies due to the increase of temperature produced during the sliding of the rubber block relative to the rough surface. Therefore, the rubber geometries and the lubricant influences on the friction heating are reported below.

### 4.6.1 Estimation of heat build-up on dry rough substrate

The combination of geometry and material effects were investigated on dry and lubricated condition to figure out their impact on hysteresis friction.

The adhesion and the heat build-up (HBU) changed the friction behavior in dry condition based on the geometry of the rubber block (see friction curve in Figure 133). Therefore, the heat build-up was investigated for the three aforementioned geometries (different ratio  $L/W$ ). This geometrical effect affected the energy dissipated of the rubber and consequently its amount converted in heat.

A dry friction test was performed on fine granite at room temperature considering a sliding distance of 4 meters and high velocity of 100mm/s in order to observe the heat build-up phenomena. The rubber temperature is measured with an infrared-camera located in front of the rubber block with a resolution of 0,2 mm (see Figure 181).

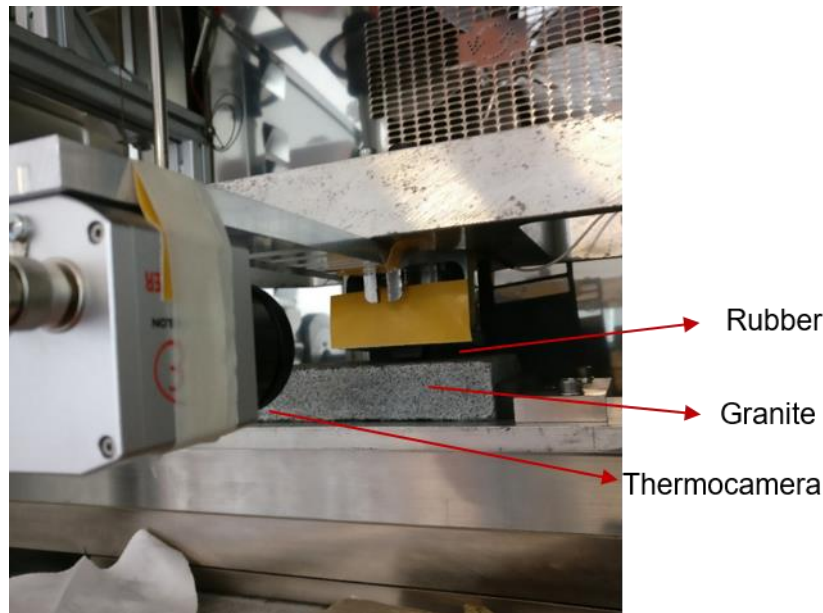


Figure 181. Set up of the friction measurement on fine granite and the measurement of the rubber temperature due to the friction heating by using an infrared camera.

Figure 182 displays a frame of the heat build-up, detected by the infrared camera, during the sliding friction of rubber on the dry fine granite at sliding speed of 100mm/s. Assuming to split the rubber in three longitudinal sections the following was defined: (i) 1° rubber layer of 2 millimeters close to the contact with the granite where the thermal effect is more pronounced because the main part of energy is dissipated in such area, (ii) 2° rubber layer with intermediate heat build-up, (iii) 3° rubber layer where no significant heat build-up is growing up.

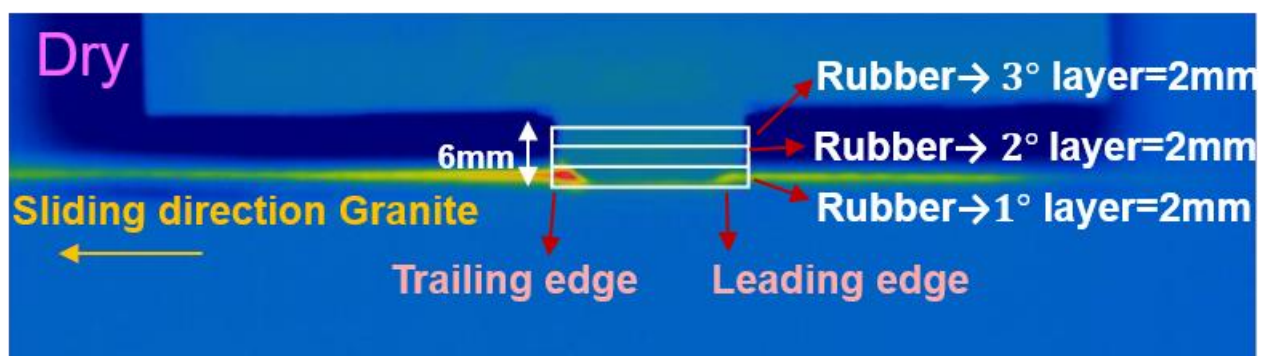


Figure 182. Visualisation of a frame detected with an infrared camera of the heat build-up occurring during sliding friction of H-CB80 compound on dry fine granite at cyclic sliding speed of 100mm/s.  $T_{air}=20^{\circ}C$ ,  $p=0.26MPa$ , sliding distance=0.1meter.

The heat build-up was more pronounced at the trailing edge. In fact, the leading edge of the rubber block continuously moves into contact with the cold road surface in front of the rubber block. Figure 183 depicts the maximum rubber temperature observed in the vertical direction  $y$  after a sliding distance of 4 meters in two different regions (trailing edge and middle sections).

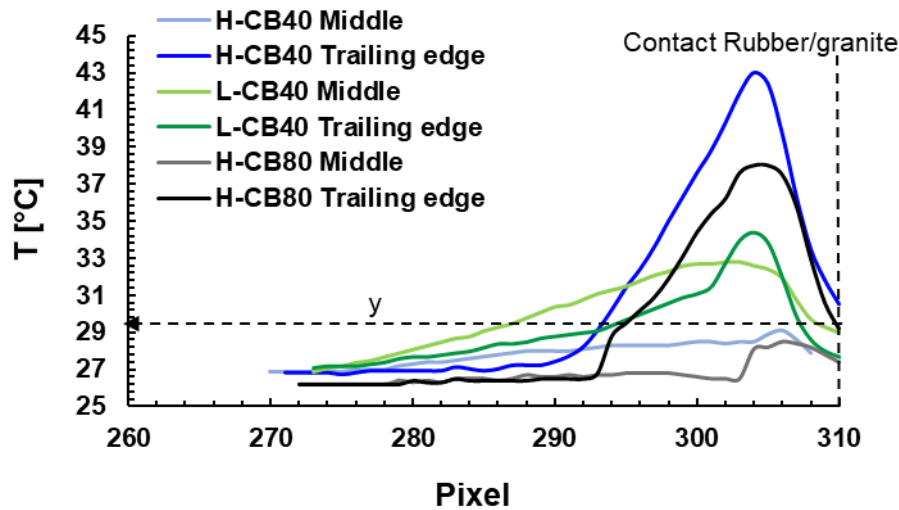


Figure 183. Rubber temperature distribution (bottom) through the rubber sample (see vertical coordinate  $y$ ) measured with an infrared camera at different paths of the rubber block (trailing edge and middle) for different materials at  $v=100\text{mm/s}$ .

The main energy dissipation produced at the interface rubber substrate was converted in heat and after that, flowed through the sample. This explained why the maximum temperature was located around  $y=0,4\text{mm}$  (pixel around 304 in the above picture) for each material. The rest of energy dissipation was dissipated in the air and in the sliding interface with the substrate by conduction. Such heat transfer is governed by the heat differential equation, which was solved in space and time domains as shown later on. The higher temperature growth appeared in H-CB40. Indeed the heat build-up resulted from two combined effects (i) real contact area, therefore the number of hot spots and (ii) amount of energy dissipated by viscoelasticity converted in heat.

The influence of the rubber block geometry on friction heating was studied. The maximum temperature (detected in the ultimate rubber layer close to the sliding interface) over the sliding time is plotted in Figure 184 for three different rubber geometries: (i)  $L/W=0,5$  short and wide rubber block, (ii)  $L/W=1$ , (iii)  $L/W=3,7$  long and narrow rubber block.

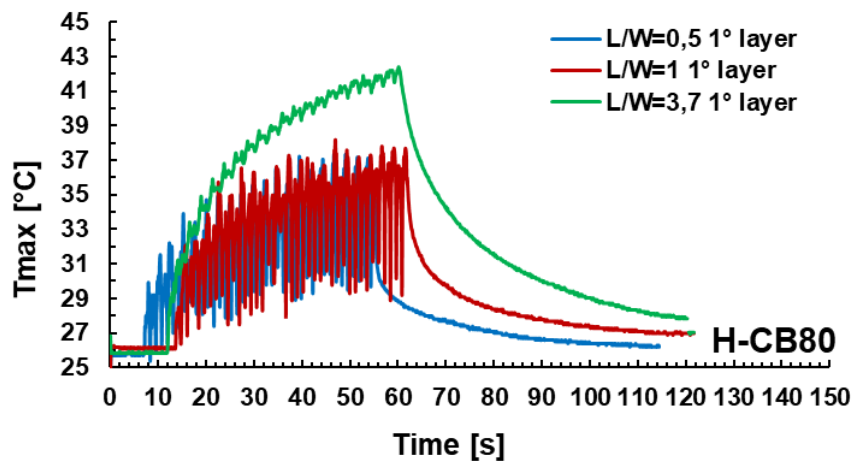


Figure 184. Max rubber temperature detected by an infrared camera in the ultimate rubber layer at the sliding interface with fine granite versus sliding time for three different geometries:  $L/W=0,5$  (blue),  $L/W=1$  (red),  $L/W=3,7$  (green).  $v=100\text{mm/s}$ , sliding distance:4meters,  $p=0.26\text{MPa}$ .

All rubber geometries exhibited a logarithmic increment of the maximum temperature with sliding time (and therefore the sliding distance) until a plateau. Two main effects were noted: first, a higher heat build-up (maximum temperature) appeared for all geometries at the trailing edge because the front part of the rubber block, also called leading edge, continuously moves into contact with the cold road surface in front of the rubber block. Second, the heat build-up was more pronounced for the long and narrow geometry (higher ratio  $L/W$ ). The friction heating manifested a stronger impact when the rubber slides parallel to the long side of the rubber block. The results were confirmed by repeating similar friction-temperature measurements on two identical rectangular rubber blocks with the same nominal area (without radius at the corner), where the rubber sample is rotated 90 degrees with respect to the second one (see Figure 185).

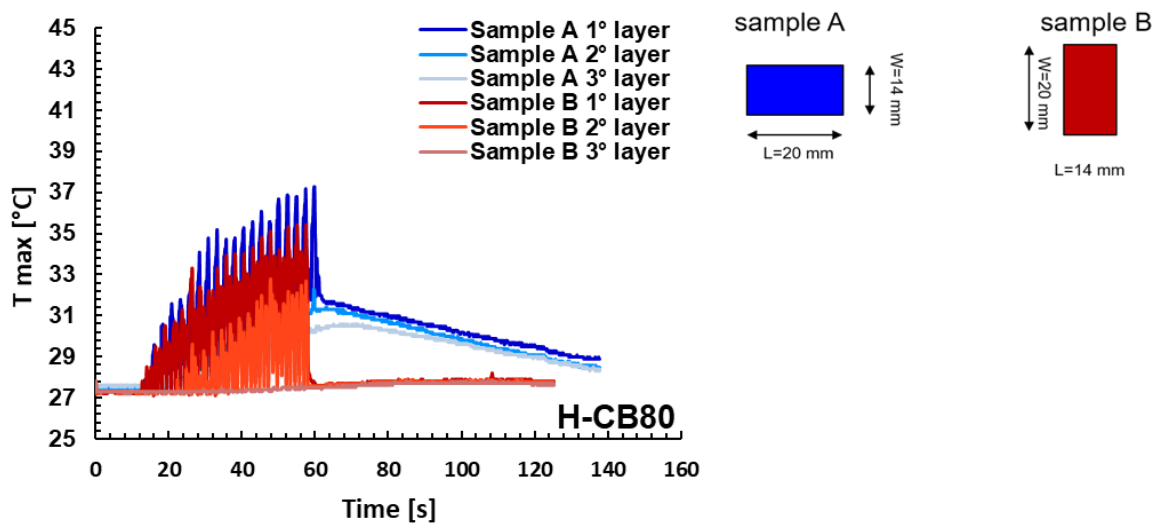


Figure 185. Measurement of the rubber temperature according to the orientation of the rubber block through different rubber layers ( $1^\circ$ ,  $2^\circ$  and  $3^\circ$ ) due to friction heating on dry fine granite. Blue: long and narrow sample, red: short and wide sample.  $v=100\text{mm/s}$ , sliding distance: 4 meters,  $p=0.26\text{MPa}$ ,  $T_{\text{air}}=26^\circ\text{C}$ .

In summary the energy dissipation determined high local temperatures in the contact regions between two bodies depending on sliding speeds (especially  $>10\text{mm/s}$ ), the geometry of the rubber sample and material properties (like loss modulus  $G''$ , heat conductivity, heat transfer coefficient) which strongly affect the friction (the so-called flash temperature) and wear behaviour. The viscoelastic properties vary causing a different friction coefficient response in comparison to the ideal isothermal condition. This is produced due to the friction heating (especially at the sliding interface) and the temperature increase of the rubber (Figure 186).

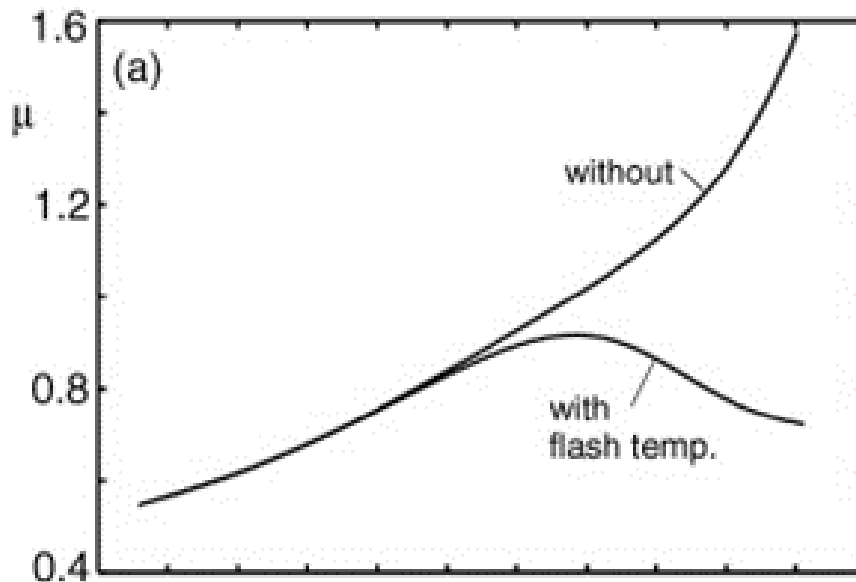


Figure 186. Simulated friction coefficient with/without considering flash temperature effect induced by heat build-up [112].

Finally, the heat build-up was simulated during sliding friction at  $v=100\text{mm/s}$  with 3d FEM in ABAQUS and compared with the infrared camera results detected in case of dry condition and material H-CB40 with  $L/W=1$  and a thickness of 6mm.

The simulation was performed in the case of simple substrate geometry to reduce the computational cost, such as a multi-indenter with a wavelength of 2 mm. The rubber and substrate were modelled as 3d deformable body (see Figure 187) assuming (i) an exponential trend of energy dissipation, generated by hysteresis, with the thickness  $y$  of the sample (see Figure 188), (ii) the total conversion of energy dissipation into heat and (iii) a linear heat flux body conduction with the sliding time through the rubber and the aluminum multi-indenter. The initial temperature for the bodies was set to  $T=20^\circ\text{C}$  as a predefined field. The coupled temperature displacement was used as a time step. The thermal conductance between aluminum and rubber was used as interaction and no thermo-mechanical coupling solution was used during the simulation. The material properties of multi-indenter and rubber are depicted in Table 17.

Table 17. Material definition of the thermo-FEM simulation.

	Rubber	Multi-indenter
Thermal conductivity K [W/mK]	0.23	205.0
Specific heat C [J/Kg K]	1880	910
Density [g/cm <sup>3</sup> ]	1.2	2.7
Mechanical behaviour	Hyperelastic +visco	Young modulus E=71GPa
Thermal conductance [W/m <sup>2</sup> ]	150	

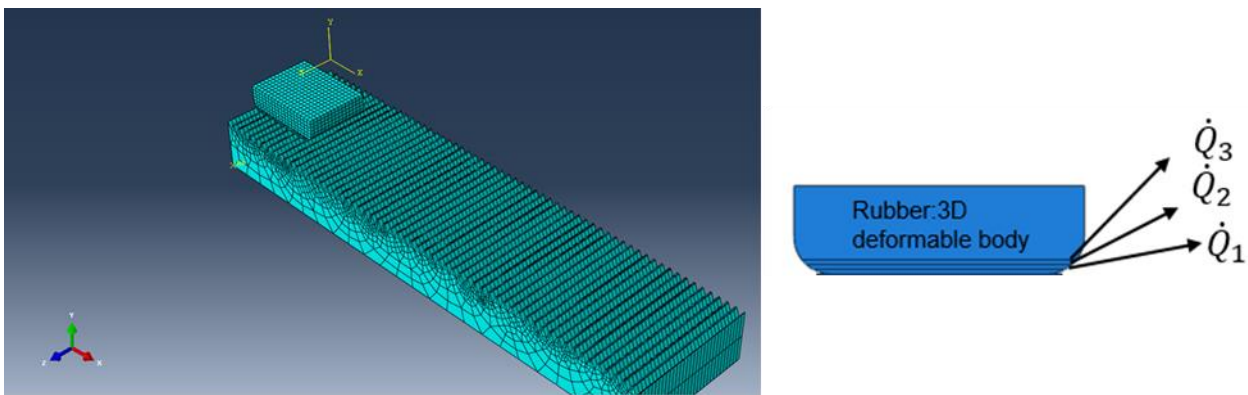


Figure 187. Set up of 3d FEM thermo-simulation (left) and the discretization of the heat flow through three thin rubber layers because of the conversion of energy dissipation into heat (right).

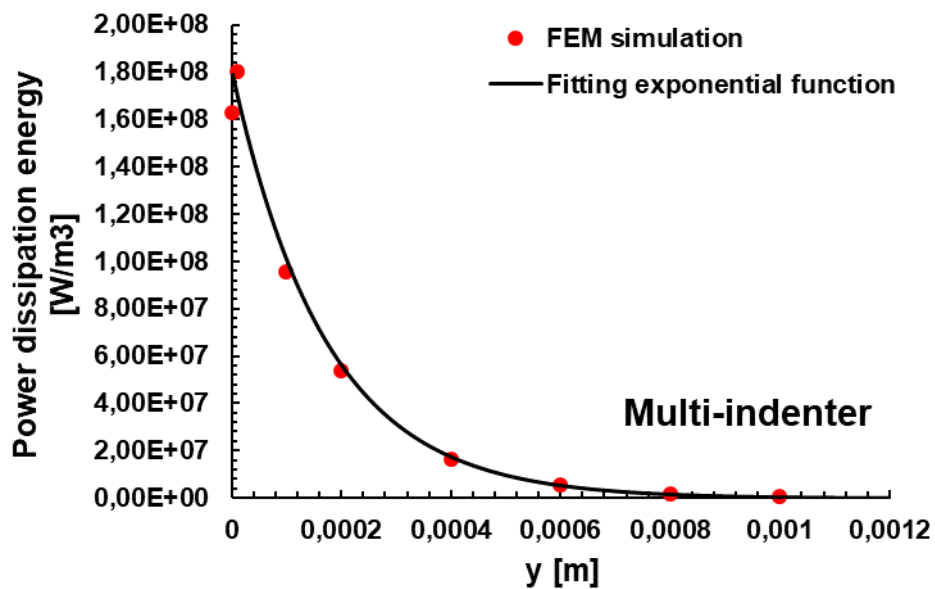


Figure 188. Trend of the dissipated energy density due to the hysteresis friction estimated by FEM and the corresponding fitting with an exponential decay function along the vertical sample direction in the case of fine granite and multi-indenter.  $v=100\text{mm/s}$ .



The nodal temperature evaluation (NT11) was extrapolated during the sliding friction. The result of the FEM thermo-simulation showed that the heat flows through the rubber sample produced an increase of 7°C locally (thickness layer 0-3mm) whereas the bulk average temperature (thickness layer 3-6mm) exhibited a lower increase  $\Delta T_{\text{average}}=3^{\circ}\text{C}$  (see Figure 189 and Figure 190). Furthermore, heat moved partially in the multi-indenter substrate by conduction causing also heat build-up in the countersurface. However, the results revealed a significant deviation in comparison with the values measured with an infrared camera due to the absence of friction heating in the current simulation induced by the adhesion effect and thermo-mechanical coupling. Further studies and refinements of the modelling are required.

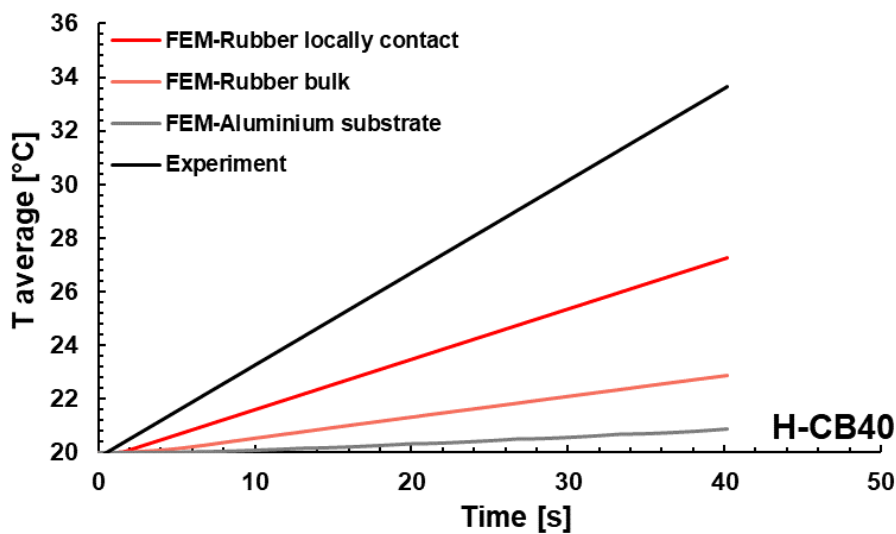


Figure 189. Comparison of the heat build-up occurrence in the experiment and FEM prediction on the rubber (local and bulk sections) and aluminium substrate.

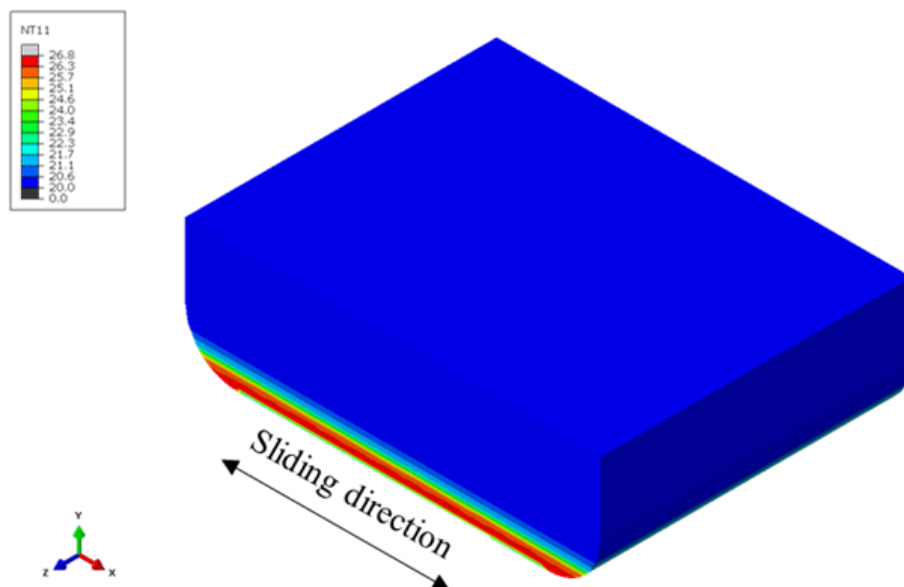


Figure 190. Estimation of the rubber nodal temperature (NT11) during sliding friction with a FEM thermal simulation.

## 4.6.2 Estimation of heat build-up on wet rough substrate

A significant change of the distribution and temperature level was found with the time and thickness of the sample. The low thermal conductivity of rubber and short contact time lead to negligible heat diffusion in the case of dry friction and high sliding velocity, consequently the temperature at the interface increases [136] [137].

In case of a lubricant at the contact interface, such as water soap mixture or water, the work expended by the asperities to deform rubber would still cause energy dissipation, but the high thermal diffusivity of the liquid medium will cool down the system. Hence, the heat transfer between rubber and liquid medium should be also taken into analysis to estimate in a proper way the temperature increase generated during wet friction, besides the dissipated energy density distribution. An infinite heat transfer coefficient was considered for the calculation of heat build-up generating in the sample during wet friction and the local energy dissipation was assumed to be exponential [91], based on the FEM simulation results. These assumptions allowed to find a solution for the heat flow differential equation presented in [163] for the case of semi-infinite solid with heat generated within it:

$$\frac{\partial^2 T}{\partial y^2} - \frac{1}{k} \frac{\partial T}{\partial t} + \frac{\dot{Q}}{K} = 0 \quad (115)$$

where T is the rubber temperature as a function of time t and space y,  $\dot{Q}$  is the rate of heat production per unit and volume, K is the thermal conductivity and k the thermal diffusivity. Assuming the heat production rate to be exponential like,  $Q = Q_0 e^{-\alpha y}$  and that the surface is kept at constant temperature, the following boundary condition apply:

$$T = \text{constant} = 0 \text{ at } y = 0 \quad (116)$$

The resulting increase  $\Delta T$  was calculated by solving the Eq. (115) in the case of semi-infinite solid with heat generated within it:

$$\begin{aligned} \Delta T = & -\frac{Q_0}{K\alpha^2} \operatorname{erf} \frac{y}{2\sqrt{kt}} + \\ & + \frac{Q_0}{K\alpha^2} \left\{ 1 - e^{-\alpha y} + \frac{1}{2} e^{(k\alpha^2 t - \alpha y)} \operatorname{erfc} \left[ \alpha\sqrt{kt} - \frac{y}{2\sqrt{kt}} \right] \right. \\ & \left. - \frac{1}{2} e^{(k\alpha^2 t + \alpha y)} \operatorname{erfc} \left[ \alpha\sqrt{kt} + \frac{y}{2\sqrt{kt}} \right] \right\} \end{aligned} \quad (117)$$

The local distribution of the dissipated energy density in the rubber block was computed during the sliding step considering ABAQUS isothermal simulations depicted in the previous sections. The increase of dissipated energy gained during a certain sliding time was divided by the period of time itself to determine the rate of dissipated energy density  $w$ . Such procedure was done in the case of

multi-indenter surface, as well as for the granite substrate, for 100 mm/s sliding speed as shown in Figure 191.

The trend of the dissipated energy density along the vertical sample direction turned out to be exponentially. Hence, the exponential function  $Q = Q_0 e^{-\alpha y}$  was used to fit this trend giving an  $R^2$  of about 0.92. Assuming the whole amount of energy loss to be converted into heat generation, they were quantified the parameters,  $Q_0$  and  $\alpha$ , necessary to determine the heat rate production and solve the Eq. (115).

The thermal diffusivity and thermal conductivity considered in the calculation for H-CB40 are  $\kappa = 1.16 \times 10^{-7} \text{ m}^2/\text{s}$  and  $K = 0.230 \text{ W/mK}$ .

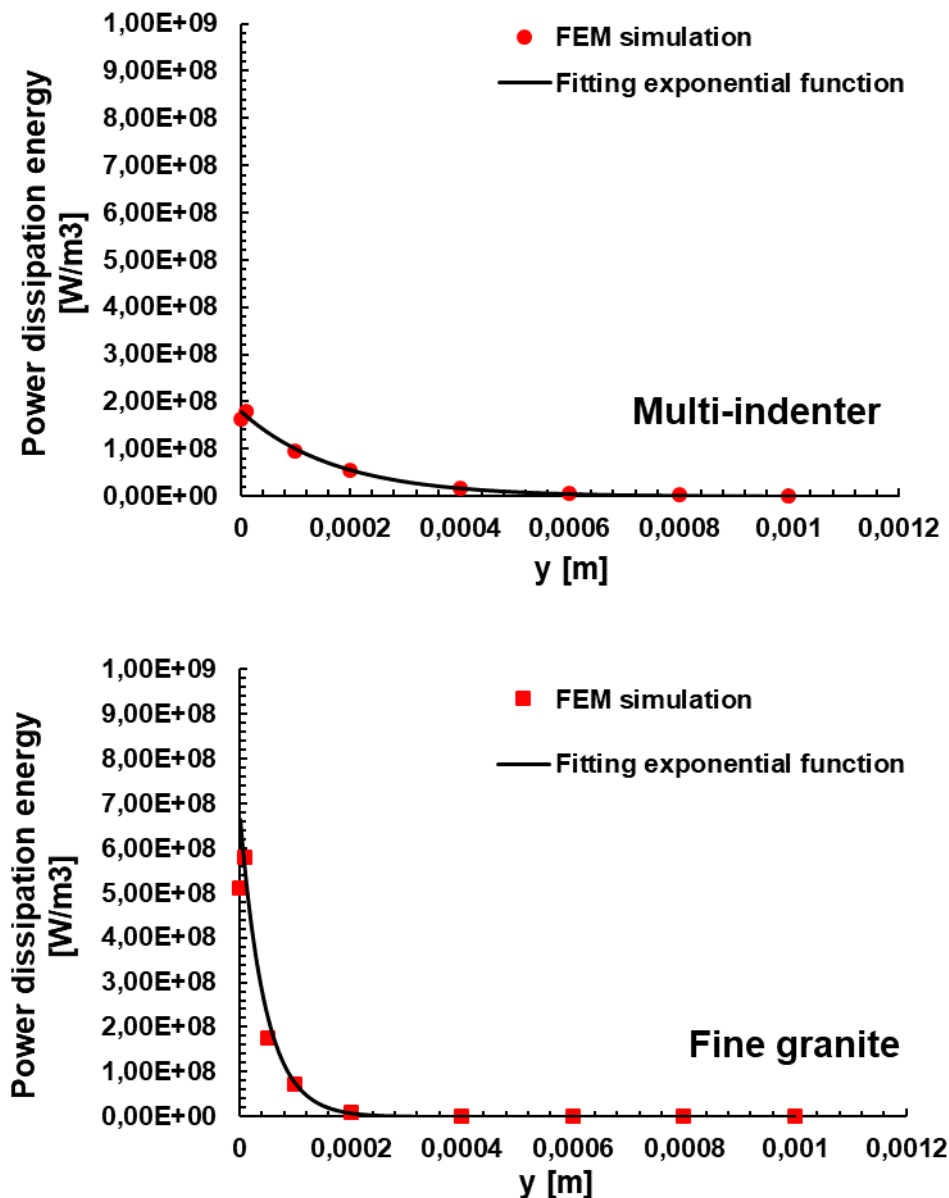


Figure 191. Trend of the dissipated energy density estimated by FEM and the corresponding fitting with an exponential decay function along the vertical sample direction in the case of fine granite and multi-indenter. H-CB40.

The energy was dissipated in a thinner layer in the case of granite. The heat build-up arising from hysteresis friction was calculated during lubricated condition and it is shown in Figure 192. The picture shows that in the case of sliding over the granite substrate the temperature increase was around 2°C whereas in the case of the multi-indenter was 7°C due to the occurrence of higher local strain. This was a simplified solution because the energy dissipation rate was assumed to be constant with the sliding time. In the real case an iterative calculation should be performed, which considers the change of material properties due to the temperature variation of sample.

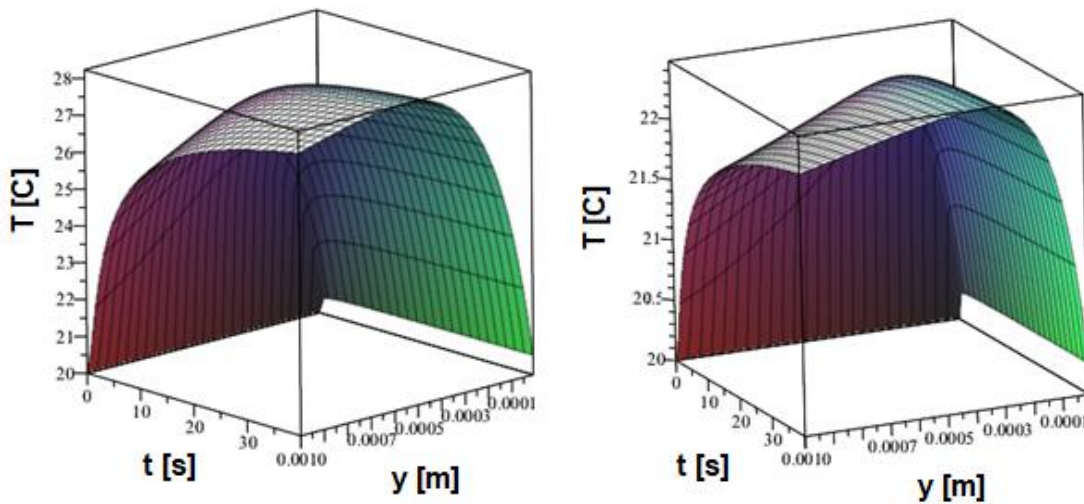


Figure 192. Temperature increases calculated by theoretical model in the case of multi-indenter (left) and fine granite (right). Sample H-CB40 slides at 100 mm/s.

## 4.7 Friction prediction on dry/wet rough surfaces

The friction problem was split into sub-issues (blocks) considering the approach displayed below (Figure 193). In this chapter, the solutions of the sub-issues were combined to solve the original friction problem regarding the grip prediction on dry and water conditions.

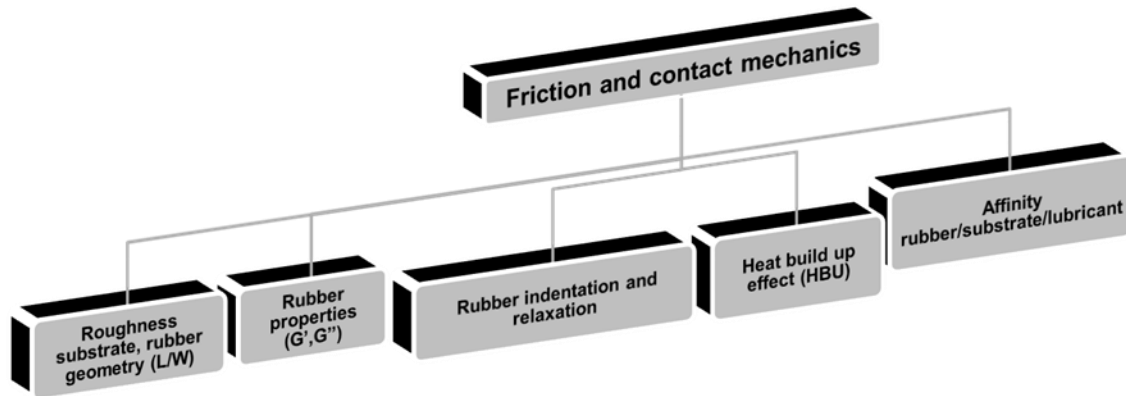


Figure 193. Problem solving of the friction behaviour.

A validation of the global response of the developed friction model (hybrid model) was done. First, a model rough surface was considered as multi-indenter, second a random real surface as fine granite. Under dry condition the hysteresis and full adhesion occurs as reported in the equations (105) and (106). The pure hysteresis induced by substrate roughness was estimated by the FEM as shown in chapter 4.3 whereas the adhesion was estimated by the analytical model shown in chapter 4.5. Figure 194 shows good prediction of the friction behaviour on dry and lubricated (water+soap5% and water) conditions, over a broad range of speeds, as a sum of adhesion and hysteresis friction.

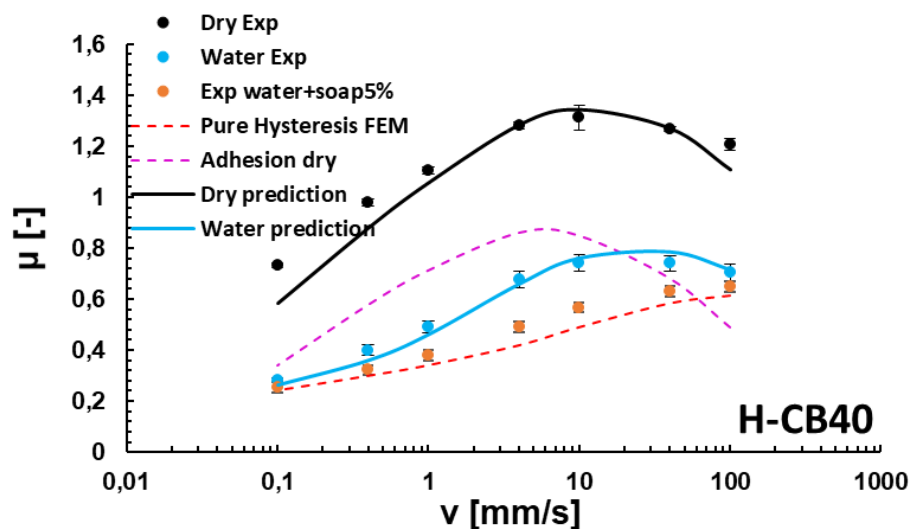


Figure 194. Prediction of the friction behaviour (dry and lubricated conditions) using a hybrid model (FEM for hysteresis and an analytical model for adhesion) in the case of H-CB40 on multi-indenter.  $T=20^{\circ}\text{C}$  and  $p=0.26\text{ MPa}$ .

The hysteresis friction (red line) was estimated by the FEM as previously shown whereas the adhesion (magenta line) was calculated by analytical model. An important outcome was the impact of hysteresis and adhesion in dry condition depending on sliding speed. An example for H-CB40 is depicted in Figure 195.

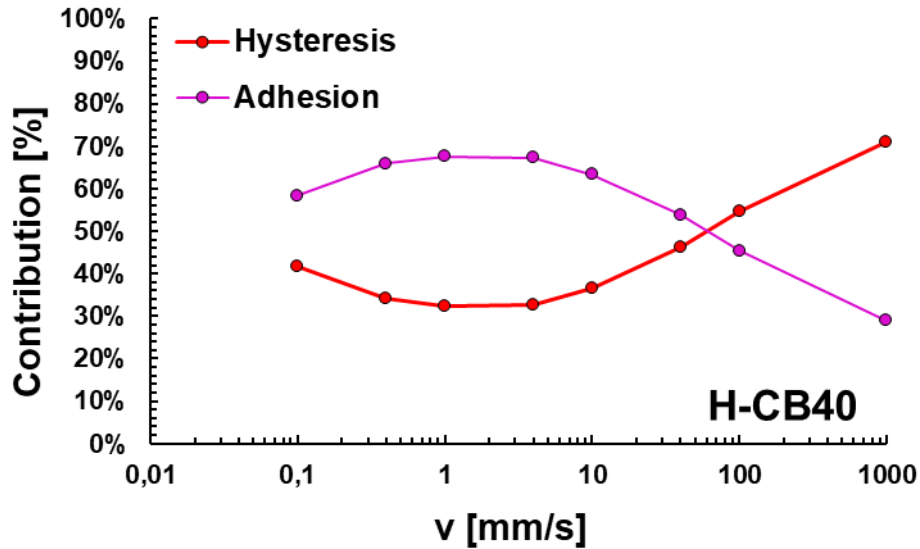


Figure 195. Impact of the hysteresis and adhesion (in %) on dry friction coefficient in the case of H-CB40 and multi-indenter surface.

Adhesion played a big role at slow speed whereas hysteresis became predominant at high sliding speed especially close to the ABS range application (~1m/s). The comparison of dry/wet experimental friction and the corresponding prediction are shown in Figure 196 in the case of the higher content of carbon black (H-CB80).

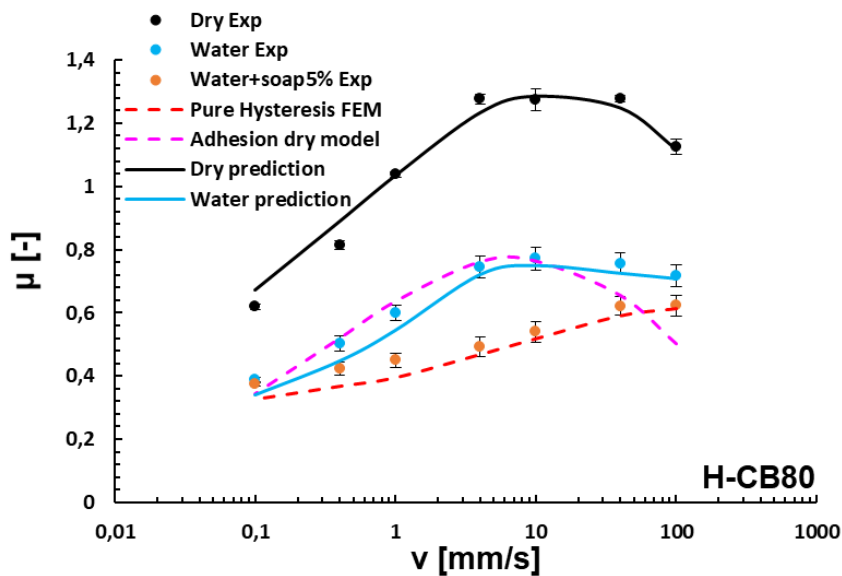


Figure 196. Prediction of the friction behaviour (dry and lubricated conditions) using a hybrid model (FEM for hysteresis and analytical model for adhesion) in the case of H-CB80 on multi-indenter.  $T=20^{\circ}\text{C}$  and  $p=0.26\text{ MPa}$ .

The adhesion is strongly dependent on the real contact surface between rubber and substrate, which is inversely proportional to the filler. The storage module  $G'$  increases with the filler content, establishing a dynamically stiffer behaviour during the sliding friction process, therefore the rubber penetrates less deeply into the cavities of the substrate and the real contact area decreases by increasing the filler amount.

Consequently, the friction behavior on aluminum dry condition is significantly influenced by the filler concentration in the elastomer mixture.

The impact of hysteresis and adhesion on dry friction is illustrated in the case of H-CB80 (Figure 197). The hysteresis contribution increases by increasing the sliding speed in comparison to the adhesion one. The crossover was located around  $v=50\text{mm/s}$ .

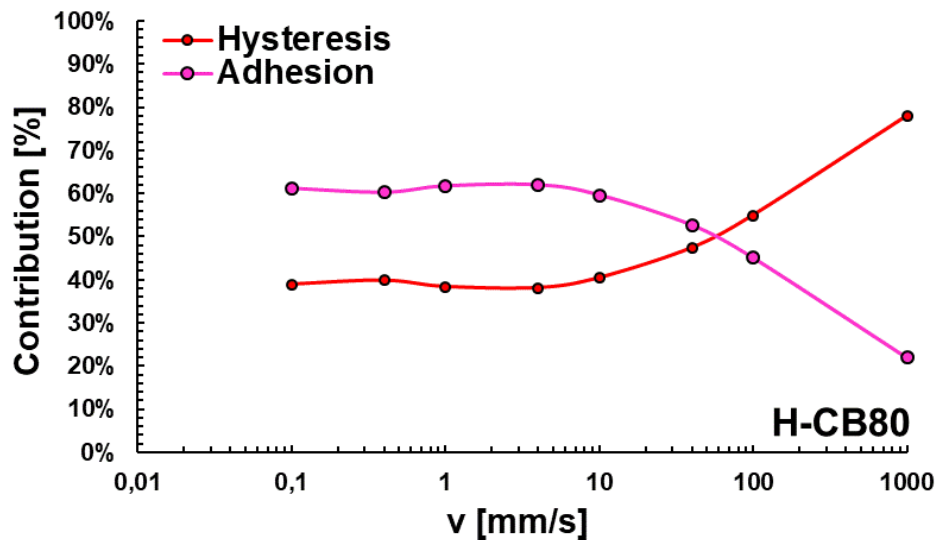


Figure 197. Impact of the hysteresis and adhesion (in %) on dry predicted friction coefficient in the case of H-CB80 and multi-indenter surface.

Figure 198 reports the prediction of dry and water grip on fine granite surface for low content of carbon black material (H-CB40) in case of a model surface (multi-indenter). In the appendix are reported the results for high content of carbon black (H-CB80).

The hysteresis friction (red line) was estimated by the FEM as shown in the previous graph whereas adhesion (magenta line) was calculated with the analytical model.

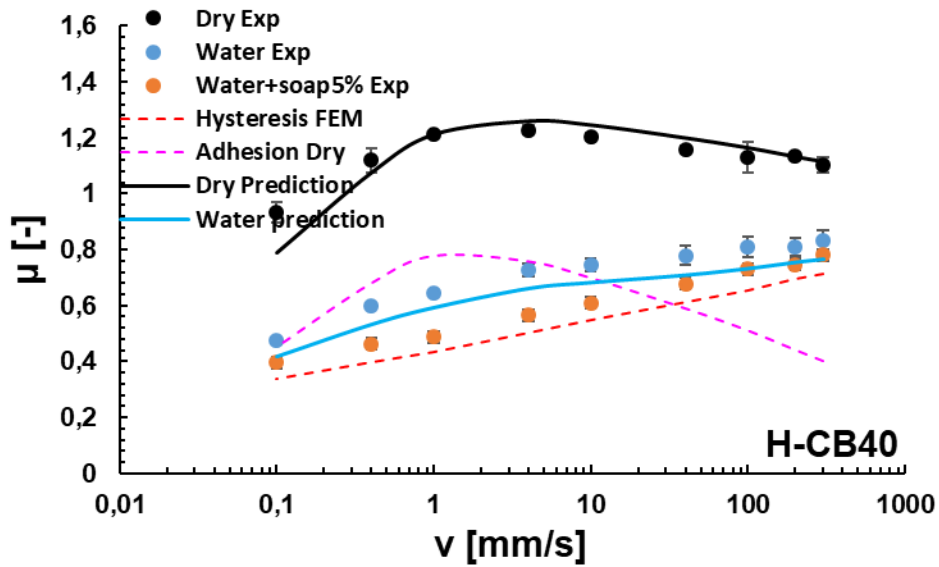
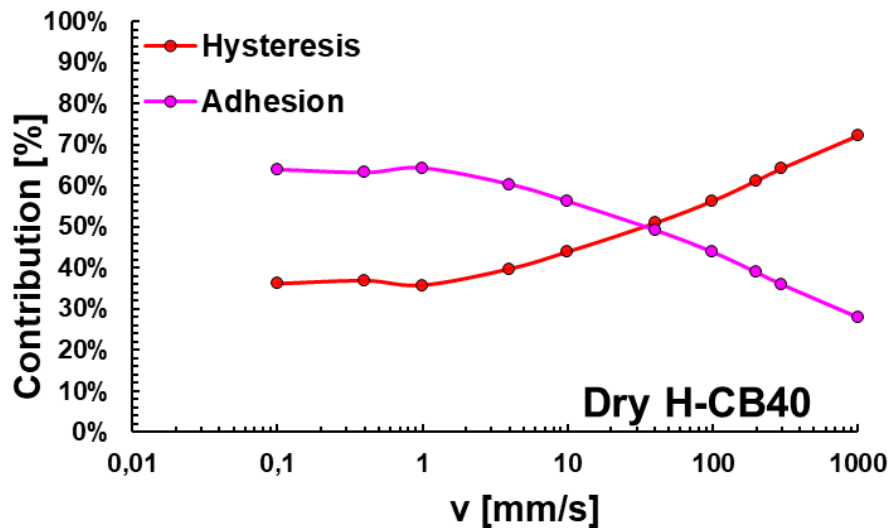


Figure 198. Prediction of the friction behaviour (dry and lubricated conditions) using a hybrid model (FEM for hysteresis and an analytical model for adhesion) in the case of H-CB40 on fine granite.  $T=20^{\circ}\text{C}$  and  $p=0.26\text{ MPa}$ .

The impact of the hysteresis and adhesion on dry and water condition in the case of fine granite is reported in Figure 199. In this case the crossover was shifted to a lower velocity and the decrease of the adhesion began before indicating a smaller cut-off length scale in comparison with the multi-indenter.





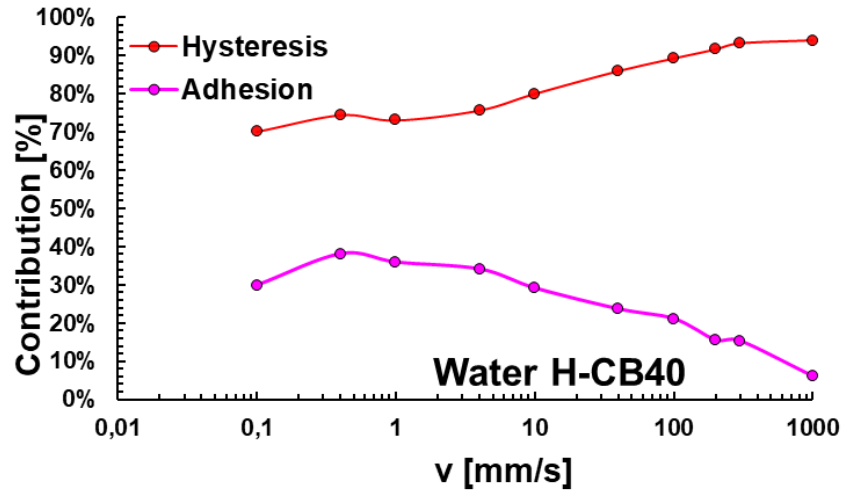


Figure 199. Impact of the hysteresis and adhesion (in %) on dry and water predicted friction coefficient in the case of H-CB40 and real rough surface (fine granite).

The results for H-CB80 in case of fine granite are reported in the appendix.

## 4.8 Dry friction master curves

In the last chapter, the dry friction master curves were constructed by applying the WLF principle as portrayed in the Grosch's work. First, friction tests were carried out up to 1,5m/s with a high-speed linear tribometer available in DIK at different temperatures in dry condition. The results in the case of multi-indenter are shown in Figure 200.

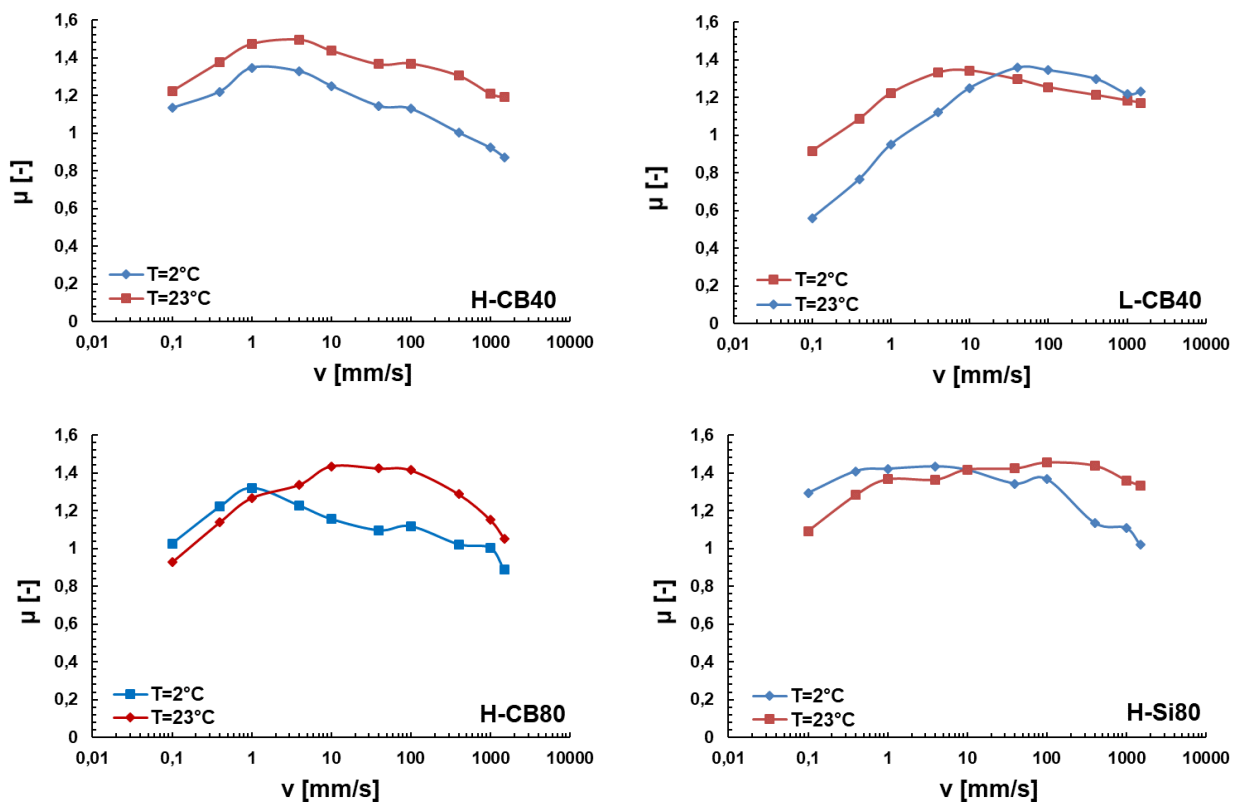


Figure 200. Friction measurements at  $T=2^{\circ}\text{C}$  and  $T=23^{\circ}\text{C}$  on multi-indenter surface.  $p=0.24\text{MPa}$ .

Second, the WLF principle was applied to construct the friction master curve, the same determined from the viscoelastic master curves. The combination of measured friction branches for different temperatures resulted in a continuous friction master curve over a broad velocity range. Figure 201 portrays the friction behaviour over a wide range of sliding speeds in the case of multi-indenter and asphalt surfaces.

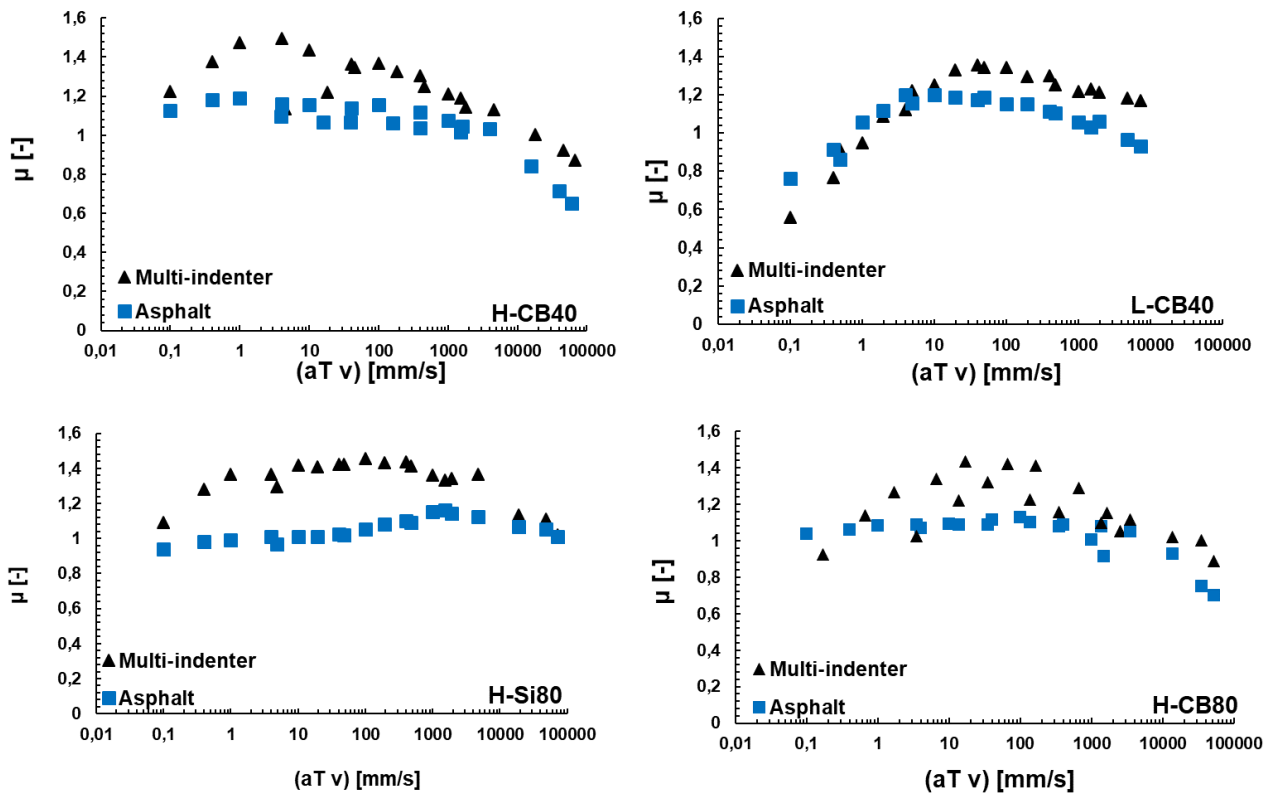


Figure 201. Dry friction master curve ( $T_{ref}=20^{\circ}C$ ) in the case of multi-indenter and asphalt surfaces.  $p=0.24$  MPa.

The strong decay of friction was denoted at high speeds by reflecting the crossing of  $G''$  peak and consequently the reduction of the energy dissipation at high speed ( $>1m/s$ ). This is clear by comparing the friction master curve of H-CB40 and L-CB40 with the corresponding loss modulus master curve of the materials (see Figure 202). Consequently, the decay of friction with the sliding speed appears before in case of HTg compounds due to the nature of the elastomer.

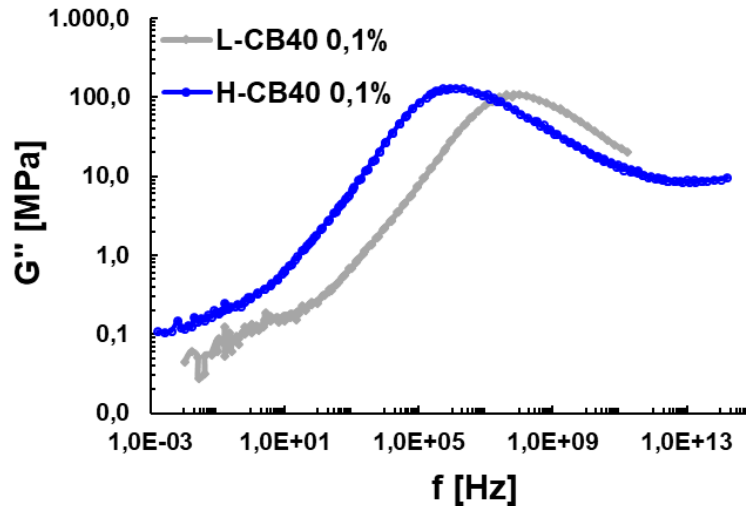


Figure 202. Loss modulus  $G''$  master curve at  $T=20^{\circ}\text{C}$  for H-CB40 and L-CB40.

Furthermore, the reduction of the adhesion level plays a role on the resulting friction behaviour. The adhesion is strongly dependent on the real contact surface between rubber and substrate (see also Eq. (110)), which decreases due to the filler increase. The storage module increases with the excitation frequency, and equivalently with the sliding speed, this results in a dynamically stiffer behavior of the material. Therefore, the rubber penetrate less deeply the cavities of the substrate surface and the real contact area while the friction coefficient decreases. Based on this, it was found that the friction behavior in dry condition was significantly influenced by the filler concentration in the elastomer mixture.

Finally, it was found a higher friction for multi-indenter in comparison to the asphalt surface due to higher real contact patch, which revealed higher grip.

By comparing the pictures in Figure 201, it was observed that the decay of the friction coefficient started at a lower sliding speed for “HTg system” in comparison to “LTg system”. This confirmed the viscoelastic nature of adhesion friction in dry condition.

## 5. Summary and conclusions

The stationary friction behaviour of elastomeric materials on rough surfaces was experimentally determined for various friction combinations and linked to the physical properties. The main topic of the thesis was the investigation of contact mechanics and friction occurring between filled rubber and rough rigid substrates during the sliding process depending on the substrate roughness, rubber-surface affinity, temperature, load, sliding speed, lubrication, geometrical parameters and viscoelastic material properties. Therefore, the complex friction process was solved by using the “divide et impera” approach.

First, the problem was split into different subtopics where each contribution was modelled and solved and afterwards a combination of the solution from each sub-problem was done to verify the global response of the friction model developed. The contact mechanics was investigated through a 2D FEM tool on different substrates to determine the main friction contribution called hysteresis which is caused by the energy losses on a broad frequency scale due to cyclic deformations of the rubber in the asperities. A friction test campaign was carried out using lubricated model sinusoidal substrates to minimize the adhesive contribution. The velocity dependence of the friction coefficient showed a correlation with the dynamic mechanical properties of rubber, confirming the viscoelastic nature of hysteresis friction.

A 2D-finite element model (FEM) was developed to investigate the friction problem. A visco-hyperelastic material model, based on the generalized Maxwell model was used to evaluate the hysteresis friction by considering time and frequency domains. The characterization of the materials was performed at high strain comparable to those expected in the friction application to identify accurate material parameters, which take into account the non-linear mechanical behaviour as well. The model was built with no tangential interaction between rubber and substrate to investigate only the contribution coming from hysteresis. The finite element analysis (FEA) performed for several filled compounds sliding over wavy model substrates confirmed the experimental findings and the strong connection between viscoelasticity and friction. To investigate the pure hysteresis contribution in the case of substrates with complex textures, FEA simulations were performed as well for randomly rough surfaces like granite. The substrate was modelled as a rigid profile in a two-dimensional model. The FEM simulation can be submitted for a speed range higher than the equipment capability under isothermal conditions. The friction coefficient estimated at high velocities can be reproduced by the experimental results applying the time-temperature superposition which is based on the WLF parameters retrieved from dynamic mechanical measurements. The overlapping obtained between the data measured at high velocities and high temperature with the points measured at low velocities and low temperature confirmed the validity to construct the friction master curve, as reported in the literature. The accuracy of the simulations was highly dependent on the material parameters adopted for the FEM, which must be determined through a complex modelling fitting procedure. As a result, the prediction of the measurements was achieved by using model compounds close to tread-like non-linear compound formulation. This can serve as a fast tool to develop tread compounds based on

laboratory data. Future investigations might consider the improvement of the material model used, since the stress softening effect was not considered, therefore deviations were found in comparison to the experiment when replicating high frequency conditions in the MHz-order usual in tyre applications.

The effect of the rubber geometry on dynamic contact mechanics was investigated through experimental and 3D FEM simulations. One of the most interesting geometry effects studied was the ratio between length  $L$  and width  $W$  of the rubber block. The nominal area was kept constant by considering three samples with different ratio between length and width (from 0,5 to 3,7). Under lubricated condition (that means in the condition close to pure hysteresis), the friction coefficient increased by reducing  $L/W$  for all sliding speeds due to the edge effects at the rubber corner. Water and dry friction did not show a clear trend due to the occurrence of adhesion and temperature effect. The geometry effects were studied with 3D-FEM friction simulations by considering the aforementioned different ratio  $L/W$ . The simulations analysed the rubber pattern effect on hysteresis friction and confirmed the increment of friction by reducing the ratio  $L/W$  because of higher energy dissipation coming from the rubber edges with a short / wide rubber block. A dependence between the energy dissipation and the local strain was found, based on the dynamic contact of the asperities with the different sections of the rubber block: leading-trailing edges and middle. A significant contribution on the energy dissipation and the resulting hysteresis friction derive from the edges which is proportional to the factor of  $(G''/G^*) \gamma^2$  extrapolated from the master curve at the excitation frequency and actual strain.

An accompanying new experimental tool was developed considering a linear friction equipment based on laser distance measurements to determine the relaxation process originated during the rubber deformation and depth of rubber indentation into the substrate cavities. This provides a physical understanding of the static and dynamic contact problems and a validation tool of the FEM model.

The experimental technique was carried out through a laser sensor placed below the substrate. The laser beam goes through a pinhole (drilled through the substrate) located exactly between two asperities, to observe the bottom of the rubber sample and thus detect the indentation statically and dynamically during sliding friction. The measurements reveal a time dependency of indentation due to material relaxation. The static indentation reflects the mechanical behaviour of the material in quasi-static condition as shown the stress-strain curves. Stiffer behaviour results in lower indentation whereas a higher permanent set induced stronger differences in the indentation level between virgin and second cycle at lower loads. Additionally, a dependence between the indentation and deformation history of the rubber occurred because of the stress softening effect. Dynamic conditions were tested by varying nominal load and sliding speed as well. The measurement was performed with a defined test setup. In the first step, the load was applied for a certain time, as a result, the elastomeric material relaxed until an equilibrium state. In the second step, the substrate was moved together with the laser sensor, keeping the sample under load and measuring the dynamic indentation with the laser sensor. It was found that the indentation reduced with the sliding speed, this was originated due to the higher stiffness or shorter contact time preventing the rubber from establishing intense contact. The speed dependence of the dynamic indentation showed an analogy with the frequency-dependent material stiffness ( $G'$ ) master curve constructed by the dynamic mechanical analysis (DMA). The temperature

dependence of indentation was evaluated by measuring it at different temperatures on multi-indenter and asphalt surfaces. A lower indentation was denoted by decreasing the temperature because of the stiffer behaviour of the material. Afterwards, the time-temperature superposition principle was applied to construct the indentation master curve. By comparing different filler system compounds, the silica mixture showed softer behaviour and faster relaxation in comparison with carbon black compounds resulting in a correlation with the viscoelastic moduli master curve. Summing up, the experimental tools and the corresponding developed FEM provided access to data that are currently not available, such as local pressures, dissipated energies, contact area and rubber indentation, all of these are crucial parameters for the prediction of the hysteresis friction.

The other main friction contribution called adhesion was estimated with the analytical Klüppel/Heinrich model. This was based on the peeling effects governed by viscoelastic crack opening mechanisms between rubber and substrate on dry and wet surface, considering the physical-chemical nature of the contact. Adhesion contribution dominated on dry tracks but played a significant role in water condition. Indeed, in water condition, the lubricant might dewet in some regions leading to the nucleation of dry patches and direct contact rubber substrate.

The so-called dry patches effect induced a partial adhesion in the contact regions where the water was wiped away due to the dewetting phenomena. The dry patches phenomenon based on the spreading coefficient  $S$ , defined as the energy balance of the interfacial free energy between substrate, rubber and liquid. Contact angle measurements were performed to determine the surface free energies of the substrate, lubricant and rubber, as well as the resulting spreading coefficient to clarify the role of the physical-chemical affinity of the system and the resulting adhesion on the friction. The water condition showed significantly higher negative value, indicating higher dry patches in comparison to other lubricants like soap or water + soap.

Based on the previous consideration it was found that the hysteresis was enhanced with a partial adhesion where the water was wiped away. The effect was estimated through the  $\alpha$  parameter: it varied between 0 and 1, it quantified the level of adhesion in water condition and depended on the spreading coefficient, the viscosity of lubricant and the stiffness of the material. The estimated  $\alpha$  values were around 10% and 35% depending on the speeds and reduced for high speeds by reducing the time for water to squeeze out of the contact.

A hybrid model was developed to check the global response of the friction prediction in dry and wet conditions by combining the solutions of the sub-topics (see the diagram block in Figure 92) such as the dynamic contact mechanism between rough substrate/rubber and the physical-chemical study of the contact patch. The hybrid model, composed by the FEM tool and an analytical model, showed good friction prediction concerning rubber geometry/material and lubricant at low macroscopic speeds where adhesion and hysteresis contributions occurred. The friction behaviour changed due to the increase of temperature in the hot spots of the contact rubber substrate, especially at dry and large speeds ( $>10\text{mm/s}$ ). Therefore, the effect of rubber geometries and the lubricant on friction heating was examined with an infrared-camera. The dry friction heating was stronger in the case of long/narrow rubber blocks (higher ratio  $L/W$ ) in comparison with the short/wide ones, that means the heat build-up is higher when the rubber slides parallel to the long side of the rubber block. The heat build-up appeared higher for all geometries examined at the trailing edge because the leading edge of

the rubber block continuously moves into contact with the cold road surface, unlike the trailing edge. By considering wet conditions, the presence of lubricant with high thermal diffusivity cooled down the system generating less heat build-up in comparison to the dry surface. An analytical solution of lubricated heat build-up was used based on the assumption the whole amount of dissipated energy was converted into thermal energy, leading to a temperature increase of the rubber specimen. The numerical simulation executed in MAPLE, using input parameters deriving from frictionless FEM simulations, solved the heat differential equation in space and time, a match was found with the temperature increase measured using IR technology. According to the flash temperature theory from Persson, the calculations showed that such temperature increase can vary depending on the sliding velocity. Therefore, for future researches, coupled thermo-mechanical models might be necessary in the case of high sliding speeds, based on iteratively calculation of the material properties, which change due to the rubber temperature increase.

# Appendix

Further results from the measurement of the S-SBR filled with silica (Si) and carbon black (CB) mechanical behavior and the corresponding fitting are shown here.

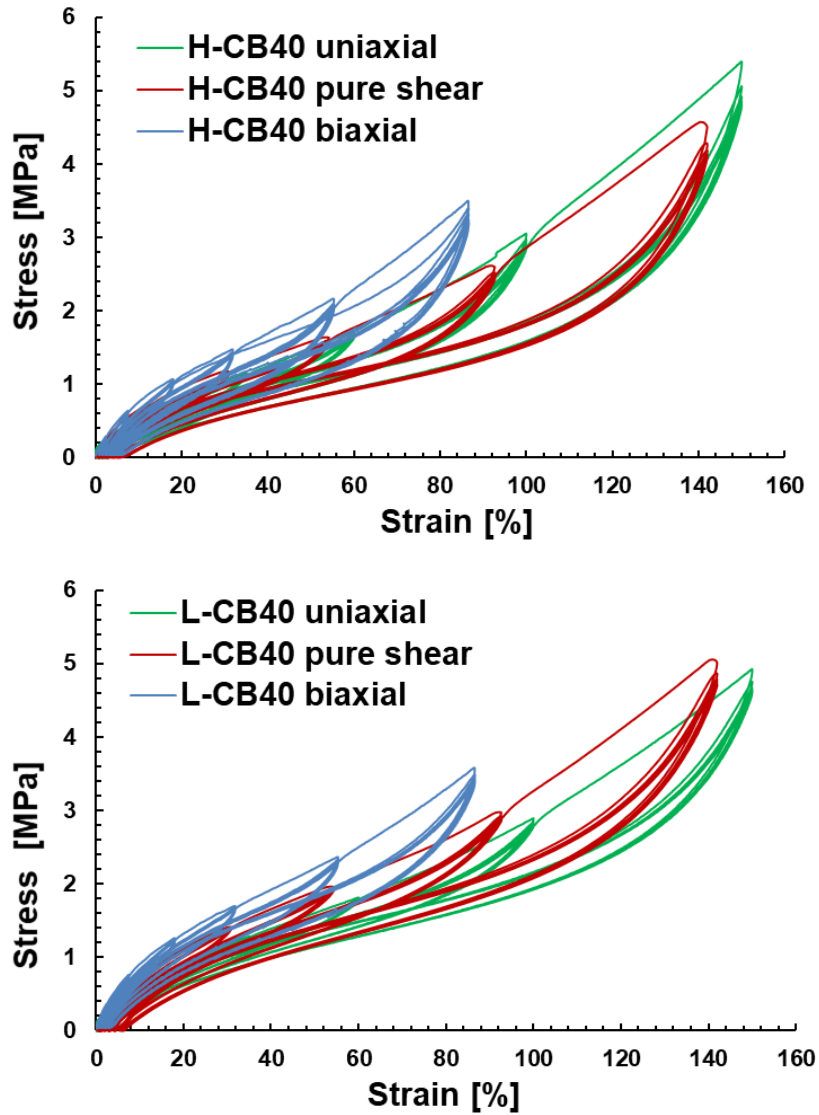


Figure 203. Stress-strain curves on uniaxial, pure shear and equi-biaxial quasi static modes test for H-CB40 and L-CB40 materials. Temperature of  $T=20^{\circ}\text{C}$  and crossbar speed of 20 mm/min for uniaxial and pure shear test and 80 mm/min for biaxial one.



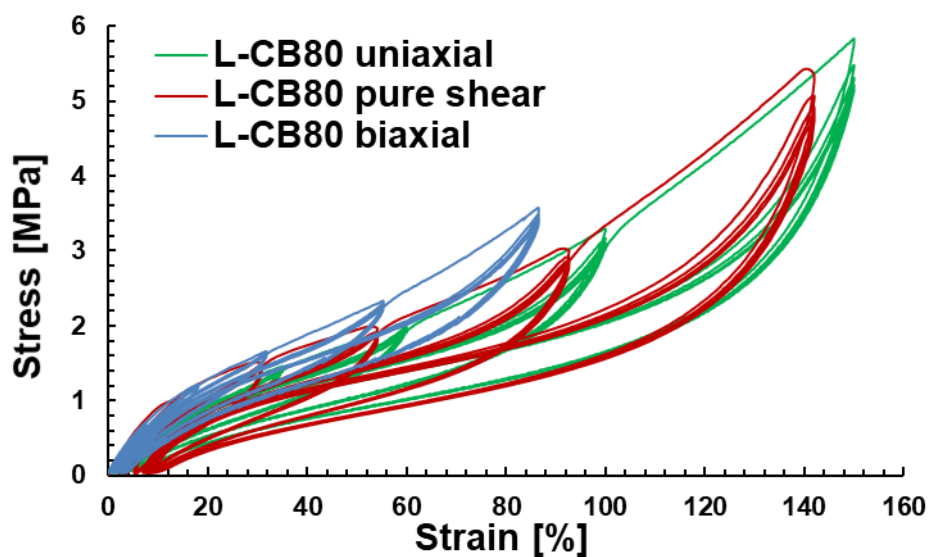


Figure 204. Stress-strain curves on uniaxial, pure shear and equi-biaxial quasi static modes test for L-CB80 material. Temperature of  $T=20^{\circ}\text{C}$  and crossbar speed of 20 mm/min for uniaxial and pure shear test and 80 mm/min for biaxial one.

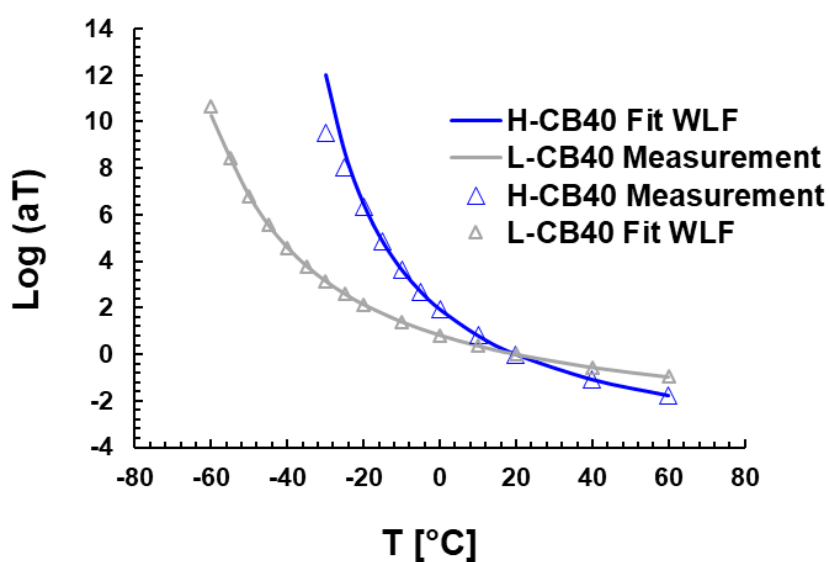


Figure 205. Fitting between the shifting factors applied to the compound H-CB40 and L-CB40 measured at 0.1 % strain.

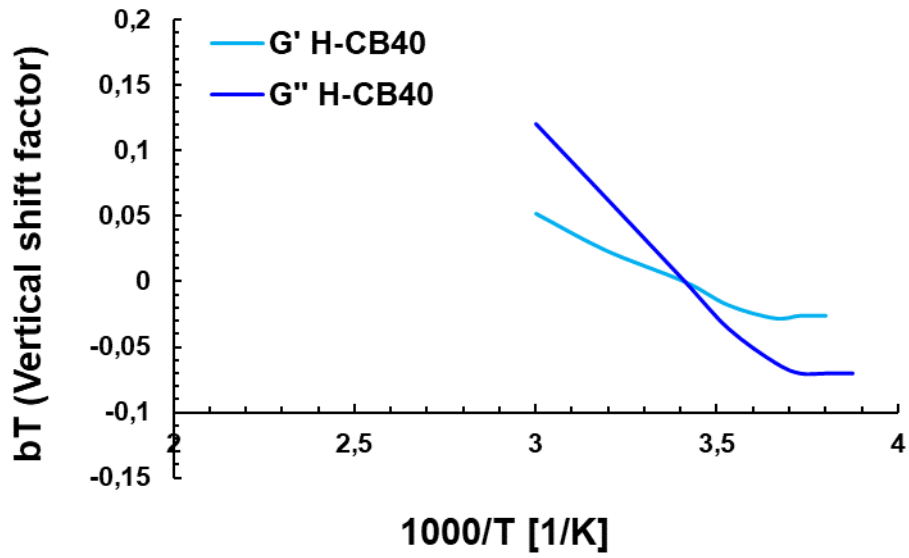


Figure 206. Application of the vertical shift factor  $b_T$  function of temperature for H-CB40.

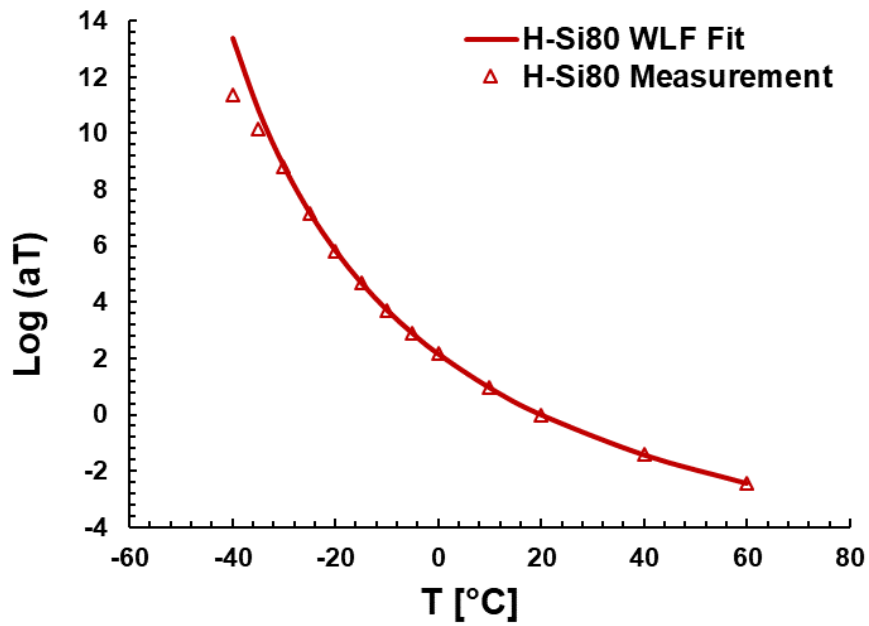


Figure 207. Illustration of the horizontal shifting factors  $a_T$  applied to the compound H-Si80 at 0.1 % strain.  $T_{ref} = 20^\circ C$ .

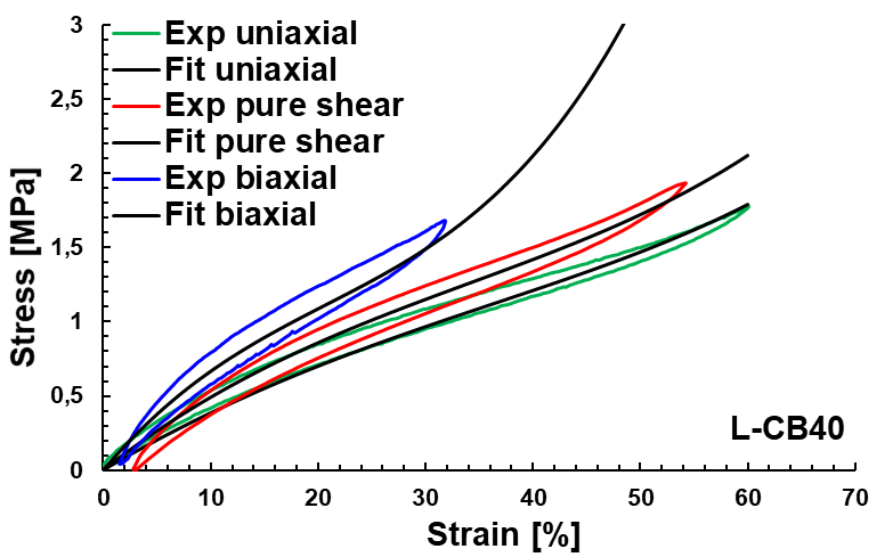
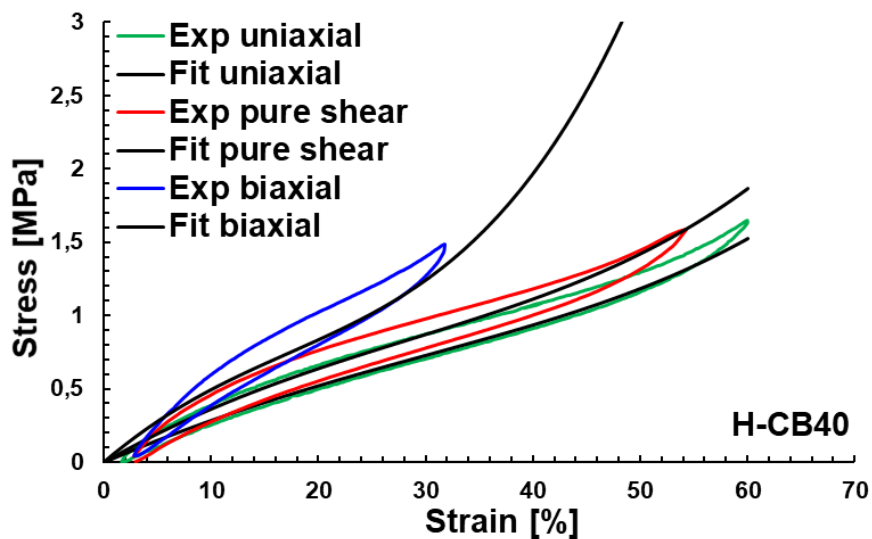


Figure 208. Fitting of the Yeoh model for compound H-CB40 (top) and L-CB40 (bottom) with the stress-strain curves measured in uniaxial, biaxial and pure shear at 20°C.

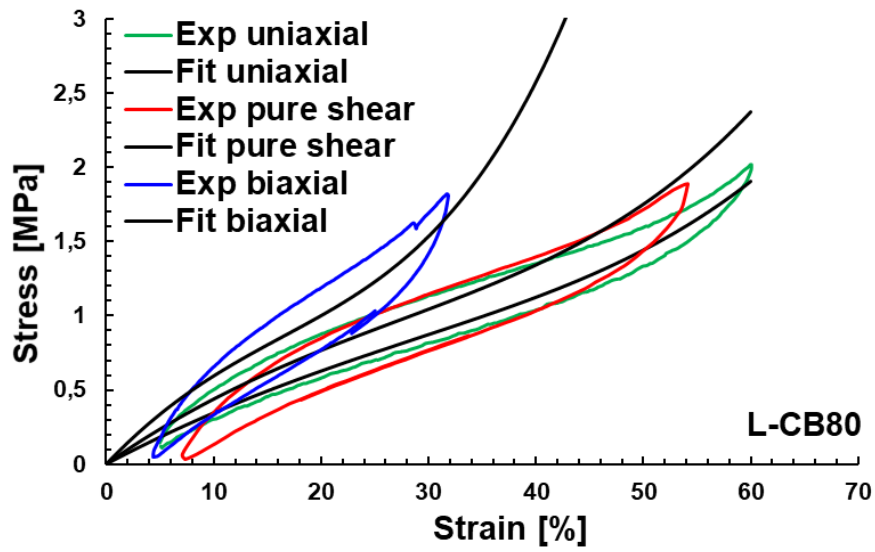
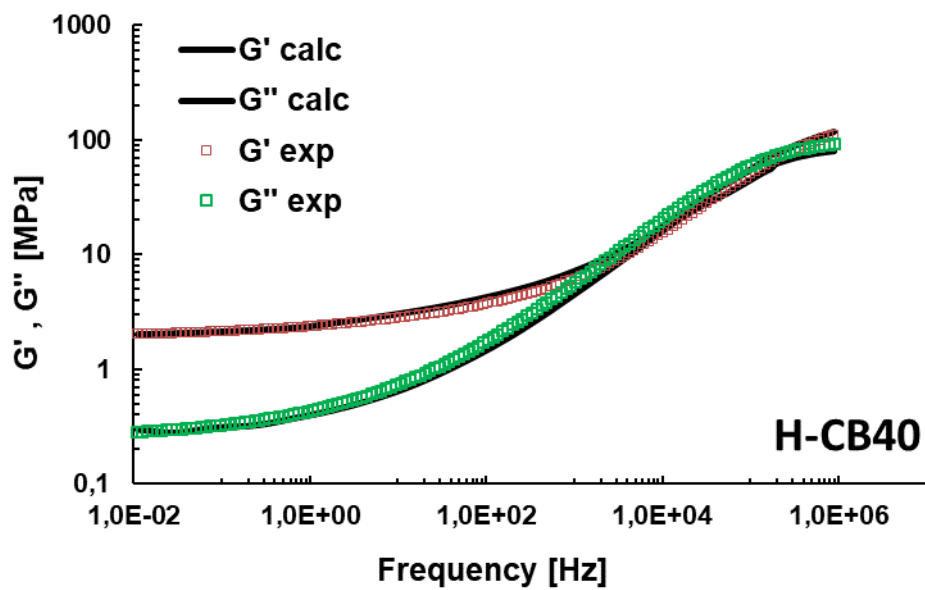


Figure 209. Fitting of the Yeoh model for compound L-CB80 with the stress-strain curves measured in uniaxial, biaxial and pure shear at 20°C.



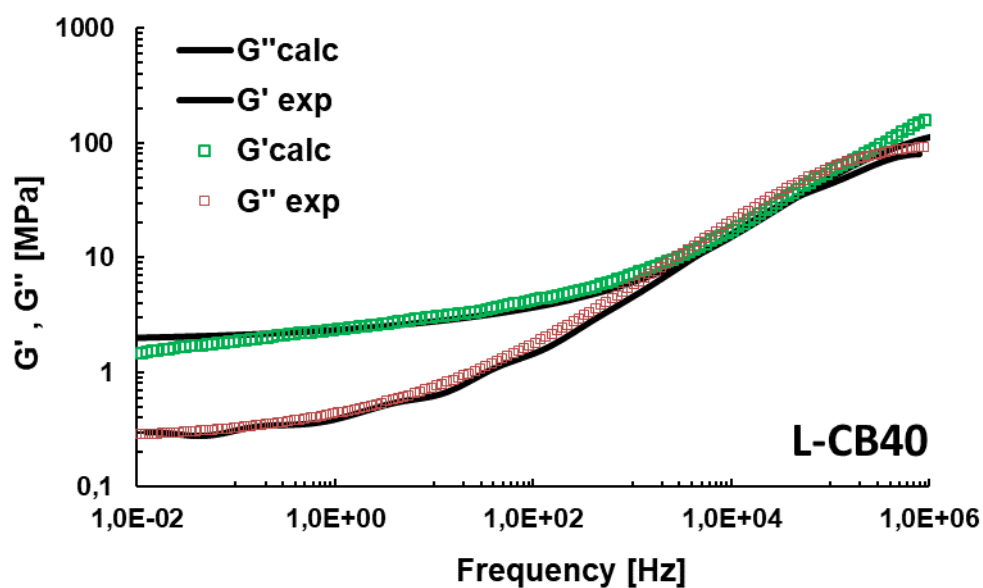


Figure 210. Comparison between the fitting Prony series and  $G'$ ,  $G''$  master curves for different compounds (H-CB40 and L-CB40) in the frequency domain. Reference temperature  $T = 20^\circ\text{C}$ ; strain level  $\gamma = 2.5\%$ .

The list of the Prony series parameters used for the material model implemented in FEA are listed in the tables below:

Table 18. Prony series parameters for compounds H-CB40, L-CB40, H-CB80 and L-CB80.

H-CB40		
ID Element	$g_i$	$\tau_i$
1	3,79739E-05	1,000E+05
2	3,7977E-05	3,415E+04
3	3,79862E-05	1,166E+04
4	3,8012E-05	3,981E+03
5	3,80795E-05	1,359E+03
6	3,82005E-05	4,642E+02
7	0,008387267	1,585E+02
8	0,000784794	6,310E+00
9	0,000805429	2,154E+00
10	0,000866983	7,356E-01
11	0,000948622	2,512E-01
12	0,001074009	8,577E-02
13	0,001330028	2,929E-02
14	0,001671782	1,000E-02

15	0,002320672	3,415E-03
16	0,003271756	1,166E-03
17	0,005019032	3,981E-04
18	0,007838279	1,359E-04
19	0,016461634	4,642E-05
20	0,023947493	1,585E-05
21	0,095926746	5,412E-06
22	0,011901241	1,848E-06
23	0,354019796	6,310E-07
24	0,02245072	2,154E-07
25	0,430354297	7,356E-08

<b>L-CB40</b>		
ID Element	$g_i$	$\tau_i$
1	0.000810673	3,162E+05
2	2.3904E-05	1,000E+05
3	5.09529E-05	3,162E+04
4	0.001608954	1,000E+04
5	3.39317E-05	3,162E+03
6	0.00050381	1,000E+03
7	1.53927E-05	3,162E+02
8	0.002347709	1,000E+02
9	6.42293E-05	3,162E+01
10	0.001411163	1,000E+01
11	0.000144505	3,162E+00
12	0.00148213	1,000E+00
13	0.000699298	3,162E-01
14	0.000928966	1,000E-01
15	0.002329291	3,162E-02
16	2.03912E-05	1,000E-02
17	0.004903319	3,162E-03
18	0.001100495	1,000E-03
19	0.008242902	3,162E-04
20	0.008679545	1,000E-04

21	0.023209362	3,162E-05
22	0.035636359	1,000E-05
23	0.122570295	3,162E-06
24	0.080017752	1,000E-06
25	0.322810061	3,162E-07
26	0.380354608	1.000E-07

<b>H-CB80</b>		
ID Element	$g_i$	$\tau_i$
1	0,9215782130	0,000120105
2	0,071469783589	0,01639517385
3	0,0055425897597	2,238038
4	0,00042983621472	305,5
5	3,33344482e-05	41703,31
6	2,585136853e-06	5692750,4
7	2,00481271e-07	777094216,6
8	1,554762563e-08	106077971657,9
9	1,205741870e-09	14480272572,7
10	9,35071049e-11	1,976643128e+15
11	7,25161734e-12	2,6982351e+17

<b>L-CB80</b>		
ID Element	$g_i$	$\tau_i$
1	0,003001652	4,125E+02
2	0,009348595	7,017E+01
3	0,004027066	1,194E+01
4	0,005476417	2,031E+00
5	0,005333523	3,455E-01
6	0,006045069	5,878E-02
7	0,006955336	1,000E-02
8	0,008503572	1,701E-03
9	0,011235194	2,894E-04
10	0,01695289	4,924E-05
11	0,029205966	8,377E-06

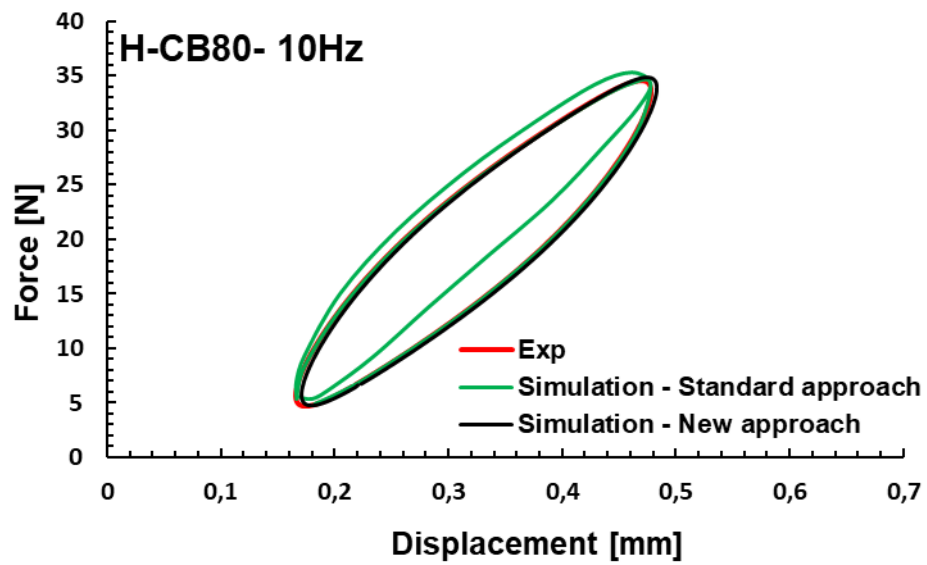


Figure 211. Comparison between dynamic test (Exp. depicted in red) and the simulations (standard and new modelling approach depicted in green and black respectively) at the frequency of 10Hz.

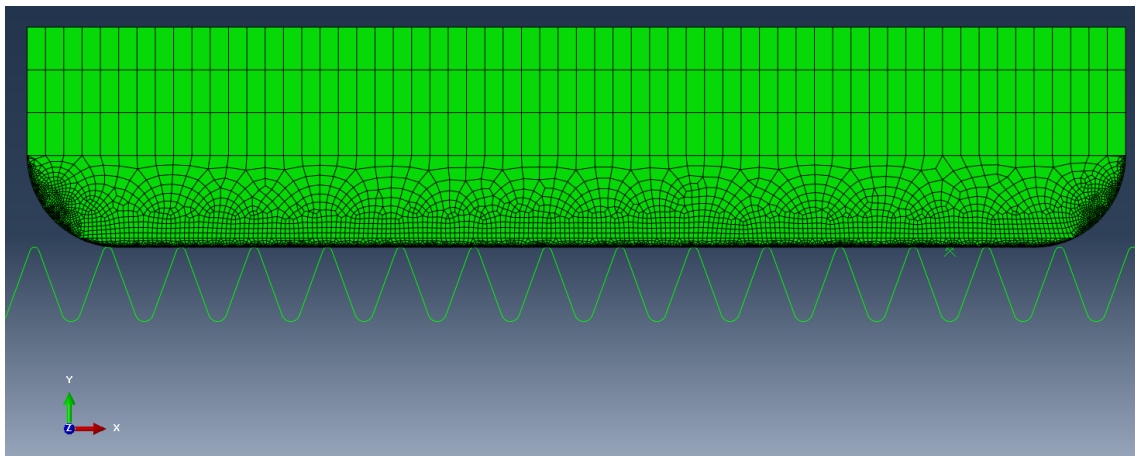


Figure 212. 2D FEM set up of the indentation simulation on multi-indenter surface.



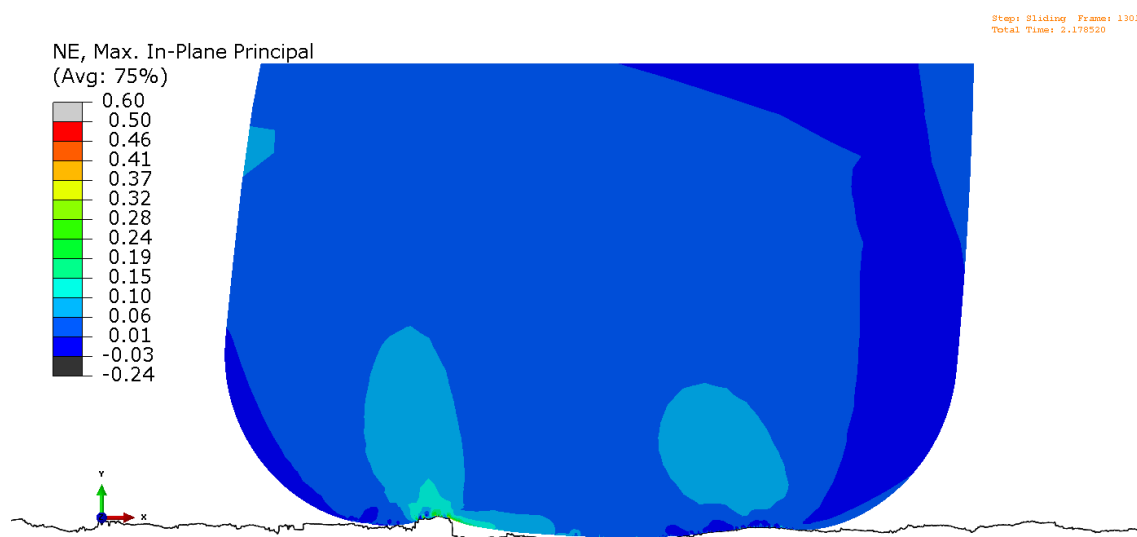


Figure 213. 2D FEM of the friction simulation on fine granite.

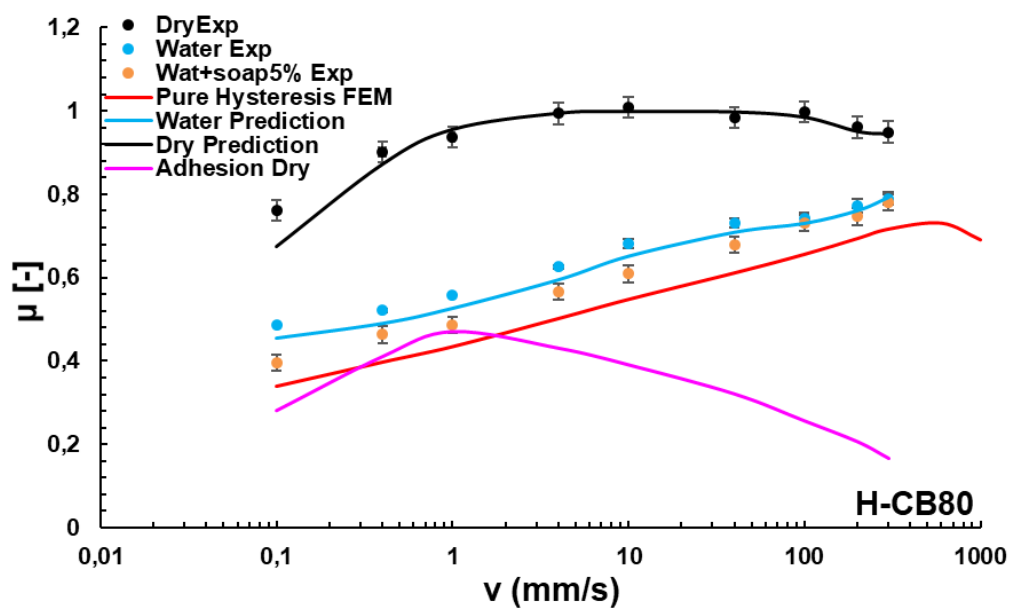


Figure 214. Prediction of the friction behaviour (dry and lubricated conditions) with a hybrid model (FEM for hysteresis and analytical model for adhesion) in the case of H-CB80 on real rough surface (fine granite).  $T=20^{\circ}\text{C}$  and  $p=0.26$  MPa.

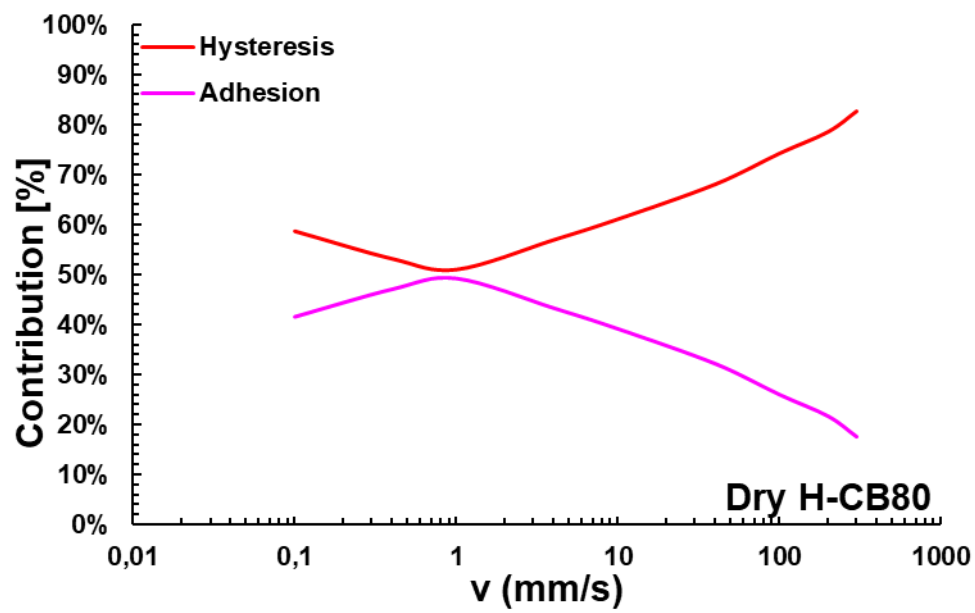


Figure 215. Impact of the hysteresis and adhesion (in %) on dry predicted friction coefficient in the case of H-CB80 and real rough surface (fine granite).

---

# References

- [1] Kautschuk und Latices - Nomenklatur, DIN 1629, 2013.
- [2] Polymere Werkstoffe; Gruppierung polymerer Werkstoffe aufgrund ihres mechanischen Verhaltens, DIN 7724, 1993.
- [3] H. Tanaka and A. Kageyu, "Structure and Biosynthesis Mechanisms of Natural-cis-Polyisoprene", *Rubber Chem. Tech.*, no. 56, p. 299, 1983.
- [4] G. M. Bristow, "Mastication of Elastomers", *Rubber Chemistry and Technology*, no. 35(4), pp. 896-905, 1962.
- [5] A. Roberts, *Natural Rubber Science and Technology*, New York, Kuala Lumpur: Oxford University Press, 1988.
- [6] D. A. Mc Gill and W. J. Joosk, "A Theory of Green Strength in Natural Rubber," *Kaut. Gummi, Kunststoffe*, no. 19, p. 962, 1987.
- [7] D. S. Campbell and K. N. G. Fuller, "Factors Influencing the Mechanical Behavior of Raw Unfilled Natural Rubber," *Rubber Chem. Technol.*, vol. 57, p. 104, 1984.
- [8] W. Hofmann, *Rubber Technology Handbook*, Hanser Publishers, 1989.
- [9] E. J. Mark, B. Erman and F. Eirich, *Science and Technology of Rubber*, Elsevier 3rd Edition, 2005.
- [10] K. H. Nordsiek, «The integral rubber concept - an approach to an ideal tire tread rubber,» *Kautsch. Gummi Kunstst.*, vol. 38, p. 178–185, 1985.
- [11] E. F. Engel, *International Institute of Synthetic Rubber Producer - Annual Meeting*, Munich, 1972.
- [12] H. E. Adams, R. L. Bebb, L. E. Forman and L. B. Wakefield, "The Impact of Lithium Initiators on the Preparation of Synthetic Rubbers," *Rubber Chem. Technol.*, vol. 45, p. 1252, 1982.
- [13] W. Kuhn, «Colloid and Polymer Science,» in "*Über die Gestalt fadenförmiger Moleküle in Lösungen*", vol. 68, Springer, 1934, pp. 2-15.
- [14] W. Kuhn, «"Gestalt und Eigenschaften fadenförmiger Moleküle in Lösungen (und im elastisch festen Zustände),"» *Angewandte Chemie*, vol. 49, pp. 858-862, 1936.
- [15] P. J. Flory, *Principles of Polymer Chemistry*, Ithaca, New York: Cornell University Press, 1953.

- [16] J. E. Mark, B. Erman and R. M., in *The Science and Technology of Rubber*, USA, 4th Edition Elsevier, 2013, p. 765.
- [17] W. Sewwandi, «Rubber filled,» 2018. [Online]. Available: <https://www.slideshare.net/WSewwandi1/rubber-fillers>.
- [18] H. D. Luginsland and W. Niedermeier, “New reinforcing materials for rising tire performance demands,” *Rubber World*, vol. 228, no. 6, pp. 34-45, 2003.
- [19] J. Neubauer, «Improving key tire performance,» *Tire Technology International, Annual Review*, pp. 10-12, 2009.
- [20] U. Goerl, A. Hunsche, A. Mueller and H. G. Koban, “Investigations into the Silica/Silane Reaction System,” *Rubber Chem. Technol.*, vol. 70, no. 4, p. 608, 1997.
- [21] J. T. Brinke, S. Debnath, L. Reuvekamp and J. Noordermeer, “Mechanistic aspects of the role of coupling agents in silica–rubber composites,” *Compos. Sci. Technol.*, vol. 63, p. 1165, 2003.
- [22] K. J. Kim and J. VanderKooi, “Moisture effects on TESPd-silica/CB/SBR compounds,” *Rubber Chem. Technol.*, vol. 78, no. 1, p. 84, 2005.
- [23] S. Mihara, R. Datta, A. Talma and W. Noordermeer, “Rubber composition”. USA Patent U.S. Patent 7923493B2, 12 April 2011.
- [24] M. J. Wang, “Effect of polymer-filler and filler-filler interactions on dynamic properties of filled vulcanizates,” *Rubber Chem Technol.*, vol. 71, no. 3, pp. 520-589, 1998.
- [25] J. L. Leblanc, «Rubber-filler interactions and rheological properties in filled compounds,» *Prog Polym Sci*, vol. 27, n. 4, pp. 627-687, 2002.
- [26] A. Mostafa, A. Abouel-Kasem, M. Bayoumi and M. R. El-Sebaie, “Rubber-Filler Interactions and Its Effect in Rheological and Mechanical Properties of Filled Compounds,” *Journal of Testing and Evaluation*, vol. 38, no. 3, pp. 347-359, 2010.
- [27] R. Rother, *Particulate-Filled Polymer composites*, Shawbury: iSmithers Rapra Publishing, 2003.
- [28] J. Donnet, R. C. Bansal and M. J. Wang, *Carbon black: Science and Technology*, New York: 2nd ed., Marcel Dekker Inc., 1993.
- [29] M. Klüppel, «The Role of Disorder in Filler Reinforcement of Elastomers on Various Length Scales,» in *Adv. Polym. Science 164*, Springer Verlag KG, 2003, pp. 1-86.
- [30] J. L. Leblanc., «Rubber-filler interactions and rheological properties in filled compounds,» *Prog. Polym. Sci.*, vol. 27, n. 4, pp. 627-687, 2002.
- [31] G. Joyce and W. Henry, “Modelling the Equilibrium Compressed Void Volume of Carbon Black,” *Rubb Chem Technol.*, vol. 79, no. 5, pp. 735-764, 2006.

- 
- [32] M. Rodriguez, "Studies on the rubber filler interactions in tyre tread compounds, MS Thesis," Tampere university of technology, Tampere, 2016.
- [33] T. C. Gruber and C. R. Herd, "Anisometry Measurements in Carbon Black Aggregate Populations," *Rubber Chemistry and Technology*., vol. 70, no. 5, pp. 727-746, 1997.
- [34] ASTM, «Standard classification system for carbon blacks used in rubber products,» *ASTM International*, 2014.
- [35] «N990 Physical and Chemical Properties PDF available from,» 2016. [Online]. Available: [http://www.cancarb.com/docs/pdf/Physical\\_Chemical\\_Properties.pdf](http://www.cancarb.com/docs/pdf/Physical_Chemical_Properties.pdf).
- [36] R. P. Brown, *Physical Testing of Rubber*, London: Chapman and Hall, 1996.
- [37] S. Mihara, «Reactive Processing of Silica-Reinforced Tire Rubber,» University of Twente , 2009 PhD Thesis.
- [38] H. S. Katz, J. V. Mileski and J. V. Melewski, in *Handbook of Fillers for Plastics*, Springer Science & Business Media, 1987, p. 467.
- [39] Ciullo and P. Hewitt, in *The Rubber Formulary*, New York, William Andrew , 1999, p. 741.
- [40] W. Dierkes, «Economic Mixing of Silica-Rubber Compounds,» University of Twente, 2005 PhD Thesis.
- [41] A. Lang, «Experimentelle und theoretische Untersuchungen zum Reibverhalten elastomerer Werkstoffe auf rauen Oberflächen.,» Gottfried Wilhelm Leibniz University Hannover, 2018 PhD Thesis.
- [42] C.-C. Peng, «Novel Rubber Nanocomposites with Adaptable Mechanical Properties,» University of Bayreuth, 2005 PhD Thesis.
- [43] A. R. Payne, *Rheology of Elastomers*, London: Pergamon Press, 1958.
- [44] A. R. Payne, «A Note on the Existence of a Yield Point in the Dynamic Modulus of Loaded Vulcanizates,» *Journal of Applied Polymer Science Ed. 3*, vol. 7, p. 127, 1960.
- [45] A. R. Payne, «Dynamic Mechanical Properties of Filler Loaded Vulcanisates,» *Rubber and Plastics Age*, vol. 42, n. 8, pp. 963-967, 1961.
- [46] A. R. Payne, «The Dynamic Properties of Carbon Black-Loaded Natural Rubber Vulcanizates Part I,» *Journal of Applied Polymer Science*, vol. 6, pp. 57-63, 1962.
- [47] A. R. Payne, «The Dynamic Properties of Carbon Black Loaded Natural Rubber Vulcanizates Part II,» *Journal of Applied Polymer Science*, vol. 6, pp. 368-372, 1962.
- [48] A. R. Payne, «Carbon Black Structure in Rubber,» *Rubber Chemistry and Technology*, vol. 36, pp. 147-155, 1963.

- [49] R. Raghunath, D. Juhre and M. Klüppel, “A physically motivated model for filled elastomers including strain rate and amplitude dependency in finite viscoelasticity,” *International Journal of Plasticity*, vol. 78, pp. 223-241, 2015.
- [50] H. Bouasse e Z. Carriere, «Sur le courbes de traction du caoutchouc vulcanise,» in *Annales de la Faculté des sciences de Toulouse: Mathématiques Vol. 5*, 1903.
- [51] L. Mullins and M. Tobin, “Theoretical model for the elastic behavior of filler reinforced vulcanized rubbers p.15,” in *Proceedings of the Third Rubber Technology Conference*, 1956.
- [52] L. Mullins, «Softening of rubber by deformation,» *Rubber Chemistry and Technology*, vol. 42, pp. 339-362, 1969.
- [53] J. Diani, B. Fayolle and P. Gilormini, “A review on the Mullins effect,” *European Polymer Journal*, vol. 45, no. 3, pp. 601-612, 2009.
- [54] J. G. R. Kingston and A. H. Muhr, “Effect of scragging on parameters in viscoplastic model for filled rubber,” *Plastics, Rubber and Composites*, vol. 40, no. 4, pp. 161-168, 2011.
- [55] A. Lion and P. Haupt, “On finite linear viscoelasticity of incompressible isotropic materials,” *Acta Mater.*, vol. 159, no. 1, pp. 87-124, 2002.
- [56] J. Retka, P. Hofer and A. Lion, “Numerische Simulation aushärtender Klebstoffe. Beiträge zur Materialtheorie (Heft 1/07),” ISSN 1862-5703, Munich, 2007.
- [57] M. Jöhlich, «Materialmodellierung,» Universität des Saarlandes, Lehrstuhl für Technische Mechanik, 2009.
- [58] G. Heinrich, «The dynamics of tire tread compounds and their relationship to wet skid behavior,» *Progress in Polymer and Colloid Science*, vol. 90, pp. 16-26, 1992.
- [59] J. C. Maxwell, «On The Dynamical Theory of Gases,» *Philos. Trans. R. Soc.*, n. 157, pp. 49-88, 1880.
- [60] T. H. Courtney, *Mechanical Behavior of Materials*, Waveland Press Inc., 2005.
- [61] N. W. Tschoegl, *The Phenomenological Theory of Linear Viscoelastic Behavior*, Springer-Verlag Berlin Heidelberg, 1989.
- [62] E. Wiechert, «Gesetze der Elastischen Nachwirkung für Constante Temperatur,» *Annalen der Physik*, vol. 286, n. 11, pp. 546-570, 1893.
- [63] J. Ferry, *Viscoelastic Properties of Polymers*, John Wiley & Sons, 1960.
- [64] D. Gutierrez-Lemini, *Engineering Viscoelasticity*, Springer, 2014.
- [65] M. Doi and S. Edwards, *The Theory of Polymer Dynamics*, Oxford: Clarendon Press, 1986.
- [66] R. Young and P. Lovell, *Introduction to Polymers (2 ed.)*, CRC Press, 1991.

- 
- [67] Properties And Behavior of Polymers, John Wiley & Sons Ltd, 2012.
- [68] M. L. Williams, R. F. Landel and J. D. Ferry, “The temperature dependence of relaxation mechanisms in amorphous polymers and other glass forming liquids,” *J. Am. Chem. Soc.*, vol. 77, no. 14, p. 3701, 1955.
- [69] J. Fritzsche, «Dielektrische Relaxationsspektroskopie und Dynamisch-Mechanische Analyse an Elastomer-Nanokompositen,» Leibniz Universität Hannover, 2009 PhD Thesis.
- [70] J. G. Meier, J. W. Mani and M. Klüppel, “Analysis of carbon black networking in elastomers by dielectric spectroscopy,” *Physical Review B*, vol. 75, p. 054202, 2007.
- [71] M. Klüppel, «Evaluation of viscoelastic master curves of filled elastomers and applications to fracture mechanics,» *Journal of Physics: Condensed Matter*, vol. 21, n. 3, p. 035104, 2009.
- [72] D. Fragiadakis, L. Bokobza and P. Pissis, “Dynamics near the filler surface in natural rubber-silica nanocomposites,” *Polymer*, vol. 52, no. 14, p. 3175–3182, 2011.
- [73] J. Fritzsche and M. Klüppel, “Structural dynamics and interfacial properties of filled-reinforced elastomers,” *Journal of Physics: Condensed Matter*, vol. 23, no. 3, p. 035104, 2011.
- [74] H. A. Kramers, «La diffusion de la lumière par les atomes,» in *Atti del Congresso Internazionale dei Fisici pp. 545-557*, Como, 1927.
- [75] R. D. L. Kronig, «On the theory of dispersion of X-Rays,» *Journal of the Optical Society of America*, vol. 12, n. 6, p. 547–556, 1926.
- [76] J. Fritzsche and M. Klüppel, “Structural dynamics and interfacial properties of elastomer nanocomposites,” in *International Committee on Composite Materials*, Edinburgh, 2009.
- [77] A. LeGal, X. Yang and M. Klüppel, “Evaluation of sliding friction and contact mechanics of elastomers based on dynamic mechanical analysis,” *J. Chem. Phys.*, vol. 123, no. 1, p. 014704, 2005.
- [78] P. Wagner, «A Multiscale FEM Approach for Rubber Friction on Rough Surfaces,» Gottfried Wilhelm Leibniz Universität Hannover, 2018 PhD Thesis.
- [79] A. LeGal and M. Klüppel, “Investigation and modelling of rubber sliding friction on rough surfaces,” *Journal of Physics D: Condensed Matter*, vol. 20, 2007.
- [80] A. LeGal, X. Yang and M. Klüppel, “Untersuchung und Modellierung der Elastomerreibung auf rauen Oberflächen,” in *Veranstaltung der Bezirksgruppe Niedersachsen der DKG*, Hanover, 2005.
- [81] A. Roberts, «A guide to estimating the friction of rubber,» *Rubber Chemistry Technology*, vol. 65, n. 3, p. 673, 1992.

- [82] B. Persson, *Sliding Friction Physical Principles and Applications*, Berlin, Heidelberg: Springer Verlag, 1998.
- [83] H. W. Kummer, «Unified Theory of Rubber and Tire Friction,» *Engineering Research Bulletin B-94. The Pennsylvania State University, Department of Mechanical Engineering. Pennsylvania*, 1966.
- [84] U. S. Sandberg, «Influence of Road Surface Texture on Traffic Characteristics Related to Environment, Economy and Safety,» Swedish National Road and Transport Research Institute, Linköping, 1998.
- [85] A. LeGal, «Investigation and Modelling of Rubber Stationary Friction On Rough Surfaces,» Gottfried Wilhelm Leibniz Universität Hannover, 2007 PhD Thesis.
- [86] J. Roth, University of Darmstadt, 1993 PhD Thesis.
- [87] D. F. Moore, *The Friction and Lubrication of Elastomers*, Oxford: Pergamon Press, 1972.
- [88] D. F. Geyer and W. Moore, “A Review of Adhesion Theories for Elastomers,” *Wear*, vol. 22, no. 2, pp. 113-141, 1972.
- [89] L. Busse, I. Boubakri and M. Klüppel, “Friction Master Curves for Elastomers Sliding on Granite in Simulation Compared to Experiment at Various Temperatures,” *Kautschuk Gummi Kunststoffe*, vol. 64, no. 5, pp. 35-39, 2011.
- [90] K. A. Grosch, «The Relation between Friction and Visco-Elastic Properties of Rubber,» *Proc. R. Soc. Lond Mathematical and Physical Sciences*, vol. 274, n. 1356, pp. 21-39, 1963.
- [91] G. Romano, «Advanced experimental investigations and finite element analysis of rubber friction on model surfaces and rough substrates,» Gottfried Wilhelm Leibniz University Hannover, 2017 Phd Thesis.
- [92] B. Persson, «Theory of rubber friction and contact mechanics,» *The Journal of Chemical Physics*, vol. 115, n. 8, pp. 3840-3861, 2001.
- [93] A. LeGal and M. Klüppel, “Modelling of rubber friction: A quantitative description of the hysteresis and adhesion contribution,” in *Austrell, Kari Constitutive Models for rubber IV Taylor & Francis*, London, 2005.
- [94] L. Busse, A. LeGal and M. Klueppel, “Modelling of Dry and Wet Friction of Silica Filled Elastomers on Self-Affine Road Surfaces,” in *Elastomere friction - theory and experiment Vol. 51*, Hannover, Springer, 2010.
- [95] P. Wagner, P. Wriggers, L. Veltmaat, H. Clasen, C. Prange and B. Wies, “Numerical multiscale modelling and experimental validation of low speed rubber friction on rough road surfaces including hysteretic and adhesive effects,” *Tribology International*, vol. 111, pp. 243-253, 2017.



- 
- [96] F. Brochard-Wyart and P. G. DeGennes, “Dewetting of a water film between a solid and a rubber,” *Journal of Physics: Condensed Matter*, vol. 6, no. 23, 1992.
- [97] A. D. Roberts, «Squeeze films between rubber and glass,» *J. Phys. D: Appl. Phys.*, vol. 4, n. 3, 1971.
- [98] T. Nishi, K. Moriyasu, K. Harano and T. Nishiwaki, “Influence of Dewettability on Rubber Friction Properties with Different Surface roughness under Water/Ethanol/Glycerol lubricated conditions,” *Tribology Online*, vol. 11, no. 5, pp. 601-607, 2016.
- [99] D. Moore, *The Friction of Pneumatic Tyres*, Amsterdam: Elsevier Scientific Publishing Company, 1975.
- [100] A. Savkoor, «Tribology of tyre traction on dry and wet roads,» in *Proc. 17th Leeds - Symp. on Tribology pp 213–228*, Lyon, 1990.
- [101] S. M. Rohde, «On the effect of pavement microtexture on thin film traction,» *Int. J. Mech. Sci.*, vol. 18, n. 2, pp. 95-101, 1976.
- [102] P. Taneerananon and W. Yandell, “Microtexture roughness effect on predicted road - tyre friction in wet conditions,” *Wear*, vol. 69, no. 3, pp. 321-370, 1981.
- [103] M. Kane and Y. Beautru, “Influence of Road Surface Microtexture on Thin Water Film Traction,” in *7th International Conference on Maintenance and Rehabilitation of Pavements and Technological Control*, France, 2012.
- [104] T. J. Goda, «Effect of Track Roughness Generated Micro-hysteresis on Rubber Friction in Case of (apparently) Smooth Surfaces,» *Tribology International*, vol. 93, pp. 142-150, 2016.
- [105] B. Persson, O. Albohr, U. Tartaglino, A. Volokitin and E. Tosatti, “On the nature of surface roughness with application to contact mechanics, sealing, rubber friction and adhesion,” *Journal of Physics: Condensed Matter*, vol. 17, pp. R1-R62, 2005.
- [106] G. Flintsch, I. L. Al-Qadi, R. Davis and K. K. McGhee, “Effect of HMA Properties on Pavement Surface Characteristics,” in *Pavement Evaluation Conference*, Roanoke (Virginia), 2002.
- [107] M. Do, V. Cerezo, Y. Beautru and M. Kane, “Modeling of the connection road surface microtexture/water depth/friction,” *Wear*, vol. 302, 2013.
- [108] M. Klüppel and G. Heinrich, “Rubber Friction on Self-affine Road Tracks,” *Rubber Chemistry and Technology*, vol. 73, no. 4, pp. 578-606, 2000.
- [109] L. Busse, «Investigation, Prediction and Control of Rubber Friction and Stick-Slip: Experiment, Simulation, Application,» Gottfried Wilhelm Leibniz Universität Hannover, 2012 PhD Thesis.

- [110] J. B. P. Greenwood and J. A. Williamson, "Contact of nominally flat surfaces," *Proceedings of the Royal Society of London. Series A. Mathematical and physical sciences*, vol. 295, no. 1442, pp. 300-319, 1966.
- [111] B. Persson and E. Tosatti, "Qualitative theory of rubber friction and wear," *Journal of Chemical Physics*, vol. 112, no. 4, pp. 2021-2029, 2000.
- [112] B. Persson, «Rubber friction: role of the flash temperature,» *Journal of Physics: Condensed Matter*, vol. 18, n. 32, pp. 7789-7823, 2006.
- [113] B. Persson, «Role of Frictional Heating in Rubber Friction.,» *Tribology Letters*, vol. 56, n. 1, pp. 77-92, 2014.
- [114] G. Fortunato, V. Ciaravola, A. Furno, B. Lorenz and B. Persson, "General theory of frictional heating with application to rubber friction," *Journal of Physics: Condensed Matter*, vol. 27, no. 17, 2015.
- [115] J. Cugliari, P. Straffi, P. Agoretti, M. Klüppel, J. Meier and F. Nanni, "Validation of the Kummer Friction Model for Rubber Compounds on Sinusoidal Tracks by FEA Simulations and Experimental Techniques," *Rubber chemistry and technology*, 2019.
- [116] B. Persson, «Adhesion between an elastic body and a randomly rough hard surface,» *The European Physical Journal E*, vol. 8, n. 4, pp. 385-401, 2002.
- [117] B. Lorenz, Y. R. Oh, S. K. Nam and S. H. Jeon, "Rubber friction on road surfaces: Experiment and theory for low sliding speeds," *The Journal of Chemical Physics*, vol. 142, no. 19, 2015.
- [118] M. Barquins, «Adherence, friction and wear of rubber-like materials,» *Wear and Friction of Elastomers. ASTM International*, vol. 158, n. 87, 1992.
- [119] B. Persson and E. A. Brener, "Crack Propagation in Viscoelastic Solids," *Physical review E71*, vol. 3, no. 036123, 2005.
- [120] H. Altenbach, *Kontinuumsmechanik: Einführung in die materialunabhängigen und materialabhängigen Gleichungen*, Berlin: 2 Ed. Springer, 2012.
- [121] P. Chadwick, *Continuum mechanics: Concise theory and problems*, Dover Publications, Mineola 2nd corr. and enl. edition., 1999.
- [122] P. Haupt, *Continuum Mechanics and Theory of Materials*, Springer-Verlag Berlin Heidelberg, 2002.
- [123] G. Holzapfel, *Nonlinear Solid Mechanics: A Continuum Approach for Engineering*, Wiley, 2000.
- [124] J. E. Hughes and T. J. R. Marsden, *Mathematical foundations of elasticity*, Courier Corporation , 1994.

- 
- [125] R. Ogden, «Non-linear elastic deformations: application to rubber like solids,» *Journal of the Mechanics and Physics of Solids*, vol. 26, n. 1, pp. 37-57, 1984.
- [126] C. Truesdell and W. Noll, *The Non-Linear Field Theories of Mechanics.*, Berlin, Heidelberg: Springer 3rd edition, 2004.
- [127] E. Guth and M. Wang, “Statistical Theory of Networks of non-Gaussian Flexible Chains,» *Journal of Chemical Physics*, vol. 20, p. 1124, 1952.
- [128] A. Sarmukaddam, «A contribution to quality and reliability of characterizing and modeling the inelastic properties of filled elastomer,» Master Thesis Hannover, 2012.
- [129] R. Rivlin, «Large elastic deformations of isotropic materials,» *Transactions of Royal Society of London Series A*, vol. 241, p. 379, 1948.
- [130] E. M. Arruda e M. Boyce, «Constitutive models of rubber elasticity: a review,» in *Mit Internal Report. available through M.C. Boyce*, 1991.
- [131] E. M. Arruda and M. C. Boyce, “A Three-Dimensional Constitutive Model for the Large Stretch Behavior of Rubber Elastic Materials,» *Journal of the Mechanics and Physics of Solids*, vol. 41, p. 389, 1993.
- [132] O. Yeoh, «Some forms of the strain energy function for rubber,» *Rubber Chemical & Technology Journal*, vol. 66, n. 5, p. 754, 1993.
- [133] M. Mohammed, «Visco-Hyperelastic Model for Soft Rubber-like Materials,» *Sains Malaysiana*, vol. 43, n. 3, 2014.
- [134] M. Charalambides, L. Wanigasooriya, J. Williams, S. M. Goh, S. and S. Chakrabarti, “Large deformation extensional rheology of bread dough,» *Rheol. Acta*, vol. 46, no. 2, pp. 239-248, 2006.
- [135] S. Goh, M. Charalambides and J. Willimas, “Determination of the Constitutive Constants of Non-Linear Viscoelastic Materials,» *Mechanics of Time-Dependent Materials*, vol. 8, no. 3, pp. 255-268, 2004.
- [136] J. Williams, *Stress Analysis of Polymers*, New York: Halsted Press, 1980.
- [137] M. Kaliske and H. Rothert, “Formulation and implementation of three-dimensional viscoelasticity at small and finite strains,» *Comput. Mech.*, vol. 19, no. 3, pp. 228-239, 1997.
- [138] H. Lorenz, J. Meier and M. Klüppel, “Micromechanics of Internal Friction of Filler Reinforced Elastomers,» in *Elastomere Friction*, Berlin, Springer, 2010, p. pp. 27–52.
- [139] J. Plagge, «On the Reinforcement of Rubber by Fillers and Strain-Induced Crystallization,» Gottfried Wilhelm Leibniz Universität Hannover , Hannover, 2018 PhD Thesis.

- [140] J. Plagge, A. Ricker and M. Klüppel, “Efficient Modeling of Inelastic Effects in Filled Rubber using Load Dependent Relaxation Times,” in *ECCMR*, Nantes, 2019.
- [141] O. Zienkiewicz and R. Taylor, *The Finite Element Method*, London: McGraw-Hill Co., 1989.
- [142] «Simulia, ABAQUS Analysis User Manual, 29.2.1,» 2010.
- [143] C. Bernardi, Y. Maday and A. Patera, “A new non conforming approach to domain decomposition: The mortar element method,” *Pitman Res. Notes Math. Ser., Pitman*, vol. 299, 1994.
- [144] “Determination of Tensile Stress strain Properties ISO 37,” 2005.
- [145] J. Cugliari, A. Lang, M. Klüppel, J. Meier, M. Giustiniano and P. Agoretti, “Advanced experimental investigation of rubber indentation during sliding friction,” in *Constitutive Models for Rubber XI*, Nantes, Pergamon Press, 2019, pp. 173-178.
- [146] «ramè-hart instrument co. Information on Contact Angle,» 2010. [Online]. Available: <http://www.ramehart.com/contactangle.htm>.
- [147] A. W. Neumann and R. J. Good, “Techniques of measuring contact angles,” in *Surface and Colloid Science, Vol. 11, R. J. Good and R. R. Stromberg (Eds)*, New York, Plenum Press, 1979, pp. 31-91.
- [148] M. Strobel and C. S. Lyons, “An essay on contact angle measurements,” *Plasma Processes and Polymers*, vol. 8, no. 1, pp. 8-13, 2011.
- [149] Y. Yuan and R. T. Lee, “Contact angle and wetting properties,” *Surface Science Techniques. Springer*, vol. 51, pp. 3-34, 2013.
- [150] V. Jones, M. Strobel and M. Prokosch, “Development of Poly(propylene) Surface Topography During Corona Treatment,” *Plasma Process and Polymer*, vol. 2, no. 547, 2005.
- [151] T. S. Meiron, A. Marmur and I. S. Saguy, “Contact angle measurement on rough surfaces,” *Journal of Colloids and Interface Science*, vol. 274, no. 2, p. 44, 2004.
- [152] L. M. Lander, L. S. Siewierski, W. J. Brittain and E. A. Vogler, “A systematic comparison of contact angle methods,” *Langmuir*, vol. 9, no. 8, p. 2237, 1993.
- [153] H. Y. Erbil, «Solid and Liquid Interfaces,» *Oxford: Blackwell*, vol. 646, 2006.
- [154] C. W. Karl, A. Lang, A. Stoll, A. Weise, M. Stoll and M. Klüppel, “Tribologische Eigenschaften beschichteter Elastomere - Teil 1: Charakterisierung der stationären Reibung gegenüber glatten Substraten,” *Kautschuk Gummi Kunststoffe*, vol. 65, no. 4, 2012.
- [155] A. DellaVolpe, C. Cassinelli and M. Morra, “Wilhelmy plate measurements on poly (N-isopropylacrylamide)-grafted surfaces,” *Langmuir*, vol. 14, no. 16, pp. 4650-4656, 1998.

- 
- [156] C. W. Karl and M. Klüppel, "Friction and wear of elastomers," *Chem. Listy*, vol. 105, p. 233, 2011.
- [157] C. W. Karl, L. Busse and M. Klüppel, "Tribologische Eigenschaften beschichteter Elastomere - Teil 2 Charakterisierung der stationären Reibung gegenüber glatten Substraten," in *Proc. 9th Rubber Fall Colloquium*, 2010.
- [158] M. Klüppel, J. Meier and M. Dämgen, "Modeling of Stress Softening and Filler Induced Hysteresis of Elastomer Materials," in *Constitutive Models for Rubber IV*, Tokyo, P.E. Austrell und L. Kari (Eds.), A. A. Balkema Publishers, Lisse, Abingdon, Exton, 2005, pp. 171-177.
- [159] G. Gabel, «Beobachtung und Modellierung lokaler Phänomene im Reifen-Fahrbahn-Kontakt,» Gottfried Wilhelm Leibniz Universität Hannover , 2009 PhD Thesis.
- [160] A. A. Lubrecht, C. H. Venner and F. Colin, "Film thickness calculation in elasto-hydrodynamic lubricated line and elliptical contacts: The Dowson,Higginson, Hamrock contribution," *Journal of Engineering Tribology*, vol. 223, no. 3, pp. 511-515, 2009.
- [161] B. O. Jacobson and B. Hamrock, "Elastohydrodynamic lubrication of Rectangular Contacts," *Nasa Technical Paper 211*, 1983.
- [162] B. Hamrock and D. Dowson, "Elastohydrodynamic Lubrication of Elliptical Contacts for Materials of Low Elastic Modulus," *NASA TN D-8528*, 1977.
- [163] H. S. Jaeger e J. C. Carslaw, *Conduction of Heat in Solids*, Oxford, pp. 78-79: Oxford University Press, 1959.

# Curriculum Vitae

Name: Jacopo Cugliari  
Nationality: Italian  
Date of birth: 02.11.1989  
Place of birth: Rome (Italy)

## Education and professional experience

- 05/2020 – present                      Product engineer at DriV Incorporated (Glinde, Germany)  
Topics: Core development of new friction products in cooperation with external partners, investigate raw material specific properties on tribological effects by systematical, statistical approaches, transition from prototyping into manufacturing globally
- 09/2016 – 04/2020                      Engineer employee at DIK (Deutsche Institut für Kautschuktechnologie e.V.) (Hannover, Germany)  
Ph.D. Student - Mechanical engineering at Gottfried Wilhelm Leibniz Universität Hannover  
Topics: Rubber friction, Dynamic mechanical response of elastomers, FEM, static and dynamic contact mechanisms, material characterization
- 01/2016 – 07/2016                      Internship at BRIDGESTONE TCE S.p.A aimed at preparing the Master's Thesis  
Topic: Optimization and validation of friction models by considering a combined experimental and numerical approach
- 10/2013 – 07/2016                      Master's Degree in Mechanical Engineering (University of Rome Tor Vergata)
- 10/2007 – 07/2013                      Bachelor's Degree in Mechanical Engineering (University of Rome Tor Vergata)